Dissertation

submitted to the

Combined Faculties of the Natural Sciences and Mathematics

of the Ruperto-Carola-University of Heidelberg, Germany.

for the degree of

Doctor of Natural Sciences

Put forward by

Christian Roca Catalá

born in Valencia

Oral examination: 22.V.2019

Optimization of the simulation framework in the Stereo Experiment to characterize the detector response and optical properties of the liquid scintillators

Referees:

Prof. Dr. Dr. h.c. Manfred Lindner

JProf. Dr. Loredana Gastaldo

Twinkle, twinkle, little star...
Though I don't know what you are,
twinkle, twinkle, through the night...

Per a la iaia que m'ensomiava en bata blanca.

Zusammenfassung

Das **Stereo** Experiment nimmt eine Pionierrolle innerhalb der Anstrengungen zum Test der sterilen Neutrino Hypothese in der Nähe von Kernreaktoren ein. Stereo beobachtet seit 2016 Neutrinosignale in etwa 10 m Abstand vom Forschungsreaktor am Institut Laue-Langevin in Grenoble, Frankreich. Die zellweise Segmentierung des Detektorvolumens erlaubt eine Analyse der Energiespektren bei unterschiedlichen Abständen. Dadurch kann die Kompatibilität des beobachteten Flusses mit unterschiedlichen Oszillationshypothesen getestet werden. Hierzu stehen entsprechende Monte Carlo Simulationen inklusive der physikalischen Prozesse im Detektor zur Verfügung. Diese Arbeit beschäftigt sich mit der durchgeführten Feinabstimmung des Simulationsmodells in **Stereo**. Speziell wurden Produktion, Transport und Quenching des Szintillationslichts im Detektor so angepasst, dass eine Übereinstimmung mit den Kalibrationsdaten vorliegt. Dies beinhaltet die Charakterisierung der Lichtausbeute, der Abschwächlänge und der Quantenausbeute der Komponenten im Flüssigszintillator. Es wurde ein neues optisches Modell für die Trennwände implementiert, das den beobachteten Anstieg des Lichtaustauschs zwischen den Detektorzellen korrekt berücksichtigt. Nichtlinearitäten in der Energieskala des Detektors wurden ebenfalls untersucht und die Simulation kann diese mit Abweichungen unterhalb von einem Prozent wiedergeben. Der Prozess des Anpassens resultierte in einer hervorragenden Übereinstimmung der rekonstruierten Energie des Signals zwischen Kalibrationsdaten und Simulationen. Dadurch ist **Stereo** in der Lage einen beträchtlichen Anteil der erlaubten Kombinationen der Oszillationsparameter inzwischen auszuschließen.

Abstract

The **Stereo** experiment is one of the pioneering efforts to test the light sterile neutrino hypothesis at short baselines from nuclear reactors. Placed at $\sim 10\,\mathrm{m}$ from the Institut-Laue-Langevin research reactor in Grenoble, France, **Stereo** is observing $\bar{\nu}_e$ signals since 2016. Given its cell-wise segmented volume, **Stereo** can perform spectral analyses at different baselines. This allows to test the compatibility of the observed flux with different oscillatory hypotheses, provided by a dedicated Monte Carlo simulation of the detector and the physics within. This thesis addresses the process of fine tuning performed on the simulation framework of **Stereo**. In particular, the production, transport and quenching of scintillation light in the detector has been adjusted to match calibration data, including the characterization of the light yield, attenuation length and fluor quantum yields of the liquid scintillator components. A new optical model for the separation walls has been implemented, successfully accounting for the increased light cross-talk between cells observed. Energy non-linearities in the response of the detector have also been investigated and reproduced in the simulation to the subpercent level. The process of tuning has lead to an excellent agreement of the reconstructed energy signal between calibration data and simulations, allowing **Stereo** to exclude a considerable portion of the allowed oscillation parameter space.

Declaration of Authorship

I, Christian Roca Catalá, declare that this thesis titled, "Optimization of the simulation framework in the **Stereo** Experiment to characterize the detector response and optical properties of the liquid scintillators" and the work presented in it are my own. I confirm that:

- This work was done wholly or mainly while in candidature for a research degree at this University.
- Where any part of this thesis has previously been submitted for a degree or any other qualification at this University or any other institution, this has been clearly stated.
- Where I have consulted the published work of others, this is always clearly attributed.
- Where I have quoted from the work of others, the source is always given. With the exception of such quotations, this thesis is entirely my own work.
- I have acknowledged all main sources of help.
- Where the thesis is based on work done by myself jointly with others, I have made clear exactly what was done by others and what I have contributed myself.

Signed:

Date: 11.III.2019

Contents

List of Abbreviations

STEREO	STErile neutrino REactor Oscillation experiment
MPIK	Max-Planck-Institut für Kernphysik, Heidelberg
LPSC	Laboratoire de Physique Subatomique et de Cosmologie, Grenoble
LAPP	Laboratoire d'Annecy-le-Vieux de Physique des Particules, Annecy
CEA	Commissariat à l'Énergie atomique et aux Énergies Alternatives, France
ILL	Intitut Laue-Langevin
Phase I	first period of data taking
Phase II	second period of data taking
RAA	Reactor Antineutrino Anomaly
SBL	Short BaseLine ($\gtrsim 100\,\mathrm{m}$)
VSBL	Very Short BaseLine ($\lesssim 100\,\mathrm{m}$)
IBD	Inverse Beta Decay
`LS`	Liquid Scintillator
LAB	Linear AlkylBenzene
PXE	PhenylXylylEthane
DIN	Di-IsopropylNaphthalene
PPO	2,5-DiPhenylOxazole (PPO)
bis-MSB	4-bis-(2-MethylStyryl)Benzene
WLS	WaveLength Shifter
`TG`	TarGet volume in **STEREO** composed by six cells
`GC`	Gamma Catcher volume in **STEREO** composed by four cells
`Cell1` - `Cell6`	six cells composing the `TG` volume
`GCFront`	short `GC` cell at the front of **STEREO**
`GCBack`	short `GC` cell at the back of **STEREO**
`GCD19`	long `GC` cell facing the D19 experiment
`GCIN20`	long `GC` cell facing the IN20 experiment
PMT	PhotoMultiplier Tube
source cell	volume where a source has been deployed
intermediate cell	volume without internal calibration tube
top	source located at 80 cm from the bottom of the calibration tube
middle	source located at 45 cm from the bottom of the calibration tube
bottom	source located at 10 cm from the bottom of the calibration tube
`MC`	ROOT tree containing true event information, only for simulations
`DATA`	ROOT tree containing PMT readout event information
$\mathcal{A}_{bot}^{top}$	asymmetry between responses at *top* and *bottom*
$\mathcal{A}_{bot}^{mid}$	asymmetry between responses at *middle* and *bottom*
$\mathcal{A}_{mid}^{top}$	asymmetry between responses at *top* and *middle*
PSD	Pulse Shape Discrimination
`FED`	Full-Energy Deposition in a single cell

SPE	Single Photo-Electron
PE	PhotoElectron (unit)
light leaks	scintillation light cross-talk between cells
$\ell\ell_{ij}$	evaluation of *light leaks* between `Cell`j and `Cell`i
energy leaks	particle of interest escaping volume
anti-Compton cut	event selection applied to cut escaping gammas

`HpM`	Height probability p Model for separation walls between cells
`LhM`	Height probability p Model for separation walls between cells
`kB`	Birks' parameter that quantifies the effect of non-linear quenching of light
$\texttt{kB}^{\mathrm{GC}}$	effective `kB` in the `GC LS`
$\texttt{kB}_{\mathrm{simu}}$	`kB` computed to the simulation of a certain set of sources
`SecM`	Stitched energy-charge Method used to estimate `kB`
`cc`	`c`alibration `c`oefficients

Introduction

Throughout the years, neutrinos have been a challenging particle to measure and catalog. They have been observed coming from all parts of the universe: from the depths of the Earth to the distant supernovas. From the very beginning, nuclear fission reactors have become a popular and widely used source of neutrinos to explore the oscillation phenomenon. However, observations through the past years have shown that the current understanding of neutrino production and propagation from nuclear reactors is insufficient to explain the observed antineutrino fluxes at short baselines. Coined as the reactor antineutrino anomaly in 2011, these measurements are characterized by about 3σ deficit between the observed and the expected antineutrino events. The hypothesis of neutrino oscillations towards light sterile states has gained popularity in recent years as a candidate to explain this anomaly.

The **Stereo** experiment has set the course to observe such oscillations at very close distances from the core of the Institut-Laue-Langevin research reactor, France. With an active volume of 2000 l of gadolinium-loaded liquid scintillator, it measures inverse beta decay processes induced by $\bar{\nu}_e$ coming from nuclear fissions at the core. The segmentation of this volume allows to investigate the energy spectra of neutrinos at different distances from the source. The observation of spectral distortions would be the smoking gun of a sterile neutrino oscillation signal. In order to quantify the compatibility of these distortions with different oscillatory hypothesis, an accurate simulation of the neutrino energy spectrum is required. The optimization of the simulation framework in **Stereo** has been the main goal of the thesis described in this manuscript, with special attention and effort put on the fine-tuning of the response of the detector.

The first two chapters constitute the introduction and motivation of the **Stereo** experiment. Chap. 1 gives a general description of neutrinos through an historical point of view, stressing the importance of the discrepancies and anomalies in the characterization of neutrinos. Chap. 2 reviews the state of the art of reactor neutrino searches, from early experiments measuring antineutrino fluxes to high precision experiments measuring the antineutrino energy spectrum at different baselines. The position of **Stereo** among these experiments is highlighted.

A general description of the **Stereo** experiment and its location is given in Chap. 3. There, the main features of the detector and the different backgrounds are described. In addition, a detailed review of the liquid scintillator, the light production mechanism and its propagation through the medium are also given. Chap. 3 also explains how the different volumes of the **Stereo** detector are calibrated, the periodicity and purposes of the different types of calibrations and the mechanical systems involved.

The thorough study and optimization of the Monte Carlo simulation framework in **Stereo** described along this manuscript has been a pivotal part on the development

of the present thesis. An accurate description of the detector and its physics through simulation is crucial to understand the observed neutrino signals and to draw quantitative statements on whether sterile oscillations are present or not. Chap. 5 details how `Geant4` is used to simulate the **STEREO** detector and the physics happening within it. In particular, it is described how scintillation light production and propagation is simulated. In this chapter it is also described the way calibration systems and sources are defined in the simulation with special interest put on the ^{54}Mn source, commonly used along this thesis in multiple analysis. Also in Chap. 5, and as a result of increase of the light cross-talk between cells due to unexpected mechanical defects during the first phase of data taking, emphasis is put on properly simulate the light collection of the different volumes. For this purpose, two alternative optical models are implemented to reproduce the effects observed in the separation walls between cells. The effect of these models is also analyzed in terms of the vertical asymmetry of the detector response, followed by fine tuning of the attenuation length of the liquid scintillator. The mechanical defects observed in the acrylic buffer of two cells during the first phase of **STEREO** are also implemented in the simulation.

In order to perform a spectral analysis for neutrino events, an accurate energy scale has been developed in **STEREO**. The energy reconstruction algorithm is fed with multiple experimental parameters. In Chap. 6 it is described how, during this thesis, the charge-energy conversion factors are systematically calculated from calibration data. At the end of the chapter, the monitoring of different experimental observables is shown and discussed for the whole range of taken data. The energy reconstruction is a crucial element in the neutrino analysis of **STEREO** and it is fed with multiple experimental parameters. A thorough analysis of the energy non-linearities of the response of the liquid scintillator is performed in Chap. 7. There, an algorithm to extract the quenching curve for data and simulation is developed and tested with calibration sources. By fitting their comparison curves, quantitative information is extracted, defining then an effective parametrization of the quenching in the simulation.

"It all began with a letter"

Shinomura

Chapter 1

Neutrino physics

The main purpose of this chapter is to introduce the neutrinos and to give a glimpse of the physics surrounding them. Since its discovery, the understanding of neutrino physics have evolved from assuming them as massless and undetectable ghosts to flavor-changing massive particles. This ever-changing description of neutrinos is much better understood when reviewing the different challenges and inconsistencies faced by physicists along the 20th century. For this reason, a particular focus on the historical motivation of neutrino physics is conveyed throughout the chapter. In Sec. 1.1, a passage through the major turning points around the discovery of the neutrino, its characterization and its different flavors, is given. In Sec. 1.2 the role of neutrinos within the Standard Model is described, including the current knowledge on their interactions and the unresolved questions. Finally, Sec. 1.3, flavor oscillations and their discovery through solar and atmospheric neutrinos are reviewed, together with their implications on the mass of the neutrinos. The past and current analysis on reactor neutrinos is left for Chap. 2.

1.1 A brief history of how neutrinos came to be

The history of neutrinos starts with the discovery of α and β rays by Ernst Rutherford [1] in 1899, initially categorized by their penetration and ionization power. Soon after the characterization of the γ rays, the particle trinity $\{\alpha, \beta, \gamma\}$ was completed. These discoveries provoked a strong interest of the community in natural radioactivity, which lead to multiple attempts to observe and catalog the properties of all types of radiation.

Different experiments on α and γ radiation presented sharply-defined decay energies connected always to the mass difference between the initial and final state of the decaying isotope. However, an initial measurement of the kinetic energy of β particles performed by Otto Hahn in 1911 already showed multiple lines of diffuse background [2]. A few years later, James Chadwick observed that this background was indeed part of the continuous spectrum defining the kinetic energy of β rays [3]. This caused confusion in the community given that a two-body decay would imply a fixed energy line for electrons. Such observation was widely reproduced for many isotopes, promptly triggering controversy about the nature of such decays. Many hypothesis were discussed during the first quarter of the century to explain a continuous spectra.

Another discrepancy emerged in 1927 with the introduction of the concept of particle spin by Wolfgang Pauli [11]. Under his new quantum framework, if an electron were to be emitted as the only spin-1/2 particle while the nucleon remained with a integer spin, then overall spin would not be conserved. In a famous letter written in 1930 [7],

he attempted to explain both problems by postulating the existence of a new spin-1/2, neutral and extremely light particle. Such particle would be emitted during the β decay together with the electron, conserving thus energy, momentum and spin. This particle was originally baptized by PAULI as the *neutron*, term that would be changed soon after by ENRICO FERMI to neutrino to better describe its light nature.

During the upcoming years the understanding of the subatomic world was continuously challenged by new theories and discoveries. Parallely to PAULI, an analogous spinorial formalism was developed by PAUL DIRAC. His work culminated in the Dirac equation [6] where special relativity and quantum physics were unified for the first time to describe free motion of spin-1/2 particles like wavefunctions extended through the spacetime. This equation predicted the existence of antimatter, implying that the electron has a positively charged partner: the positron. In 1932, both the positron and the neutron were discovered by CARL ANDERSON [12] and CHADWICK [13], respectively. These discoveries allowed ENRICO FERMI to formulate his β decay model [8] two years later, where he combined all the recently discovered pieces of the puzzle. This formalism was inspired on the concept of charged currents developed some time before by DIRAC for quantum electrodynamics [5]. In the theory of FERMI, a four-fermion set of currents would interchange weak charges in a point-like interaction which intensity is governed by the Fermi constant G_F. Under this assumption, all possible interactions are essentially described by the same underlying processes. However, kinematic factors involving the distribution of available energy and momentum in the initial and final states affect the overall reaction rate. The β decays were finally described as,

$$n \to p + e^- + \nu \,,$$

where the neutrino $\nu \equiv \bar{\nu}_e$ is introduced for the first time as a flavorless and unique particle. The formalism developed by FERMI gave the tools to calculate observable rates and lifetimes from many processes, and in some cases even their prediction, like for the electron capture [9]. This model built the foundations to what in the future would become as the electronweak theory that unifies the electromagnetic and weak interactions [24, 26].

Since the discovery of nuclear fission in 1938, scientists were aware of the incredibly intense flux of antineutrinos that had to be produced in this type of processes. However, their detection required an immense amount of material to interact with. The logistics that lead to the discovery of the neutrino still had to wait almost two decades. During the early 1950s, several groups started unveiling the deep potential of organic liquid scintillators to detect ionizing particles. Their high concentration of hydrogen atoms made them an excellent target for Inverse Beta Decay (IBD) interactions,

$$\bar{\nu}_e + p \to n + e^+ \,,$$

provided that the positron generates a scintillation signal inside the liquid. It was then when CLYDE COWAN and FRED REINES thought that they could use it to observe neutrinos from nuclear fissions [14]. The deep implication of REINES in the Manhattan Project, Los Alamos, played an important role on their initial choice of using a nuclear fission bomb as the neutrino source. However, the final approach was to opt for a more stable setup that could operate continuously. Thus, in 1953 COWAN, REINES et al. set to observe neutrinos coming from decaying fission fragments from uranium at the Hanford site, U.S. Soon after the experiment was boved to the Savannah River Power

Plant, U.S [14]. Their detector was based in three main tanks full of liquid scintillator were the neutrino would interact. To better discriminate the neutrino signal from the background, two additional tanks filled with cadmium chloride ($CdCl_2$) loaded-water installed between the scintillator volumes. The task for these was to moderate the neutrons from the IBD and let them be captured by the cadmium. The capture is followed by a release of energy as a gamma cascade that can be detected and characterized. The average time between the flash of light from the positron-electron annihilation and that from the neutron capture is a few microseconds. Electronic circuits were designed to detect this delayed-coincidence signature and provide a powerful mean to discriminate IBD signals from background noise. This mechanism was pivotal to the interpretation of nuclear reactors as useful sources of neutrinos. In Chap. 2 an extensive review of nuclear reactor neutrino experiments is given, focusing on the neutrino oscillation observation and the search for sterile neutrinos.

The neutrino reaction rate observed in the Reines and Cowan experiment was in agreement with the predicted cross section in the order of 10-20 barn [15], proclaiming thus the existence of the neutrino particle. This lead to a delayed Nobel Prize award to Reines in 1995, and a posthumous recognition to a by the time deceased Cowan. Their experiment funded the basis of modern neutrino search using organic liquid scintillators, and to this date most of reactor neutrino experiments, including **Stereo**, use a similar detection principle and coincidence search.

Several experimental inconsistencies on interaction branching ratios made physicist hypothesize about an unobserved second type of neutrino. The confirmation of its existence came by the hands of Leon Lederman, Melvin Schwartz, Jack Steinberger et al. in 1962 when they performed the first direct detection of a muon neutrino ν_μ. They were pioneers on the production of neutrinos via an accelerator experiment. They managed to focus a proton beam onto a beryllium target. The mesons produced from this collision were guided into a decay tunnel where they were supposed to decay in flight into neutrinos,

$$\pi^\pm \to \mu^\pm + \overset{(-)}{\nu}_\ell \,.$$

The ℓ denotes the type of neutrino, of course still unknown at that time. Finally, the smoking gun came from the direct observation of the neutrino interaction,

$$\bar{\nu}_\ell + p \to n + \ell^+ \,,$$
$$\nu_\ell + n \to p + \ell^- \,,$$

where $\ell^\pm$ denotes the corresponding charged lepton. Since only muons and no electrons where observed in the final state, it had to be concluded that these neutrinos where different from the already known electron neutrinos measured by Reines, Cowan et al. A second type of neutrino had been discovered [16], fact that earned Lederman, Schwartz and Steinberger a Nobel prize in 1988.

The third charged lepton, later called the τ lepton, was discovered in 1975 by the team of Martin Lewis Perl using the SPEAR e^+e^- colliding ring at the Stanford Linear Accelerator Center (SLAC). Coincidentally, Perl was co-laureate together with

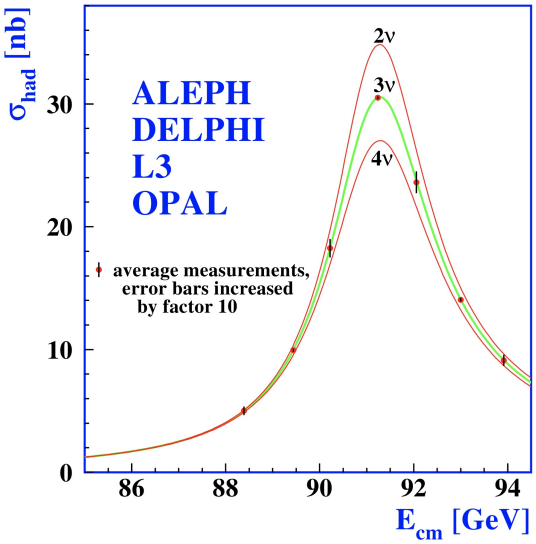

Figure 1.1: Cross section measurement in $e^-e^+ \to$ hadron reactions of the four LEP detectors, ALEPH, DELPHI, OPAL and L3, at energies around the Z resonance. Data compared to expected cross-section assuming different amounts of weakly interacting neutrinos that couple with the Z boson. [19].

Reines for the Nobel prize in 1995 for this discovery. Soon after the first observation of τ, continuous measurements of its decays immediately evidenced missing energy and momentum. This fact was attributed to the existence of a third type of neutrino, already coined as ν_τ. Reaffirming these observations, measurements of the decay width Γ_Z of the Z boson in the late 1980s showed indications of a missing neutrino. This decay width can be expressed as,

$$\Gamma_Z = \Gamma_{ee} + \Gamma_{\mu\mu} + \Gamma_{\tau\tau} + \Gamma_{\text{had}} + \Gamma_{\text{inv}} \,,$$

where the first three terms are the widths of decays into e, μ and τ leptons and Γ_{had} is the sum of the widths of decays into u, d, s, c and b quarks. The invisible width $\Gamma_{\text{inv}} = N_\nu \Gamma_{\nu\nu}$ covers the decays into light neutrinos with N_ν the number of light ($m_\nu < m_Z/2$), weakly interacting neutrino generations, which was in principle unknown. This number can be expressed in terms of hadron and charge lepton observables [20], and thus can be inferred from measurements. In 1989, all four experiments in the Large Electron Positron collider (LEP) at CERN presented a value of $N_\nu = 3.10 \pm 0.04$ [19], displayed in Fig. 1.1. However, it was not until the early 2000s when a direct observation of the third kind of neutrino by the DONUT experiment at Fermilab confirmed the existence of at least three neutrinos [18]. In a similar fashion as for the observation of ν_μ, neutrino beams from accelerator were used. 800 GeV protons were focused by the Tevatron and made collide with a tungsten target. From these collisions, the charmed mesons D were heavy enough to decay into

$$D_S \to \tau + \nu_\tau \,.$$

The observation of a τ as the only lepton in the interaction vertex would lead unequivocally to the observation of a charged current interaction with ν_τ. With a observation of only four events out of 203 neutrino interaction, and against an expected background of < 0.2 events, the last particle of the Standard Model was confirmed to

exist.

In 2006, the final determination of $N_\nu = 2.9841 \pm 0.0083$ was presented in conjunction by all four experiments at LEP [20], accounting for the whole five year period of data taking at the Z resonance. This measurement perfectly agrees with the current understanding of the Standard Model and most of the observations to this date. As mentioned before, this does no exclude the possible existence of either heavy, or light but non-interacting neutrinos. The latter are commonly known as sterile neutrinos and findings of recent reevaluations of reactor neutrino experiments, described in Sec. 2.3.1, may be interpreted as indications for their existence. The confirmation or refutation of this hypothesis is one of the goals of the **STEREO** experiment.

1.2 Neutrinos within the Standard Model

1.2.1 Introduction to the Standard Model

The Standard Model (SM) is the current framework describing modern particle physics. It is a quantum field theory that describes three of the four fundamental interactions: strong, weak and electromagnetic. It also categorizes the fundamental particles into spin-1/2 fermions as leptons and quarks, and integer spin bosons. One of the fundamental principles that defines the SM is its invariance under local gauge transformations. To ensure such invariance a so-called *gauge* boson needs to be attributed as the fundamental force carrier between interacting particles. Because of the underlying gauge symmetry of the theory and according to the theorem of NOETHER [4], each of the three fundamental interactions must have an associated conserved Noether charges. For the strong interaction, defined by the SU(3) unitary group of transformations, this charge is known as *color* and it is carried by gluons. Electromagnetic and weak interactions are mathematically unified under a single $\mathrm{SU}(2)_L \otimes \mathrm{U}(1)_Y$ transformation group. This last interaction is the only one experienced by neutrinos and will be reviewed in detail in Sec. 1.2.2.

1.2.2 Electroweak interactions

The first attempt to describe weak interactions can be considered to be the beta decay theory developed by FERMI [8]. Throughout the next decades different measurements shown consistently that, unlike strong and electromagnetic interactions, weak decays seemingly violated parity symmetry $\mathcal{P}$ [21]. A $\mathcal{P}$ transformation of a process inverts the space coordinates of the events in it $P(x, y, z) \rightarrow (-x, -y, -z)$. The violation of this supposedly fundamental symmetry of nature would change the perception of how reality shapes, and thus it needed to be proven. During the early 1950s, the theoretical physicists TSUNG DAO LEE and CHEN NING YANG [21] observed clear evidences of this on Kaon decays, and proposed an experimental setup to specifically test $\mathcal{P}$ violation that was carried out by the team of CHIEN-SHIUNG WU. They cooled down a ^{60}Co source to cryogenic temperatures and polarize it with an external magnetic field, and observed the direction of the electron emitted from the β decay, which was expected to be isotropic if parity were to be conserved. The results showed that electrons were most commonly emitted contrary to the polarization of the atoms. Defining the helicity $\mathcal{H}$ of a particle as the projection of its spin along its direction of motion,

Table 1.1: Classification of fermions in the SM according to their representation under $SU(2)_L$ transformations.

	1st Generation	2nd Generation	3rd Generation	Isospin
Left-handed quarks	$\begin{pmatrix} u \\ d \end{pmatrix}$	$\begin{pmatrix} c \\ s \end{pmatrix}$	$\begin{pmatrix} b \\ t \end{pmatrix}$	$\begin{pmatrix} 1/2 \\ -1/2 \end{pmatrix}$
Right-handed quarks	u_R, d_R	c_R, s_R	b_R, t_R	0
Left-handed leptons	$\begin{pmatrix} e \\ \nu_e \end{pmatrix}$	$\begin{pmatrix} \mu \\ \nu_\mu \end{pmatrix}$	$\begin{pmatrix} \tau \\ \nu_\tau \end{pmatrix}$	$\begin{pmatrix} 1/2 \\ -1/2 \end{pmatrix}$
Right-handed leptons	e_R	μ_R	τ_R	0

$$\mathcal{H} = \vec{s} \cdot \frac{\vec{p}}{|p|},$$

it can be concluded that electrons observed by Wu et al. had predominantly negative, or left-handed, helicities. From Wu's experiment can also be concluded that, by virtue of momentum conservation, antineutrinos were emitted opposite to the electrons displaying thus a right-handed helicity. This displayed a maximal violation of the symmetry [22] and also proved inadvertently that the universe is left-handed. The discovery of a broken fundamental symmetry took the scientific community off-guard and shook the grounds of the understanding of nature.

The direct measurement of the helicity of neutrinos came soon after in 1957 by the hands of Maurice Goldhaber, Lee Grodzins and Andew Sunyar [23]. In their experiment a sample of ^{152}Eu is set to decay via electron capture into an excited state of ^{152*}Sm. From spin and momentum conservation the two products ^{152*}Sm and ν_e have opposite polarization and direction. By measuring the momentum of the recoiling nucleus and the polarization of its de-excitation gamma, Goldhaber and company could measure the left-handed helicity of neutrinos.

To account for all the new findings on the weak interaction, in 1958 Richard Feynman and Murray Gell-Mann established the mathematical structure of the weak interaction in what is known as V-A, or vector minus axial vector, theory [24]. Under this extended version of Fermi's theory, only particles (antiparticles) with left (right)-handed chirality could interact weakly. The chirality of a particle is quantum mechanical property that defines the way it transforms under Poincare transformations. In a way, it can be considered as the Lorentz invariant analogue to helicity. For massless particles both chirality and helicity are equivalent. This theory was highly successful accounting for parity violation. However, the absence of a description for a force carrier and other mathematical difficulties prevent this from being a complete theory. It would have to wait until the 1960s when Sheldon Glashow [25] and Abdus Salam [26] decided to work with a combination of two symmetry groups: $SU(2)_L \otimes U(1)_Y$. The corresponding gauge bosons for this symmetry are the three W bosons of weak isospin from $SU(2)_L$ (W_1, W_2, and W_3), and the B boson of weak hypercharge from $U(1)_Y$. The correspondent conserved charges are the weak isospin $\vec{T} = \{T_1, T_2, T_3\}$ and the hypercharge Y. Fermions could then arranged in left-handed doublets and right-handed singlets, according to their weak isospins as shown in Tab. 1.1.

Indeed, this classification responded clearly to the fact that only left-handed fermions

and right-handed antifermions had been observed participating in weak interactions and thus would not be invariant under $\mathrm{SU}(2)_L \otimes \mathrm{U}(1)_Y$ transformations. The opposite happens for right-handed fermions and left-handed antifermions, remaining invariant under this symmetry transformations. This classification required for more convenient decomposition of the Dirac spinorial ψ wavefunctions into right and left-handed parts

$$\psi = \psi_R + \psi_L \,,$$

so each one would transform accordingly under $\mathrm{SU}(2)_L \otimes \mathrm{U}(1)_Y$

$$\begin{aligned} \psi_L &\xrightarrow{\mathrm{SU}(2)_L \otimes \mathrm{U}(1)_Y} \psi'_L \equiv \mathrm{e}^{i\vec{\alpha}\cdot\vec{T} + i\beta Y} \psi_L \,, \\ \psi_R &\xrightarrow{\mathrm{SU}(2)_L \otimes \mathrm{U}(1)_Y} \psi'_R \equiv \mathrm{e}^{i\beta Y} \psi_R \,. \end{aligned}$$

However, despite the huge success achieved by the electroweak unification it still had to deal with a compelling explanation for the mass of the fermions. The most general fermionic mass term for some Dirac field is given by

$$\mathcal{L}_{\mathrm{mass}} = m_D (\overline{\psi}_R \psi_L + \psi_R \overline{\psi}_L) \,,$$

where m_D is the Dirac mass of such field. This term is clearly non-invariant under SU(2) transformations and therefore cannot be taken into account in the gauge theory. Under this assumption fermions must be massless, fact that contradicts all empirical evidence. Similarly, mediator gauge bosons W_1, W_2, W_3 and B are also defined massless. Although these bosons had not been observed directly yet, the intrinsic weakness and short-range of the weak force firmly suggested that they had to be massive. This was already pointed out in 1939 by Oskar Klein [10], who estimated their mass to be approximately 100 times larger that the proton mass. To resolve the mass problem without breaking gauge invariance, Steven Weinberg [27] proposed to include into the theory the concept of Spontaneous Symmetry Breaking (SSB) of $\mathrm{SU}(2)_L \otimes \mathrm{U}(1)_Y$ into $\mathrm{SU}(2)_L$ and $\mathrm{U}(1)_{QED}$, which had been recently developed independently by Peter Higgs [29], by Robert Brout and Francois Englert [30], and by Gerald Guralnik, Tom Kibble and Carl Hagen [31]. This formalism is often known as the Glashow-Weinberg-Salam (GWS) formalism. The simplest approach starts by introducing a new $\mathrm{SU}(2)_L$ isospin doublet

$$\Phi = \begin{pmatrix} \phi^+ \\ \phi^0 \end{pmatrix} \,,$$

where ϕ^+ and ϕ^0 are the charged and neutral scalar fields respectively. The gauged scalar Lagrangian can be written as

$$\mathcal{L}_{\mathrm{Higgs}} = \underbrace{(D^\mu \Phi)^\dagger D_\mu \Phi}_{\mathcal{L}^{\mathrm{Kin}}_{\mathrm{Higgs}}} - \underbrace{\mu^2 \Phi^\dagger \Phi - h(\Phi^\dagger \Phi)^2}_{-V(\Phi)} \,, \tag{1.1}$$

where both terms of the Lagrangian are built gauge invariant. The potential term $V(\Phi)$, resembling a parabolic function, requires $h > 0$ to be bound from below. At the same time, for a parameter $\mu^2 > 0$ the potential has only the trivial minimum $\Phi = 0$ and therefore it is required that $\mu^2 < 0$. In this scenario $V(\Phi)$ has an infinite set of degenerate states with minimum energy, satisfying

$$(\Phi_0^\dagger \Phi_0) = \frac{-\mu^2}{2h} = \frac{v^2}{2}\,,$$

where $v = \sqrt{-\mu^2/h}$ is the so-called vacuum expectation value. The degeneracy of ground states comes straight from the fact that $v \neq 0$, and thus all points in the complex plane with radius $v/\sqrt{2}$ satisfy the minimum condition. Once a particular ground state is chosen, the $\mathrm{SU}(2)_L \otimes \mathrm{U}(1)_Y$ symmetry gets spontaneously broken to the electromagnetic subgroup $\mathrm{U}(1)_{QED}$. The latter remains a true symmetry of the vacuum by construction, so only the neutral scalar field can acquire a vacuum expectation value. Now, the scalar doublet can be written as an excitation from the ground state

$$\Phi_0 = \frac{1}{\sqrt{2}} \begin{pmatrix} 0 \\ v + H(x) \end{pmatrix}$$

where $H(x)$ is the excitation of the field, corresponding to the Higgs boson. The masses of the gauge bosons are derived from the kinetic term of the lagrangian of the Higgs field [32],

$$\mathcal{L}^{\mathrm{Kin}}_{\mathrm{Higgs}} = (D^\mu \Phi)^\dagger D_\mu \Phi = \frac{1}{2}\partial_\mu H \partial^\mu H + \left(\frac{g^2}{4} W_\mu^\dagger W^\mu + \frac{g^2}{8\cos^2\theta_W} Z_\mu Z^\mu \right) .$$

Here g is the weak interaction coupling constant, θ_W is the Weinberg angle and W_μ, Z_μ are the gauge fields. The following rotation has been performed to the neutral-current bosons

$$\begin{pmatrix} Z \\ \gamma \end{pmatrix} = \begin{pmatrix} \cos\theta_W & \sin\theta_W \\ -\sin\theta_W & \cos\theta_W \end{pmatrix} \cdot \begin{pmatrix} W_3 \\ B \end{pmatrix} ,$$

while $W^\pm = \frac{1}{\sqrt{2}}(W_1 \mp i W_2)$. The vacuum expectation value of the neutral scalar Φ has generated a quadratic term for the $W^\pm$ and Z, giving them mass without violating gauge invariance. The remaining neutral boson γ is still massless and corresponds to the gauge boson of the symmetry group $\mathrm{U}(1)_{QED}$ which can be identified as the photon. The masses of Z and $W^\pm$ bosons can be related by $\cos_W$ as

$$m_Z \cos\theta_W = m_W = \frac{1}{2} v g\,.$$

However, θ_W nor m_W and m_Z are predicted by the model, and had to wait a decade to be measured experimentally. In 1983, the Super Proton Synchrotron (SPS) at CERN observed unequivocally the resonances of W [33, 34] and Z[35, 36] bosons. Carlo Rubbia, current spokespersons of the UA1, and Simon van der Meer, who developed the stochastic cooling technique for the UA2 experiment, were promptly awarded with a Nobel Prize in 1984.

Fermions also acquire mass by coupling with the Higgs field. It has been seen previously that a standard fermion mass term is not allowed due to gauge invariance. However, after the introduction of an additional scalar doublet into the model, a following gauge-invariant fermion-scalar coupling can be constructed in the form of

$$\mathcal{L}_{Yuk} = -y(\overline{\psi}_L \Phi \psi_R + \overline{\psi}_R \Phi \psi_L)\,,$$

for each fermion field. The free parameters y are called the Yukawa couplings after Hideki Yukawa work on elementary particles in 1934 [28]. This term couples left and right handed fermions to the Higgs field, and if the doublet has a non-zero v fermions can acquire a finite mass. For any charged lepton,

$$\begin{aligned}\mathcal{L}_{\text{Yuk, lep}} &= -\frac{y_\ell}{\sqrt{2}}\left[(\nu_\ell, \bar{\ell})_L \begin{pmatrix} 0 \\ v+H \end{pmatrix} + \bar{\ell}_R(0, v+H)\begin{pmatrix}\nu_\ell \\ \ell\end{pmatrix}_L\right] \\ &= -\frac{y_\ell v}{\sqrt{2}}\bar{\ell}\ell - \frac{y_\ell H}{\sqrt{2}}\bar{\ell}\ell\,,\end{aligned}$$

with identical structure for the quark sector. In $\mathcal{L}_{\text{Yuk, lep}}$, the masses of the charge leptons are given by $m_\ell = \frac{y_\ell v}{\sqrt{2}}$, while the term $\frac{y_\ell H}{\sqrt{2}}$ represents the strength of the lepton-Higgs interaction. Since the Yukawa couplings y_ℓ are free parameters in this theory, the SM cannot predict nor explain the mass of any fermion. However, no term has been explicitly written for neutrino fields. In fact, since there has been no observational proof of the existence of ν_R or $\bar{\nu}_L$, neutrinos are technically not able to couple with the Higgs. Unfortunately for the SM, neutrinos do have mass. In Sec. 1.3.1 it is explained how neutrinos were found to be massive particles via flavor oscillations, and in Sec. 1.3.2 some popular mass-generation mechanisms are discussed.

1.3 Neutrinos beyond the Standard Model

1.3.1 Flavor oscillations

In the early 1960s, weak interactions and neutrino physics were quite well understood by the recently developed GSW formalism. While charged fermions finally acquired mass via the Higgs mechanism, the absence of right-handed neutrinos made them unable to couple with the Higgs field and thus remained massless. In principle this was not a problem, specially since beta decay experiments consistently shown that neutrinos had to have a tiny mass, if any. However, some inconsistencies started arising with the first detection of electron neutrinos arriving from the core of the sun. In 1970, the Homestake experiment lead by Raymond Davis [55] found that indeed the flux of these neutrinos was halved with respect to what was predicted by the standard solar model. This discrepancy, which became known as the solar neutrino problem, remained unresolved for approximately thirty years, while possible problems with both the experiment and the solar model were investigated, but none could be found.

A decade prior the Homestake experiment, Bruno Pontecorvo had predicted the phenomena known as neutrino oscillations [43, 44]. His assumption required for at least two different families of neutrinos, with non-zero but indistinguishably different masses. According to this idea, electron neutrinos from the core of the sun could oscillate into undetectable flavour on their flight to Earth, creating a visible deficit on their flux. Right after the first observation of muon neutrinos, in 1962 Ziro Maki, Masami Nakagawa and Shoichi Sakata refined the model and extended it to multiple families of neutrinos [45]. Once the first evidences of the neutrino solar problem start appearing, the Pontecorvo-Maki-Nakagawa-Sakata model of neutrino oscillations gain relevance. The concept implies that neutrino eigenstates $|\nu_\alpha\rangle$ appearing in weak interactions are not the same as the eigenstates defining their propagation through space $|\nu_i\rangle$, which are

also the eigenstates with well-defined mass m_i and kinematics. Like for any change of basis in a Hilbert space, both sets of eigenstates can be connected via a complex unitary matrix $\mathbf{U}_{\text{PMNS}}$,

$$|\nu_\alpha\rangle = \sum_i \mathbf{U}_{\alpha i} |\nu_i\rangle \quad |\nu_i\rangle = \sum_i \mathbf{U}^*_{i\alpha} |\nu_\alpha\rangle \ .$$

A complex unitary matrix has a total of 18 degrees of freedom that are reduced to 9 due to the unitary condition ($\mathbf{U}\mathbf{U}^\dagger = 1$). The most common representation of the remaining 9 parameters is by introducing 3 real mixing angles θ_{12}, θ_{23} and θ_{13}, and 6 complex phases. 3 of the complex phases can be reabsorbed into the neutrino fields, and the 3 remaining phases are defined as the CP-violation phase δ, and the two Majorana phases α_{21} and α_{31}. With this parametrization, the $\mathbf{U}_{\text{PMNS}}$ matrix takes the form,

$$\mathbf{U}_{\text{PMNS}} = \begin{pmatrix} 1 & 0 & 0 \\ 0 & c_{23} & s_{23} \\ 0 & -s_{23} & c_{23} \end{pmatrix} \cdot \begin{pmatrix} c_{13} & 0 & s_{13}\mathrm{e}^{-i\delta} \\ 0 & 1 & 0 \\ -s_{13}\mathrm{e}^{-i\delta} & 0 & c_{13} \end{pmatrix} \cdot \begin{pmatrix} c_{12} & s_{12} & 0 \\ -s_{12} & c_{12} & 0 \\ 0 & 0 & 1 \end{pmatrix} \cdot \begin{pmatrix} 1 & 0 & 0 \\ 0 & \mathrm{e}^{\alpha_{21}} & 0 \\ 0 & 0 & \mathrm{e}^{\alpha_{31}} \end{pmatrix} ,$$

where $\cos\theta_{ij} = c_{ij}$ and $\sin\theta_{ij} = s_{ij}$. This is one of the most common parametrizations of the PMNS matrix [54], although an infinite number of possible parametrizations exist. This model has been successful in explaining the appearance and disappearance of flavors of neutrinos after they have traveled a certain distance. The mass eigenstates can be described as stationary, and their propagation through space $\vec{x}$ and time t can be described by a plane wave solution in the form of,

$$|\nu_i(\vec{x}, t)\rangle = \mathrm{e}^{i\vec{p_i}\cdot\vec{x}}\mathrm{e}^{-iE_i t} |\nu_i(0,0)\rangle \ ,$$

where the time and space translation operators have been used over the initial neutrino state $|\nu_i(0,0)\rangle$ with eigenvalues E_i and $\vec{p_i}$, respectively and defining energy and momentum of the correspondent neutrino plane wave. In the ultrarelativistic regime, $|\vec{p_i}| = p_i \gg m_i$ and the following approximation can be made,

$$E_i = \sqrt{m_i^2 + p_i^2} \simeq p_i + \frac{m_i^2}{2p_i} \simeq E + \frac{m_i^2}{2E} ,$$

where $c = 1$. Then, the probability amplitude can be calculated as,

$$P_{\alpha\beta}(t) = |\ \langle\nu_\alpha|\nu_\beta(t)\rangle\ |^2 = \sum_{i,j} \mathbf{U}_{\alpha i}\mathbf{U}^*_{\beta i}\mathbf{U}_{\alpha j}\mathbf{U}^*_{\beta j} \exp\left(\frac{-i\Delta m_{ij} L}{2E}\right) ,$$

where $\Delta m^2_{ij} = m_i^2 - m_j^2$ is the mass splitting between mass eigenstates i and j. After applying unitary conditions and separating real and imaginary components, this equation can be rewritten as,

$$\begin{aligned} P_{\alpha\beta}(L,E) = \delta_{\alpha\beta} &- 4\sum_{i>j} \mathfrak{Re}[\mathbf{U}_{\alpha i}\mathbf{U}^*_{\beta i}\mathbf{U}_{\alpha j}\mathbf{U}^*_{\beta j}] \sin^2\left(\frac{\Delta m^2_{ij} L}{2E}\right) \\ &+ 2\sum_{i>j} \mathfrak{Im}[\mathbf{U}_{\alpha i}\mathbf{U}^*_{\beta i}\mathbf{U}_{\alpha j}\mathbf{U}^*_{\beta j}] \sin\left(\frac{\Delta m^2_{ij} L}{2E}\right) , \end{aligned} \tag{1.2}$$

where $t = L$ has been used due to $c = 1$, being L the baseline between emission and detection. If the mass states are not all exactly degenerated and the off-diagonal elements of $\mathbf{U}$ are non-zero, then oscillations can occur. $P_{\alpha\beta}(L)$ can be defined as the survival probability for the case where $\alpha = \beta$ and it is the foundation of disappearance experiments that look for deficits of neutrinos of certain flavors. On the contrary, when $\alpha \neq \beta$, $P_{\alpha\beta}(L)$ becomes the oscillation probability and it is used on neutrino appearance experiments. As will be explained in Chap. 3, **STEREO** is a very-short baseline ($L \sim 10\,\mathrm{m}$) experiment studying the reactor $\bar{\nu}_e$ disappearance.
Regardless of its popularity in the late 1970s, the described formalism of neutrino oscillations still required more experimental evidences to be proven. Drawing on the work done by DAVIS, MASATOSHI KOSHIBA used an underground nucleus decay detector in the Kamioka mine in Japan, KamiokaNDE, to measure neutrinos . A series of upgrades on the dectector in 1985, KamiokaNDE-II, made it sensitive enough to detect electron antineutrinos from SN1987A, a supernova which was observed in the Large Magellanic Cloud in 1987. The direct detection of neutrinos from this supernova [56] confirmed the sun as a source of neutrinos and also the deficit observed by DAVIS. Parallely, KamiokaNDE-II also observed a factor two deficit on muon neutrinos from the atmosphere, enlarging the cases of disappearance of neutrinos [57]. This is commonly known as the atmospheric neutrino anomaly. For their crucial breakthrough in observing cosmic neutrinos, both DAVIS and KOSHIBA earned a Nobel Prize award in 2002.
Lower energy regions of solar neutrinos coming from proton-proton fusions were observed in detail by gallium experiments in the early 1990s like SAGE [61] and GALLEX [62], confirming the solar neutrino deficit previously observed. The impact of this experiments in the reactor antineutrino anomaly will be reviewed in Sec. 2.3.2. However, the definitive proof of neutrino oscillations had to wait until the end of the 1990s decade. Located in the same place as its predecessors KamiokaNDE and KamiokaNDE-II, in 1998 the Super-Kamiokande experiment provided a very precise measurement of the disappearance of atmospheric muon neutrinos and the correlated appearance of electron neutrinos [58]. The evidence of neutrino oscillations from solar neutrinos took a little bit longer until 2001, when the SNO experiment presented the first clear result on solar electron antineutrino disappearance in favor of tau and muon antineutrino appearance [59]. For the combined efforts of Super-Kamiokande and SNO, TAKAAKI KAJITA and ARTHUR MCDONNALD were awarded a Nobel Prize award in 2015.

Currently, in early 2019, the status of neutrino oscillations can be summarized by the parametrization of the PMNS matrix [54],

$$\Delta m^2_{21} = (7.37 \pm 0.18) \cdot 10^{-5}\mathrm{eV}^2\,, |\Delta m^2_{31}| = (2.56 \pm 0.04) \cdot 10^{-3}\mathrm{eV}^2\,,$$
$$|\Delta m^2_{32}| = (2.54 \pm 0.04) \cdot 10^{-3}\mathrm{eV}^2\,,$$

$$\text{NH: } \sin^2\theta_{12} = 0.297 \pm 0.013\,, \quad \sin^2\theta_{23} = 0.425 \pm 0.021\,,$$
$$\sin^2\theta_{13} = 0.0215 \pm 0.0008\,, \quad \delta/\pi = 1.38^{+0.26}_{-0.19}\,,$$

$$\text{IH: } \sin^2\theta_{12} = 0.297 \pm 0.013\,, \quad \sin^2\theta_{23} = 0.589 \pm 0.068\,,$$
$$\sin^2\theta_{13} = 0.0216 \pm 0.0008\,, \quad \delta/\pi = 1.31^{+0.29}_{-0.20}\,.$$

The Majorana phases α_1, α_2 are still unknown. Recent results by T2K and NOνA accelerator experiments presented at the Neutrino 2018 conference shed some light into the mass hierarchy of neutrinos and on the CP violation phase δ. By means of ν_e and $\bar{\nu}_e$ appearance channels, both experiments showed an exclusion of $\delta = 0, \pi$ with a 2σ and 3σ confidence level respectively, pointing at possible first sighting of CP symmetry violation in the lepton sector. Similarly, the first indications of normal mass hierarchy were found with 3σ confidence level for NOνA.

1.3.2 Neutrino Mass

So far it has been discussed how neutrinos have been proven to be massive particles, fact that in principle lies beyond the current understanding of the SM. Nevertheless, there is no constraint that forbids the Higgs field to couple with non-interacting right-handed neutrinos. In fact, minimal extensions can be done ad hoc to the Yukawa Lagrangian in order to include interaction of the type $\nu_R H \nu_L$. In these extensions, it is always assumed that ν_R do not interact weakly and thus cannot be observed. New Yukawa couplings y_ν have to be included that in an homologous way to y_ℓ, giving rise to mass terms of the type $m_\nu = y_\nu v/\sqrt{2}$. However, these type of couplings cause some discomfort among the community because they need to be orders of magnitude lower than the charged lepton couplings y_ℓ to explain the small scale of the neutrino mass. At the present time, the stringent value for the neutrino mass from β decays comes from the Troitzk experiment as $m_{\nu_e} < 2.05\,\text{eV}$ at 95% confidence level [48], supported by other independent measurements like from the Mainz experiment [49]. The upcoming KATRIN experiment [50] could improve this result with a planned sensitivity of $m_{\nu_e} \sim 0.2\,\text{eV}$. Cosmological models are also able to theoretically bound the mass of all interacting neutrinos. Depending on the model complexity and input data $\sum_i m_i < (0.3 - 1.3)\text{eV}$ [54], which is in agreement with experimental measurements of m_{ν_e}.

A popular mass-generation mechanism for neutrinos that accounts for the large discrepancies of mass between leptons, is the see-saw mechanism [53]. There are many variants of this model, but all of them share the core concept where both left and right-handed neutrino masses are inversely correlated like in a see-saw. In this mechanism, neutrinos are assumed to be Majorana particles [52]. The right and left-handed fields of a Majorana particle can be related by a conjugation charge transformation C

$$\psi_R = C\bar{\psi}_L^T\,.$$

In this scenario, such particle would be its own antiparticle,

$$\psi^c = (\psi_L C\bar{\psi}_L^T)^c = \psi\,.$$

Such condition can only be satisfied by neutral particles. The only fundamental fermions that can be Majorana particles are neutrinos. Under this assumption, one can construct Majorana mass term for neutrinos that do not violate gauge invariance

$$\begin{aligned}\mathcal{L}_L^{\text{Majorana}} &= -\frac{1}{2} m_L \bar{\nu}_L^c \nu_L + \text{h.c}\,,\\ \mathcal{L}_R^{\text{Majorana}} &= -\frac{1}{2} m_R \bar{\nu}_R^c \nu_R + \text{h.c}\,.\end{aligned}$$

Introducing the Majorana particle condition into a standard Dirac mass Lagrangian,

$$\begin{aligned}\mathcal{L}^{\text{Dirac}} &= -\frac{1}{2} m_D \bar{\nu}_R \nu_L + \text{h.c} \\ &= -\frac{1}{2} m_D \bar{\nu}_R^c \nu_L - \frac{1}{2} m_D \bar{\nu}_L^c \nu_R - \frac{1}{2} m_R \bar{\nu}_R^c \nu_R - \frac{1}{2} m_L \bar{\nu}_L^c \nu_L + \text{h.c}\,.\end{aligned}$$

The first two terms correspond to the fermionic Dirac mass term and violate gauge invariance. However, they can appear after the SSB through a Higgs mechanism, like the Dirac masses of the charged leptons. The two remaining terms have been described above and correspond to the Majorana mass terms for right and left-handed neutrinos. In matrix form, the Lagrangian can be seen as

$$\mathcal{L}^{\text{Dirac}} = -\frac{1}{2} (\bar{\nu}_L^c \bar{\nu}_R) \begin{pmatrix} m_L & m_D \\ m_D & m_R \end{pmatrix} \begin{pmatrix} \nu_L \\ \nu_R^c \end{pmatrix} + \text{h.c}\,. \tag{1.3}$$

The Lagrangian has been written in terms of the chiral states ν_L and ν_R. These fields do not have a definite mass because of the non diagonal m_D terms in the mass matrix, in a similar way as for the SM flavor neutrinos. The mass matrix can be diagonalized, obtaining then the two eigenmasses,

$$m_{1,2} = \frac{m_R}{2} \left(1 \pm \sqrt{1 + 4 \frac{m_D^2}{m_R^2}} \right) \rightarrow m_1 \simeq m_R\,, \quad m_2 \simeq \frac{m_D^2}{m_R}\,. \tag{1.4}$$

Given the relationship between m_1 and m_2, it is clear that if one of the eigenmasses goes up, the other goes down, and vice versa. The mass parameter M_D can be generated from Yukawa interactions with the Higgs field, in the conventional standard model fashion. Since M_D does not correspond to the observable mass of the neutrinos, but is expected to be around $\sim 100\,\text{GeV}$, y_ν would not have to be necessarily small. By the virtue of this mechanism, each generation of the observed neutrinos would then acquire a mass term $m_2 \sim 1\,\text{eV}$, while giving raise to a heavy mass eigenstate of the order of Grand Unification Theories (GUT) $\sim 10^{15}\text{GeV}$ [53].

"As your flesh bears the sigil, your name shall be known as that of a recusant"

Xemnas

Chapter 2

Reactor Neutrino Experimental Status

Nuclear fission reactors are a powerful source of antineutrinos, well-spread around the globe and used in a multitude of experiments to study neutrino oscillations. This chapter will present an overview of the different approaches taken to study neutrinos from reactors, arguing their utility and impact in the current knowledge on neutrino physics. The generation of experiments placed at baselines of $< 100\,\text{m}$ from nuclear reactors during the 1980s and 1990s constituted the first generation of Very Short Baseline (VSBL) experiments, and their achievements will be described in Sec. 2.1. Following these, another group of experiments with improved technology and energy discrimination capabilities were placed at larger distances from reactors $\gtrsim 1\,\text{km}$. These Short Baseline (SBL) detectors will be described and analyzed in Sec. 2.2. All the measurements performed by VSBL and SBL experiments have refined the understanding of the neutrino spectra coming from nuclear reactors with different fuel and characteristics. However, also several anomalies have been unveiled in the recent years, presenting additional challenges for present and future reactor neutrino experiments. All of this is discussed in detail along Sec. 2.3, together with possible solutions to this conundrum. Finally, Sec. 2.4 explores current efforts at VSBL to measure the reactor neutrino spectra with high precision, to give some insight on the existing anomalies and to observe possible sterile neutrino signals.

2.1 First Generation of Very Short Baseline Experiments

The solar neutrino problem troubled the physicist for several decades since its discovery, until the confirmation of neutrino oscillations. During these years, some experiments were set to measure neutrinos from nuclear fission reactors and replicate the flux deficit observed from the sun. In 1980, the ILL experiment used almost 400 liter of liquid scintillator to measure the neutrino flux from the Institut Laue-Langevin HEU-based reactor at approximately 9 m of baseline. This is the same location as the **Stereo** experiment with a similar baseline. The ILL showed for the first time a reactor neutrino spectrum although no evidence of oscillation was found, with a experimental to prediction ratio of $R = 0.89 \pm 0.15$ [65]. One year later, the Bugey experiment placed a similar liquid scintillator-based detector at two baselines 13.6 m and 18.3 m from the Bugey nuclear reactor, France. Their measurement at two positions was regarded as less depending on the knowledge of the initial spectrum or other detector systematics, since a relative measurement can be done. Their final result showed, contrary to what was observed by ILL, a disappearance of neutrinos at the 3σ level [66]. In 1986, the ILL detector was transferred to a more powerful commercial reactor at Gösgen nuclear power plant in Switzerland. They measured antineutrino signals at three different distances using a similar method than Bugey, finding a good agreement with the non-oscillatory

hypothesis, both in rate and spectrum [67]. This measurement excluded de facto past results from Bugey that indicated possible oscillation of neutrinos. Some years later, in 1995, the Bugey-3 experiment placed three new detector modules at 15 m, 40 m and 95 m away from the Bugey reactor with the aim to observe again antineutrino disappearance. However, this time the results concluded that no oscillation was taken place and enhanced further the exclusion region of the oscillation parameter space [68].

2.2 Short-Baseline Reactor Neutrino Experiments

Throughout the 1990s there were great efforts to directly observe neutrino oscillations for different neutrino fields. It has been discussed previously how SNO and Super-Kamiokande experiments ended up proving neutrino oscillations from solar and atmospheric neutrinos. During that time there was also a great interest in measuring possible oscillations for neutrinos coming from nuclear reactors. Experiments from previous decades already observed electron antineutrinos from nuclear fission, but the large uncertainties associated to these experiments prevented them to make big statements on whether there was oscillation or not. To prove or disprove the existence of electron antineutrino oscillations, the Chooz [69] and Palo Verde [70] experiments were commissioned and placed at relatively Short Baseline (SBL) from their respective nuclear reactors. Both experiments counted with detectors filled with gadolinium-loaded liquid scintillator and used the IBD as the neutrino detection principle. One of the main differences between both detectors was the fact that the one in Palo Verde was segmented, in opposition to the homogeneous detector in Chooz, resulting in a better background rejection by Chooz. The results from both experiments, published in 1999, concluded that the atmospheric neutrino oscillations did not involve $\bar{\nu}_e$, and set an upper limit for $\sin(2\theta_{13}) < 0.12$ at 90% confidence level, assuming $\Delta m_{13} = 0.0024\,\mathrm{eV}^2$. However, their analysis were not compatible only with the oscillation hypothesis, and final characterization of θ_{13} had to wait until the next generation reactor neutrino experiments.

CP violation phase δ comes from a three flavor framework, only possible for a value of $\theta_{13} > 0$. Furthermore, the current observation of neutrino mass hierarchy was only possible for sufficiently large values of $\theta_{13} \gtrsim 0.01$ [71]. For these reasons, the measurement of θ_{13} took priority as the atmospheric and solar neutrino oscillatios were well stablished. To palliate the main drawbacks of the two previous main reactor neutrino experiments, new proposals had to perform a paradigm shift. This shift came as a relative measurement with two detectors, placed at different base-lines from the reactor. The first one, often called near detector would be very close to the origin of neutrinos while the second would be placed at the oscillation maximum of neutrinos. By doing this, uncertainties from reactors and correlated uncertainties from detectors would cancel out and a high precision measurement could be achieved. Three main experiments, Double Chooz, Daya Bay and RENO, were finally commissioned for this task. The first confirmation of $\theta_{13} > 0$ and the disappearance of $\bar{\nu}_e$ came by the hands of Double Chooz in 2011 [73] with a nominal power of $8.5\,\mathrm{GW_{th}}$ and two detectors. In 2012, Daya Bay presented the first measurement of θ_{13} with 5σ confindence level [74] with a nominal power of $17.4\,\mathrm{GW_{th}}$ and eight detectors, followed by RENO [75] with a nominal power of $16.8\,\mathrm{GW_{th}}$ and six detectors. These experiments are often referred as the high precision reactor experiments, where the near-far cancellation has been crucial

for the sub-percent-level systematics achieved. To the present date, 2019, all three of them continue their analyses with further statistics.

2.3 Reactor Neutrino Flux Prediction

Predicting the flux of neutrinos emitted from a nuclear reactor has proven to be a cumbersome task for physicists since the dawn of reactor neutrino experiments. An accurate calculation of the energy spectrum and integrated flux of reactor neutrinos is crucial for the experiments to draw any conclusions on neutrino oscillations. The main challenge when calculating such flux is to take into account all contributions from fission products of the different isotopes fueling the reactor. Most fission products are unstable, heavy nuclei and are always neutron rich. This means that they tend to stabilize by a succession of β-decays, each one emitting a $\bar{\nu}_e$. On average, six neutrinos are generated in the transit of a fission product to a stable isotope, which leads to an isotropic flux of about $\sim 10^{17}\nu\mathrm{s}^{-1}\mathrm{MW}^{-1}$ [88]. Most commercial reactors are fueled with Lowly Enriched Uranium (LEU), which means that the uranium used is only composed by ^{235}U isotope by a few percent, being the rest ^{238}U. The former is fissile with thermal neutrons and it is the main fuel used by the reactor. The ^{238}U isotope also contributes to the fission process by converting to ^{239}Pu after a n-capture. ^{239}Pu can either fission with thermal neutron or transition to ^{241}Pu via two β-decays, isotope that can also fission in the same way. This process, that is also depicted in Fig. 2.1, contains a cumbersome amount of associated β decays, which in turn have a determined antineutrino spectrum depending on the total energy of the process. In addition, the ^{239}Pu and ^{241}Pu concentration increases with the burnup over the fuel cycle of a reactor, varying the expected $\bar{\nu}_e$ spectrum over time. Contrary to commercial nuclear reactors, research reactors are mostly fueled by Highly Enriched Uranium (HEU). An example of this type of reactors is the one at the ILL where **Stereo** operates. HEU is composed by $> 90\%$ of ^{235}U and operates at shorter run periods. At the end of each cycle, the core is refueled with fresh ^{235}U. The decay chain is dominated by the fission products of ^{235}U and the shorter reactor cycles usually make the burnup contribution negligible.

There are two schools of thought concerning the estimation of reactor neutrino flux. One way is to follow the standard nuclear data tables, and iteratively combine *ab initio* thousands of decay branches of the fission products. One of the first calculations of this type came in 1981 by the hands of Vogel et al. [82]. Such a first-principle calculation is challenging due to missing or inaccurate data even with modern nuclear databases, and for this reason such calculations were performed with relatively large uncertainties ($\sim 10\%$) [82]. The second way consists on experimentally measuring the β spectrum per fission of each isotope. Due to energy conservation, these spectra can then be inverted to obtain their respective antineutrino distributions. This treatment is often called the *conversion* method, and gained popularity with the high-precision spectroscopy held at the ILL in the 1980s [78, 79, 80]. Neutrino spectra from ^{235}U, ^{239}Pu and ^{241}Pu fission products were studied in detail, obtaining uncertainties around $2-5\%$. During these experiments, however, no *conversion* measurement of ^{238}U was performed. The combination of the ILL spectra and the ^{238}U *ab initio* spectrum from Vogel et al. is commonly referred as the ILL-Vogel model.

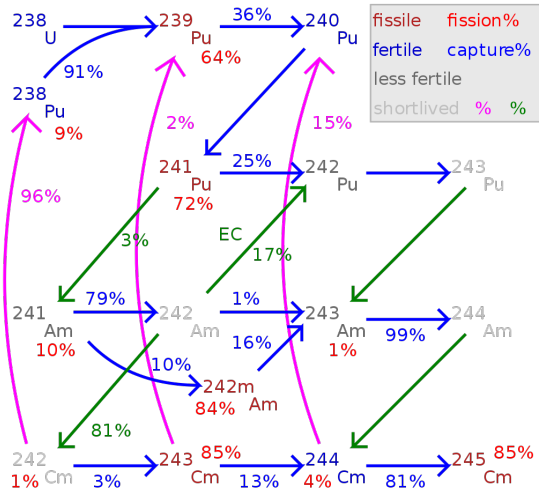

Figure 2.1: Scheme of the transitions that ^{238}U undergo before producing a fissile isotope. The main fission processes come from ^{239}Pu and ^{241}Pu isotopes.

2.3.1 Rate and Shape Anomalies in Reactor Antineutrino Flux

In 2011 and during the development of the last generation of SBL neutrino oscillation experiments, the reactor antineutrino flux was reevaluated. The ^{235}U, ^{239}Pu and ^{241}Pu spectra previously measured at the ILL were re-analyzed by Huber [89] using an improved *conversion* method. Parallely, the *ab initio* spectrum of ^{238}U was recomputed by Mueller et al. [90]. The combination of both complementary spectra conforms the Huber-Muller model, and its comparison with the old ILL-Vogel model shows a deficit of about $\sim 3.5\%$ in the total integrated flux of neutrinos. In Fig. 2.2 the shape

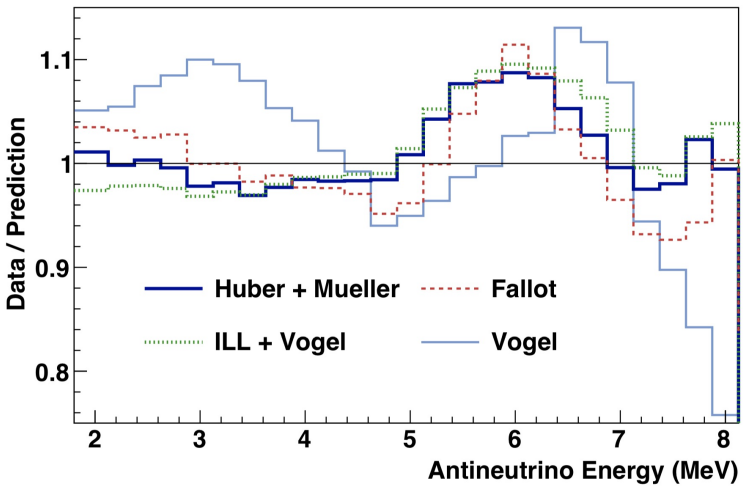

Figure 2.2: Ratio between Daya Bay antineutrino energy spectrum [74] and expectations according different models. Models used: two *ab initio* calculations, Vogel [82] and Fallot [86]; and two *conversion* models ILL-Vogel [78, 79, 80, 82] and Huber-Muller [89, 90]. A clear shoulder can be observed in the energy area of 5-7 MeV.

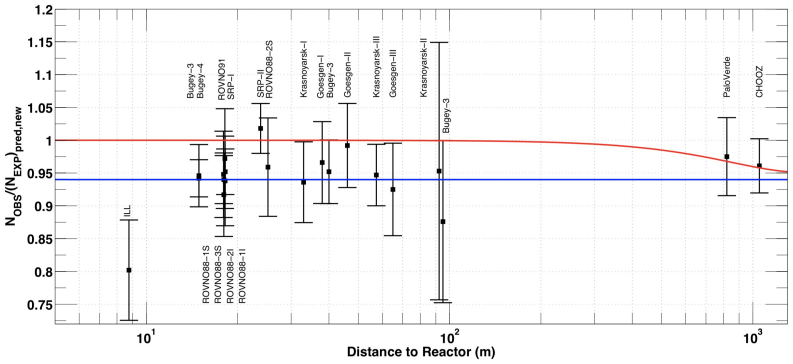

Figure 2.3: Ratio between observed and expected IBD rates of the 19 VSBL reactor neutrino experiments held in the 1980s and 1990s[91]. Expected rates calculated for the Huber-Mueller mode. Results portray a tension with unity of almost 3σ.

comparison of both models can be seen together with *ab initio* calculations from Vogel and Fallot.

Following the studies from Huber and Mueller, Mention reviewed a number of reactor neutrino experiments performed in the 1980s and 1990s. The measurements of 19 experiments with baselines between 9 m and 95 m were revisited [91]. At first, the original results from all experiments were reproduced from published data and then were compared to the old expected fluxes using the ILL-Vogel model. The ratio between observed and expected fluxes were perfectly compatible with unity for most of the cases. Then, the expected fluxes were updated according to the Huber-Muller model using the most recent value of the IBD cross-section, leading to an increased deficit of 6.5%. Thus, the ratio between expected and observed antineutrino flux became $R = 0.928 \pm 0.024$ [120], situated at 3σ from the unity as can be observed in Fig. 2.3. This deficit is known as the Reactor Antineutrino Anomaly (RAA). In the next years, the new generation of high precision reactor experiments validated this discrepancy [92], with particular focus on the high energy region of antineutrino energy. In 2014, Double Chooz observed a particular 4σ excess of neutrinos at ~ 5 MeV with respect to the model [93]. This shoulder is often referred as the shape anomaly of the antineutrino energy spectra. Such effect was later confirmed by Daya Bay and RENO [92, 94].

Since the consolidation of these two anomalies, there have been many indications to possible solutions. Some studies suggest that the shape anomaly may come from incorrect beta spectrum measurements used in the *conversion* method [98]. A counterargument against this suggestion is that the anomaly was observed with comparable magnitude at reactors with HEU fuel and reactors with mixed fuel. Other studies hypothesize that incorrectly predicted $\bar{\nu}_e$ production rates of certain fission isotopes could be the cause for one or both anomalies [99]. Exploiting the different mixtures of ^{235}U, ^{238}U, ^{239}Pu and ^{241}Pu between HEU and LEU reactors, differences in their observed antineutrino spectra could point to the responsible isotope for the anomalies, if any. Different scenarios extracted from [99] are depicted in Fig. 2.4. Recent measurements of the evolution of reactor fuel content at the Daya Bay experiment showed a variation in detection rates inconsistent with the current modeling of $\bar{\nu}_e$ production by individual

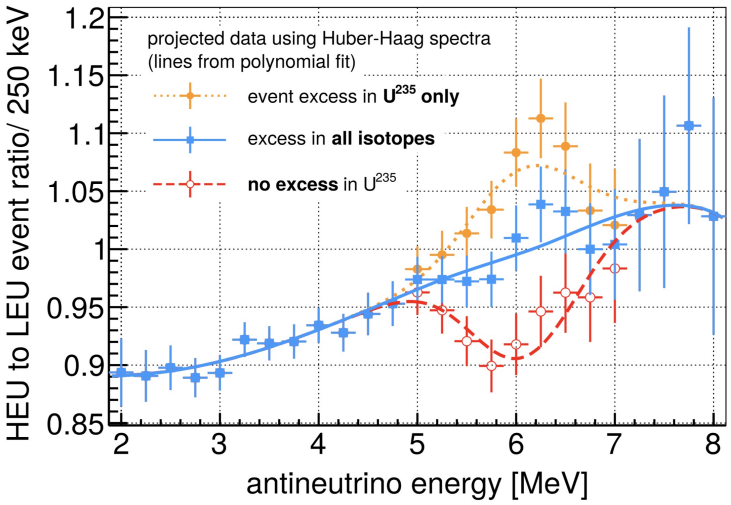

Figure 2.4: Expected ratio between HEU and LEU antineutrino energy spectra for different hypothesis. The shapes serve as an indication of which isope is responsible for the anomaly. Reference spectrum is Huber-Haag model. [99].

fission isotopes. This discrepancy, according to Daya Bay, may be at least partially responsible for the RAA [100]. Most of the new generation VSBL experiments described in Sec. 2.4, including **STEREO**, are currently measuring neutrino spectrum from HEU-fueled reactors, which could give an important insight on the cause of the shape anomaly.

Regarding the RAA, one of the most controversial explanations for the measured antineutrino flux deficit could come from the introduction of an additional neutrino oscillation. This idea was already proposed by MENTION et. al [91] during the first observation of the RAA. Such oscillation would transform part of the observable flux into one or more types of non-interacting neutrinos, often known as sterile neutrinos. The lack of means for observing such particles would translate into an effective deficit of the experimental IBD rates. In the short baseline approximation where the oscillations driven by the atmospheric and solar mixing angles are negligible ($L < 100\,\mathrm{m}$), and adapting Eq. 1.2 to a 3+1 neutrino model, the survival probability of $\bar{\nu}_e$ becomes

$$P_{ee}(L,E) = 1 - \cos^4\theta_{14}\sin(2\theta_{13})\sin^2\left(1.27\frac{\Delta m^2_{13}L}{E_{\bar{\nu}_e}}\right) \tag{2.1}$$

$$- \sin(2\theta_{14})\sin^2\left(1.27\frac{\Delta m^2_{14}L}{E_{\bar{\nu}_e}}\right), \tag{2.2}$$

where the following substitution has been made,

$$\sin^2\left(\frac{\Delta m^2 L}{4E_{\bar{\nu}_e}}[\text{natural units}]\right) \equiv \sin^2\left(1.27\frac{\Delta m^2 L}{E_{\bar{\nu}_e}}\frac{[\text{eV}]^2[\text{km}]}{[\text{GeV}]}\right). \tag{2.3}$$

The oscillation amplitude is given by the sterile mixing angle θ_{14}, and the corresponding oscillation frequency by the mass splitting Δm^2_{14} between sterile mass state and m_1. In order to explain a deficit of reactor $\bar{\nu}_e$ observed at baselines of $\sim 10-100\,\mathrm{m}$, the mass splitting $\Delta m^2_{41} \lesssim 1\,\mathrm{eV}^2$. This implies that the sterile neutrino has also to be

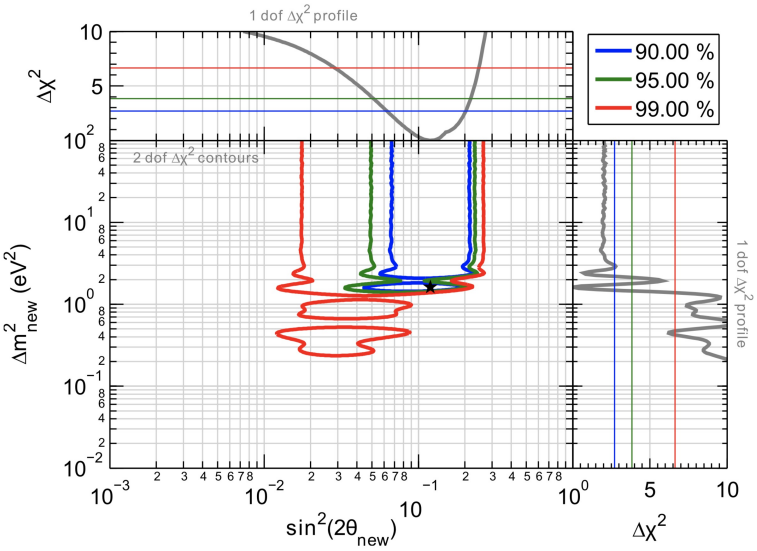

Figure 2.5: Allowed regions in the $\Delta m^2_{41} - \sin^2(2\theta_{14})$ parameter space from the combination of reactor neutrino experiments discussed in this section, and gallium and MiniBooNE experiments described in Sec. 2.3.2 and Sec. 2.3.3. The data has been fitted to the 3+1 neutrino oscillation hypothesis with the best fit being at $|\Delta m^2_{14}| > 1.5\text{eV}^2$ and $\sin^2(2\theta_{14}) = 0.14 \pm 0.08$ at 95% confidence level [91].

very light, although heavier than SM neutrinos. The oscillation length of such neutrinos would be at the meter level and would be averaged out at distances $> 15\,\text{m}$. Then, a raster scan was performed in the $\Delta m^2_{41} - \sin^2(2\theta_{14})$ plane where the expected rates in the experiments were simulated for each set of oscillation parameters. By comparing expected and observed rates, parameter ranges in disagreement with the experiments can be excluded. The allowed regions of parameters at different confidence levels can be seen in Fig. 2.5. Combining the data of all considered reactor oscillation experiments the no-sterile-oscillation hypothesis is disfavored at 96.5% C.L., with $\Delta m^2_{41} > 0.23\,\text{eV}^2$ and $0.02 < \sin^2(2\theta_{14}) < 0.21$.

2.3.2 Gallium anomalies

During the decade of 1990 there was an enormous interest on proving the existence of neutrino oscillations. As has been explained in Chap. 1, the solar neutrino problem would not be resolved until the late 1990s by the SNO experiment. Before that, two gallium-based experiments, SAGE [108] and GALLEX [106], attempted to investigate the low energy region, $< 1\,\text{MeV}$, of solar neutrinos spectrum coming from proton-proton fusion process in the core of the sun. In order to calibrate the detector response, GALLEX and SAGE performed each two series of dedicated runs where intense ^{51}Cr and ^{37}Ar were introduced near the center of the detector. These sources only decay via electron capture, emitting in the process a ν_e of a few hundreds of keV. The detection principle using gallium is,

$$\nu_e + {}^{57}\text{Ga} \rightarrow {}^{71}\text{Ge} + e^- \,. \tag{2.4}$$

To compute the expected number of events, the total cross-section for this process was predicted by BAHCALL [107]. The contribution from a ground state to ground state

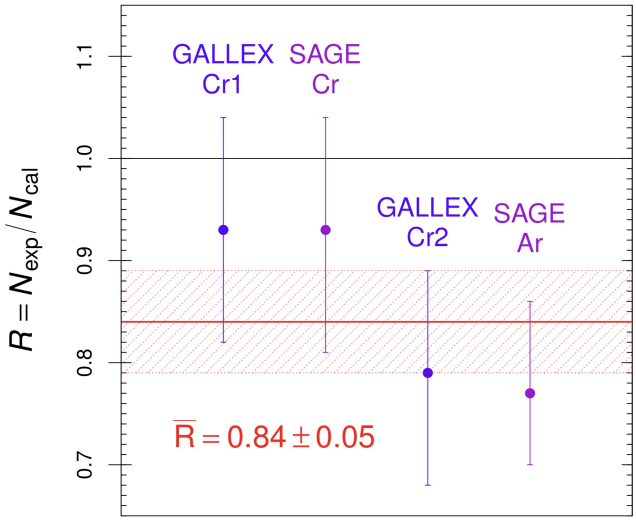

Figure 2.6: Ratio between measured and expected neutrino signals in the GALLEX [106] and SAGE [108] experiments.

transition was calculated with good precision from the measured rate of the inverse process, the electron capture decay of ^{71}Ge. However, transitions from excited states of ^{57}Ga contribute up to a 5% and can only be approximated using nuclear models, increasing the overall uncertainty on the total cross-section. The final result of the calibration of SAGE and GALLEX portrayed an unexpected deficit of detected neutrinos, with a measured to expected ratio of $\overline{R} = 0.84 \pm 0.05$ [120]. The individual measurements can be seen in Fig. 2.6. Mention et al. included the gallium anomaly experiments together with the SBL experiments to show the RAA [91]. The uncertainties from these measurements were reviewed by Giunti in 2012 and were determined insufficient to explain the deficit. Coming from radioactive sources, the results from GALEX and SAGE complement reactor based experiments and reinforce the sterile neutrino hypothesis in detriment of reactor-related explanations.

2.3.3 Other anomalies

Besides the deficits observed in all the experiment comprising the RAA, there have been other anomalies in the past decade. One of the first anomalous measurements was observed by the short baseline LSND experiment [103]. This LS-based detector was observing beams of neutrinos generated from the Los Alamos accelerator. Accelerated proton beams were focused on a target and from their interaction π^+ and π^- were produced. Negative pions are largely stopped and absorbed in the beamstop, while positive pions can propagate. The π^+ decay in flight produced μ^+ that also decay into neutrinos,

$$\mu^+ \to e^+ \nu_e \bar{\nu}_\mu \,. \tag{2.5}$$

The main decay of muons cannot trigger an IBD in the LS, but unexpectedly results from LSND showed a 3.8σ excess of IBD events as well as a deficit in $\bar{\nu}_\mu$. Their conclusion was that coming from non-standard oscillations $\bar{\nu}_\mu \to \bar{\nu}_e$ with Δm^2 between $0.2 - 10\text{eV}^2$ at a baseline of 30 m.

To confirm the observations of LSND, the MiniBooNE experiment was build in 2002. Neutrinos produced at the Fermilab accelerator were directed at a detector filled with 800 tons of mineral oil and lined with almost 1300 PMTs. The mechanism of production and detection was fairly similar to the one at the LSND. The oscillation analysis in the $\bar{\nu}_\mu \rightarrow \bar{\nu}_e$ and $\nu_\mu \rightarrow \nu_e$ channels both showed and excess of $\bar{\nu}_e$ and ν_e respectively, reaffirming the results from LSND in 2013 [104]. Recently in 2018, MiniBooNE published a new result confirming the oscillatory hypothesis. According to their measurements, an charged-current excess for both $\bar{\nu}_e$ and ν_e channels of 460.5±99.0 (4.7σ) [105] has been observed for a two-neutrino oscillation hypothesis. Their data is consistent in energy and magnitude with the excess reported years before by LSND, and the significance of the combined excesses is 6.0σ, which would be enough to claim a discovery.

2.4 Very short baseline experiments - state of the art

Since the RAA and gallium anomalies were introduced in 2011, there have been many experiments that set to sail to terra incognita looking for sterile neutrino oscillations. All of them share a close proximity to the reactor source of neutrinos, for the oscillation length induced by a sterile neutrino in the eV scale is only a few meters [91]. Another common factor for these VSBL experiments is the detection technique, drawn from the past generation of SBL reactor neutrino detectors. In all cases antineutrino interacts with a scintillator material, either liquid or plastic, producing a correlated signal. A detailed description of the IBD imprint in a LS is explained in Sec. 3.1.1. The reactors chosen for these experiments are of both types, HEU and LEU, which most probably will give a definite insight on the effect of the fraction of isotopes in the neutrino spectrum. This difference in the enrichment of the fuel is correlated to the type of reactor, either commercial or for research, which plays an important factor on the final statistics and sensitivity of results. All the experiments, summarized in Tab. .2.1, are already running and have been presenting first results during the year of 2018. In the following paragraphs, the most prominent features of all of them will be described.

The PROSPECT experiment [109] is located at the High Flux Isotope Reactor (HFIR) of the Oak Ridge National Laboratory (ORNL), USA. With a compact reactor core of about 40 cm of width and 50 cm of height, the HFIR is a research reactor fueled by HEU at 85 MW. The detector is a $2.0\times1.6\times1.2\,\mathrm{m}^3$ rectangular volume filled with 3000 l of LS, divided in 154 optically separated cells of $120 \times 15\times15\,\mathrm{cm}^3$ by a grid of reflective plates. Each one of the cells counts with a two-sided PMT readout that is fully immersed in the scintillator. Contrary to **Stereo**, the LS is doped with a ^{6}LiCl to a mass fraction of 0.1%. The use of LiLS is not a common technique in the neutrino detection experiments due to its specially low light yield, its high toxicity and flammability. However, a dedicated effort from the PROSPECT collaborators has been taken to develop a low-toxicity and low-flashpoint LS utilizing a commercial scintillator base of di-isopropylnapthalene (DIN). The neutrino detection principle is the IBD, and the neutron is either captured by hydrogen or lithium,

$$^6\mathrm{Li} + n \rightarrow \alpha + {}^3\mathrm{H} + \gamma\,(4.79\,\mathrm{MeV})\,. \tag{2.6}$$

The n-capture produces two highly ionizing particles which deposit their energy very locally and can be identified by pulse shape discrimination techniques. In October 2018, PROSPECT published their first result on the sterile neutrino search. The detection of

around 25000 IBDs with a resolution of $\sigma/E = 4.5\%$ at 1 MeV, allowed PROSPECT to constraint a significant portion of the neutrino oscillation available parameter space at a 95% confidence level, disfavoring the best fit of the RAA at 2.2σ [110].

The NEOS experiment observes neutrinos from the same source as RENO: the 2.8 GW_{th} commercial reactor of the Hanbit power plant, Korea. The LEU-based core is not compact, having a diameter of 3.1 m and a height of 3.8 m. The detector consists on a cylindrical volume of 1 m diameter and 120 cm length, filled by Gd-loaded (0.5%) LS. 19 eight-inch PMTs are placed at both extremes of the cylinder to perform the readout of the signal from the IBD. The cylinder is located at 23.7 m distance in a gallery below reactor walls, leading to an overburden of $\sim$ 20 m.w.e. In 2016, NEOS presented their phase I results with an approximate IBD rate of 2000 events per day, a signal to background ratio of 22 and a resolution of $\sigma/E = 5\%$ at 1 MeV [115]. NEOS was able to reproduce the neutrino spectrum shape anomaly at 5 MeV shoulder for the first time for a very short baseline experiment. They also observed no strong sign of sterile neutrino in the detector sensitivity, excluding the best fit of the RAA with a 90% confidence level while limiting the oscillation parameters to $\sin^2(2\theta_{14}) < 0.1$ and $\Delta m^2_{14} = [0.2, 2.3]\text{eV}^2$, and with a best fit of $\sin^2(2\theta_{14}) \approx 0.05$ and $\Delta m^2_{14} \approx 1.7\,\text{eV}^2$ [116]. Since the end of the refurbishing of the detector in 2018, phase II of the experiment has been ongoing with 500 live days of data planned.

The highly segmented detector of the DANSS [113] experiment is placed at $10-12$ m from the core of the 3 GW_{th} commercial power reactor in Kalinin, Russia. The experiment is located underneath the reactor pool and above an extended reactor core of a height of 3.5 m and a diameter of 3.1 m fueled with LEU. Because of its location, DANSS counts with a relatively large overburden of $\sim$ 50 m.w.e that attenuates cosmic radiation by a factor 6. The detector has a cubical shape of $1 \times 1 \times 1\,\text{m}^3$ and it is mounted on a liftable platform that allows the measurement the neutrino flux at three heights, 10 m, 11 m and 12 m below the core. The target for IBD is composed by 2500 polystyrene-based extruded scintillator strips of $1 \times 4 \times 100\,\text{cm}^3$ with a thin Gd oxid surface coating. The purpose of this coating is two-fold: light reflection and neutron capture. The strips are crossed by three wavelength-shifter fibers, the central one being readout by a silicon photomultiplier (SiPM). The rest of the fibers are readout in groups of 50 by a total of 50 intercrossing modules of PMTs. The energy resolution is dominated by the light collection through the fibres and is given as $\sigma/E = 34\%$ at 1 MeV, possibly one of the major drawbacks of the experiment. Due to the proximity to the powerful reactor an average of $\sim$ 5000 IBDs are observed per day. In November 2018 DANSS presented preliminary results on the exclusion of the parameter space of sterile neutrino oscillations, with 966k of antineutrino detected [114]. Their best fit is at $\sin^2(2\theta_{14}) \approx 0.05$ and $\Delta m^2_{14} \approx 1.4\,\text{eV}^2$, in good agreement with NEOS results.

At the BR2 research reactor in Belgium, the SoLi∂ collaboration[111] measures neutrino oscillations at short baselines. Like the HFIR, the BR2 reactor is filled with HEU fuel, with a core diameter of less than 50 cm and a power of 85 MW_{th}. The baselines accessible by SoLi∂ in this site varies from 6 m to 9 m. The detector is based on a composite scintillator desgin. The target where neutrinos interact consists of a series of $5 \times 5 \times 5\,\text{cm}^3$ cubes of polyvinyl toluene (PVT), an organic scintillator that is used as the IBD target. Each one of the cubes is wrapped with reflective Tyvek sheets in order to guarantee optical isolation themselves and improve light collection. Two

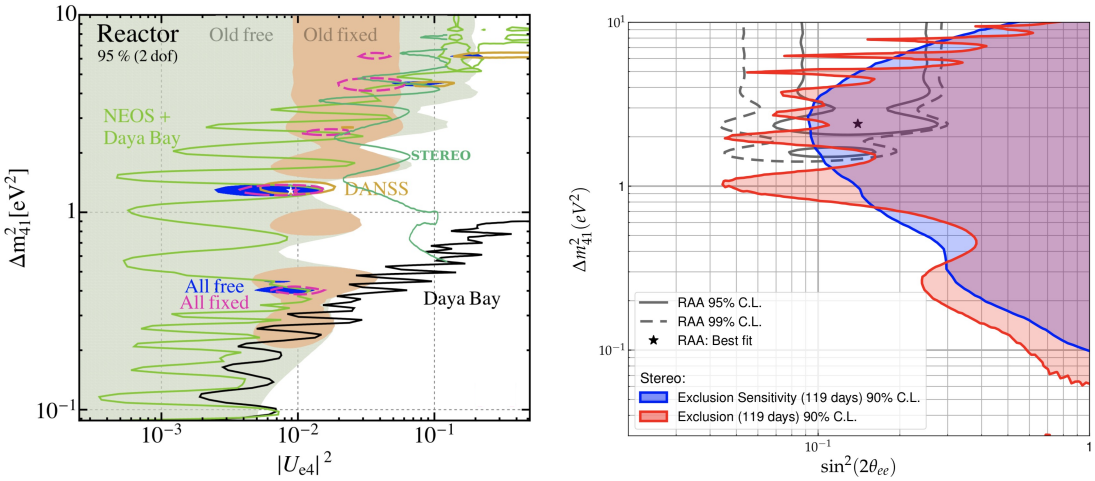

(a) **(b)**

Figure 2.7: (a) Expected sensitivity on the noscillation parameter space for the current VSBL reactor experiments[119]. (b) Exclusion contour of the oscillation parameter space for **Stereo** [127] using *Phase I and II* data (119 days). The RAA values and contours are from [91].

sides of the cubes are in contact with two layers of ^{6}LiF:ZnS(Ag) inorganic scintillator. The positron energy is deposited in the PVT, while neutrons are captured by the ^{6}Li (Eq. 2.6) sheets some microseconds later. The reaction products from the neutron capture are highly ionizing particles, causing the population of long lived excited states in the ZnS(Ag), thus allowing for pulse shape discrimination. The signals are read out by arrays of wavelength shifting fibers coupled in one side to a SiPM and a mirror in the opposite side, with a tested resolution of $\sigma/E = 14\%$ at 1 MeV. In February 2018, the construction of SoLi∂ Phase 1 (1.6 tons) was completed. Approximately 150 days of reactor ON data have been taken by the end of 2018 [112].

In the vecinity of the very compact SM-3 reactor, in Russia, the Neutrino-4 experiment has been set up [117]. The core is fueled by HEU and conveys a power of 90 MW$_{\text{th}}$. The segmented detector is divided in 50 vertical sections filled with Gd-loaded (0.1%) LS that detects neutrinos via IBD. It is installed above a movable platform that can change the baseline from 6 m to 11 m. Like **Stereo** at the ILL, Neutrino-4 is located at ground level with an overburden between 4 and 12 m.w.e, depending on the position of the platform. Unlike other experiments using LS like **Stereo** or PROSPECT, Neutrino-4 LS is not tuned to provide good pulse shape discrimination capabilities. Instead, the segmentation of the detector is used to identify positron events by their topology. Their achieved resolution is $\sigma/E = 16\%$ at 1 MeV. In 2018, the Neutrino-4 collaboration published their first results on the sterile neutrino search. In these results, they claimed the observation of a sterile neutrino oscillation with $\Delta m^2_{14} \approx 7.34\,\text{eV}^2$ and $\sin^2(2\theta_{14}) = 0.39$ with a 2.9σ confidence level [118], while excluding the RAA and gallium anomaly with a 97% confidence level. Such observations are in contradiction with current parameter limits imposed by Daya Bay, MINOS and Bugey-3 experiments to active-to-sterile oscillations[121]. It is also in contradiction with recent results from NEOS and DANSS and with the exclusion limit from PROSPECT.

Table 2.1: Summary of currently running VSBL reactor neutrino experiments.

	Stereo	PROSPECT	NEOS	DANSS	SoLi∂	Neutrino-4
Power [MW_{th}]	58	85	2800	3100	50-80	100
Location	France	USA	Korea	Russia	Belgium	Russia
Overburden [m.w.e]	15	< 1	20	50	10	4-12
Baseline [m]	9-11	7-9	24	11-13	6-9	6-12
IBD rate [day^{-1}]	400	750	2000	5000	450	200
Signal/Background	0.9	1.4	23	33	3	0.5
σ/E at 1 MeV [%]	8	4.5	5	34	14	16

The description of the **Stereo** experiment will be reserved for Chap. 3. Results for the first phase of data taking with almost 70 days of reactor-on were initially announced in the Rencontres du Moriond 2018 conference [125] and in the International Neutrino 2018 conference, in Heidelberg [126]. These showed compatibility of neutrino measurements with the null oscillation hypothesis, excluding the best fit of the RAA at $\sim 99\%$ of confidence level. New results combining up to almost 120 days of reactor-on will be presented in the upcoming Rencontres du Moriond 2019 conference [127], held some weeks after the handing of this manuscript. Although not yet public, early March 2019, the current exclusion contour for **Stereo** can be seen in Fig. 2.7(b).
The summary of all current initiatives for the sterile neutrino search is depicted in Tab.2.1. Their predicted sensitivities are displayed in Fig. 2.7(a) together with the parameter space for oscillation allowed by the RAA and gallium anomaly.

"It's a dangerous business, going out your door. You step onto the road, and if you don't keep your feet, there's no knowing where you might be swept off to."

Tolkien

Chapter 3

The **Stereo** Experiment

Since the publication of the RAA paper, discussed in Sec. 2.3.1, the interest on eV range sterile neutrinos have skyrocketed. The **Stereo** experiment (STErile neutrino REactor Oscillation) was proposed in 2013 [122] and since then it aims to investigate this anomaly and give some insight on the existence of light sterile neutrinos. **Stereo** is the result of a collective effort of different institutes, namely the Commissariat à l'Énergie atomique et aux Énergies Alternatives (CEA) in Saclay, the Laboratoire de Physique Subatomique et de Cosmologie (LPSC) in Grenoble, the Laboratoire d'Annecy-le-Vieux de Physique des Particules (LAPP) in Annecy and the home institution of the writer of this manuscript, the Max-Planck-Instutut für Kernphysik (MPIK) in Heidelberg. The source of antineutrinos chosen for **Stereo** has been already mentioned to be the research nuclear reactor of Institute Laue-Langevin (ILL) in Grenoble, France, and which also collaborates in the experiment. The particularities of the experimental site and its effect on **Stereo** will be discussed in Sec. 3.1. The physical description of the detector is split in two parts covering the inner volumes where neutrinos are observed and the outer sections designed mainly to shield them, described in Sec. 3.2 and 3.3 respectively. The description of the Liquid Scintillator (LS) used to trigger the neutrino signal is detailed in Sec. 3.4, together with the definition of the most important aspects of ionization in LS and the correlated scintillation of light. Finally, due to its importance in future chapters, a thorough description of the calibration systems is detailed in Sec. 3.6.

3.1 Location of Stereo at the ILL

The ILL reactor core consists of a 37 cm wide and 80 cm tall cylinder, earning thus the title of most compact nuclear reactor in France. The ILL itself is a research institution, which means the reactor is not used for commercial purposes. For this reason, the reactor is switched on and off cyclically throughout the year for maintenance and refilling purposes. These periods are called reactor-on and reactor-off respectively and are used by **Stereo** in different ways: on-periods constitute the data taking time of the detector, while off-periods serve as background characterization time necessary to understand the response of the detector during on-periods. The ILL usually undergoes 3-4 reactor-on cycles per year, of about 50 days each one. The rest of the time the reactor is switched off.

The power at which the ILL reactor runs is also characteristic from research facilities, being 58 MW_{th} and hence some orders of magnitude below the commercial reactors. It remains constant during the on-periods with subpercent level variations. Another characteristic of this reactor is the isotopic concentration of the fuel. It belongs to the HEU reactors with about 10 kg of highly enriched (93%) ^{235}U. The corresponding

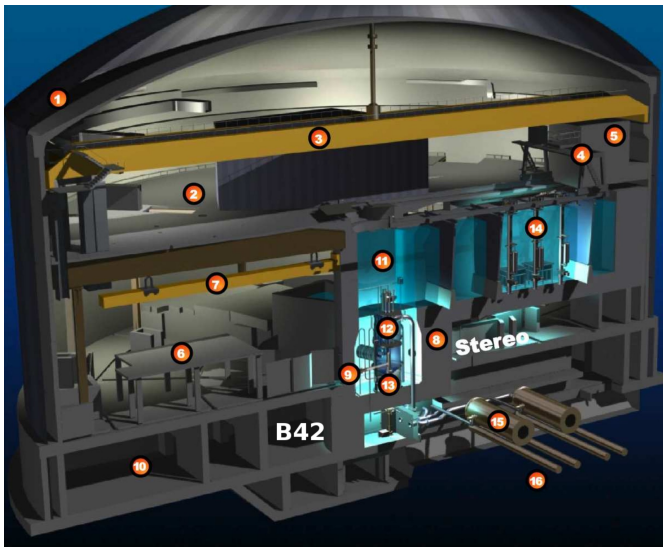

Figure 3.1: Placement of **STEREO** at the ILL. The detector is in level C, at the same level than the reactor barely 10 m away from it.

β (and thus $\bar{\nu}$) spectrum of a pure ^{235}U is the most precisely known since spurious isotopic contributions can be ignored, reducing the systematic uncertainty of the overall spectrum.

The **STEREO** detector is placed at the casemate PN3, being initially crossed underneath by the H7 neutron beam tube, at level C in the ILL research facility. The H7 tube was finally removed in 2017 because of degradation of its structure. The placement of **STEREO** is not the same as for the latest neutrino experiment in the ILL which was placed at the B42 room. This new placement has the advantage of being at the same level than the reactor core, while being similarly close to it. Both placements can be observed in Fig. 3.1. Due to the design of the ILL facility, the PN3 casemate is located at ground level, leading to an increased rate of cosmic background. However, as can be seen in Fig. 3.2, the water channel of the reactor is placed above **STEREO** which grants an additional shielding versus background from above.

Surrounding the reactor core there are other experiments that depend on their respective neutron tubes. For example, the closest neighbors of **STEREO** are IN20 and D19 experiments, and they use the neutron beams H13 and H11 respectivelt for their research. The impact of these neutron beams on **STEREO** will be discussed in Sec. 3.3.1.

The casemate PN3 is only 8 m away from the reactor core, hence the location of **STEREO** at a very short baseline from it allows an ideal situation for the study of eV sterile neutrinos, as discussed in Sec. 2.3.1. Surrounding the casemate there are a series of different experiments using intense neutron beams from the core, and often releasing gamma radiation that can affect **STEREO**. Above the **STEREO** detector is located a water channel used to transfer the new and the spent reactor fuel from the outside to the reactor core and viceversa, as displayed in Fig. 3.2. This channel consists of a U-shaped structure made of 1.9 m thick concrete walls and filled with 6 m of water, leading to an overburden of about 15 m.w.e. that is specially relevant since **STEREO** is at ground level, as noted in the paragraph above.

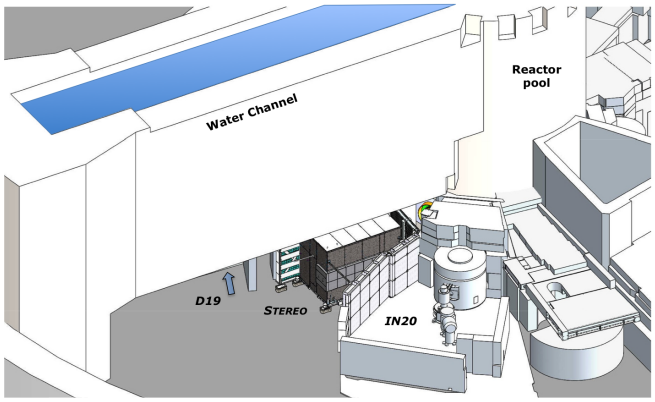

Figure 3.2: 3D view of the STEREO location. It is situated in next to the reactor, right below the water channel of the reactor and surrounded by the D19 and IN20 experiments.

3.1.1 Antineutrino Detection Principle: Inverse Beta Decay

In Chap. 1, it has been discussed how REINES, COWAN et al. created a crucial precedent of neutrino detection via the IBD process. Current reactor neutrino experiments, like STEREO, are no exception and use this interaction as detection principle, as has been discussed in Chap. 2. As a reminder for the reader from Chap. 1, the IBD is characterized by an antineutrino interaction with a proton, transforming it into a neutron while releasing a positron,

$$\bar{\nu}_e + p \rightarrow n + e^+ \,. \tag{3.1}$$

The particularity of such process is the correlated signal obtained from the non-simultaneous detection of the positron and the neutron. The detection of the positron is usually called *prompt* signal because it happens much sooner than the detection of the neutron, often called *delayed* signal. Both of them together create a characteristic correlated signal.

Prompt Signal

The kinetic energy of the e^+ translates directly into the energy of the antineutrino, so one can measure its the energy spectrum by observing the spectrum of the positron. Assuming massless neutrinos, the energy balance of the interaction leads to

$$E_\nu = m_n - m_p + m_e + K_e \,, \tag{3.2}$$

where m_i denotes mass of the particle i and K_e stands for the kinetic energy of the positron. Here it has been assumed that the kinetic energy of the neutron is negligible since $K_n \sim 10\,\text{keV}$. Now, considering that the signal of the positron is characterized by its annihilation with an electron, one needs to add the energy of two $0.511\,\text{MeV}$ gammas[1] to the visible energy of the signal. This means that

$$E_{vis} = K_e + 2 \times 0.511\,\text{MeV} \,. \tag{3.3}$$

[1] Mass of the electron/positron is $m_e = 0.511\,\text{MeV}$.

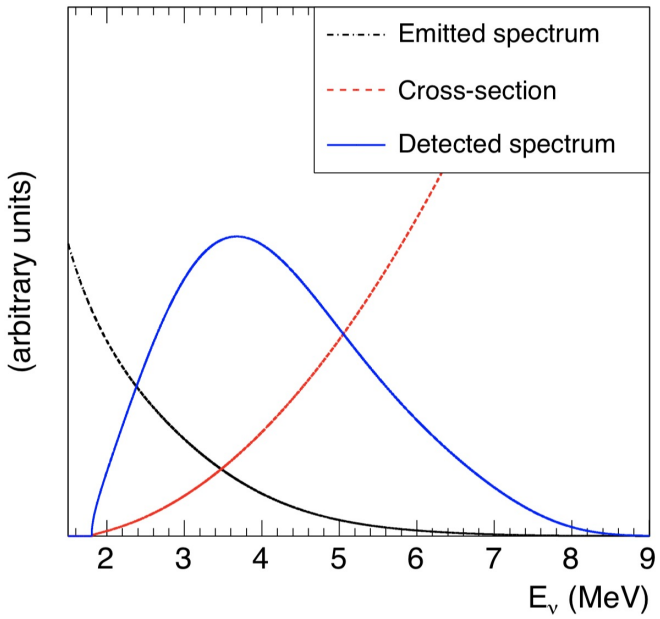

Figure 3.3: Illustration with arbitrary units of the detected antineutrino spectrum (blue solid curve) via IBD detection [90]. Reactor flux used in the case of pure ^{235}U fissions (black dashed-dotted curve). IBD cross section taken from Eq. 3.6 (red dotted curve).

Plugging 3.3 into 3.2 and using the neutron-proton mass difference $m_n - m_p = \Delta = 1.293\,\text{MeV}$, one obtains that

$$E_\nu = \Delta + m_e + E_{vis} - 2 \times 0.511 = E_{vis} + 0.784\,\text{MeV}\,, \tag{3.4}$$

is the relationship between visible (positron) energy and antineutrino energy. From this kinematic study immediately comes that the IBD has a relatively high energy threshold of

$$E_\nu^{th} = \frac{(m_e + m_n)^2 - m_p^2}{2m_p} \approx 1.806\,\text{MeV}\,, \tag{3.5}$$

which inherently requires that the E_{vis} spectrum starts at 1.022 MeV. In Fig. 3.3 it is represented the effective spectrum of reactor antineutrinos that can be observed via IBD. The combination of the fission spectrum with the IBD cross section (to zeroth-order) [84]

$$\sigma^{(0)} = \frac{2\pi}{m_e^5 \tau_n f} K_e p_e\,, \tag{3.6}$$

creates a particular distribution that peaks round 3-4 MeV. In Eq. 3.6, τ_n is the measured free-neutron lifetime, f is the phase space factor, and finally p_e is the momentum of the positron.

Other nuclear targets for IBD with lower threshold energies than hydrogen exist, but these energies usually are not enough to release free neutrons and they stay attached to the nucleus. Without neutrons, there is not correlated signal and it is difficult to reduce

the background events as will be discussed in further sections. Thus, nuclear targets other than the proton have not yet been used for reactor neutrino detection.

Delayed Signal

As discussed before, one of the main features of using the IBD as detection principle is the generation of a correlated signal. This is also one of the main advantages of using such interaction. The detection of the prompt signal is used mainly to reconstruct the energy of the initial neutrino, as exposed above, but the tagging of the coincidence comes from the detection of the delayed signal.

Relatively slow neutrons originating from the IBD will lose their energy mainly by elastic scattering with nuclei of the medium (see Sec. 3.4.2), and after some time they will be finally captured by some isotope. As will be discussed in Sec. 3.4, LS in STEREO is doped with a gadolinium-based compound, enabling neutron capture in gadolinium nuclei. This process creates a heavier isotope nucleus in an well-defined excited state that immediately decays releasing a gamma cascade in the following fashion:

$$ {}^{A}_{Z}\mathrm{Gd} + n \rightarrow {}^{A+1}_{Z}\mathrm{Gd}^{*} \rightarrow {}^{A+1}_{Z}\mathrm{Gd} + \sum_{i} \gamma_i \,. \tag{3.7} $$

The possible combinations of intermediate states i for each decay is exceedingly large. However, the total energy of the de-excitation always adds up to $\sum_i \gamma_i \approx 8\,\mathrm{MeV}$, with small variations depending on the initial isotope of gadolinium. The neutron capture signal is generally characterized by the time at which it is observed, typically around $\sim 20\,\mu\mathrm{s}$ after the prompt. This time-delayed signal, if reconstructed properly, unequivocally identifies the whole coincidence as an IBD. However, the proper reconstruction of these events is not always straightforward because of geometrical limitations, escaping energy from many gammas and indirect correlated background, which will be discussed in Sec. 3.3.1.

Neutrons can also be captured by other nuclei besides gadolinium, with different associated gamma emissions. However, these emissions are at lower energies and generally overlap with ranges where background is more prominent. Among these other possible captures, the most common is in ever-present hydrogen nuclei in the LS, with an associated mono-gamma emission at 2.22 MeV. The cross-section of captures in hydrogen is orders of magnitude lower than in gadolinium, but the major abundance of the former makes it equally relevant. As will be seen in future sections, the neutron capture in hydrogen is used for several purposes in STEREO like calibration and monitoring. Other captures less common are carbon, with and emission of around 5 MeV, and boron from STEREO shielding, with an emission of around 3 MeV [149].

3.1.2 Data Taking Timeline

STEREO detector was finally installed in November 2016, the time when the first data taking started. The first month was considered as a commissioning phase that helped to understand better the response of the detector and thus to determine the optimal Data AQuisition (DAQ) parameters. A total of 66 days of reactor-on data taking were recorded in what is labelled as *Phase I*. Two reactor-off periods were also included, for a total of 45 days [128]. *Phase I* was followed by a one year long reactor shutdown

due to necessary maintenance tasks, visible as the long hiatus in Fig. 3.4. This forced a temporal retraction of **STEREO** detector, period that was used to perform some repairs and shielding improvements.

Phase II started in October 2017 with approximately 120 of reactor-off data [129]. In February 2018 the first reactor-on data of this phase was taken lasting for almost two months. There were two additional cycles of reactor-on during spring and fall of 2018, respectively. To the date of handing of this manuscript, **STEREO** has had a total of 119 days of reactor-on and 211 of reactor-off of data taking during *Phase II*.

3.2 Inner Volumes

The inner detector of **STEREO** can be divided in three main subvolumes. The innermost part of the detector is subdivided in six identical cells and it is called neutrino Target (`TG`). Surrounding the `TG`, an external volume called Gamma Catcher (`GC`) is placed, and it is subsequently subdivided in four different volumes corresponding to the four sides of **STEREO**. The disposition of volumes can be seen in Fig. 3.5 where the cross section of the detector is depicted. Finally, to complete the inner detector, at the top of each of the aforementioned subvolumes an acrylic buffer is placed containing a set of photomultiplier tubes (PMTs). All volumes are filled with different liquids. More details about the individual volumes are given in the following sections.

3.2.1 Neutrino Target

The `TG` acts as a fiducial volume of the whole detector, and although it is not the only place where IBD can occur, it is where neutrons are intended to be captured. Most of the cuts for neutrino signal require certain energy deposition in the `TG` volume to be accepted. It consists of an acrylic aquarium with 12 mm thick walls of inner dimensions $2.233 \times 0.889 \times 1.230\,\mathrm{m}^3$. The volume is divided longitudinally in six smaller cells optically separated from each other by highly reflective separation walls. This volume is filled with an organic `LS` based on linear alkylbenzene and doped with a gadolinium compound to enhance the neutron capture and detection of the delayed signal (see Sec. 3.4). Regardless of the optical separation, the `LS` is physically communicated from cell to cell by a small opening at the bottom of the walls. This ensures liquid homogeneity for all cells and avoids inducing any pressure difference on the walls due to liquid

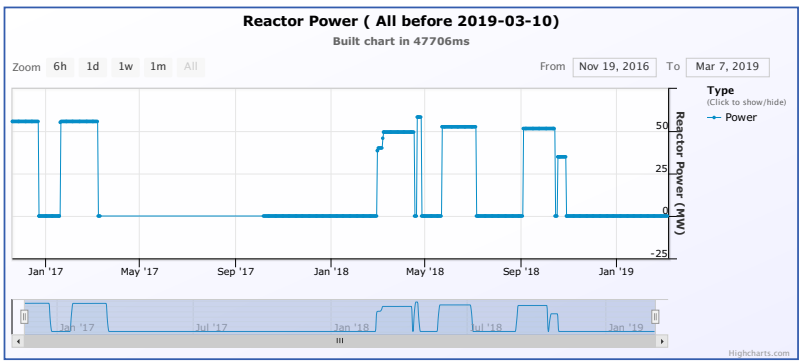

Figure 3.4: Time evolution of the ILL reactor power. Several periods of reactor-on can be clearly seen followed by reactor-off hiatus.

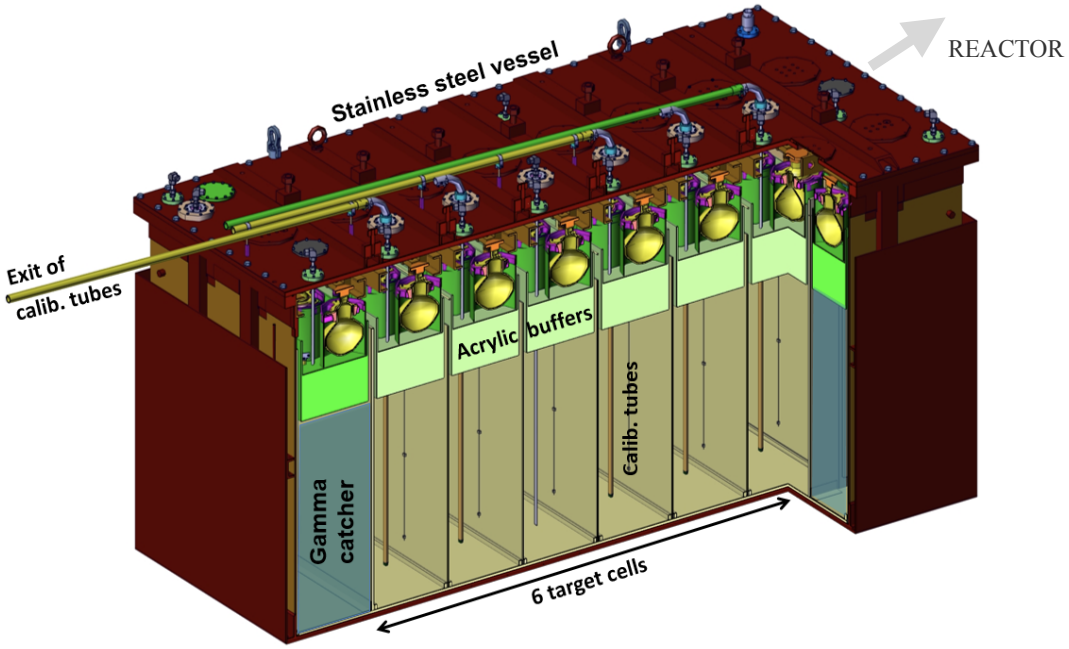

Figure 3.5: Cross-section of the inner detector of **Stereo**. 6 identical cells define the TG volume, surrounded by the GC volume. The acrylic buffer, placed on top of the cells, keep the PMTs within a oil bath that optically couples them with the LS. The calibration tubes, described in Sec. 3.6, are also shown on the top of the TG.

level imbalance.

Reflective walls are constructed as a sandwich of several layers, where the pivotal part is the film of VM2000^{TM} Enhanced Specular Reflector (ESR) placed at the very center. The reflector is subdivided in two layers separated by a thin nylon net that ensures an air gap (100 µm) between them and enhances the reflectivity of the sandwiches. To finish the sandwich, the reflector is covered by two acrylic plates after a small air gap. In Fig. 3.6 a sketch of the sandwich is depicted. To release pressure off the plates and to effectively communicate the liquid of the cells, the bottom corners have a cut of 45° at 20 mm from the edges. The reflectivity achieved is 100% for angles higher than 42° due to total reflection, and above 98% for smaller angles. However, this reflectance does not hold at the borders of the walls, where the sealing of the airgap and the liquid communication allows for optical cross-talk between cells. This behavior is expected and designed to lead to a 5% light leak between TG cells. A detailed study of the light cross-talk between volumes is described in Sec. 5.3.3.

3.2.2 Gamma Catcher

The TG fiducial volume is enclosed within a larger double walled stainless steel vessel of inner dimensions $3.096 \times 1.536 \times 1.505\,\mathrm{m}^3$. This outer volume, as its own name reveals, is designed to detect escaping gammas from events generated in the TG while also works as an active veto for residual background reaching the inner detector. It is filled with a LS very similar to the one in the TG, also based in LAB, but not loaded with gadolinium.

It is divided in four subvolumes that are optically separated from each other in the same fashion as TG cells do. Two of the cells, called GCBack and GCFront, are situated at the back and the front of the TG and have a similar size as the cells from there. The two remaining cells, called GCD19 and GCIN20, are located at the sides of STEREO facing experiments D19 and IN20 respectively, and are 30 cm thick and cover the full length of the inner detector.

The separation walls between TG-GC and GC-GC have double ESR sandwitches, so the optical separation is larger than between TG cells. Also there are no communicating holes in these separation walls. The light cross-talk is still existent, being $< 2\%$, but it is lower than between TG cells.

3.2.3 Acrylic Buffer and Photomultiplier Tubes

In STEREO, the readout system is done by a set of 48 8-inch Hamamatsu PhotoMultiplier Tubes (PMTs), which are located at the top of the inner detector. 24 of them are divided into the six cells conforming the TG at a reason of 4 PMTs per cell. The remaining 24 are left for the GC, being 4 of them placed on top of each of the GCFront and GCBack, and the 16 remaining split into GCD19 and GCIN20. As a part of this thesis, these PMTs have been tested and characterized to ensure a correct functionality. This work is presented in Chap. 4. The model of the PMTs, depicted in Fig. 3.7, is a R5912-100 characterized by its hemispherical surface with a super bialkali (SBA) photocathode. The SBA has a particularly high quantum efficiency, about 35% at 430 nm, that helps enhancing the response of the detector. More details about the quantum efficiency of the PMTs and its implementation in the simulation of STEREO can be found in Sec. 5.5.

Light generated in the LS is eventually reflected upwards thanks to the reflective plates at the sides and at the bottom of the volume. In order to homogenize the light collection as much as possible, the PMTs are separated from the LS of the cells by a 20 cm thick acrylic block. These blocks are chemically compatible with the liquid and share a similar refraction index, making them effectively transparent to light. To

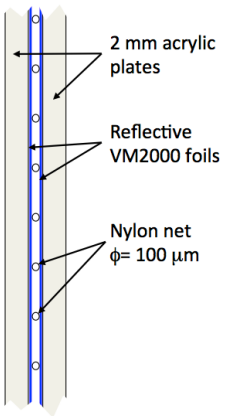

Figure 3.6: Sketch of the important parts constituting the separation walls between cells. From the outside to the inside: 2 mm acrylic plates, reflective VM2000^{TM}foils, and in the center the nylon net spacing with an air gap both foils.

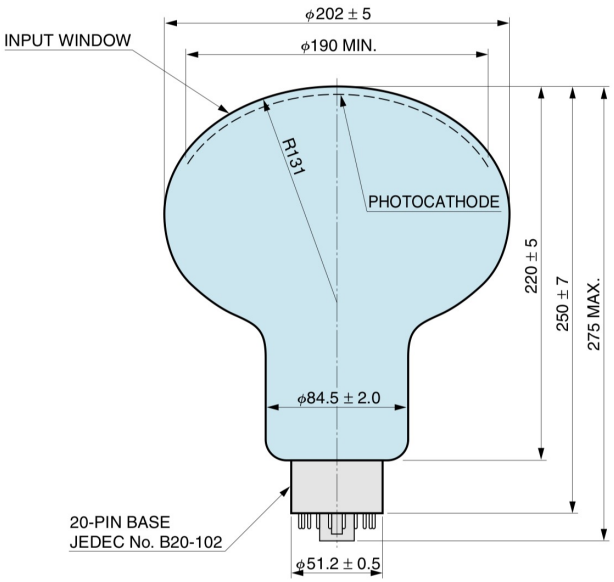

Figure 3.7: Diagram representing the parts and dimensions of a 8-inch Hamamatsu R5912 PMT. [160]

avoid light losses, these blocks are also surrounded by reflectors. The acrylic is optically coupled to the PMTs by a bath of mineral oil in which they are submerged.

3.3 Outer Volumes and Background

In **Stereo**, background signals can be classify in two types: correlated and accidental. Correlated background refers to any composition of particles that can mimic in any way a correlated signal, prompt and delayed included, that could be mistakenly tagged as an IBD. Accidental background, in contrast, constitutes a single particle detection that mimics either the prompt or the delay signal, interfering in a real IBD event. Possible candidates for background come basically from two different sources: the reactor and its experiments, and cosmic background. After extensive background characterization measurements, specific shielding measures were taken for stop as much as possible the impact of neutrons and gammas from these sources. Details about both nature of the backgrounds and their respective countermeasures are given in the next subsections.

3.3.1 Reactor Related Background

As described previously, **Stereo** is located at barely 10 m from the reactor core at the ILL. This situation is responsible for multiple reactor-related sources of background. This background is composed basically by neutrons and gammas, and the source of both particles are most of the times correlated. More concretely, background neutrons generally interact with the surroundings of the detector generating the emission of gammas, (n, γ), either by activation of the material or by neutron capture.

As can be seen in Fig. 3.8, **Stereo** is placed in PN3 casemate and it is surrounded primarily by IN20 and D19. The neutron tubes corresponding to each one of the three

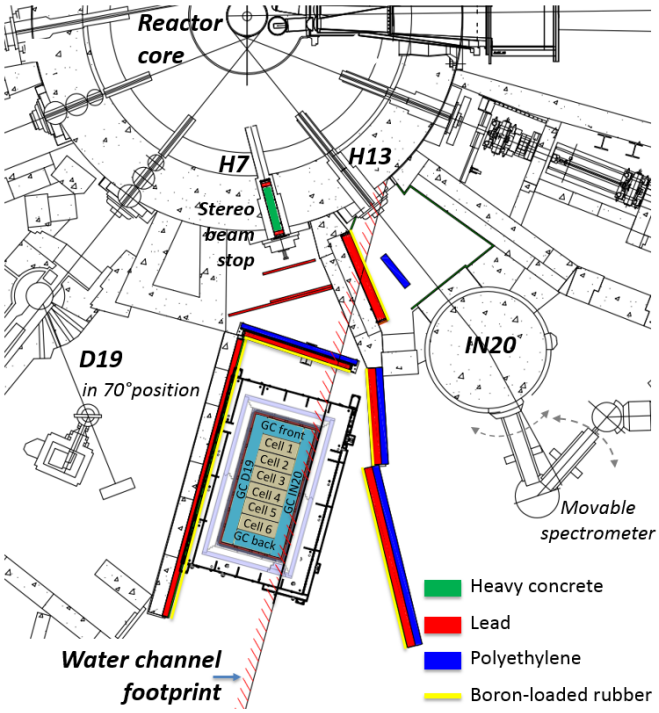

Figure 3.8: Sketch of the casemate PN3 viewed from the top. Neighboring experiments D19 and IN20 are placed in from of the exit of neutron tubes H11 and H13, respectively.

areas are H7, H13 and H11, respectively. Specially tailored background-measurement campaigns have been done in STEREO to try to characterize the reactor-related background. To seize the source of thermal neutron background, measurements were performed with a ^{3}He tube placed at several locations. The results clearly showed neutron emissions from four main areas: the H7 tube plug, the H13 casemate, the reactor core and the IN20 instrumental area.

Gamma measurements were performed using a high resolution germanium detector. Although its high energy efficiency is low, it was used to identify possible sources of (n, γ) reactions. The main sources found were ^{56}Fe and ^{27}Al as neutron capture from the structural materials of the PN3 casemate. Also, traces of ^{16}N decay were found coming from cooling water circuit of the reactor, flowing below STEREO [147].

3.3.2 Cosmic Radiation Background

Muons are a very important source of correlated background for STEREO. As mentioned previously, the fact that the detector is placed at ground level affects the rate of those cosmic rays observed. After correcting for the effect of atmospheric pressure, the muon rate arriving to the STEREO detector reaches an average of 660 s^{-1} at 1020 hPa with some time variations.

The way cosmic muons create correlated signals is by nuclear spallation in the liquid scintillation and surrounding materials. As a result of the collision, radioactive nuclei and fast neutron are generated. As will be discussed in Sec. 3.4.2, fast neutrons collide

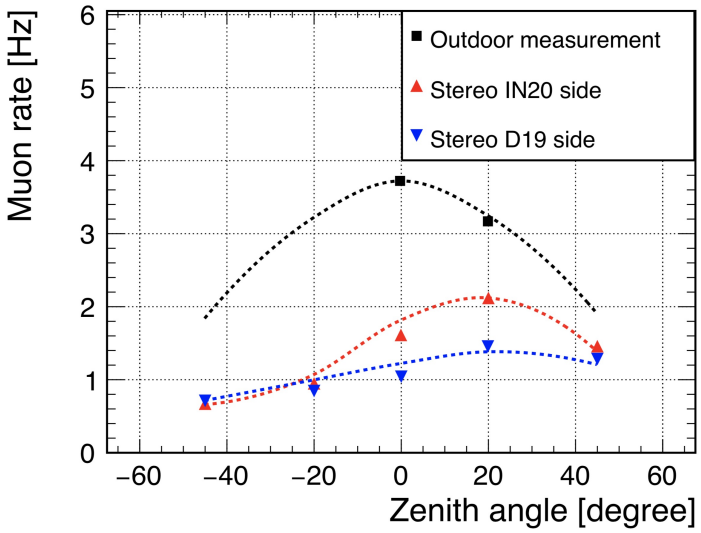

Figure 3.9: Measurement of muon rates for different incident angles both in the detector area and outside the reactor. The overburden from the water transfer channel gives up to a factor 4 reduction on the rate, but due to its geometry the effect is not symmetrical. In dashed lines appear the muon rate from the CRY libraries, used in the **STEREO** simulation after proper scaling. [156]

continuously with nuclei in the LS, transferring them some energy in the form of kinematic recoil. The recoil is quickly converted into scintillation light and acts as a prompt signal. After $\sim 20\,\mu s$ of slowing down and thermalization, the neutron is captured and creates a delayed signal. The combination of both constitutes the correlated signal that mimics an IBD.

The first shielding to cosmic background comes from the aforementioned transfer channel, conveniently placed above **STEREO** detector. The 15 m.w.e. proportioned by it leads up to a factor 4 of muon rate reduction, as displayed in Fig. 3.9. However, this plot also shows a dependence on the zenithal angle coming from the non-symmetric placement of **STEREO** with respect to the transfer channel.

3.3.3 Muon Veto

Besides the overburden, to further enhance the reduction of cosmic background an active water Cerenkov muon veto was placed on top of **STEREO**, exactly covering the detector and shielding. It is filled up to the 25.6 cm mark with demineralized water, which radiates Cerenkov light [40] when high energy muons cross the volume. 20 PMTs (see Sec. 3.2.3) are placed in the veto to detect cosmic radiation, after it has been wavelength-shifted to $\sim$ 420nm by some 4-Methylumbelliferone (4MU) WLS compound dissolved in the water.

When a muon crosses the veto, the signal can be easily identified by requesting a saturation of the PMTs in any given cell of the inner detector together with a high energy deposition in the veto volume itself. This condition is easily met due to the high energy carried by muons (for more details on ionization of the LS see Sec. 3.4.2). After the muon-induced prompt signal has been tagged, one can veto data acquisition

for a reasonable amount of time, i.e 100 µs, so that any background correlated signal gets rejected. Continuous studies of neutrino runs have shown that the probability of identifying a cosmic event crossing the veto, called muon veto efficiency, is $(99.5 \pm 0.1)\%$ for both reactor-on and off data [124].

3.3.4 Passive Shielding

In STEREO there are two main ways to shield the detector. Borated polyethylene and boron-loaded rubber (B4C) to thermalize and capture neutrons, and mainly lead to attenuate gamma rays. A sketch of the shielding parts of STEREO can be seen in Fig. 3.8.

When investigating neutron background from H7, a series of MCNPX [154] simulations showed that the initial plug of the tube, containing lithium, generated a sizable amount of fast neutrons via ^{6}Li activation. Hence, the plug was changed to a new one composed by boron, lead and heavy concrete, which reduced considerably the rate of neutrons.

The port of H13 extracts an intense beam of fast neutrons for the IN20 experiment that, although not going directly to the PN3 casemate, can easily diffuse and reach the detector. For that reason, the H13 casemate bordering on Stereo was reinforced by borated polyethylene to thermalize and capture the diffused neutrons that would go otherwise to the detector. To palliate the residual gammas, the thickness of an existing lead wall inside the H13 casemate was increased from 10 to 20 cm and the casemate was covered with boron-loaded rubber from the inside.

Surrounding the STEREO area a 2.4 m high wall of external shielding is placed. The front wall between STEREO and the reactor core is composed by 10 cm of polyethylene and 10 cm of lead. Facing D19 there are 10 cm of lead and 30 cm of concrete. On the IN20 side there are 15 cm of lead and 15 cm of polyethylene. With at least 10 cm thickness in each direction, the outer lead layer (total 58.9 t) serves to mitigate the residual γ-ray background in the STEREO area. As high energy γ rays from the decay of ^{16}N passing through the floor of the detector have been observed, the thickness of the lead layer below the detector is 20 cm.

Besides all the external setup around PN3 casemate, a passive shielding of about 65 tons made of 5% borated polyethylene and a lead outer layer encloses the STEREO detector to further protect it, as displayed in Fig. 3.10. The thickness of this layer varies according to the needs of each of the sides of STEREO detector, ranging from 15 cm to 30 cm. Such massive shielding requires a heavy structure to accommodate it, reason why STEREO stands on the area with the largest allowed load per square meter in the reactor building.

3.3.5 Magnetic Shielding

Some PMT characteristics like sensitivity or dark current, are very susceptible to the presence of external magnetic fields. The IN20 experiment uses superconducting Helmholtz coils generating intense magnetic fields up to 15 T. Therefore, special care on magnetic shielding is taken in STEREO to avoid any degradation on the coincidence signal. In order to reduce the effect of external magnetic fields special shielding has

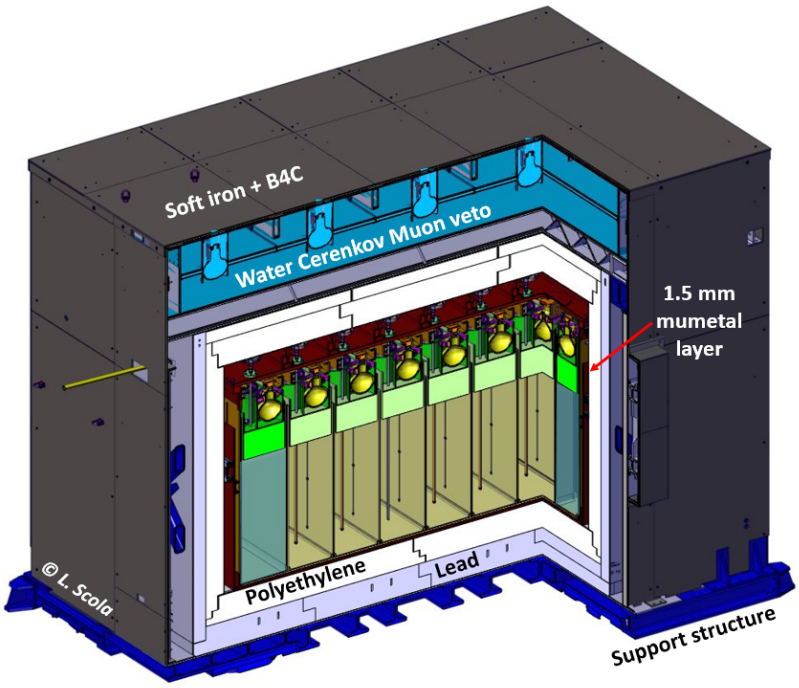

Figure 3.10: Passive shielding enclosing the detector. Includes lead and polyethylene layers for gamma and neutron radiation, soft iron and mu-metal to isolate from magnetic disturbances and a water Cerenkov muon veto for cosmic rays.

been designed. It consists of 10 mm of ARMCO soft iron that completely surrounds the **Stereo** shielding structure and a layer of mu-metal of 1.5 mm enclosing the detector volume. At the PMT level, concentric layers of 1 mm each were used to wrap them forming a cylindrical shape around them, two for veto PMTs and one for `TG` and `GC` PMTs.

The magnetic shielding proved to be effective during IN20 operating at high magnetic fields, allowing a smooth data taking with no noticeable variations in `TG`/GC PMTs. Up to 20% fluctuations for veto PMTs were observed due to their major exposure to the fields [123]. However, their variations did not induce any efficiency loss thanks to the low threshold compared to the high light deposition of muons.

3.4 Liquid Scintillator

Since their first use in the Reines and Cowan experiment, discussed in Chap. 1, organic `LS` have been the basis for groundbreaking contributions in low-energy neutrino physics. They are easy and relatively cheap to produce while providing a dense enough target volume for neutrino interactions. `LS` have also the advantage of being adaptable to the circumstances and needs of a given experiment by simply adding or subtracting solvents, reagents or fluors to the final mix. In the following sections the particularities of the scintillation mechanisms of `LS` will be described, empathizing the concrete case of **Stereo**.

3.4.1 Liquids Description in Stereo

The LS in **Stereo** has been produced by the Max-Planck-Institut für Kernphysik (MPIK). The MPIK has a history of being heavily involved in the production of many LS from past experiments, like Borexino [60] and Double Chooz [77]. This extensive knowledge has proved very practical to cater for the special needs of the **Stereo** detector.

The total volume is filled with 1800 liter of LS which is in turn a compound of several organic scintillators [131]. Namely: 75wt.% of Linear AlkylBenzene (LAB), 20wt.% of PhenylXylylEthane (PXE) and 5wt.% of Di-IsopropylNaphthalene (DIN). These percentages are kept the same for both LS used for TG and GC volumes.
Traditionally the most common solvent for high light yield scintillators in neutrino experiments has been pseudocumene (PC). Nowadays, however, safety considerations have taken ground and the focus shifted to high flash point solvents, like LAB, PXE and DIN. The counterpart is a lower light yield in comparison to PC. The main component in **Stereo**, LAB, has a slightly lower light yield than other typical organic scintillator solvents. However, it compensates by being specially versatile due to its high transparency to scintillation light, material compatibility and low price. The second solvent, PXE, increases the light yield and is a high flash point solvent as well. Finally, the small amount of DIN was introduce to provide the experiment with specially high pulse shape discrimination capabilities [130]. However, recent laboratory measurements performed at the MPIK [131] by Buck et al. showed inconclusive results about the positive effect of DIN on the pulse shape discrimination of the LS of **Stereo**, discussed in Sec. 3.4.4.
As stated before, to perform the neutron capture in the LS a small concentration of a Gd-loaded compound is added. In the particular case of **Stereo** it is Gd-β-diketonate ($Gd(thd)_3$) in a concentration of 0.2wt.%. This amount ensures an efficient Gd-neutron detection without compromising with the LS light yield.

The emitted scintillation spectrum from the solvent needs to be shifted to the most sensitive wavelength region of the PMTs. For this reason, the WaveLength Shifters (WLS) are diluted in small concentrations in the final mix. Their absorption band overlaps with the emission band of the solvent while their emission band is at lower energies. This overlap is usually large enough to ensure an efficient energy transfer between the molecules. Although for some applications it is sufficient to have just one WLS in the scintillator mixture, a secondary WLS may be added to improve the attenuation length of the scintillator. The main dopant is typically added at concentrations of few g/l while the secondary WLS usually has concentrations less than 20 mg/l. In **Stereo**, those fluors are 2,5-DiPhenylOxazole (PPO) and 4-bis-(2-MethylStyryl)Benzene (bis-MSB) with a concentration of 7 g/l and 20 mg/l respectively for TG. Besides PPO there are several other fluors that have a better overlap with bis-MSB. However, the absorption band of PPO overlaps the one of the highly quenching $Gd(thd)_3$ molecule, making this fluor specially suitable for **Stereo**. PPO is also specially suitable due to its low toxicity, high solubility in the organic solvent and transparency. The fluors used in the GC are the same than for TG to keep consistency between both LS. However, concentration of PPO has been lowered to 3 g/l due to the absence of gadolinium. This reduction lead to less self-absorption from the PPO and in consequence an increase of the attenuation length. This will be discussed in more detail in Sec. 5.3. The second fluor, bis-MSB, has been kept with the same concentration.

Therefore, usual scintillation around 280 nm is shifted by PPO to values around 350 nm so that the bis-MSB can finally rise its wavelength up to 420 nm, lying within the optimal region of the PMTs. Because of the large scale of the neutrino detectors, several absorption and re-emission processes may take place between the initial scintillation and the optical light read by the PMT. This forces the WLS to have a very high re-emission quantum yield ($\sim 85\%$ [130]) and not too high concentration to ensure minimal losses and keep the total light yield high.

3.4.2 Molecular Excitation and Ionization

Organic LS are very sensitive to ionizing particles. These particles lose their energy mainly by electromagnetic interaction with the material during their way across it. LS proportionally transform that energy into scintillating light that is visible by the detection system. When orbital electrons are promoted to higher energy levels while still bound to a molecule, the process is called excitation. If enough energy is transferred to the electron, it can be detached from the molecular bindong, leaving behind a positive ion. This process is called ionization. In general, excitation is the preferred processes for its better energy resolution, less ionization quenching and faster pulse shape of the signal [159]. For now on, molecular ionization and excitation will be used indistinctly under the scintillation production context.

Charged particles

The rate at which the energy is lost in the material depends on the nature of the particle in question and its energy. As discussed in Sec. 3.1.1, in **Stereo**, the only ionizing particles that will be exciting the molecules of the LS will be electrons/positrons, photons and neutrons. Charged particles can lose energy in different ways that depend on their energy. For highly energetic charged particles, most of the energy is lost via two radiative processes, as can be observed in Fig. 3.11. The first one is the Bremsstrahlung [41] caused by the deceleration of charged due to the influence of the Coulomb field of the nuclei. The second one is the Cerenkov radiation [40], caused when a charged particle travels through a material faster than light speed in such material. As the particle slows down, the main contribution for energy loss is by inelastic scattering with orbital electrons of the material, i.e molecular ionization. The frontier between high and low energy electrons can be seen in Fig. 3.11 to lay around the ~ 10 MeV. The range of energies of the positron signal in **Stereo** corresponds to the low energy group, and the mean rate of energy loss for them can be approximated by the Bethe-Bloch formula as follows,

$$\frac{dE}{dx} = 4\pi N_A r_e^2 m_e c^2 \frac{Z}{A}\frac{1}{\beta^2}\left[\ln\frac{\gamma m_e c^2 \beta\sqrt{\gamma-1}}{\sqrt{2}I} + \frac{(1-\beta^2)}{2} - \frac{2\gamma-1}{2\gamma^2}\ln 2 + \left(\frac{\gamma-1}{4\gamma}\right)^2\right], \tag{3.8}$$

where N_A is the Avogadro number, r_e is the electron radius, Z, A are the atomic and weight numbers of the absorber respectively and I is the mean excitation energy of the absorber material. Molecular ionization is responsible of producing scintillation light and will be discussed in more detail in section 3.4.3.

Photons

Photons in **STEREO** can be subdivided in two well-defined categories according to their energy. The first category contains photons in the $\sim$ MeV range and are usually referred as gammas. In **STEREO** these can either come from radioactive calibration sources, see Sec. 3.6, with energies between 0.630 and 4.44 MeV; from neutron-capture related emissions, see Sec. 3.4.2, with a varied range of energies around ~ 1 MeV; or from the electron-positron annihilation of the prompt signal from the IBD, with a definite energy of 0.511 MeV. As can be seen in Fig. 3.12, gammas of these energies within a carbon-based liquid like the LS in **STEREO** will mostly interact via Compton-scattering with orbital electrons of the medium until their energy is low enough to be captured in a photoelectric effect. Pair production also contributes, but is heavily outweighted by the other two processes at energies < 10 MeV.

The second type of photons define the scintillation light, which energy is at the $\sim$ eV level. The production and propagation of scintillation light in LS is described in detail in Sec. 3.4.3. The main process available for photons at these energies are the photoelectric and molecular excitation processes.

Neutrons

Neutrons, in the same fashion as other particles described above, can interact with matter in different ways depending on their energy. Most generally neutrons can be labeled as:

- Slow neutrons: energies lower than 1 eV.
- Epithermal neutrons: energies between a few eV and a few keV.
- Fast neutrons: energies above the 10 keV mark.

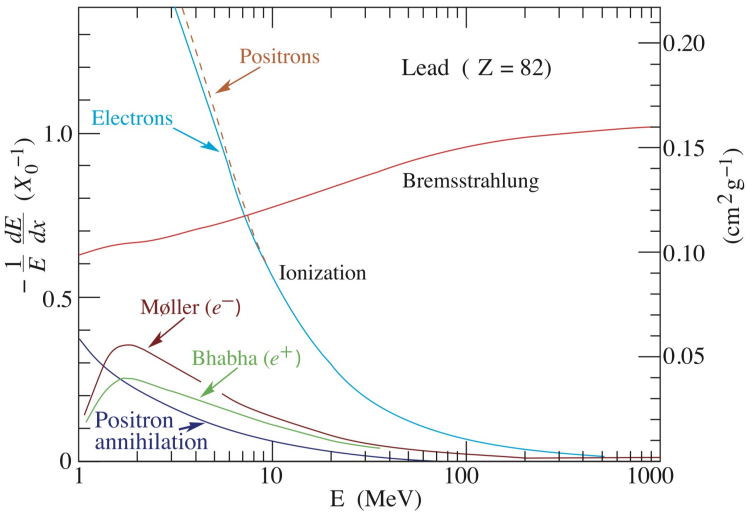

Figure 3.11: Fractional energy loss per radiation length described in lead as a function of electron or positron energy. Electron (positron) scattering is considered as ionization when the energy loss per collision is below 0.255 MeV, and as Møller (Bhabha) scattering when it is above [54].

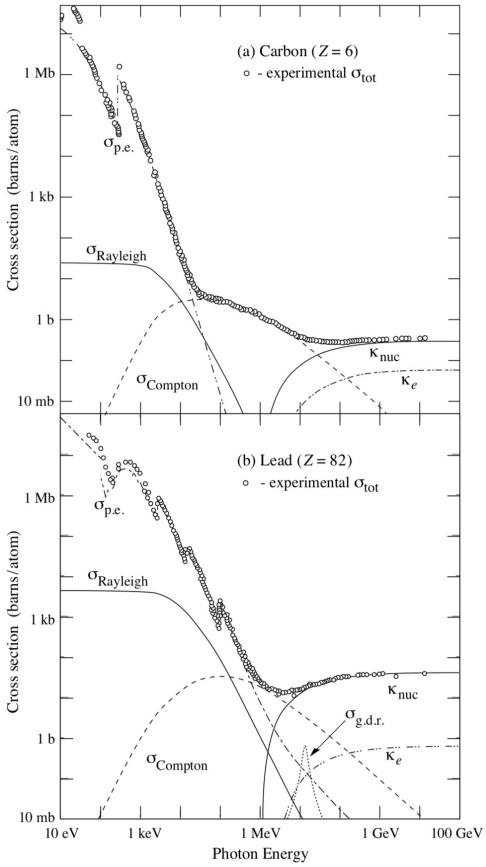

Figure 3.12: Photon total cross sections as a function of its energy in carbon (up) and lead (lead), showing the contributions of different processes: σ_{pe}: atomic photo-electric effect; σ_{Rayleigh}: Rayleigh (coherent) scattering–atom neither ionized nor excited; $\sigma_{Compton}$: Compton scattering off an electron; $\kappa_{e,nuc}$: pair production, electron/nuclear field [54].

In **Stereo**, both epithermal and fast neutrons are generated in different situations. The former, as discussed in Sec. 3.1.1, are generated from the IBD, with $E \sim 15\,\text{keV}$, together with a positron. The latter, with energies up to the MeV, come mostly as spallation neutrons in lead from cosmic muon background as described in Sec. 3.3.2. In any of the cases, because neutrons are neutral and heavy they interact in fewer ways than the charged leptons. In fact, inside the LS they can basically scatter with or be captured by nuclei.

At high energies, the cross-section for neutron-nucleus scattering is orders of magnitude higher than neutron capture. Thus, fast neutrons start losing energy by colliding with atomic nuclei. During these collisions a significant fraction of the kinetic energy of the neutron can be transferred as nuclear recoil. These recoiling nuclei behave similarly to any other heavy charged particle, ionizing the LS and generating an observable scintillation. This scintillation can be tagged by means of pulse shape discrimination, discussed in Sec. 3.4.4, and used to identify spallation neutrons. The mass of the nucleus determines the maximum kinetic energy transferable during the two-body scattering [159]. Hydrogen nuclei, i.e protons, have a mass almost identical to neutrons and thus they can be transferred most of the kinetic the energy in one scattering. Therefore,

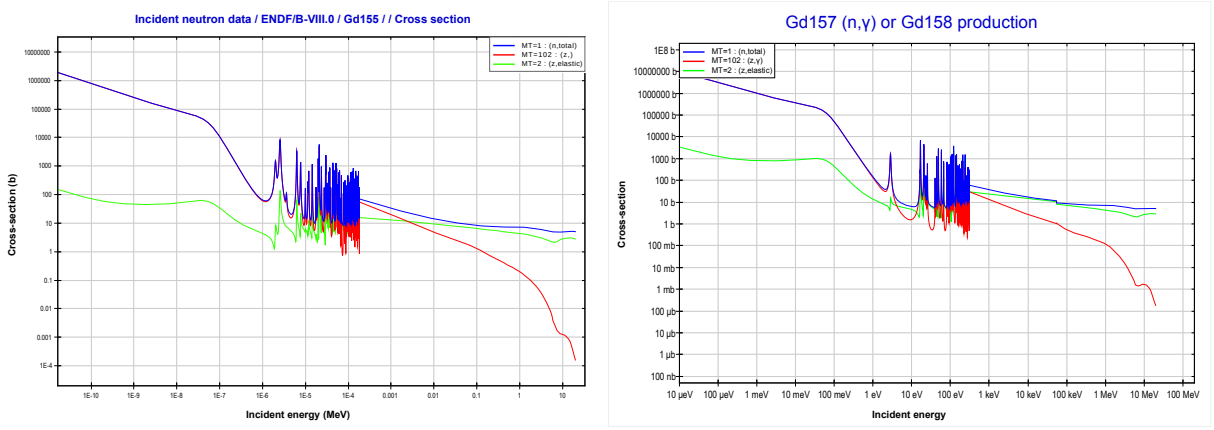

(a) **(b)**

Figure 3.13: Evaluated cross sections for n-capture, and elastic scattering processes for neutrons in Gd solutions using ENDF/B-VIII nuclear reaction data libraries [150]. Plots produced from the JANIS service of the Nuclear Energy Agency (NEA) [151].

proton recoil signals mimic the kinetic energy spectrum of fast neutrons reaching the detector. Heavy nuclei can also be scattered by neutrons. However, the energies transferred are usually small and, as will be discussed in Sec. 3.4.3 for general low energy charged particles, relatively quenched. The process of continuous scattering described is called moderation and it is the basis for controlled nuclear fission in a reactor core.

Either by enough moderation or because they come from an IBD, epithermal neutrons keep slowing down beyond the keV range. At this point the rate of collision has dropped considerably due to the low kinetic energy of the neutron. This final stage of slowing down to the same energies as the surrounding nuclei is called thermalization. Once neutron and nuclei are in thermal equilibrium, the cross-section of a neutron capture is already high enough to compete with the scattering cross-section, and hence the neutron is promptly captured. Not all nuclei have the same cross-section for such process, and the density of certain elements like gadolinium and the abundance of its isotopes play a crucial role on the expected capture time of neutrons in the LS. As an example, Fig. 3.13 displays the evolution of scattering and neutron capture cross-sections in terms of kinetic energy.

3.4.3 Scintillation Light

Production Mechanism

In summary, the main feature of any LS is indeed to produce scintillation light when an ionizing particle passes through the liquid so the detection system can observe it. The scintillation principle of organic scintillators is based on molecular excitations, as described in [159].

A large part of the composition of these liquids are aromatic molecules, mostly ring-structured benzene, which ground state, from now on called S_{0v} where S denotes that

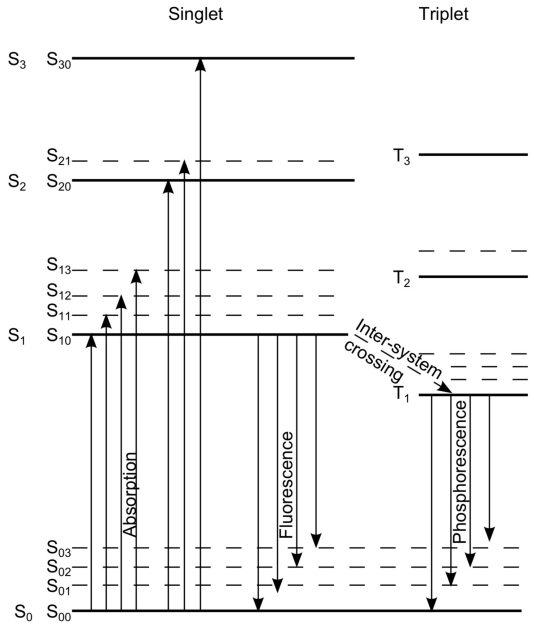

Figure 3.14: Energy levels of a fluorescent molecule [159]. An incident particle can excite an electron into the excited singlet or triplet states. The higher excited states rapidly decay into the lowest excited states S1 and T1, which decay emitting light through fluorescence and phosphorescence process respectively.

It is a singlet of spin 0[2]. It is important to note that for each electronic configuration, including also the ground state, there are a certain number of vibrational excited states v with energy differences of the order of $\sim 0.15\,\text{eV}$.

Molecular excited states can be singlets S_{1v} or triplets T_{1v}[3], to which a molecule can be brought from the initial ground state after an external energy transfer by an ionizing particle. All possible electronic configurations of the molecules of interest can be found in Fig. 3.14.

The faster, and usually majority, component of the scintillation light comes from the deexcitation of the singlet states. After ionization, higher excited states rapidly are radiationless converted to vibrationally excited states S_{1v} via internal conversion, which end up dissipating their vibrational energy thermally. These processes take in total less than 1 ns to take place, where the thermalization of vibrational states takes most of the time. The next step is the fluorescent decay $S_{10} \rightarrow S_{0v}$ which for most scintillators takes a few ns. This emission is usually of the order of $\sim 4\,\text{eV}$ or $\sim 300\,\text{nm}$. If the final state is not in vibrational equilibrium, the emitted radiation has too low energy to be reabsorbed and thus the scintillator becomes transparent to its own fluorescence. Otherwise, the solvent can reabsorb its own radiation and thus a WLS reagent needs to be added to the liquid. More about the propagation of the scintillation in the next subsection.

[2]Singlets are non-degenerate states with only one possible magnetic orientation
[3]Triplets are energy degenerate states with three different magnetic orientation, in this case $\pm 1, 0$

The secondary, and quite often smaller, component of the scintillation light comes from the deexcitation of the triplet states T_{nv}. The lifetime of the triplet state is characteristically much longer than the excited singlet state because triplets require a spinflip to decay to the ground singlet state. This process that can take up to 1 ms, six orders of magnitude more than the fluorescent decay and is commonly known as phosphorescence. Indeed, no acquisition system could work out such a delayed signal. However, there is a faster channel for a triplet decay that can be used together with the main fluorescent signal. A bimolecular interaction can happen when two molecules radiationless transition simultaneously from two triplet T_{10} states to two singlets S_{1v} and S_{0v}. The former can decay normally via fluorescence typically after $\sim 100\,\text{ns}$ from the initial ionization, i.e slow fluorescence.

Whether the excited state will be singlet or triplet depends mainly on the type of ionizing particle and its particular energy deposition per length unit dE/dx. Singlet states characteristically are created for small energy transfers, when the electron simply jumps up to a higher state. Triplet states, on the contrary, tend to be created when a high enough energy transfer releases the electron from the molecule and soon after recaptured [159]. The ratio between singlet and triplet excitations per event, i.e fast and slow components of the signal respectively, is often used as method for particle identification, the pulse shape discrimination reviewed in Sec. 3.4.4.

Non-Linearities and Birks' Law

Although the scintillation produced by the `LS` depends on the energy deposited, the relation is not always completely linear. Highly ionizing particles tend to degrade the resulting light output during the ionization, occurring specially at the end of the track of the particle when dE/dx is at its highest [159]. This is due to damaged molecules dissipating energy radiationless, and its commonly known as light quenching. Birks [42] found a semi-empiric formula that describes the quenching of scintillation light:

$$\frac{dL(E)}{dx} = \frac{L_0 \left(\frac{dE}{dx}(E)\right)}{1 + \texttt{kB} \left(\frac{dE}{dx}(E)\right)}. \tag{3.9}$$

where L_0 is the scintillation nominal value and `kB` is an intrinsic magnitude of the liquid called Birks' parameter, and quantifies how sensitive is the material to quenching. In Eq. 3.9 `kB` appears in the denominator together with dE/dx in such a way that:

1. For high ionization, $\frac{dE}{dx} \cdot \texttt{kB} >> 1$, the quenching is maximal and $\frac{dL(E)}{dx} \propto L_0/\texttt{kB}$.
2. For low ionization, $\frac{dE}{dx} \cdot \texttt{kB} << 1$, the quenching is minimal and $\frac{dL(E)}{dx} \propto L_0$.

Since dE/dx depends on the energy E of the particle, one can conclude that for high energy particles the quenching of the light is less relevant than for low energy particles. All ionizing particles have their scintillation light quenched, but it has been observed that the effect is bigger for gammas than for electrons. In case of positrons, since their signal is composed by a charged ionizing particle plus two gammas from its annihilation, the light's quenching shares electron-like and gamma-like contributions.

The understanding of the quenching is crucial for the spectral analysis of **Stereo**. The extraction of an effective `kB` for simulations with calibration data has been an important topic in the work of this thesis, and it is discussed in detail in Chap. 7.

Propagation

Scintillation light will have to travel a certain distance before it is observed by the detection system. During its travel, it will continuously interact with the molecules of the liquid leading to either deflections from its path, change of wavelength or complete dissipation. The three microscopic processes influencing the light in such a way are the following,

1. Rayleigh scattering. Elastic scattering by spheres much smaller than the wavelength of the radiation, like the molecules in the solvent.
2. Mie scattering. Elastic scattering by spheres much larger than the wavelength of the radiation, like dirt or dust particles suspended in the liquid.
3. Absorption of the light by molecules, which is either re-emitted or converted into invisible light to the detection system like infrared light or heat.

All of these will impact the probability of a photon to be dissipated along their journey x through the scintillator:

$$P(x) = e^{-x/\lambda}\,. \tag{3.10}$$

Following this concept, one can define the attenuation length of the photons in such medium λ as the distance when only $1/e$ particles have nor been absorbed. Impurity levels in the chemicals of the solutions are most relevant for the attenuation length since typically light absorbed by them is not re-emitted. The attenuation length can be also defined as a sum of contributions of the different effects mentioned above,

$$\frac{1}{\Lambda} = \frac{1}{\Lambda_{\text{Rayleigh}}} + \frac{1}{\Lambda_{\text{Mie}}} + \frac{1}{\Lambda_{\text{Abs}}}\,. \tag{3.11}$$

The way the light is absorbed and re-emitted on a `LS` depends on its components. As stated in the previous subsection, the photon emission for benzene-like solvents is typically around $\sim 4\,\text{eV}$ or $\sim 300\,\text{nm}$. Depending on the final vibrational state the energy can vary slightly, and in the case of a transition to the absolute ground state S_{00} this light can be reabsorbed by the solvent. To prevent this, as mentioned above, WLS are added to the mix to shift the wavelength of the emission to higher values, effectively separating the absorption and emission spectra.

It is of great importance to ensure that the absorption peak of the WLS matches the emission range of the solvent. However, making sure that the shifted light lands on the sensitivity range of the detection system is crucial. The scintillation light seen by the PMTs in a large scale `LS` detector is typically above 350 nm, being the optimal wavelength in **Stereo** around 430 nm. In such cases a secondary WLS is needed to shift the light to higher wavelengths, provided its absorption spectrum matches the emission spectrum of the primary WLS. The probability of re-emitting the absorbed light is commonly known as the quantum yield of the fluor, and this number is intended to be as close to 1 as possible. Lower quantum yields would lower the total efficiency of the liquid, by converting scintillation light into radiationless energy transfer. Studies on the quantum yield of the fluors with simulations will be discussed in Sec. 5.1.2.

3.4.4 Pulse Shape Discrimination

It has been already discussed in Sec. 3.4.3 the difference between scintillation produced by excited singlets S_{1v}, fast contribution, and triplets T_{1v}, slow contribution. Since triplets prefer higher energy depositions than singlets, scintillation time distribution will in turn depend on dE/dx and thus on the nature of the ionizing particle. This means that analyzing the shape of the signal one can identify, to a certain degree, the particle originating the scintillation. This method, already referred in previous sections, is called Pulse Shape Discrimination (PSD).

The main use of PSD in **STEREO** is to reject background of fast neutrons. As described in Sec. 3.3.2, the kinetic energy of these neutrons is transformed in proton recoil, and hence in scintillation that acts as a prompt signal. However, protons have a higher dE/dx than the positron from the IBD. Such background events excite more triplet states than positrons and are therefore characterized by a longer component in the scintillation pulse. Proton and positron events, in this context, can also be named after their interactions in the liquid, i.e nuclear and electronic recoils respectively.

Exhaustive measurements of the PSD capabilities have been recently carried out at the MPIK [131]. There, a AmBe source of 1.11 GBq activity was used. The results, observed in Fig. 3.15, are displayed in terms of two different magnitudes: the Late Light Ratio (LLR) in Fig. 3.15(a), which is a quotient between the charge integrated at the tail of the distribution and the total charge of the signal; and the Figure of Merit FoM $\sim (\mu_n - \mu_e)/(\sigma_n + \sigma_e)$ in Fig. 3.15(b), that represents the separation between the two normal distributions modeling the proton (μ_n, σ_n) and positron (μ_e, σ_e) population of events, being (μ_i, σ_i) the mean and standard deviation of the population i.

The measurements show that electronic and nuclear recoil are visibly separated at a LLR of ~ 0.02 and ~ 0.05 respectively. The fit of the population distributions for both cases, represented as the y-z axis in Fig. 3.15(a), yield a separation observed in Fig. 3.15(b) as a FoM $= 0.87 \pm 0.06$. This value is larger than the published value in

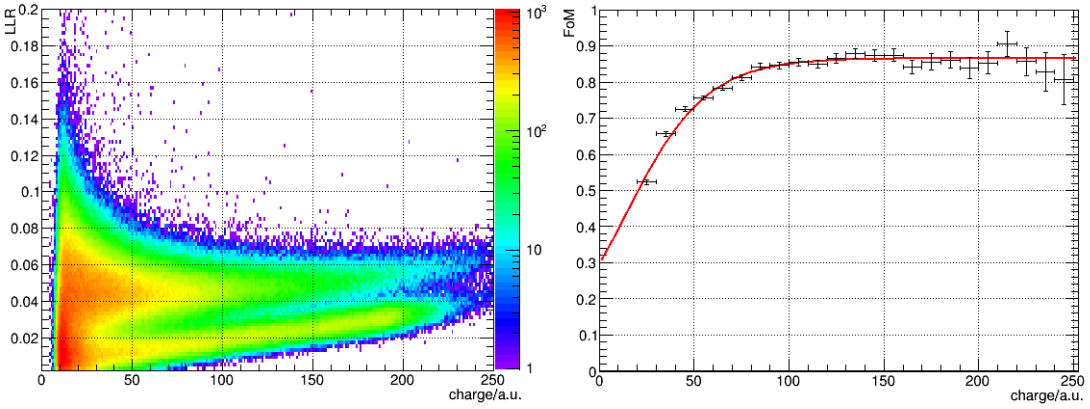

(a) **(b)**

Figure 3.15: (a) Distribution of LLR in terms of charge deposited in the PMT. The two contributions from electron and nuclear recoils are visibly identifiable. (b) Separation of both contributions can be seen as the FoM represented here [131].

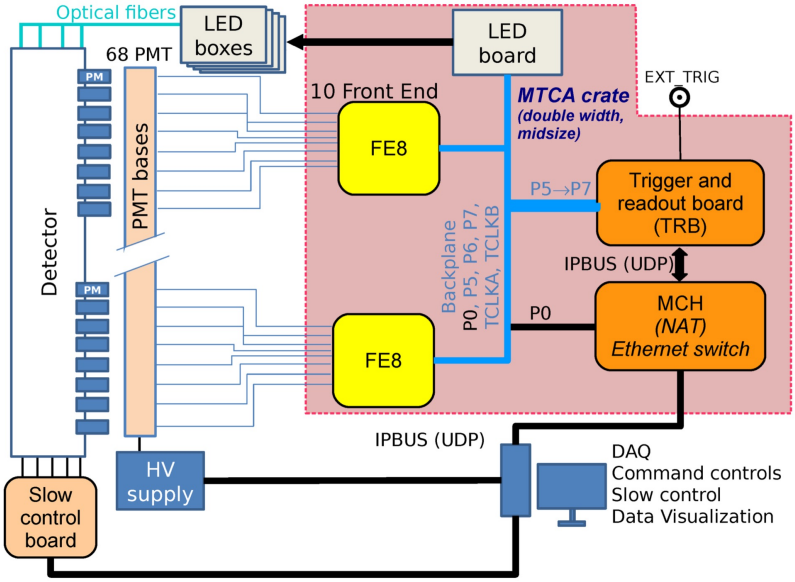

Figure 3.16: Scheme describing the working principle of the **Stereo** electronics [145].

[124] due to geometrical limitations of the setup used at the MPIK.

The results with semiloaded scintillators showed an inconclusive effect from the DIN, contrary to what was expected, and an extraordinary improvement coming from the PXE. It was also found that Gd-loaded scintillator compositions performed better than their non-loaded counterparts [131].

3.5 Electronics, Data Acquisition and Monitoring

The data acquisition in **Stereo** uses the standard DAQ system at the ILL, called NOMAD [148]. As discussed in previous sections, the detection system in **Stereo** is composed by 48 PMTs for the inner detector, and 20 PMTs for the muon veto volume. Signal from those PMTs is divided at first level in ten 8-channel front-end electronic boards (FE8) that can be amplified for single PE measurements. To hold all the electronics, a single microTCA crate has been designed for **Stereo**. The FE8 can be grouped by cells in sums of four (TG, short `GC` cells) or eight (long `GC` cells) channels over which trigger conditions can be parsed via a trigger and readout board (TRB). For the muon veto, channels of adjacent PMTs are clustered. This first trigger (T1) is set to approximately 300 keV per cell which corresponds roughly to 1600 ADC units. A threshold of 650 ADC units, corresponding to 32 PE, is also applied on the muon veto.

For every channel, both total and tail charge of the signal are processed. For this end, a constant fraction discriminator (CFD) algorithm is used to determine the start time of the pulse. The total charge is used to measure the energy of the signal, while the tail is applied for PSD purposes. In standard acquisition mode, only CFD time, tail charge and total charge for all channels are sent to the TRB. This limitation on the data size allows a reduction of dead-time associated with the processing and hence an

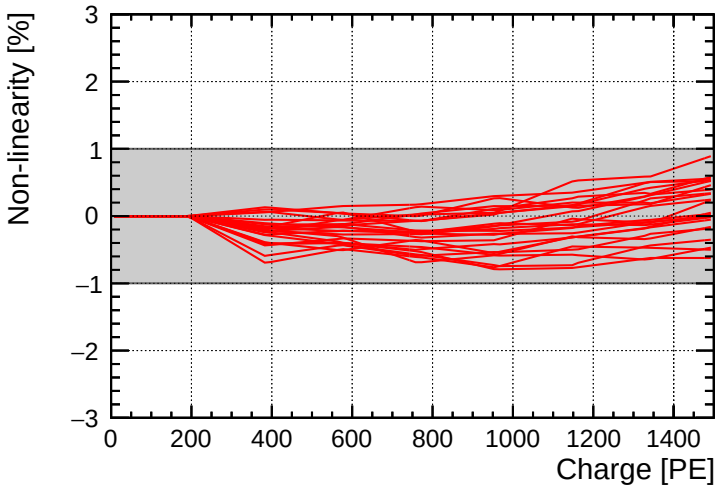

Figure 3.17: Linearity of the response of PMTs in STEREO. All PMTs show a linear response within the 1% range for charges at least up to 1500 PE per PMT [123].

instantaneous trigger rate of $3.6 \cdot 10^6$Hz.

A second trigger T2 is applied to computed data by the TRB. This trigger allows a more refined selection of valid events within desired energy windows. This trigger is set to reject events with energy below 200 keV in both `TG` and `GC`, and lower than 70 PE in veto. Finally, data of T2 events are sent to the computer disk.

Together with the FE8 and TRB, inside the microTCA crate there is also a board driving a set of LED boxes used for PMT calibration and monitoring of the acquisition system. Dedicated LED runs are taken inbetween neutrino runs to make sure PMTs electronic response is linear at all times. A summarized diagram of the electronics in STEREO is shown in Fig. 3.16 [145]. LED runs are used continuously to study electronic non-linearities on the PMTs. A set of 5 LEDs are switched on for each PMT, with frequencies which are multiples of each other so that all possible combinations can be obtained. By comparing charges obtained from the sum of PMTs with only one LED and one PMT with multiple LEDs, one can get important information on the scaling of the electronics. In Fig. 3.17 the linearity of the electronics in STEREO can be seen. For all the detector PMTs, the deviations from linearity are lower than 1%, fulfilling the experimental requirements.

A sixth LED is included in the board, emitting UV light, that is used to directly excite the wavelength shifter of the liquid. As can be seen in Fig. 3.18, there are 5 boards of LEDs: one for the veto PMTs and the other four for `TG` and `GC` PMTs. The boxes are placed outside the shielding, and light is carried by optical fibers from there to diffusive teflon balls placed within the inner detector and used to ensure isotropic light emission.

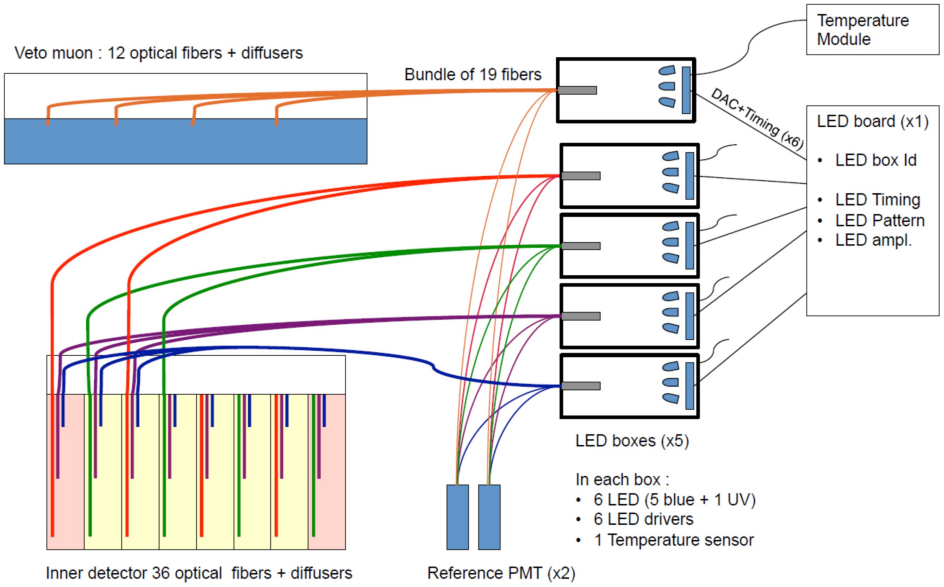

Figure 3.18: Organization of the LED boxes performing linearity calibrations regularly on the detector.

3.6 Calibration Systems

Characterization of the detector response in **STEREO** is performed by continuous calibration sessions with radioactive sources. Tab. 3.1 displays the list of calibration sources used during *Phase I* and *Phase II* of **STEREO**. The set of gamma sources has been selected in such a way that covers a wide range of prompt energy, allowing a good understanding of the energy spectra available in **STEREO**. The clean mono-energetic gamma emission from ^{54}Mn is used in a weekly basis to monitor the evolution of the response of the detector and also to provide a stable energy reconstruction over time. The analysis of such calibration runs and their use in the energy reconstruction has been an important part of this thesis, and it is described in detail in Chap. 6. The rest of gamma sources are used every few months to perform energy linearity studies. More concretely, during this thesis they have been used to calculate an effective quenching factor `kB`, already described in Sec. 3.4.3, for the simulation of non-linearities in **STEREO**. A detailed description of this process is documented in Chap. 7.

One of the sources in Tab. 3.1 has been used for neutron-capture efficiency studies. This is the AmBe source, that emits neutrons which are 60% of the time accompanied by a single gamma emission of 4.44 MeV. These emissions can mimic a correlated signal and its analysis is fundamental to build up the knowledge on how neutron capture happens in the detector, its timings, and energy spectrum.

It has been already mentioned that the **STEREO** detector is divided in multiple subvolumes with independent responses. To provide each of them with an equally independent characterization, a manifold set of calibration systems have been implemented. They are mainly defined by the way the source is deployed and the topology of the events generated. The three systems are portrayed in Fig. 3.19, and can be labeled as:

Table 3.1: List of all the calibration sources used during the two phases of data taking in **STEREO**.

Source	$E_{\gamma 1}$	$E_{\gamma 2}$	Activity (kBq)	Availability
^{68}Ge	0.511	0.511	90	*Phase I and II*
^{124}Sb	0.603	1.690	2.4	*Phase I*
^{137}Cs	0.662	-	37	*Phase I and II*
^{54}Mn	0.835	-	90	*Phase I and II*
^{65}Zn	1.100	-	3.3	*Phase I*
^{42}K	1.524	-	3.3	*Phase II*
^{60}Co	1.170	1.330	50	*Phase I and II*
^{24}Na	1.137	2.750	5.9	*Phase I and II*
AmBe	2.220 (H n-cap)	4.443	250 $\cdot 10^3$ (^{241}Am)	*Phase I and II*

- Internal: sources are deployed inside the different cells via calibration tubes.
- External: sources are deposited inside a vessel that moves around the detector as a pantograph.
- Underneath: sources are introduced in a semiautomatic vessel crossing beneath the cells.

Although all systems have been used at one point or another, the most extensively methods to calibrate have been internal and external. Weekly and monthly scheduled calibration runs have allowed a precise characterization of all the volumes in **STEREO**. More details about each specific system are given in the following sections.

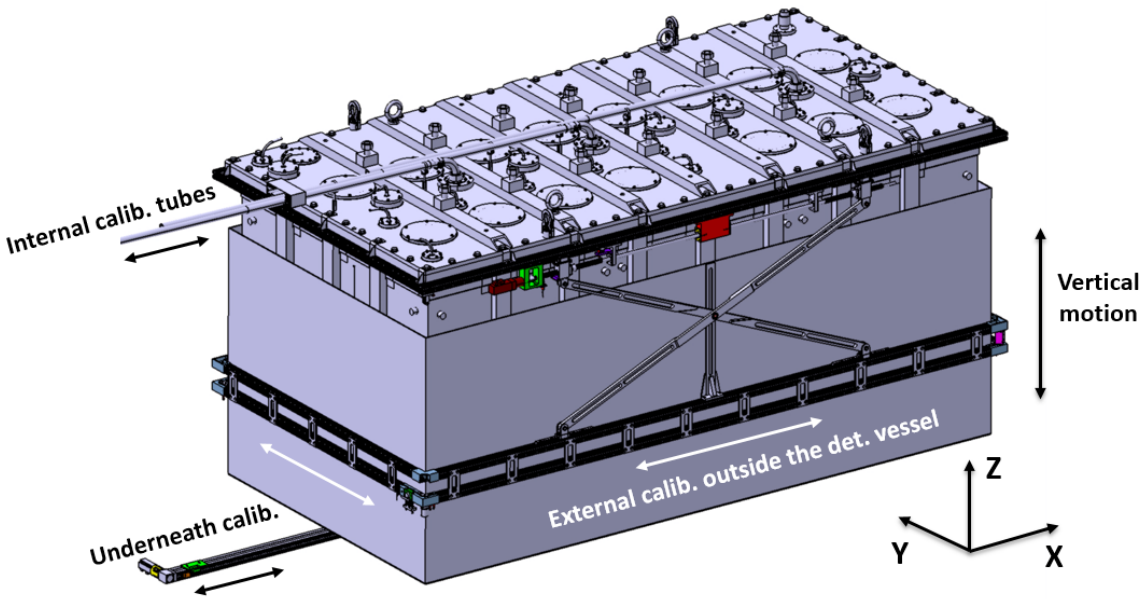

Figure 3.19: 3D drawing of the inner detector with all calibration systems attached: internal tubes, external pantograph and underneath rail.

3.6.1 Internal Calibration

Reactor antineutrinos cross effortlessly all the shielding of **STEREO** and they interact directly with the liquid on its inside. Thus, the ideal way of calibrating the detector like the one of **STEREO** is to place a source as close to the `LS` as possible. Submerging a source within the liquid would carry a myriad of technical and safety problems, even worse if the source got lost inside the volume. However, a system of internal calibration is designed in such a way that the sources can be deployed inside the volumes and retrieved easily, without any contamination. This is done via a set of steel tubes of 2 cm diameter that cross from top to bottom of the some of the cells.

The radioactive sources are placed in small aluminum capsules, depicted in Fig. 3.20, and then attached to a wire to control its movement. Then they are pushed down the tubes and left for a determined amount of time at different heights. Since the detection system is placed at the top of the detector, see Sec. 3.2, the attenuation length plays a major role in creating small inhomogeneities on the detection depending on the distance of the source from the PMTs. This asymmetry on the response of the detector can be characterized very effectively by using the internal calibration just described. Placing sources at different heights allows to create a response mapping of all the cells.

Initially, in *Phase I* of the experiment, there were tubes only in `Cell1`, `Cell4` and `Cell6`, in such a way that both borders and the center of the detector would be similarly calibrated. The initial choice of placing only three calibration tubes was taken because they were sufficient for a correct characterization of all cells, since from readout of cell's response can be done by placing a source in the neighboring cells. Also, every tube added would take on fiducial volume of liquid reserved for the IBD.

During the commissioning of the experiment it was found out that cells in **STEREO** without calibration tubes would actually benefit from it more than the other way around. So regardless of the pro points of using as few tubes as possible, during the reparations undergone before the start of *Phase II* in August 2017, two extra calibration tubes were introduced in `Cell2` and `Cell5`. In Chap. 6 all the details of the calibration roadmap traveled by **STEREO** will be discussed.

Calibration runs are performed using NOMAD, in the same fashion as neutrino runs

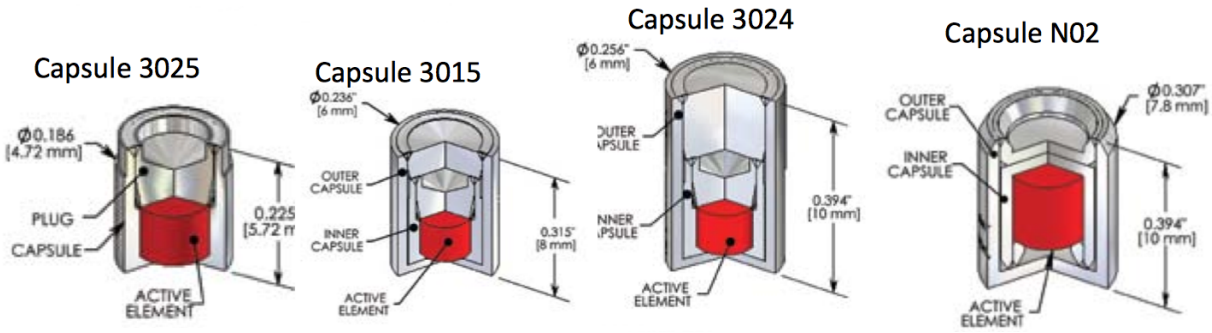

Figure 3.20: Drawings of the different source holders and their dimensions. In red, the location of the radioactive source.

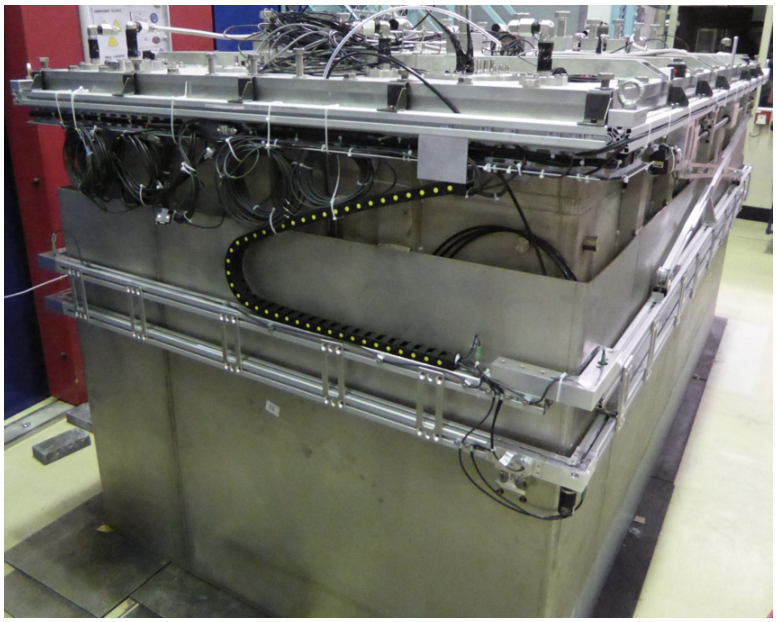

Figure 3.21: Photograph of the external-pantograph calibration system in STEREO before its installation around the detector. Constructed at LAPP, Annecy.

and routine LED calibrations, and they require different DAQ trigger settings and thus the stopping of neutrino runs altogether. Calibration runs also have customized run settings that depend on the source deployed and system used.

3.6.2 External Calibration

Besides calibration through internal tubes described in the previous section, the signal of the detector can be also characterized from the outside. As depicted in Fig. 3.21, a mechanical structure following a pantograph-like pattern was disposed surrounding the inner detector, within the volume enclosed by the passive shielding. Through an access door in the shielding one can access the calibration vessel and introduce there any source holder. Then, the motion of the source can be controlled by a dedicated software to map any desired position around the detector.

One of the main advantages of the pantograph system is its design. It is built in such a way that can easily map the response from all the two-dimensional surface of the inner detector, specially helpful to study spatial inhomogeneities. Due to its proximity to the GC, it is good way to characterize with high statistics the response of the four composing subvolumes, which are not specifically covered by internal calibration. Finally, the motion of the vessel is automatized making the calibration easier and less prone to human error.

The main drawback of using an external calibration system is intrinsic to its nature: it is outside the detection volume. Even more, is separated from it by a layer of stainless steel that forms the inner detector's vessel. Emitted gammas often scatter on the material between the calibration system and the liquid scintillation leading to a

higher rate of lower energies, commonly known as Compton plateau. This means that the statistics for full energy deposition events in TG cells is lower than using internal calibration, forcing longer and less effective calibration runs. However, as mentioned before, it is the preferred option to calibrate the GC.

"Amazing grace!
I once was lost, but now am found,
was blind, but now I see."

Newton

Chapter 4

Testing of the PMTs

In Sec. 3.2.3, it has been described how **Stereo** uses 48 8-inch R5912-100 Hamamatsu PMTs to readout the scintillation signal from the LS. Before their installation on top of the detector, and as part of the work done during this thesis, all of them have been tested and characterized. Such tasks were performed at the MPIK in 2015 for all of them plus 2 spare ones. From there, the PMTs were afterwards shipped to the LPSC in 2016, where a second round of careful cross-checks were also performed with an independent calibration setup to ensure an homogeneous response before installation. Firstly, a review of the testing facility and equipment will be provided in Sec. 4.1. In Sec. 4.2 the optimal voltage at which each PMT has to be operated for a gain of $3 \cdot 10^6$ will be calculated, which will be important for the Single Photo-Electron (SPE) measurements in Sec. 4.4 from which the Peak-to-Valley (P/V) ratio and Transit Time Spread (TTS) will be extracted for each PMT. Before performing any measurement, as described in Sec. 4.3, the dark count rate of the PMTs will be checked to ensure stable response and low background conditions. Finally, the chapter will conclude with a small study on the Afterpulse (AP) probability and associated effects in **Stereo**, in Sec. 4.5.

4.1 Testing Setup at the *Faraday Chamber*

The testing facility used at the MPIK was built initially to characterize the PMTs for the Double Chooz experiment [161]. The $12\,\mathrm{m}^2$ steel box chamber where the PMTs are placed for the testing can be described as a Faraday chamber, which shields its interior from any external electric fields. To avoid overexposure of the PMTs, the chamber is also tight-sealed from all light and any residual light reflection have been removed by covering the inner walls with black fire-proof fabric. The PMTs have been orderly placed in different slots of a vertical structure divided in 6 rows and 5 columns specially suited to hold series of PMTs. Each of them has been covered by a μ-metal cylinder to prevent any magnetic contamination.

The front-end electronics processing the signal from the PMT were based on a set of standard Nuclear Instrumentation Modules (NIM), composed of a sixteen channel amplifier followed by an octal discriminator and an octal linear fan-out. The last two modules send the signal to the VME crate of acquisition units: the Charge-to-Digital Converter (QDC) and to the Time-to-Digital Converter (TDC), respectively. All trigger signals and gate widths for the measurements were provided by the MPIC-board, which was developed at the electronic workshop at MPIK. This board provides up to 15 logic signals with free programmable gate widths and delays. In order to avoid electronic noise and heat coming from the aforementioned front-end electronics, the DAQ system and the HV supply were located outside the Faraday chamber. The cables connecting

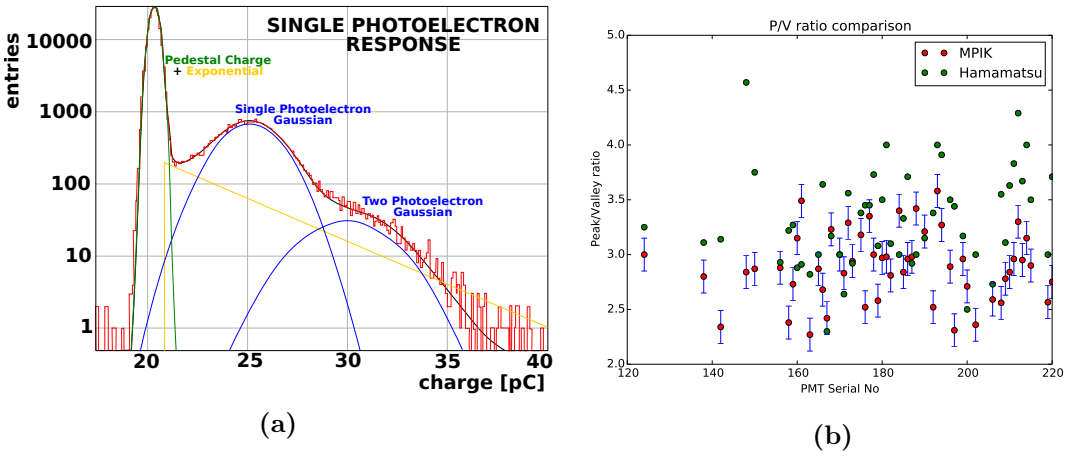

Figure 4.1: (a) SPE spectrum for a specific PMT set to its optimal voltage. Visible contributions from the pedestal Gaussian plus decaying exponential, SPE Gaussian and MPE Gaussian. (b) Peak-to-valley distribution for the PMTs in **Stereo**. In Red, values measured at the MPIK. In green, values provided from the manufacturer for a gain $G = 10^7$.

with the PMTs cross the wall through a small aperture at the bottom. The HV and the signals were immediately decoupled by the dedicated dual-splitting basis attached to the PMTs.

Each one of the slots containing PMTs in the holding structure was oriented towards one LED light. These LEDs were configured to produce light of a wavelength of 380 nm, with tunable intensity for each channel that allows from SPE to Multiple Photo-Electron (MPE) studies. The LED board was directly controllable from the 12-channel trigger board, developed by the electronic workshop at MPIK. This VME-module is able to generate NIM-based logic triggers after an appropriate signal from the software arrives. It then acts as a trigger for the LED board, and its arrival time is measured as strobe in a free channel of the trigger board. This last signal is specially important for time measurements.

4.2 Gain Calibration and Optimal Voltage

The first analysis performed on the PMTs was to calibrate the voltage HV_{opt} at which they should be operated. This value is defined as the voltage required for each PMT for a final gain after the amplification process of $G_{\text{opt}}(HV_{\text{opt}}) = 3 \cdot 10^6$. It is very important to set all PMTs with identical gains so they give the same response to SPE signals. This is specific gain is the nominal value that was intended in standard conditions during the upcoming data taking of **Stereo**. Amplified charge and gain are related as

$$Q(HV) = G(HV) \cdot q_e, \tag{4.1}$$

where q_e is the elementary charge. A typical SPE signal looks like the one in Fig. 4.1(a), where the optimal gain $G_{\text{opt}}(HV_{\text{opt}})$ has been already set. This translates into $Q_{\text{opt}}(HV_{\text{opt}}) = 4.8\,\text{pC}$ per PE from Eq. 4.1. From Fig. 4.1(a), it can be differentiated the pedestal as the dominant peak at around $\sim 20\,\text{pC}$, followed by the SPE contribution and finally some residual MPE events at the tail.

The three contributions that can be seen in Fig. 4.1(a) can be fitted as three Gaussians plus a decaying exponential. Naming the Gaussian mean values as μ_{ped} and μ_{SPE} for the pedestal and the SPE respectively, the charge $Q(HV)$ corresponding to a SPE signal is

$$Q(HV) = \mu_{\text{ped}} - \mu_{\text{SPE}}. \tag{4.2}$$

From Eq. 4.1, one can easily translate from SPE charge to the correspondent gain for a given HV. Therefore, to find the HV_{opt}, a series of SPE measurements with LED were performed.

Assuming poissonian statistics, tuning the LED at SPE level would still lead to a non-negligible number of MPE signals from the PMT. Therefore, the intensity was tuned down until only 10% of the triggers generate a response. In such a case, only 0.5% of the times there is a MPE signal, leaving an almost pure SPE measurement, like the one shown in Fig. 4.1(a).

The total trigger rate of LED pulses was 1 kHz, but the event rate is only a 10% of that. Thus in order to get statistically significant samples, around 400k events, the measurement times had to be 400 s. Using as a reference the nominal optimal voltages provided by Hamamatsu for $G = 10^7$, a set of 8 different HV_i around that value were scanned. The relationship between the SPE charge $Q(HV_i)$ and the correspondent high voltage HV_i is exponential, portrayed in Fig. 4.2. This exponential can be parametrized as:

$$Q(HV) = N \cdot HV^p, \tag{4.3}$$

where N is the normalization factor and p the degree of the exponential. Eq. 4.3 also holds for $Q_{\text{opt}}(HV_{\text{opt}})$, and therefore the fit parametrization can be rearranged in

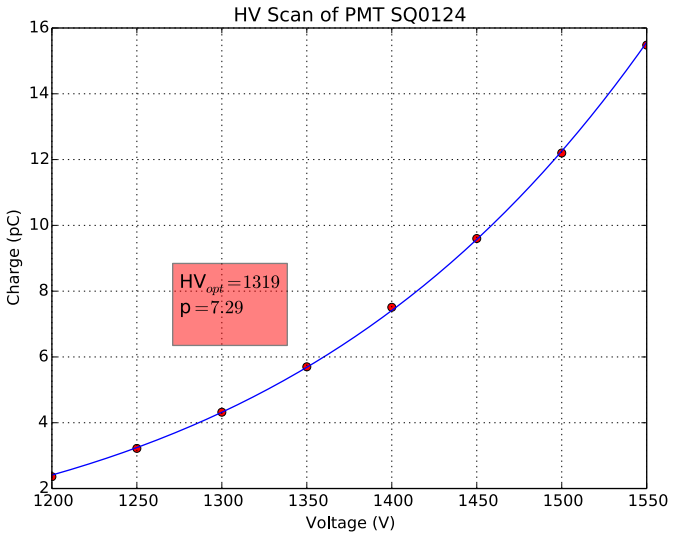

Figure 4.2: SPE charge - high voltage scan for a specific PMT. In blue, exponential fit described in Eq. 4.3.

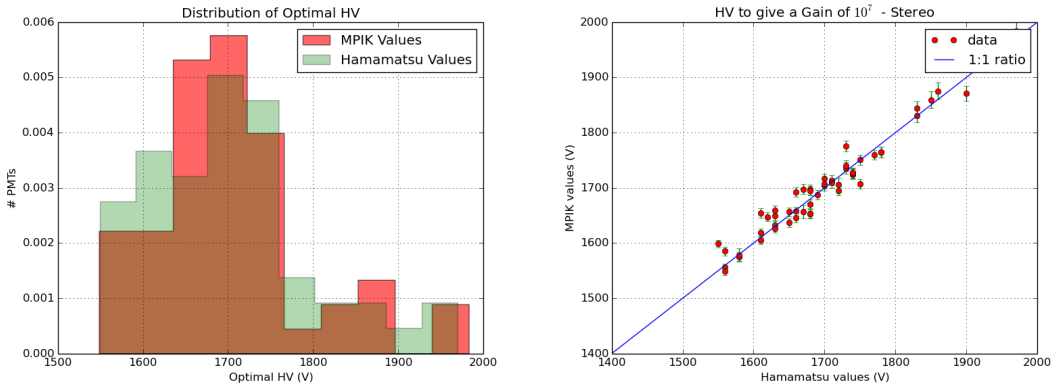

(a) **(b)**

Figure 4.3: Optimal high voltage HV_{opt} distribution for the PMTs in **Stereo**. a) Comparison with manufacturer values of the distribution's shape. b) One-to-one comparison with manufacturer values. All numbers scaled for a gain $G = 10^7$

the following manner,

$$\begin{aligned} Q(HV) &= Q_{\text{opt}} \left(\frac{HV}{HV_{\text{opt}}} \right)^p \\ G(HV) &= G_{\text{opt}} \left(\frac{HV}{HV_{\text{opt}}} \right)^p . \end{aligned} \tag{4.4}$$

In order to compare the results of these measurements with the nominal values of the manufacturer, all the fits were also performed using $G_{\text{opt}}(HV_{\text{opt}}) = 10^7$. In Fig. 4.3 the comparison between optimal and nominal high voltages is depicted.

In Fig. 4.3(b) it can be seen that ratio between manufacture and measurement for most of the HV_{opt} lies within the 3% range, so the discrepancies are not considered critical. The population distribution portrayed in 4.3(a) also shows a good agreement for both data sets.

4.3 Dark Count Rate

The cathode of a PMT is designed to be extremely sensitive so that it can resolve signals from individual photons. However, this increased sensitivity makes the PMT prone to unwanted triggers, like the dark currents. Once a high voltage is setup between the cathode and the anode at end of the multiplication tube, thermal emission of electrons from the cathode can generate cascades. These cascades are indistinguishable from regular SPE signals. Therefore dark currents within a PMT need to be characterized and kept under an acceptable rate in order to have reliable readouts.

Throughout the testing process, every time a new batch of six PMTs was introduced into the Faraday chamber, a stabilization period was needed to lower the dark count rate. This is because any photocathode that has been exposed to ambient light remains excited for a period of 12-24 hours. The stabilization period for all PMTs was measured together with the average rate of dark counting afterwards. During the measurements the temperature inside the chamber was stabilized by air conditioning at $(22 \pm 1)^{\text{o}}$ C,

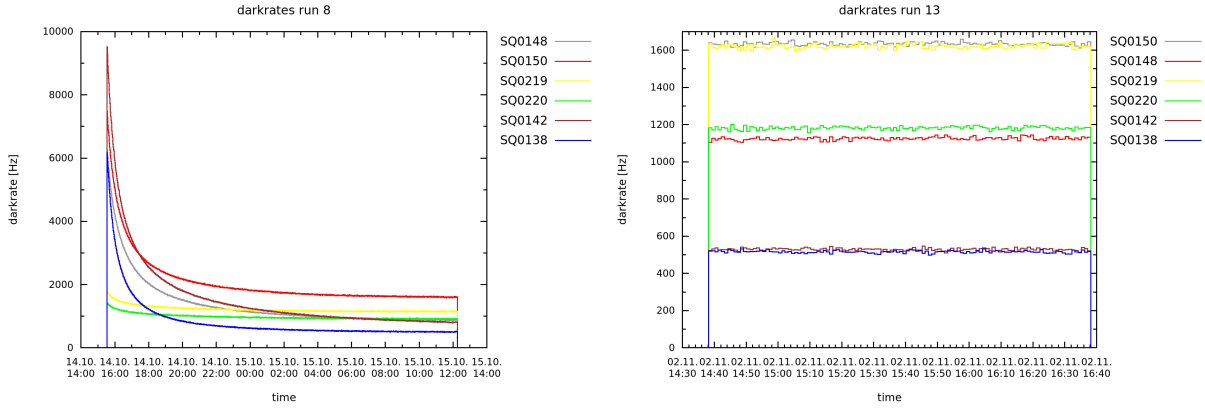

(a) **(b)**

Figure 4.4: a) Dark rate stabilization phase for different PMTs. b) Dark rate stable phase after $\sim$ 24h for the same PMTs.

approximately the same temperature at which the detector runs nowadays. In Fig. 4.4 the typical behavior of different PMTs during the stabilization (left) and after the stabilization (right) of the dark rates is shown.

As seen in Fig. 4.4(b), the fluctuations of dark counts through time are purely statistical and no PMT had deficient behavior in that regard. In Fig. 4.5 the time-average dark rates for all the PMTs are displayed, leading to a mean value of $(1185 \pm 432)\text{s}^{-1}$. Uncertainties of the time-averages are too small to be observed in Fig. 4.5, and thus the uncertainty of the mean comes mainly from the dispersion of the values. They are also compared with the nominal values provided by the manufacturer, Hamamatsu, for each of the PMTs. The overall factor $\sim$ 2 gap between the average count rate comes

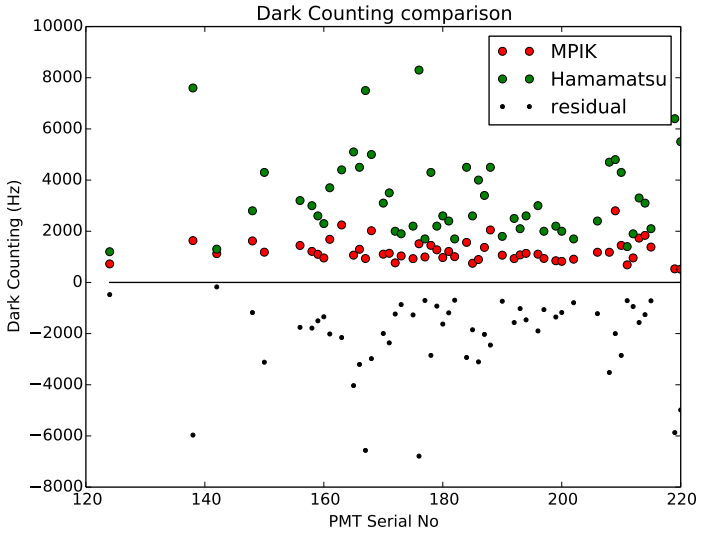

Figure 4.5: Dark rates for all the PMTs measured at the MPIK (red) compared with manufacturer (green). The bottom part distribution is the residual coming from the subtraction of the two values for each PMT.

from the fact that the HV supplied to the PMTs at the MPIK was lower. However, in terms of individual fluctuations it can be seen that all of them performed better than the expectations, and most of them remain within the standard deviation mentioned above.

4.4 SPE Response, Peak-to-Valley Ratio and Transit Time Measurements

Once the optimal voltage HV_{opt} has been measured for each PMT, a detailed analysis of the SPE response can be made. The first step was to measure the P/V ratio, which is defined as the quotient between the maximum of the SPE peak (P) and the lowest point of the distribution between it and the pedestal (V). Before performing the ratio, the pedestal contribution has been subtracted from both values. The results shown in Fig. 4.1(b) yield an average peak-to-valley of $P/V = 2.9 \pm 0.3$. This value lies below the one provided by the manufacturer as a consequence of using a lower amplification at the MPIK. Larger gains imply higher response for SPE events, shorter transit times and smaller statistical time spread.

The time response of the PMTs is mainly determined by the transit time taken for a PE signal to reach the anode right after being created in the photocathode. This time depends on the amount of dynodes composing the PMTs and also on the voltage applied between cathode and anode. A typical transit time distribution for a given PMT can be seen in Fig. 4.6(a), where the time origin $t = 0$ is flagged by the strobe signal of the trigger board. Here it can be seen that an average transit time for a PE is about $\sim 200\,\text{ns}$, with some late-pulses appearing around $50 - 80\,\text{ns}$ afterwards. Late-pulses are generally created from PE initially reflected backwards in the first dynode and being re-accelerated.

More important than the average transit time of PEs in a PMT, is the statistical spread of such time. This magnitude is the TTS and it is defined as the Full Width

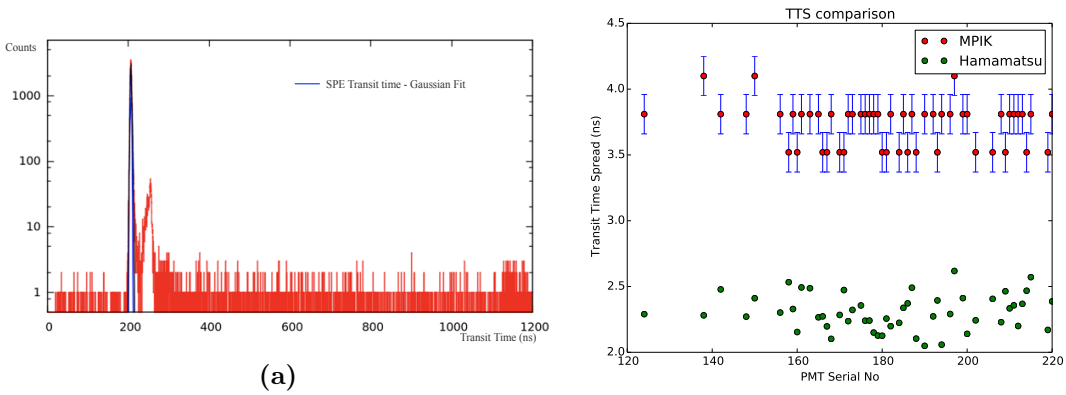

(a) (b)

Figure 4.6: a) Transit time of SPE signal for a specific PMT. Main pulse at $\sim$ 200 ns and late pulse around $\sim$ 80 ns later. b) Transit time spread comparison with manufacturer values at a gain of $G = 10^7$

Half Maximum (FWHM) of the transit time peak of Fig. 4.6(a). The averaged TTS for the PMTs in **Stereo** is TTS= (3.73 ± 0.16)ns, close to 2% of the total transit time. The observed distribution of TTS is depicted in Fig. 4.6(b) together with the values from the manufacturer, which displays systematically shorter times than the ones from the MPIK. Like for the peak-to-valley ratio, this is due to the larger gain used by the manufacturer when measuring the TTS.

4.5 Afterpulses

PMTs are commonly constructed with an evacuated glass housing that isolates cathode, anode and dynodes from the outside. However, there is always some residual gas that stays inside after the sealing. This gas can be ionized by the PE on its way from the photocathode to the first dynode. The resultant positive ion is driven towards the photocathode due to the high voltage, creating a delayed avalanche of electrons. These secondary electrons constitute an AP signal. A leakage of air inside the PMT would lead to a steady increase of AP signals, which after some time could lead to fake coincidences. For that reason, the probability of appearance of AP signals was characterized for the all PMTs in **Stereo**.

AP measurements were performed by means of SPE signals from the LED. To consider an arriving signal as possible AP, it needs to fulfill some criteria. From the trigger board time precision of $\Delta t = 16$ ns, and assuming a safe margin for late pulses of ~ 100 ns, a time window of about 160 ns was restricted to the main pulse. Such time window would start with the first hit reaching the electronics (200 ± 16)nsafter the trigger, following the results from the transit time measurements from the previous section. If a signal were interpreted as a main pulse, any other signal read after the 160 ns time window would fill the AP distribution.

An example of an AP distribution can be found in Fig. 4.7, from where several contributions can be seen adding up to the final spectrum. The largest part comes from a decreasing exponential function created by the afterglow of the LEDs. After every

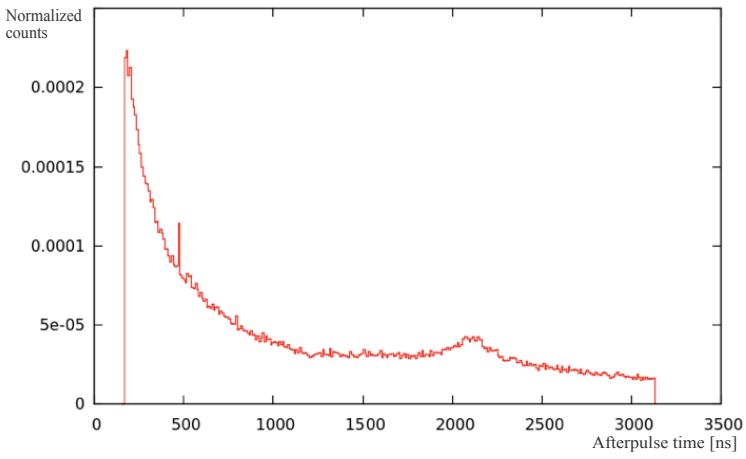

Figure 4.7: Afterpulse time distribution for a specific PMT. Visible contributions: decaying exponential from LED's afterglow, constant dark rate and two afterpulses at ~ 500 ns and ~ 2200 ns.

trigger, the diode generating light in the LED stays luminescent for a brief amount of time until all electrons have recombined and no more photons are emitted. The second largest contribution comes from the basal dark counting observed as a continuous background in the distribution. Finally, a couple of peaks can be seen coming from the AP signals themselves. In Fig. 4.7 two specific contributions can be observed: H_2^+ at 500 ns and CO_2^+ at 2200 ns. The time gap between them comes from the fact that the heavier the ion is the longer it takes to arrive at the photocathode to generate the signal.

The specific calculation of the AP probability per SPE event follows the work performed for Double Chooz's PMTs [162]. The external software used to manage the DAQ had already implemented a probability calculation subroutine based on these results. First, the probability $P_{S,i}$ of observing any signal after the main pulse on the time bin i was extracted directly from the AP distribution in Fig. 4.7 for every PMT. This probability is in turn the product of the probability that no signal occurred in the time period before bin i, and the probability P_i of measuring at least one signal in bin i,

$$P_{S,i} = \prod_{k}^{i-1}(1 - P_k)P_i. \tag{4.5}$$

The program would fit the distributions of the different background sources, LED afterglow and dark count, and obtain their respective probabilities of triggering a signal $P_{ag,i}$ and $P_{dc,i}$. Merging both probabilities as a single background contribution $P_{bg,i}$, Eq. 4.5 can be rewritten in terms of $P_{bg,i}$ and the AP probability for bin i [162],

$$P_{S,i} = \left(\prod_{k}^{i-1}(1 - P_{bg,k})\right) \cdot \left(\prod_{k}^{i-1}(1 - P_{AP,k})\right) [(1 - P_{bg,i})P_{AP,i} + P_{b,i}]. \tag{4.6}$$

From $P_{S,i}$ and the known distribution of the background $P_{bg,i}$, the AP probability $P_{AP,i}$ can be extracted. The last step is to calculate the total probability as

$$P_{AP} = 1 - \prod_{i}(1 - P_{i,AP}). \tag{4.7}$$

The values of P_{AP} for all the PMTs can be observed in Fig. 4.8, leading to an average and standard deviation of $\bar{P}_{AP} = 0.018 \pm 0.03$. Since P_{AP} is calculated in an iterative procedure, the statistical uncertainty is calculated for each time bin individually, while the errors of the preceding bins are propagated to the next bin. The initial signal and background uncertainties are assumed to be Poissonian $\sim \sqrt{N}$. The AP probability showed in Fig. 4.8 is below 3% with a confidence level of 95%, which displays an excellent behavior of the PMTs. To exemplify this, a rough estimation of the effect of afterpulses can be performed for a ~ 8 MeV gamma emission after a n-capture in gadolinium. Assuming all scintillation light from the gamma event is confined in the TG, this corresponds to roughly 2000 PE of collected charge in the PMTs. Using $\bar{P}_{AP} = 0.018$ as the average AP probability per PE of all PMTs involved in the readout of the signal, an average of 36 AP would be generated. From [162] it is known that an AP carries an average of 4.95 PE of charge for Double Chooz PMTs. Approximating a similar behavior for **Stereo** PMTs it is straighforward to see that the charge carried by the 36 AP is about 178 PE, which is barely above the T1 trigger threshold on **Stereo** DAQ, depending on the charge spread throughout the cells, as described in Sec. 3.5.

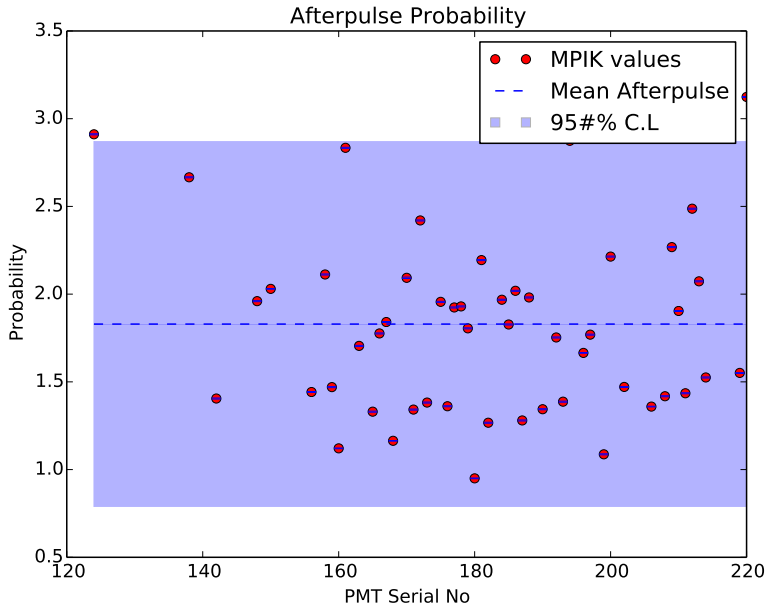

Figure 4.8: Afterpulse probability distributions for the whole set of PMTs. The dashed blue line corresponds to the mean value and the blue area covers the 3σ area.

4.6 Summary

As part of the work done for this thesis, the PMTs installed at the top of the `TG` and `GC` volumes were characterized. This chapter describes the protocol followed to test each one of 50 PMTs at the *Faraday Chamber* in the MPIK, facility prepared specially for this regard.

The first task performed, described in Sec. 4.2, has been to characterize the optimal voltage at which the PMTs should be operated to yield a gain of $G_{\text{opt}}(HV_{\text{opt}}) = 3 \cdot 10^6$. The optimal gain chosen for PMT operation in **Stereo** differs from the one used by the manufacturer Hamamatsu $G_{\text{Hama}}(HV_{\text{Hama}}) = 10^7$, fact that has impacted some of the results. Regardless, the comparison of the optimal voltage distribution between measurements and manufacturer lies at the unity within a 3% range.

The dark count rate has been observed in Sec. 4.3. After a 12-24 hours of stabilization inside the *Faraday Chamber* at 22° C, the dark counting has been measured for all PMTs, yielding a mean value of $(1185 \pm 432)\text{s}^{-1}$ which is approximately a factor two smaller that the value from the manufacturer. Results also show a smaller dispersion between values, with no PMT with dark rate higher than $3000\,\text{s}^{-1}$.

The single photoelectron response has also been analyzed for the PMTs. The peak-to-valley ratio for the single photoelectron lies at $P/V = 2.9 \pm 0.3$ which allows a clear identification of the peak with respect to the pedestal contribution. This value is in agreement with the values from Hamamatsu. The transit time of photoelectrons through the PMT has been measured with single photoelectron signals to be around 200 ns, with a relatively small spread of $TTS = 3.73 \pm 0.16\,\text{ns}$. This value is almost a

factor two above the nominal values, explained by the more than a factor three larger gain used for the measurement by the manufacturer.

Finally, in Sec. 4.5, the effect of the afterpulses in the PMTs has been analysed. The probability of afterpulse per PE has been found to be $\overline{P}_{AP} = 1.8 \pm 0.3\%$, which is too low to create an afterpulse signal that surpassed the T1 trigger threshold.

All in all, results showed a good and very stable response of all the PMTs, in agreement with the information provided by the manufacturer. As a consequence, no PMTs were returned or replaced. Their final installation on the acrylic buffer in 2016 was performed soon after the characterization presented in this manuscript, and until the present date in 2019 all 48 PMTs tested are still fully functional.

"What is real? How do you define 'real'? If you are talking about what you can feel, smell, taste and see, then 'real' is simply electrical signals interpreted by your brain."

Morpheus

Chapter 5

Monte Carlo Simulation in **Stereo**

The **Stereo** simulation is based in `Geant4` [155] and covers most of the structure of the detector, physics that can happen within its boundaries and the calibration systems used. Throughout this section, the tuning of the simulation code will be described with a special emphasis on the implementation and testing of the properties of the `LS`. In Sec. 5.2 it is described how the calibration systems are implemented and the computation of the different radioactive sources used during the calibration periods. By comparing the simulated response to radioactive sources with calibration data, as portrayed in Sec. 5.3 additional information can be extracted to fine tune the simulation code. At the end of the chapter, some remarks on the neutron diffusion physics of the **Stereo** simulation will be given in Sec. 5.4. Also some remarks on the implementation of a more accurate quantum efficiency for the PMTs of `TG` and `GC` will be given in Sec. 5.5.

5.1 Cross-check of Optical Properties of the Liquid

In the simulation process, first the whole volume of possible interactions is created. This includes the setting up of the geometrical volumes and the isotopic composition of each physical volume within them. The dedicated optics of **Stereo** are also imported during the first step of the simulation. They cover the composition of the liquid scintillators and how they create and propagate light during the event. Such information is retrieved from custom data files describing:

- concentration of each component of the liquid,
- quantum yield of the fluors,
- molar extinction of each component of the liquid,
- total light yield and emission spectra of the liquid,
- refractive indices of the materials,
- reflectance and transmittance of the different surfaces,
- and quantum efficiency of the PMTs.

Therefore, detailed information about the interaction liquid is provided to the software. All components involved in the final `LS` are strictly tabulated and described in terms of their molecular formula, density and other properties. The quantities of each of the main solvents are calculated in terms of percentage of the main volume occupied,

as described in Sec. 3.4. Afterwards, the fluors are added in terms of concentration in the final admixture, assuming the LS does not increase its volume but only its density.

Once the geometry is generated, the physics that happen within it are defined. It is important to find a tight equilibrium between computation time and effective results for the simulation in question. Having all possible physics included in it is a cumbersome task, computationally speaking, and for that reason only the relevant (and possible) physical processes are usually defined. In STEREO, the most common low-energy processes are enabled, including hadronic and electromagnetic interactions. Some examples are hadronic elastic scattering, neutron capture, electron ionization or electron-positron annihilation.

At this point the setup is ready and events may start happening. An event contains all information from the creation of the initial particle to the deletion of all daughters coming from it. Each one of these particles is defined as a track within Geant4, and they carry information of their position, energy and momentum. This information is constantly updated as the time passes and the particle moves and interacts. The actions undertaken by the tracks through the liquid are resolved by series of *steps*. As for any Monte Carlo algorithm, the more steps in a simulation the more accurate it gets. In STEREO, the step action are carried over by the SteppingManager, a Geant4 class that determines the mean free path the particle will undergo given the cross sections of the different available processes, defined at the start of the simulation.

Scintillation, however, has a dedicated set of algorithms adapted to the STEREO software. The optical properties used to produce and move light within the detector have been described above, and most of them come from laboratory measurements. The production of the liquid and the measurement of its properties has been carefully done at the MPIK for both TG and GC volumes. During every step, the algorithm gets relevant information from all tracks and determines the amount and characteristics of scintillation light that will be created, one photon at a time. Photons might be absorbed and re-emitted by the liquid and reflected by the walls many times before they are virtually gone. This can happen either by being: absorbed but not re-emitted, which is controlled by the attenuation length of the liquid; transmitted away from the given volume, which is controlled by the optical properties of the walls; caught and readout by the PMTs. All these processes will happen before the next step of the main tracks is computed.

Once all the desired events are computed, the results are stored in two different information trees that can be afterwards analyzed. One tree, MC, is filled by all the Monte Carlo true information, e.g energy, position or momentum of all the particles. The second tree, DATA, stores the information collected by the simulated detector, which mimics the real data obtained daily at the ILL.

5.1.1 Hydrogen Fraction and Proton Number

As described in Sec. 3.4, all the organic compounds forming the LS are composed mainly by hydrogen and carbon. It has been explained also in Sec. 3.4.2 that hydrogen can compete with gadolinium in terms of neutron capture cross-section due to its higher abundance. Therefore, a good control of the amount of hydrogen present in the detector

Table 5.1: Chemical properties of the components of the liquid scintillator computed in the simulation of **Stereo**. Concentration is either given in volume percentage for the solvents or directly in mass per unit of volume for the solutes (fluors and gadolinium complex). Solutes are assumed to occupy virtually no volume and hence their total quantity is calculated a posteriori with respect to the total solvent volume. Finally Z_H and Z_C stand for the number of H and C atoms per molecule respectively.

Component	concentration	ρ [kg/l]	M [kg/mol]	Z_H	Z_C
LAB	77 % in vol.	0.86	0.246	30	18
PXE	18 % in vol.	0.99	0.210	18	16
DIN	05 % in vol.	0.96	0.212	20	16
PPO	7.0 g/l	-	0.221	11	15
Bis-MSB	20 mg/l	-	0.310	22	24
$Gd(thd)_3$	8.1 g/l	-	0.707	57	33

is very important for the neutron studies. The proton number of the liquid scintillator is defined as the total amount of hydrogen atoms N_H in it, and the correspondent hydrogen fraction f_H is the relative mass of hydrogen in the liquid. This last magnitude have been measured experimentally at TU München by elemental analysis [136], yielding $N_H^{exp} = (1.084 \pm 0.011) \cdot 10^{29}$ and $f_H^{exp} = 0.1145 \pm 0.0011$. The MC simulation needs to accurately represent these two numbers, otherwise correction factors need to be applied. In Tab. 5.1 the basic chemical properties of the simulated components of the liquid are displayed.

The total amount of liquid in the `TG` volume is $V_{TG} = 1813\,\text{l}$, taken from the official production and filling summary. The simulation has been corrected accordingly to match the liquid level in the detector for each of the two data taking phases. The mass of the components in the liquid for the Monte Carlo simulation can be seen in Tab. 5.2. There, $m_H = n \cdot Z_H \cdot M_H$ is the mass from each component held by $n_H = n \cdot Z_H \cdot N_A$[1] hydrogen atoms.

The total mass of the liquid in the Monte Carlo obtained from Tab. 5.2 is $m_{TG} = 1638\,\text{kg}$ is about 30 kg higher than the mass measured during the filling. This discrepancy of about $\sim 1.8\%$ could be mostly covered by the geometrical uncertainties of the detector. Using m_{TG}, the total proton number N_H can be calculated as

$$N_H = N_A \cdot \sum_i n_H^i \cdot Z_H^i = 1.1088 \cdot 10^{29}. \tag{5.1}$$

N_H differs from the experimental value $N_H^{exp} = (1.090 \pm 0.011) \cdot 10^{29}$ by $\sim 1.8\%$ due to the discrepancy on the liquid mass aforementioned. This implies a correction factor of $c = 0.983 \pm 0.010$ in the amount of hydrogen in simulations. The hydrogen fraction can also be calculated as

$$f_H = \frac{\sum_i m_H^i}{m_{TG}} = 0.1143, \tag{5.2}$$

which is perfectly in agreement with the experimental value of $f_H^{exp} = 0.1145 \pm 0.0011$. This time there is no major discrepancy between the numbers because the difference in the mass of the liquid does not change the relative amount of hydrogen in it.

[1] N_A stands for Avogadro's number $N_A = 6.022 \cdot 10^{23}$, as the number of objects in a mol of matter.

Table 5.2: Amount of each components in the LS in terms of mass, number of mols n, mass of hydrogen atoms m_H and number of hydrogen atoms n_H.

Component	mass [kg]	n [mol]	m_H [kg]	n_H [10^{27}]
LAB	1200.57	4880.41	146.41	88.17
PXE	323.08	1538.52	27.69	16.65
DIN	87.02	411.50	8.21	4.94
PPO	12.69	57.43	0.63	0.38
Bis-MSB	0.04	0.12	< 0.01	< 0.01
$Gd(thd)_3$	14.67	20.70	1.18	0.72

5.1.2 Quantum Yield of Fluors

As discussed in Sec. 3.4, STEREO LS contains two different fluors that act as wavelength shifters and drive the scintillation's frequency to the optimal range for the PMT read-out. Scintillation light is absorbed by the fluors and re-emitted with lower frequency. The overall probability of re-emission after absorption is called quantum yield, and it is desirable that this value does not differ much from unity. Otherwise, light is killed by absorption lowering the total efficiency of the detector.

Literature common values of fluorescence quantum yields for PPO and bis-MSB differ up to ranges of 20-30%. As suggested by BUCK et. al [130], the reasons of such disagreement are multiple. The process to determine the quantum yield of fluors depends heavily on how the measurements are carried on, including the sample concentration, solvent choice and geometry of the volume, among others. In [130] is also discussed a set of measurements of quantum yields of several molecules, including PPO and bis-MSB, performed at MPIK. Regardless of the difficulties to control systematic uncertainties enumerated before on this kind of measurements, results are in agreement with most literature values yielding the following quantum yields for PPO and bis-MSB fluors respectively, both dissolved in cyclohexane,

$$\phi_{\text{PPO}} = 0.842 \pm 0.042 \quad (303 - 358\,\text{nm}), \tag{5.3}$$
$$\phi_{\text{bMSB}} = 0.863 \pm 0.043 \quad (345 - 418\,\text{nm}). \tag{5.4}$$

In [130] it is also measured the effect of using different solvents. Specially relevant for STEREO are the results obtained for LAB, which is the main component of the LS. However, since this solvent has a strong self-emission below 340 nm that completely overlaps PPO absorption and emission spectra, only quantum yields for bis-MSB were measured. The results show an increase of quantum yield of this fluor of about 10%. The simulation in STEREO uses then the following quantum yields for the fluors,

$$\phi_{\text{PPO}} = 0.849 \pm 0.042 \quad (290 - 330\,\text{nm}), \tag{5.5}$$
$$\phi_{\text{bMSB}} = 0.940 \pm 0.047 \quad (300 - 380\,\text{nm}), \tag{5.6}$$

where a +10% correction has been applied to ϕ_{bMSB} with respect to Eq. 5.3, and the relative error of laboratory measurements on ϕ_{bMSB} has been extrapolated. Both yields can be read as averages within a limited scintillation range. Although the actual

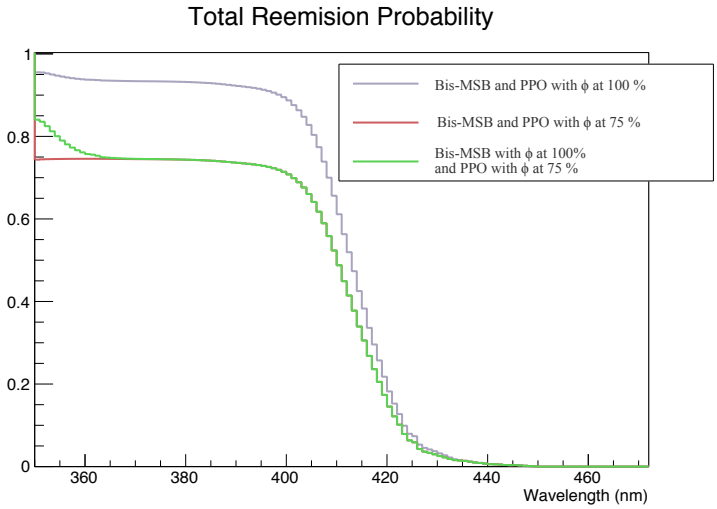

Figure 5.1: Total re-emission probability of the LS in the simulation in terms of scintillation light wavelength. In gray, with nominal QY for the fluors. In red, with QY for both fluors reduced by 25%. In green, nominal QY for PPO and reduced by 25% for bis-MSB.

dependence with wavelength is not fully known, they can be fairly assumed to be similar to step functions with the step being at the average value. Passed this constant region, which in turn is determined by the molecular structure of the fluor, the tail of the quantum yield distribution drops rapidly to zero and no scintillation is re-emitted. In Fig. 5.1 the step function of the total re-emission of the liquid is plotted for different combination of quantum yields.

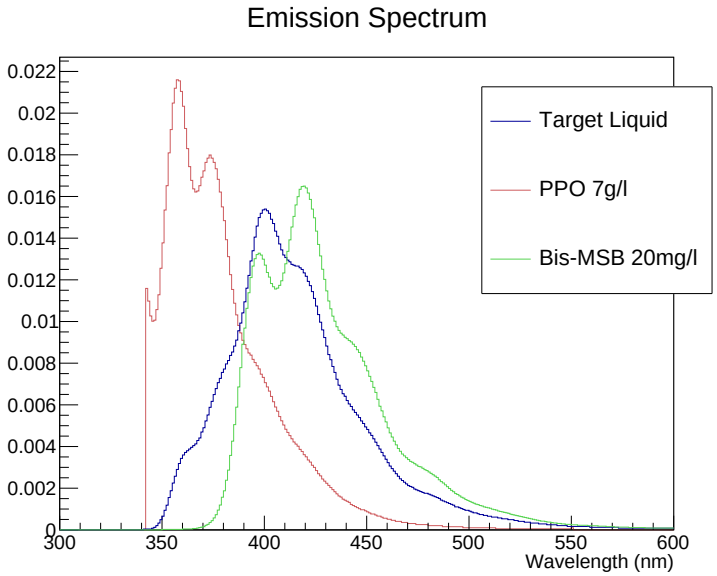

Figure 5.2: In red and green: emission spectrum of the two fluors individually, PPO and bis-MSB. In blue, the final emission spectrum of the liquid. The contributions of both fluors can clearly be guessed in the final spectrum. The effect of the PPO is downweighted by the influence of LAB.

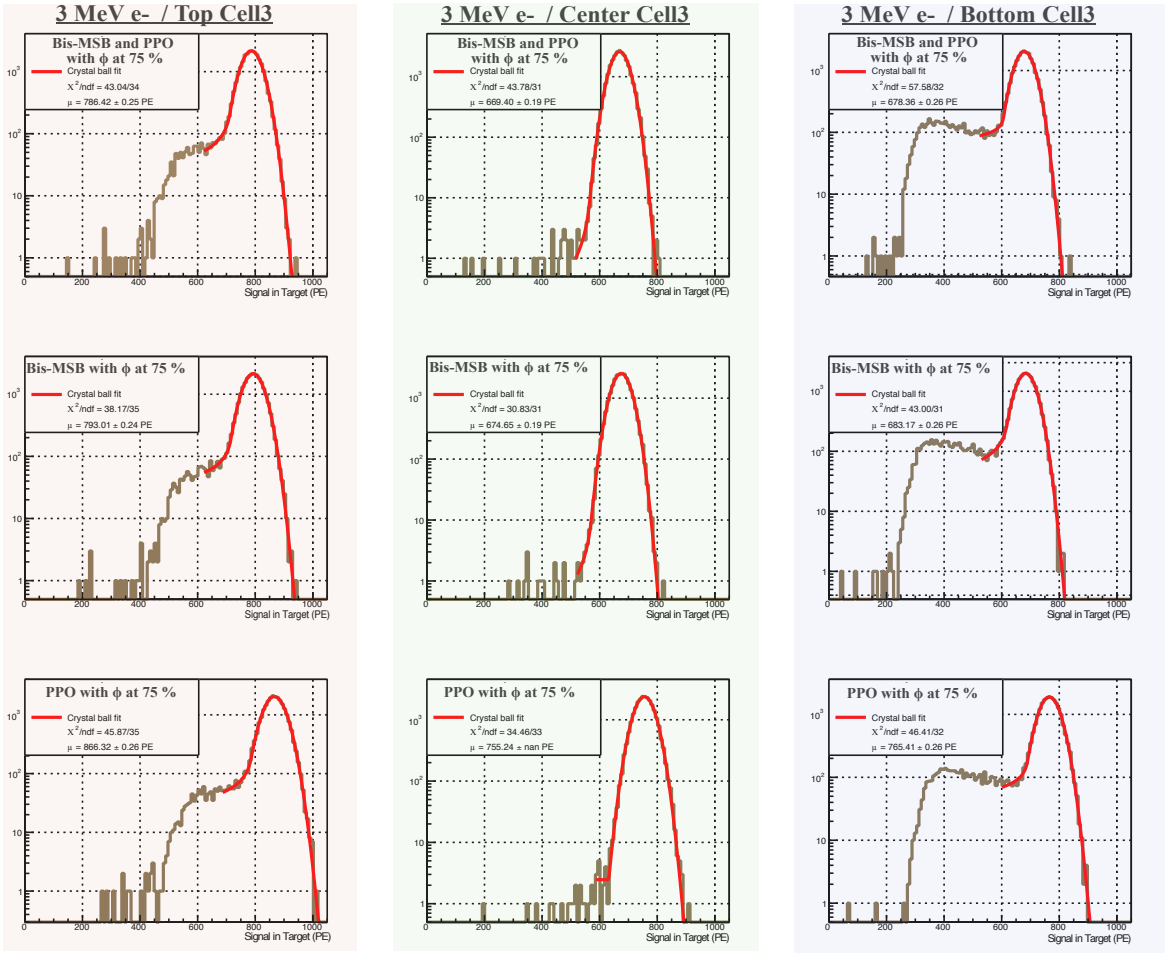

Figure 5.3: Simulated 3 MeV electrons at different heights inside `Cell3`. Each row of the plot's grid portrays a different quantum yield composition. From left to right, the plots represent *top*, *middle* and *bottom* events. The fit function used is *GaussExp*, described in App. B.

It has been already discussed that there are some experimental uncertainties on the expected quantum yield for the different fluors in `LS`. The impact of such uncertainties on the response of the detector can be investigated with simulations. PPO excitations are promptly transferred to bis-MSB, whereas bis-MSB emission propagates through the full detector and can be absorbed and re-emitted several times. Thus, one can expect that the effect of quantum yield discrepancies are less relevant for PPO than bis-MSB. This can be observed in Fig. 5.2.

In order to test the effect of fluctuations on the QY of the fluors, several simulations with different ϕ_{bMSB} and ϕ_{PPO} in the `LS` of the `TG` have been produced. Mono-energetic electrons of 3 MeV have been generated inside `Cell3`, although the results can be easily extrapolated to any other cell. The initial momentum of the particles is set to be isotropic. The origin vertices of these electrons are all at the center of the cell longitudinal and transverse wise, but differ on the vertical axis. Three different heights are chosen: at 10 cm from the top of the detector; at 10 cm from the bottom of the detector; and at 45 cm from the bottom of the detector, i.e at the center. The main

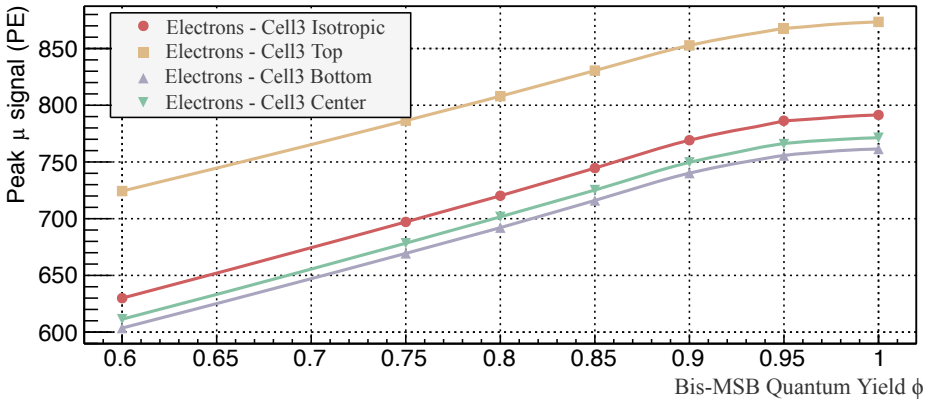

(a)

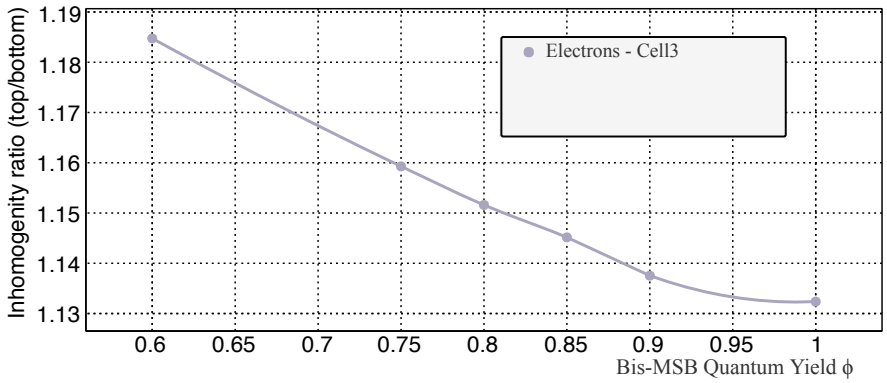

(b)

Figure 5.4: Simulated 3 MeV electrons in `Cell3` for different ϕ_{bMSB} values for `LS` in `TG`. (a) Mean μ from the fit in terms of the ϕ_{bMSB} used in the simulation. (b) Ratio between signals from events at the top and at the bottom of the detector, in terms of ϕ_{bMSB} used in the simulation.

purpose of generating simulations at different heights is to study the effect of the QY on the vertical inhomogeities of the detector response.

The signal obtained from these simulations can be seen in Fig. 5.2. The charge has been collected using all the PMTs in the `TG`. Using also signal from `GC` would potentially mix responses from different simulated liquids, and for this reason has been excluded. The charge distributions have been fitted using a *GaussExp* function described in App. B, from where the mean *mu* has been extracted. By comparing μ between plots, qualitative statements can be made about the effect of ϕ_{bMSB} and ϕ_{PPO} on the response. Overall, from Fig. 5.3 it is quite visible for all positions that variations in ϕ_{bMSB} affect the response in much higher degree than ϕ_{PPO}. The response where both ϕ_{bMSB} and ϕ_{PPO} are at 75% (first row in Fig. 5.3), and the response where only ϕ_{bMSB} has been lowered (second row in Fig. 5.3), only differ by $\sim 1\%$. However, these two responses differ by a $\sim 10\%$ with the third case where only ϕ_{PPO} is at 75% (third row in Fig. 5.3). This reveals that 25% discrepancies on ϕ_{bMSB} can impact substantially the final response of the detector. In contrast, even though the concentration is two orders of magnitude higher than bis-MSB, the same effect is not visible for the PPO.

In order to quantify the impact of the QY on the vertical inhomogeities of the response, an additional set of simulations with different ϕ_{bMSB} values have been produced, keeping ϕ_{PPO} at nominal value. These simulations are also in `Cell3` with the same particularities as for the other simulations described above. The parameter μ from the fit, representing the mean of the Gaussian contribution of the signal, is presented in Fig. 5.4 for each value of ϕ_{bMSB} used in the simulations. There it is shown that the response is reduced with ϕ_{bMSB} in a non-linear fashion, where two regions can be distinguished below and above $\phi_{\text{bMSB}} \sim 0.9$. On one side, for values of $\phi_{\text{bMSB}} < 0.9$ the decrease of the signal is approximately linear with respect to the decrease of ϕ_{bMSB}. On the other side, for $\phi_{\text{bMSB}} > 0.9$ the signal is stable within the $< 2\%$ range from the nominal value. These results state again the large dependency of the detector response on the QY of the fluors.

The evolution of the vertical inhomogeneities on the response can be observed in Fig. 5.4(b). There the quotient between signals at the top and at the bottom of the detector have been plotted for each ϕ_{bMSB}. This ratio increases as ϕ_{bMSB} decreases, which is the expected behavior of the response of the liquid. As discussed in Sec. 3.4.3, scintillation light is attenuated as it travels through the liquid. This attenuation is partially due to fluor molecules absorbing and not re-emitting the light. Since scintillation light generated at the bottom of the detector, it has to travel in average larger distances and the attenuating effect is magnified. The result is then Fig. 5.4(b), and in a similar fashion as in Fig. 5.4(a), there is an approximately stable region for $\phi_{\text{bMSB}} > 0.9$.

5.2 Calibration Systems and Sources

Sources and calibration systems mentioned in Sec. 3.6 had to be manually programmed specifically for the simulation. Calibration through internal tubes had priority when developing the calibration systems in `Geant4`, for it is the most frequently used system. The simulation macros were adapted to allow the user to easily select the tube and height for the deployment of the source. Internal calibration also categorizes all cells into two groups depending on whether sources can or cannot be deployed in them. The first group is named *source cells* and the second *intermediate cells*. It must be noted that most of calibration runs used from three to five different heights consistently. Tab. 5.3 lists the most common positions for the sources and the respective naming convention used throughout this work.

Table 5.3: Nominal values of height position of sources used during internal calibration runs. Height in z-axis measured from the bottom of the tube and not the bottom of the cell. During most of this paper names and not distances will be used to make reference to internal positions of the sources.

z-axis [mm]	name
800	*top*
600	*mid-top*
450	*middle*
300	*mid-bottom*
100	*bottom*

External calibration has been partially implemented, allowing only for source placement at different coordinates outside the detector volume. The movement of the trolley or any other type of automatization has not been coded. Finally, underneath calibration has not been yet properly implemented.

The way radioactive sources shown in Tab. 3.1 have been introduced is as particle guns. The price of being too accurate on the representation of the source would be computationally expensive. Simulating a decaying isotope is a resource-intensive task, since the transition through all intermediate states have to be computed for every event. The profit from doing this, in contrast, is negligible. Therefore, only the most relevant emissions are generally computed.

Mono-gamma emitters like ^{54}Mn or ^{137}Cs are introduced in the simulation as a single gamma particle creation with random direction. ^{65}Zn also includes an infrequent emission of a positron instead of the gamma approximately a 3% of the times. The absence of correlations between emissions, including angular or time dependences, makes single gamma emitters the simplest and most practical ways to compare data and simulations. An example of such comparison can be seen in Fig. 5.5, where the discrepancy has been defined as the relative residual:

$$\eta_i = 1 - \frac{h_i^{\text{data}}}{h_i^{\text{simu}}}, \tag{5.7}$$

where i denotes each of the bins of data and simulation distributions h_i^{data} and h_i^{simu} respectively. In Fig. 5.5 standard anti-Compton cuts, described in Sec. 6.1.1, have been applied.

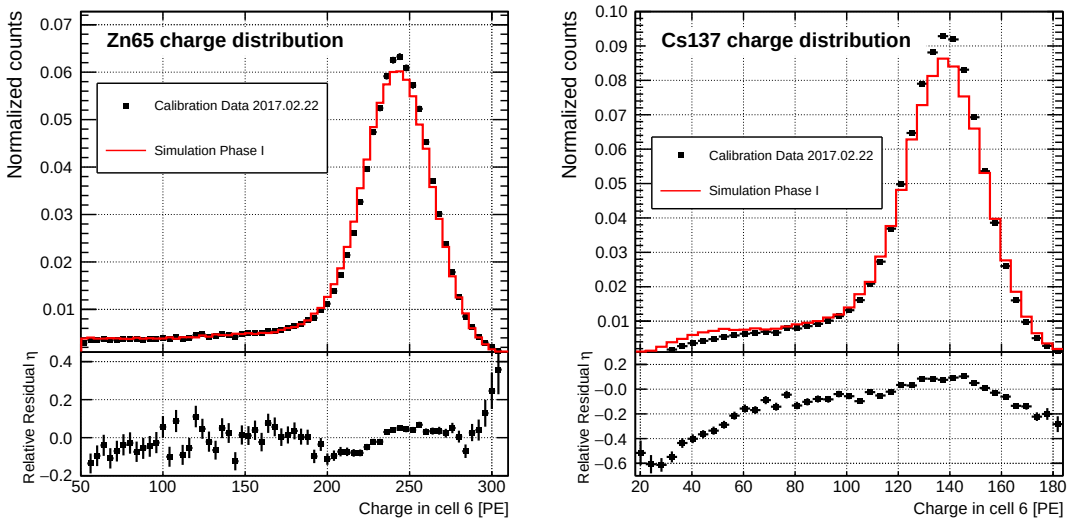

(a) **(b)**

Figure 5.5: Data and simulation charge spectra for (a) ^{65}Zn and (b) ^{137}Cs. Source is deposited in `Cell6` and charge is also collected uniquely in PMTs from `Cell6`. Both histograms for each source have been normalized. At the bottom, residual η has been calculate for each bin.

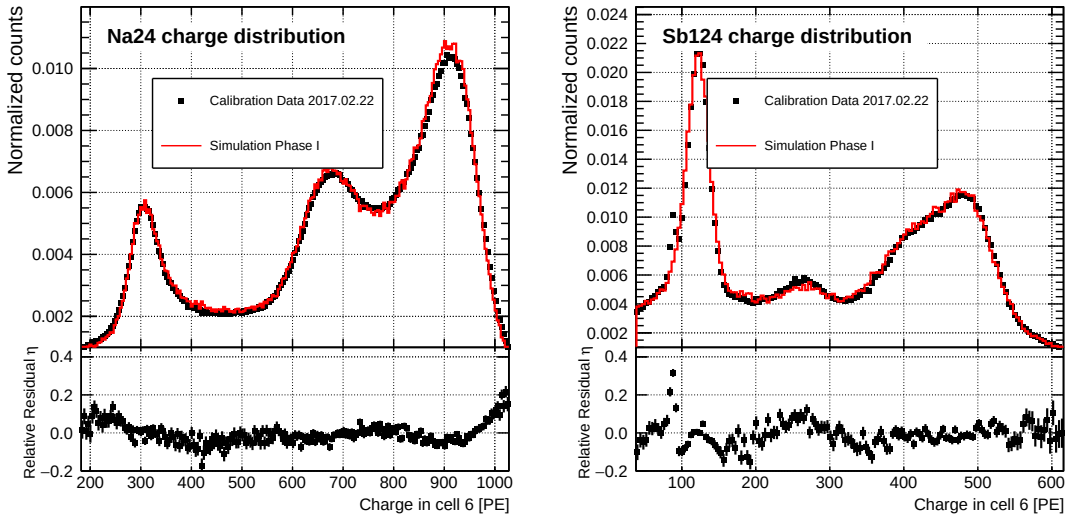

(a) (b)

Figure 5.6: Data and simulation charge spectra for (a) ^{24}Na and (b) ^{124}Sb. Sources are deployed in `Cell6` at *middle* and charge is also collected uniquely in PMTs from `Cell6`. Both histograms for each source have been normalized to unity. At the bottom, relative residual η has been calculate for each bin.

Bi-gamma emitters as ^{24}Na and ^{60}Co, are generated as two correlated gammas and one electron particle gun which are created simultaneously in the capsule. In Fig. 5.6(a), an example of a ^{24}Na spectrum for data and simulation is compared.

Multi-gamma sources can be in some cases more challenging to adapt to simulations, specially when multiple intermediate states are involved. An exception to the simplifying approach discussed so far to generate radioactive sources is the ^{124}Sb. The ^{124}Sb isotope can decay into a myriad of excited states of ^{124*}Te that will also pass through multiple intermediate steps before reaching the ground level. The manual computation of such decay tree is a cumbersome job that has been simplified by directly generating a standard ^{124}Sb ion particle gun, defined in the `Geant4` libraries. As can be seen in Fig. 5.6, spectra from data and simulation agree within the 2% around the area of the two main simultaneous emissions at 0.603 MeV and 1.690 MeV, and the double peak at 2.293 MeV.

The second exception is the AmBe source. As described in Sec. 3.6, the energy of the neutron emitted depends on the kinematics of the interaction between the α particle and the ^{9}Be isotope. Like for any other process involving neutrons discussed in Sec. 3.4.2, computing the actual physics of the AmBe neutron emission can be challenging. In **STEREO**, the path of using data measurements of the energy spectrum of fast neutrons coming from AmBe source was taken, performed at the MAX IV Laboratory, Sweden [165].. Once the neutron spectrum is imported the simulation generates a neutron particle gun with kinetic energy taken from it. Simultaneously to the neutron, around a 60% [165] of the times also a gamma emission will be created. The neutron energy spectra with and without gamma emission is depicted in Fig. 5.7. The rate of neutron emission was also programmed to be 10 kHz, so that the same pileup inefficiencies would happen for data and simulation.

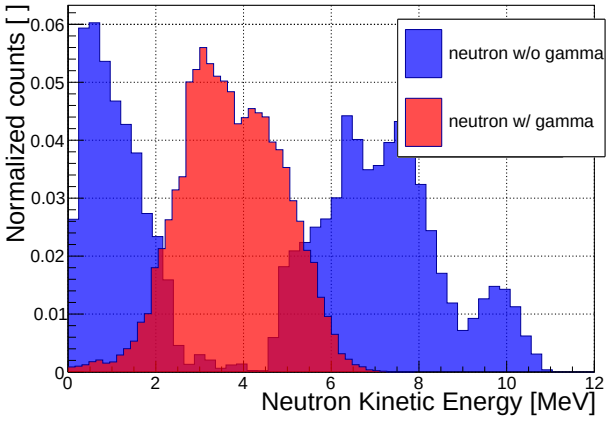

Figure 5.7: True energy distribution for simulated neutrons emitted by AmBe source. In red, events where 4.4 MeV gamma has been emitted alongside the neutron. In blue, events where only neutrons have been emitted. Distribution extracted from [165].

5.3 Optimization of Simulated Response, Detector Geometry and Liquid Scintillator Properties

5.3.1 Attenuation Length

In Sec. 3.4.3 it has been discussed how scintillation light propagates through the LS and how the attenuation length plays a role on the final response of the detector. However, the total attenuation length can be interpreted also as a combination of the relative contributions of each of the components of the liquid. Each of them has a specific molar extinction distribution $\epsilon_i(\lambda)$ that determines how strongly light with a given wavelength λ is attenuated. The relative attenuation length Λ_i can be calculated according to Beer-Lambert law as:

$$\Lambda_i(\lambda) = \log_{10}(e)\frac{M_i}{\epsilon_i(\lambda)\cdot c_i}, \tag{5.8}$$

where c_i and M_i are the concentration and the molar mass of the component i respectively. Eq. 5.8 assumes a linear relation between the attenuation of light and the impurities in the liquid, which holds true for the low concentrations of impurities in the purified liquid of **STEREO** for wavelengths $\lambda > 400$ nm. The extinction coefficients for all three solvents, the two fluors and the gadolinium complex have also been measured at the MPIK [131]. In Tab. 5.4 the attenuation lengths of the individual components, computed with Eq. 5.8, are listed for $\lambda = 430$ nm.

Table 5.4: Attenuation lengths for the different components of the LS at $\lambda = 430$ nm, under the assumption that all the other components do not contribute to the absorption. The inverse addition of all them (Eq. 5.9) is also displayed in the last column. [131]

Component	LAB	PXE	DIN	PPO	bis-MSB	$Gd(thd)_3$	total
$\Lambda_{\text{Gd-loaded}}$ (m)	23	35	33	41	176	94	7.0
$\Lambda_{\text{Gd-unloaded}}$ (m)	23	35	33	95	176	-	8.4

The calculation of the total attenuation length is obtained as the inverse sum of all the contributions

$$\frac{1}{\Lambda_{\text{total}}} = \sum_i \frac{1}{\Lambda_i}, \tag{5.9}$$

since the additive magnitude is the attenuation $A = \frac{1}{\Lambda}$ and not the length. The wavelength dependence of Λ_{total} for TG liquid is shown in Fig. 5.8. These values are in agreement with the measurements performed using the mixed LS after production, being $\Lambda^{TG}_{\text{total}} = 6.9\,\text{nm}$ m and $\Lambda^{GC}_{\text{total}} = 9.7\,\text{m}$ [131]. The different attenuation length in TG and GC comes directly from the primary fluor PPO, as can be clearly seen on their individual contributions in Tab.5.4. Since the unloaded LS does not contain gadolinium, the concentration of PPO can be, and has been, reduced. The process of purification is usually more complex and less effective in non-liquid materials like powder of fluors. These impurities affect the attenuation of light in the final mixture, and because PPO is halved in the unloaded LS, the attenuation length in GC is larger than for TG.

In the **STEREO** simulation, the attenuation length of the liquid is constructed in the same manner. Molar extinctions calculated in [131] are introduced as data files for each component. During the definition of the scintillation physics, the total attenuation length of the liquid is calculated for all wavelengths by using Eq. 5.8 and Eq. 5.9 and stored in the temporal files of the simulation. This method allows an easy adjusting of molar extinctions and concentrations of the liquids, given that the total attenuation length is recomputed automatically.

An accurate reconstruction of the attenuation length in the simulated liquid is crucial to reproduce the vertical inhomogeneities on the response of the detector. As mentioned in Chap. 3, events closer to the PMTs tend to leave larger signals since their scintillation has to travel shorter distances than for those generated near the bottom. The signal asymmetry $\mathcal{A}^{\text{A}}_{\text{B}}$ between two positions A and B is defined as the discrepancy between the detector responses to a source deployment in said positions. When using mono-gamma

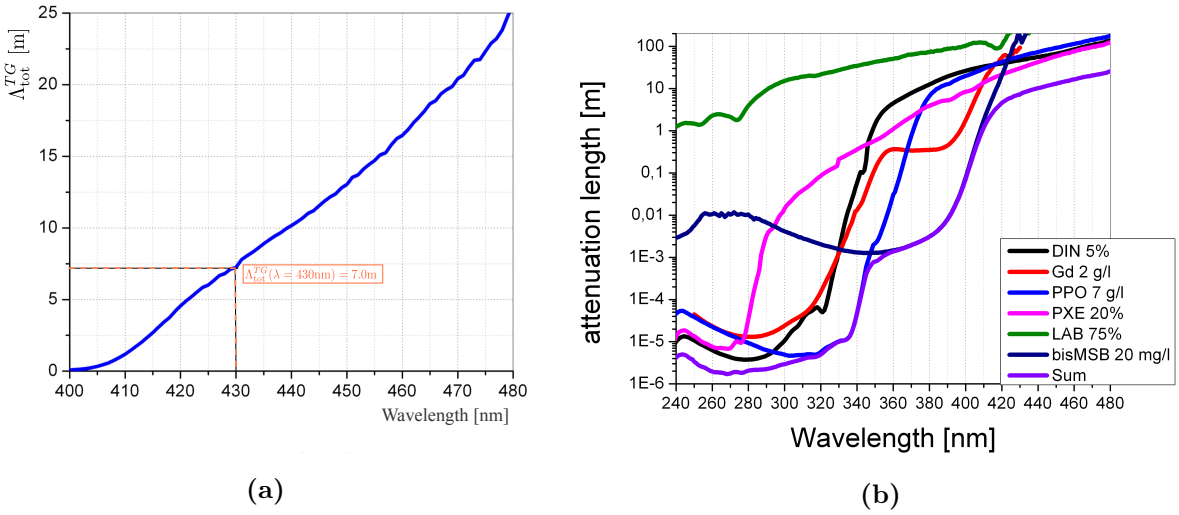

(a) **(b)**

Figure 5.8: Attenuation length dependence on wavelength λ of scintillation. (a) Total attenuation length for LS in TG volume $\Lambda^{TG}_{\text{total}}$. (b) Individual contribution Λ_i to the total attenuation length for the different components i of the LS [131].

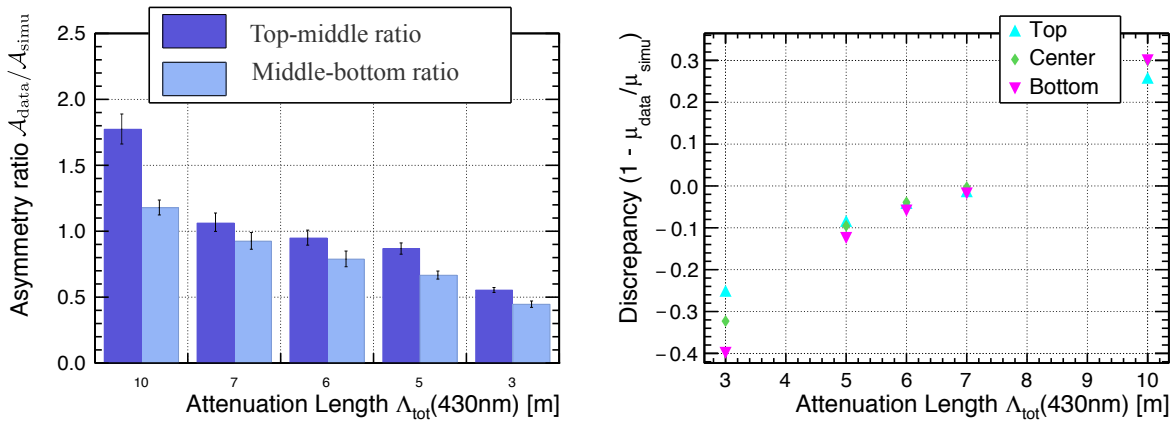

(a) **(b)**

Figure 5.9: (a) Asymmetry $\mathcal{A}_{bot}^{top}$ (dark blue) and $\mathcal{A}_{bot}^{mid}$ (light blue) ratio between data and simulation for different values of $\Lambda_{\text{total}}^{\text{TG,sim}}$. Uncertainties come from error propagation of the uncertainties of the fit, see Eq. C.4. (b) Data to simulation $\mu_{\text{data}}/\mu_{\text{simu}}$ ratio for ^{54}Mn source deployment at different heights inside `Cell4`. Simulations with different $\Lambda_{\text{total}}^{\text{TG,sim}}$ have been used. Uncertainties come from error propagation of the uncertainties of the fit, see Eq. C.3.

sources it can be written down as:

$$\mathcal{A}_{\text{B}}^{\text{A}} = 2 \cdot \frac{\mu_A - \mu_B}{\mu_A + \mu_B} \tag{5.10}$$

where μ_A and μ_B are the mean of the peaks from the fitted spectrum. To cross-check the implementation of the attenuation length, the compatibility of $\mathcal{A}_{bot}^{top}$ between *Phase II* data and simulation has been tested. For this purpose, a set of ^{54}Mn simulations at different heights inside `Cell4` have been produced for a wide range of $\Lambda_{\text{total}}^{\text{TG,sim}}$, obtained by carefully tuning the molar extinction of the main solvents. The range chosen lies around the experimental value of $\Lambda_{\text{total}}^{\text{TG,exp}} \sim 7\,\text{m}$ [2], including a set of decreasing $\Lambda_{\text{total}}^{\text{TG,sim}}$ until 3 m to exclude any unexpected degradation. A high value of 10 m has also been included to test the effect of an overoptimistic attenuation length in the simulation.

The asymmetries $\mathcal{A}_{mid}^{top}$ and $\mathcal{A}_{bot}^{mid}$ obtained for each one of the simulations have been compared to calibration data in Fig. 5.9(a). This comparison is represented in terms of a ratio between data and simulation asymmetries, with a divergent tendency as the values of $\Lambda_{\text{total}}^{\text{TG,sim}}$ drift away from $\Lambda_{\text{total}}^{\text{TG,exp}} \sim 7\,\text{m}$. As the attenuation length of the simulation decreases, the asymmetry between positions observed increases and the detector response becomes more and more heterogeneous. This is displayed in Fig. 5.9(a) as an ever decreasing $\mathcal{A}_{\text{data}}/\mathcal{A}_{\text{simu}}$ ratio. On the contrary, the simulation with $\Lambda_{\text{total}}^{\text{TG,sim}} \sim 10\,\text{m}$ shows a reduced and too optimistic $\mathcal{A}_{mid}^{top}$ for the simulation, leading to a higher-than-unity ratio. The one simulation depicting a ratio close to unity corresponds precisely to $\Lambda_{\text{total}}^{\text{TG,sim}} \sim 7\,\text{m}$, showing good agreement with *Phase II* data. This result also confirms the liquid stability in terms of its attenuation length since the experimental measurements before *Phase I*. In Sec. 6.3.2 the time evolution of the attenuation length will be

[2] Every attenuation length mentioned during the present and following paragraphs of the section refers to the specific value of Λ_{total} for a wavelength of $\lambda = 430\,\text{nm}$.

depicted.

Another way of looking at the compatibility of vertical asymmetries in data and simulation comes from Fig. 5.9(b). There, the discrepancy from the unity of the ratio $\mu_{\text{data}}/\mu_{\text{simu}}$ is portrayed for the different values of $\Lambda_{\text{total}}^{\text{TG,sim}}$. The positive value of the discrepancy at higher attenuation lengths shows a clear overshoot in simulation making the ratio $\mu_{\text{data}}/\mu_{\text{simu}}$ too small. On the contrary, for lower values of $\Lambda_{\text{total}}^{\text{TG,sim}}$ the behavior is exactly the opposite and the response of the simulated detector is below the one observed in data. It is also visible that *top* deployments are less sensitive to the changes on the attenuation length, while events from *bottom* suffer the largest impact. The results show a nice agreement for the three positions at $\Lambda_{\text{total}}^{\text{TG,sim}} \sim 7\,\text{m}$ like in Fig. 5.9(a). The absolute scale where the points in Fig. 5.9(b) lie can be tweaked via the Light Yield tuning, as will be explained in Sec. 5.3.4.

5.3.2 Leak of Oil in Acrylic Buffer

The first weeks of *Phase I* were dedicated to commission the detector. During this time a sudden and noticeable decrease on the response of `Cell4` and `GCFront` was observed. A mechanical defect on the glued corner of the buffer vessel allowed the n-dodecane on the inside to leak into the `TG`. This happened only for the buffer above the two cells mentioned.

The effect on the detector response is detailed in Sec. 6.3, and overall can be summarized as a loss of about 50% of the signal coming from the affected cells. The total mass of leaked oil is about 40 kg , which is approximately a 2.5% of the roughly 1600 kg of `LS`. This is not a critical amount, specially considering both liquids are chemically

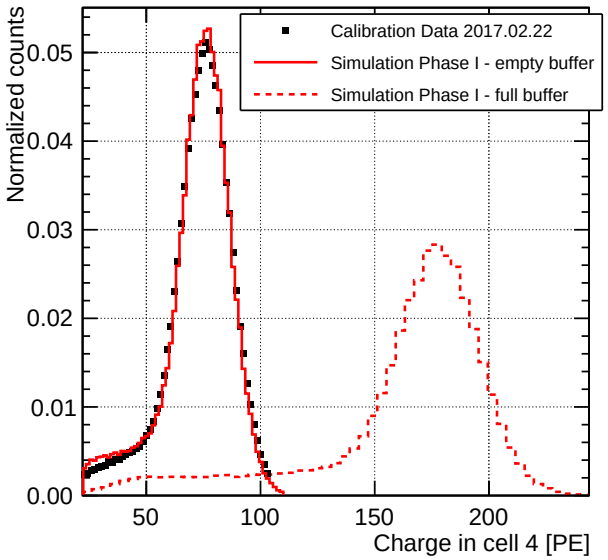

Figure 5.10: Response of `Cell4` for ^{54}Mn 54 placement at *middle* for data and simulation. Both simulations with full and empty acrylic buffer represented.

compatible and share similar properties in terms of light propagation. The most impactful consequence of the leak is the empty buffer itself and thus the loss of optical contact between cells and PMTs. The n-dodecane has a similar refractive index n as the acrylic and the `LS` ($n \sim 1.5$) and therefore the light gets transmitted easily from medium to medium. Contrarily, air has a refractive index of $n_{air} \approx 1$ which results in total reflection phenomena when light from `TG` encounters the change of medium.

In order to account for the degraded light output in data, the simulations have been adapted accordingly. The most effective approach to do so comes from generating specific buffer volumes filled with air instead of n-dodecane, and place them on top of `Cell4` and `GCFront`. In Fig. 5.10 it is compared the simulated responses of the detector to ^{54}Mn deployment with buffer normal conditions and leaked buffer, and regular data from *Phase I*. In general terms, the correction matches properly the reduced distribution displayed by calibration data, albeit it has slightly smaller resolution. The mismatch of the resolution is related to second order optical effects from factors like an imperfect depletion of oil from the buffer in the real detector.

As described in Sec. 3.6, internal calibration tubes are placed at a fixed position within some of the cells. Under normal conditions, a high scintillation light containment is achieved and thus internal calibration is sufficient to characterize the relatively uniform response of the volumes. Geometrical dependencies come mainly from the distance between the event to the PMT and can be measured by placing sources at different heights in the tube. However, the absence of optical coupling between cell and PMTs due to an empty buffer could affect geometrical dependencies in unforeseen ways. The existence of possible irregularities have been investigated with simulated ^{54}Mn data.

Placement of the calibration tubes in the simulation need to be edited directly from the geometry files, while the macro files can stay untouched. For this analysis, three different positions have been chosen for the tube in `Cell4`: standard at $(x = 120, y = 0)$ mm, in the same position as data (point A); centered at one of the sides at $(x = 120, y = 400)$ mm, to observe the effect of one wall (point B); and in one

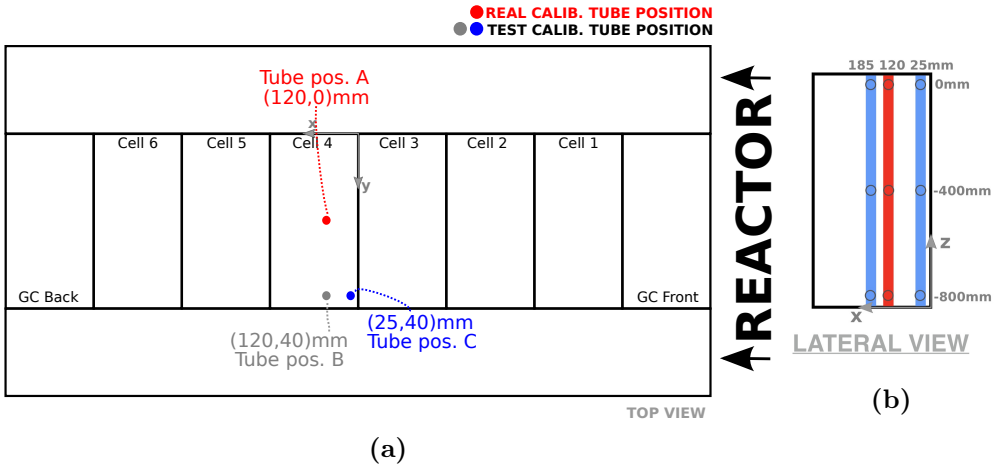

(a) (b)

Figure 5.11: Calibration tube positioning A,B,C in `Cell4` in test simulation. (a) Inner detector projection in the plane (x,y). (b) `Cell4` projection in the plane (x,z). All histograms have been normalized.

of the corners at $(x = 25, y = 400)$ mm (point C). The projection of these placements in the (x, y) and (x, z) planes can be seen in Fig. 5.11.

The comparison between simulation and data responses for empty and full buffer has been already displayed in Fig. 5.10. The mono-gamma peak of ^{54}Mn have been fitted to a *GaussExp* function, defined in App. B, and from such fit the mean μ and standard deviation σ of the main peak of the distribution have been extracted. The dependence of μ with the position of the source and the tube configuration is displayed in Fig. 5.12(a) and Fig. 5.12(b) for simulations with full and empty buffer of `Cell4` respectively. The trend shown in these figures portrays a greater response for simulations at higher positions, as expected due to the shorter distance between the source and the PMTs. It also displays greater response for simulated sources far from the edges of the cells where the leaks are larger. Both results are expected for the case with full buffer, and such trend is also confirmed for the case with empty buffer in almost identical manner. In both configurations the fit mean μ for point A is between 1.5% and 3% larger that point C, being point B between them. Ratios between signals from different tube positions compatible for both simulations with empty and full buffer.

Similarly to the analysis with mean of the fit μ, some information for the different simulations can be inferred from the standard deviation σ of the respective fits. More concretely, the resolution $\Delta\mu$, defined as $\Delta\mu = \dfrac{\sigma}{\mu}$, has been compared between the two cases, as depicted in Fig. 5.13. The better resolution for all three points A, B and C is achieved the closer the source is to the center of the cell, as expected for the full buffer simulation. It has to be noted that, by definition, lower $\Delta\mu$ value equals to better resolution. Light from *top* events travels either very short distances when emitted upwards, and very long distances when emitted downwards. Light traveling longer distances has higher chances of being absorbed than traveling short distances. The contrast between these two topologies leads to a wider distribution for the main peak. Light from the

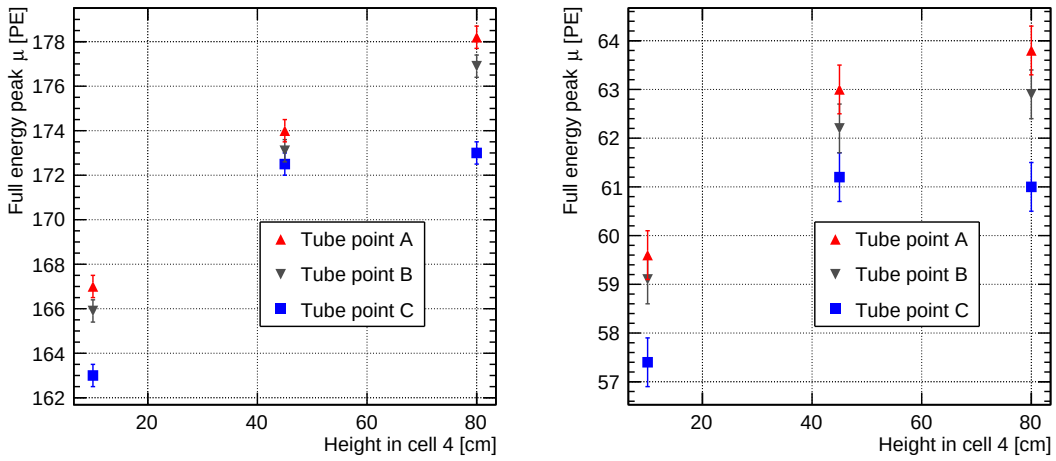

(a) **(b)**

Figure 5.12: Fitted mean μ of the peak for simulated response of `Cell4` to ^{54}Mn 54 placement at different heights using different tube configurations: (a) Acrylic buffer is full. (b) Acrylic buffer is empty.

events generated at *bottom*, regardless the emission direction, have to cross the entire cell and in average are absorbed more frequently. This widens the peak distribution from the lower charge end of the peak. For both *top* and *bottom* events, proximity to the borders also contributes to the overall loss of light and hence the widening of the peak distribution. However, *middle* events are the most heterogeneous type of events in terms of light travel path and the less impacted by border effects. All these expectations are clearly confirmed by results in Fig. 5.13 for both empty and full buffer simulations.

However, in absolute values, a worsening of $\Delta\mu$ by almost a factor two in the simulation with empty buffer can be observed. Such effect can simultaneously be observed in calibration data from Fig. 5.10. In general, the total resolution of a Gaussian-like signal can be factorized in two different contributions,

$$\Delta\mu_{tot}^2 = \Delta\mu_{stat}^2 + \Delta\mu_{sys}^2. \tag{5.11}$$

$\Delta\mu_{stat}$ accounts for the quantum nature of the photon counting statistics. Scintillation light in `LS` has been considered to follow Poissonian statistics, and thus $\Delta\mu_{stat} \sim \frac{1}{\sqrt{\mu}}$. The term $\Delta\mu_{sys}$ accounts for systematic effects on the light generation, transmission and collection in the detector. As an illustrative example, systematic contributions for both *middle* simulations with full and empty buffer at point A, have been compared. Using Eq. 5.11 on the full buffer simulation results, the systematic contribution to the resolution is $\Delta\mu_{sys} = 0.082$, where $\Delta\mu_{stat} = 0.076$ and $\Delta\mu_{tot} = 0.112$. In the empty buffer case, the statistical resolution worsens due to a lower counting of photons, giving $\Delta\mu_{stat} = 0.127$. From Fig. 5.13 it can be extracted that $\Delta\mu_{tot} = 0.182$. Thus, the systematic contribution to the total resolution from Eq. 5.11 is $\Delta\mu_{sys} = 0.131$, $\sim 62\%$ higher than the value obtained for the simulation with a full buffer.

Therefore it can be concluded that the leak of the oil from the acrylic buffer affected in several ways the light collection of `Cell4` and `GCFront`. The individual response

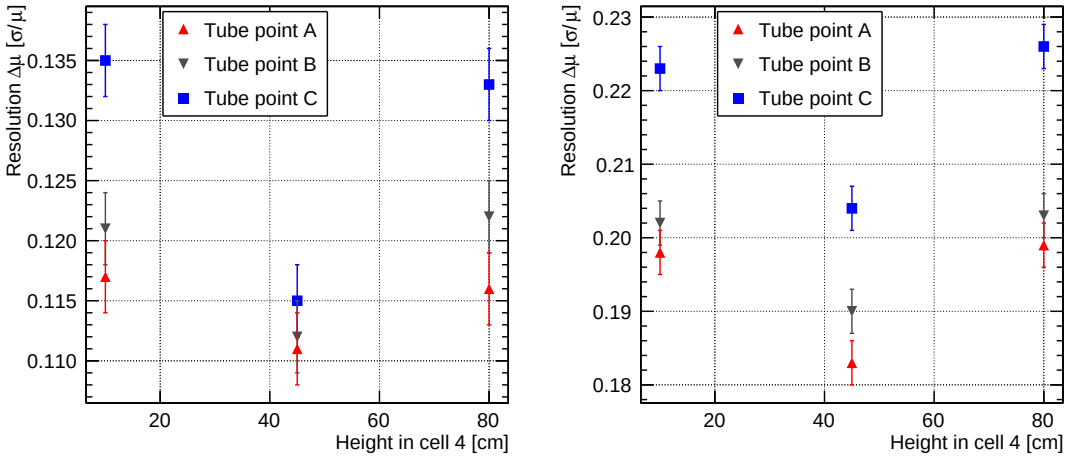

(a) **(b)**

Figure 5.13: Peak resolution $\Delta\mu$ for simulated response of `Cell4` to ^{54}Mn 54 placement at different heights using different tube configurations: (a) Acrylic buffer is full. (b) Acrylic buffer is empty.

of the cell decreased overall about a 60% due to the lack of optical coupling between liquid and PMTs and total reflection effects between acrylic and air. The leak did not affect quantitatively the already existing geometrical asymmetries. However, resolution in these cells has decreased roughly by a factor ~ 1.6. The decrease of the signal is not sufficient to account for the reduced resolution and a additional systematic contribution of $\sim 60\%$ has been found.

5.3.3 Cell-to-cell Light Cross-Talk

Before describing the details of the light cross-talk between cells, a clear definition of this phenomenon ought to be presented. The energy deposition of a particle is considered to happen in a volume when its correlated molecular ionizations and/or excitations in the liquid happen in that volume. However, this volume is not necessarily where all of the light is observed. For instance, once the emission gamma from a ^{54}Mn atom decay ionizes the liquid of a given cell, the scintillation produced may travel to another cell and be observed there. Scintillation light produced and detected in different cells is said to have leaked. When not only light, but also the ionizing particle leaves the origin cell, the energy has also leaked. The average nominal percentage of light leaked from `Cell`i to `Cell`j, without accounting for *energy leaks*, is known as the light cross-talk, or *light leaks*. In terms of deposited charge, *light leaks* from an event originated in `Cell`i towards `Cell`j can be defined as

$$\ell\ell_{ij} = \frac{Q_i}{Q_j}, \tag{5.12}$$

where Q_i and Q_j are the charges deposited in `Cell`i and `Cell`j respectively. To ensure high energy deposition in the origin cell, usually conditions on the collected charge distribution are applied when $\ell\ell_{ij}$ is used. More details about this are given in Sec. 6.1.1. Fig. 5.14 depicts example topologies for *light leaks* and *energy leaks* from one cell to another, when using calibration sources.

During the commissioning time at the begining of *Phase I*, an unexpected increase of the light cross-talk between cells was observed. As it is described in Sec. 6.3.1, after some weeks the evolution of the *light leaks* slowed down and the response of the detector stabilized. The cause of the incident was a loss of tightness at the peripheral glue fixing the separation walls to the cell [123]. This would allow liquid to get into the sandwich volume and fill the air gap between the acrylics, reducing the reflectivity of the ESR film as a consequence. The optical reflectance and transmittance of the film were initially tested during the construction of the prototype of the STEREO detector at CEA in Saclay [133]. The results showed that the transmittance of the film was only optimal when it was optically coupled with air. It being submerged in liquid was seen to affect in non trivial ways the optical properties of the film [132].

To first order, the leak of liquid into the separation walls has not affected the total light collection in the detector but the optical cross-talk between cells increased from the nominal value of 5% to an average of $\sim 15\%$. The impact on the individual response of the cells is not homogeneous and has been quantified individually for each separation wall between cells. In Fig. 5.15 a diagram of the averaged percentage of light leaked from cell to cell is shown for *Phase I*. A more detailed evolution of *light leaks* is depicted in Fig. 6.8. The details of the method used to obtain them is discussed in App. A, and

relies on the observation and characterization of cosmic muon events. The highest *light leaks* values are represented in red and correspond to `Cell4` and `GCFront`. According to Eq. 5.12, the reduced collection efficiency of these cells imply higher $\ell\ell_{ij}$ when compared to the collected charge in neighboring cells. This is clearly visible on the asymmetry between $\ell\ell_{ij}$ and $\ell\ell_{ji}$ for the same cells i and j. Taking `Cell4` as an example, $\ell\ell_{45}$ $\sim$ 35% show large *light leaks* while $\ell\ell_{54}$ $\sim$ 5% represents a specially low value. From these numbers, it can be understood that the collection inefficiency of `Cell4` not only enhances $\ell\ell_{45}$, but also reduces $\ell\ell_{54}$ proportionally. In Sec. 5.3.2 it is shown that the signal of `Cell4` and `GCFront` have been reduced by a 60% with respect to their nominal values. If one takes into account a correction of the type

$$\ell\ell'_{ij} = \frac{Q_i/0.4}{Q_j}, \quad \ell\ell'_{ji} = \frac{Q_j}{Q_i/0.4} \tag{5.13}$$

the resultant $\ell\ell'_{ij} \sim \ell\ell'_{ji} \sim 0.14\%$ are in tune with the rest of enhanced *light leaks* observed for cells with full buffer, depicted in yellow in Fig. 5.15. Therefore, in order to properly account of the unusually high *light leaks* for `GCFront` and `Cell4`, the simulation requires the implementation of the leak in the acrylic buffer detailed in Sec. 5.3.2. Finally, the rest of green arrows depict the cases where no liquid entered the sandwich and thus they retained their reflectance and nominal values for the *light leaks*.

Initially, simulations in **STEREO** were not prepared to account for defective walls between cells. For this reason, a set of enhancements were quickly added to the code when the increase of *light leaks* was first observed. These changes responded to an immediate need to adapt simulated response to the real detector signal. Several approaches were taken into account while the problem was being investigated and characterized. The most obvious way to address the problem would be to directly adapt the reflectance R and transmittance T of the ESR to match the most recent data. However, this approach cannot give a pragmatic solution to each individual separation plate and would reduce

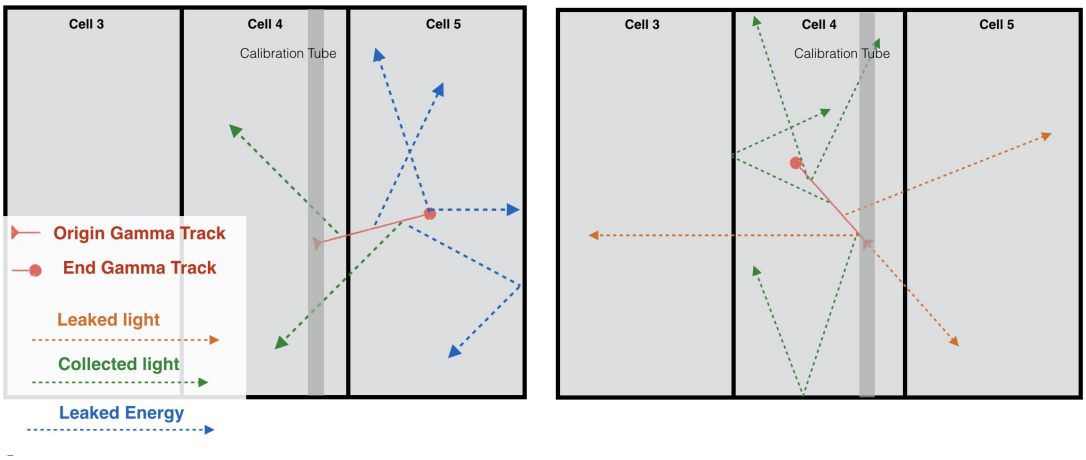

(a) (b)

Figure 5.14: Representation of different topologies of ^{54}Mn 54 events in `Cell4`. (a) Gamma travels to `Cell5` where it deposits most of the energy, constituting a typical event with high amount of *energy leaks*. (b) Gamma stays in `Cell4` and deposits all its energy there, albeit some light is leaked towards neighboring cells constituting *light leaks*.

the total response of the detector by allowing light to leak out of the inner detector. Another option would be to address the issue as a geometrical problem where some paths have opened to light between the cells. This option is difficult to implement because it would require a good knowledge of the location of the geometrical defects. Furthermore, such an explanation would generate in principle a higher amount of leaks than the ones observed and possibly some obvious inhomogeneities in the response. The most viable approach, thus, was to take into account some liquid leaks into the separation walls that degrade the optical properties of the film, as it has been anticipated above.

Two different models have been thoroughly implemented into the simulation to account for the liquid in the walls and the loss of reflectance. In what follows, they are named as Homogeneous Probability p Model (`HpM`) and Liquid Height h Model (`LhM`). The `HpM` has been developed during *Phase I* data taking, and thus its main features has been tested with data from that time. On the contrary, `LhM` is the natural continuation of `HpM` and therefore tested mainly using *Phase II* data.

Homogeneous Probability p Model in *Phase I*

The first correction applied to the simulation in **STEREO** to account for the increased *light leaks* was the `HpM`. These modifications assumed a degraded optical properties of the entire reflective foil inside the separating walls of some cells. Initially, these foils were implemented in the simulation as almost perfectly reflective plates with a small $T = 0.015$ for light incidence angles $\theta < 48^{\circ}$. Tab. 5.5 lists the exact values of T and R for the different optical configurations of the separation walls used. It must be noted that nominal *light leaks* lie around the 5% not only because of T, which is too small to alone explain them, but also due to the existence of communicating apertures at the bottom of each wall, as described in Sec. 3.2. Fig. 5.16 shows the results of the reflectance studies performed by Janeck M [164] for VM2000$^{\text{TM}}$reflective films. Both plots portray a high reflective capabilities of the reflector, with a low diffusion rate for

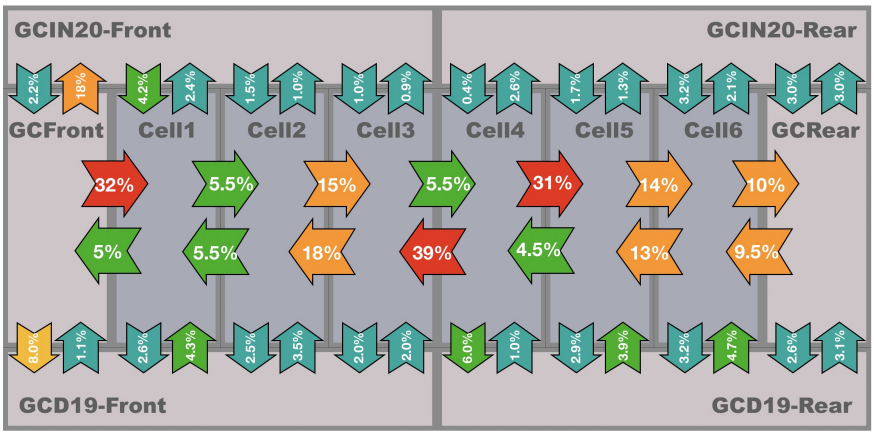

Figure 5.15: Detector projection in the (x, y) plane. The numbers display the average *light leaks* between cells calculated using cosmic muons [134] from standard neutrino runs (see App. A). Information extracted from *Phase I* on 22.II.2017.

any incident angle of the light.

The values for R and T on the walls were originally statically coded with no dependency on the material surrounding the nylon net inside. Under the new approach, new values for R and T were needed to represent the liquid in the wall. According to the laboratory measurements of the prototype mentioned before, incident light at small angles with respect to the normal of the surface would not reflect anymore. As depicted in Tab. 5.5, for $\theta < 8^{o}$ the tables turn and $R \sim 0$ and $T \sim 100$. As the incident angles increase, T starts gaining more relevance as R decreases. This continuum between $8^{o} < \theta < 34^{o}$ has been implemented in a pragmatic way, where the averaged values for both T and R are used for any incident light in this range. A specific and accurate angular dependence for T and R implied a troublesome implementation more computationally intensive than desired. Since the angular distribution of the photons hitting the walls can be considered isotropic, an averaged response could be implemented without adding any inaccuracies on response of the detector. For angles $\theta > 34^{o}$, the original configuration for T and R is used.

In order to account for the different increases on the light cross-talk of the separation walls along the detector, the probability p has been introduced in the simulation. With the tweaked configuration described until now for the reflective foil either submerged in liquid or not, there would only be two different results for the *light leaks*. The probability p enters into play as an artificial probability for a photon to hit liquid and not air after crossing the acrylic surrounding the reflective foil. This interpretation assumes both models coexist inside the same wall, like in an scenario where some liquid has filled partially the wall but not completely. However, in this case, the distribution of air and liquid is homogeneized and controlled only by the probability p. This probabilistic approach serves as a starting point to the `LhM` model, discussed in the next section.

An example of how the response of an individual cell evolves with the probability

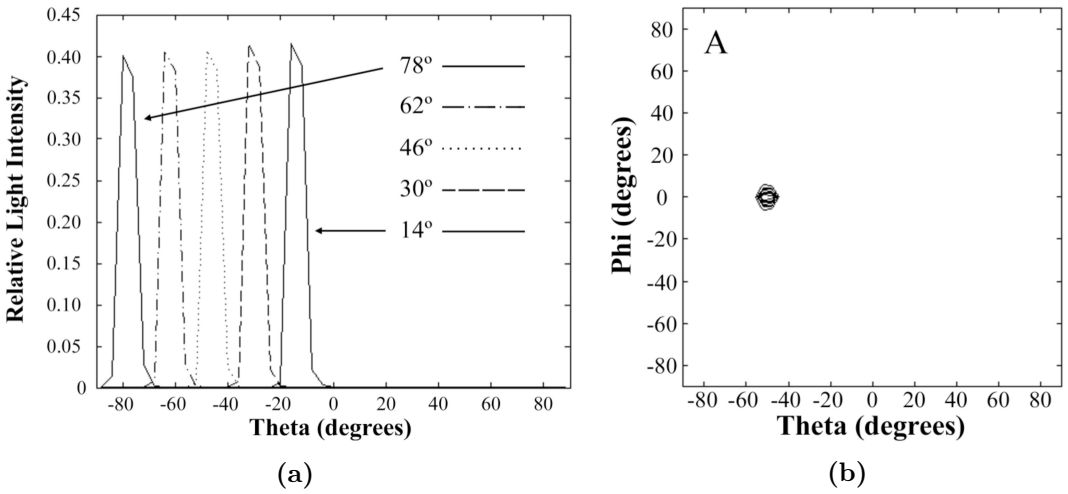

Figure 5.16: Using $\lambda = 440\,\text{nm}$ light, distribution of reflected angles $\theta\prime$ in VM2000$^{\text{TM}}$for (a) a series of incident angles θ for a single orientation angle of the foil ϕ =cnst; (b) an incident angle of $\theta = 50^{o}$ and different orientation angles of the foil ϕ [164].

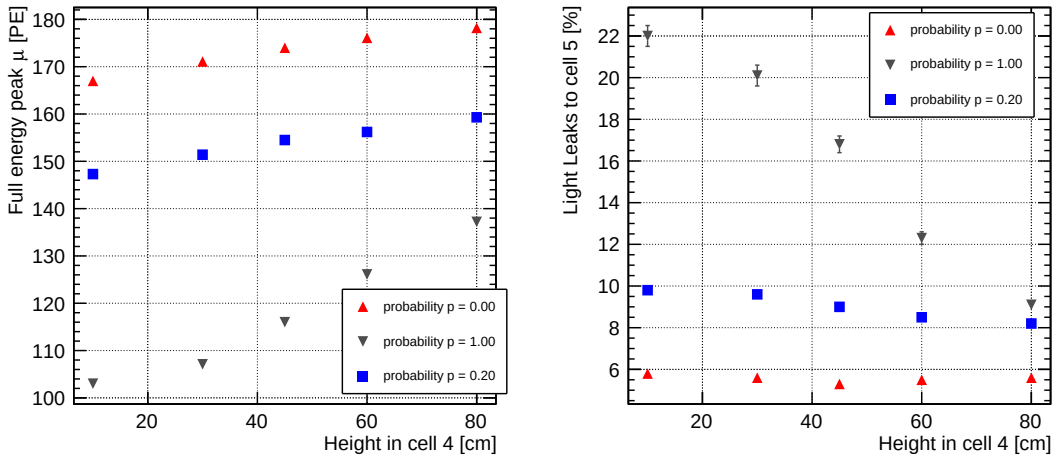

(a) (b)

Figure 5.17: Evolution of the individual cell response and *light leaks* in terms of height of deployment of a simulated ^{54}Mn source. Three different cases portrayed: in red, regular configuration for separation walls. In gray, separation walls completely flooded with `LS` using a $p = 1.0$. In blue, separation walls partially filled with `LS` using a $p = 0.20$.

p can be seen in Fig. 5.17. In this particular case, a simulation of ^{54}Mn in `Cell4` has been used for illustrative purposes. It must be noted that this simulation does not include corrections with regard to the leak of the oil from the acrylic buffer described in Sec. 5.3.2. In red it is showed the standard behavior of the simulation with no tuning on the *light leaks*, and together with it in blue and gray simulations with $p = 0.20$ and $p = 1.0$ are portrayed. Indeed the response of the cell increases as the source is placed closer to the PMTs. However, for higher p this increase is more noticeable being closer to a 40% between *bottom* and *top* for $p = 1.0$. Values for *light leaks* more than double between *top* and *bottom*. For $p = 0.20$ the effect is weaker but still noticeable, specially for *bottom*. This leaves clear testimony about how impactful p is for events near the bottom of the detector. This is a consequence of a higher number of reflections needed for scintillation generated at the *bottom* to reach the PMTs being than for the *top* positions. For each photon reflection in the wall, a new process where either reflection or transmission is chosen happens. Indeed, for large p value the chances of transmission through the wall increase.

In order to tune the values p for the different walls, the requirement of matching *light*

Table 5.5: Angular dependence of Reflectance R and Transmittance T of the separation walls in simulation. Two cases are presented: gap between foils flooded with `LS` or kept in normal conditions with air.

	Wall filled with air		**Wall filled with `LS`**		
	$\theta > 48^o$	$\theta < 48^o$	$\theta > 34^o$	$34^o > \theta > 8^o$	$\theta < 8^o$
Reflectivity R (%)	100	98.5	98.5	66.7	0
Transmittance T (%)	0	1.5	1.5	33.3	100

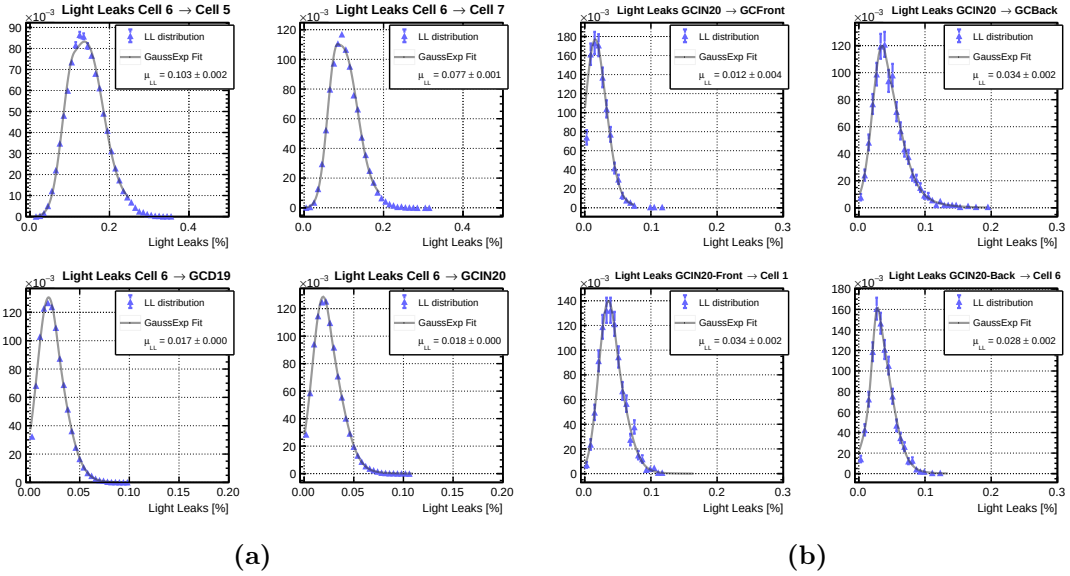

Figure 5.18: *light leaks* distribution from `Cell6` and `GCD19` to their neighboring cells for simulation after tuning using `HpM`. Events extracted from ^{54}Mn deployments through internal calibration at *middle* position.

leaks between data and simulation is required. As mentioned above, *light leaks* in data are obtained from cosmic background measurements. Given the perpetual nature of cosmic rays, monitoring of *light leaks* can be performed several times a day. Measuring cosmic rays does not require any special setup and does not interfere with regular data taking any more than standard background rejection would. This approach, however, is not used to calculate *light leaks* in simulations. Soon after the start of *Phase I*, the compatibility of *light leaks* by using ^{54}Mn calibration runs and cosmic rays was proven [143] for both data. Therefore, the tuning of light cross-talk in simulation, as for many other tuning endeavors, has been performed via ^{54}Mn deployments in different cells. The main reason of using simulated ^{54}Mn and not simulated cosmic rays is a better understanding and definition of the events in terms of position and energy. Contrarily to real data, calibration sources can be simulated as many times as desired in as many configurations as needed.

To calculate $\ell\ell_{ij}$ from `Cell`i to `Cell`j using simulated ^{54}Mn, the true information of the energy deposited in each volume is needed. For this analysis it is crucial that only events where no gamma has escaped `Cell`i are considered. Any escape of energy would contaminate the sample with scintillation produced outside the cell, and this scintillation would be incorrectly considered part of the *light leaks*. Therefore, a very restrictive cut on the deposited energy $E_{i,dep}$ in `Cell`i $0.833\,\text{MeV} < E_{i,dep} < 0.835\,\text{MeV}$ is applied in the simulation to the whole set of events. This condition is easily fulfilled for *source cells*. However, *intermediate cells* require as a prerequisite that the gamma emission leaves immediately the *source cell* without producing any ionization, so that all the energy from the decay can be deposited in the *intermediate cell* in question. This means that these cells will count with much less statistics to work with that any *source cell*.

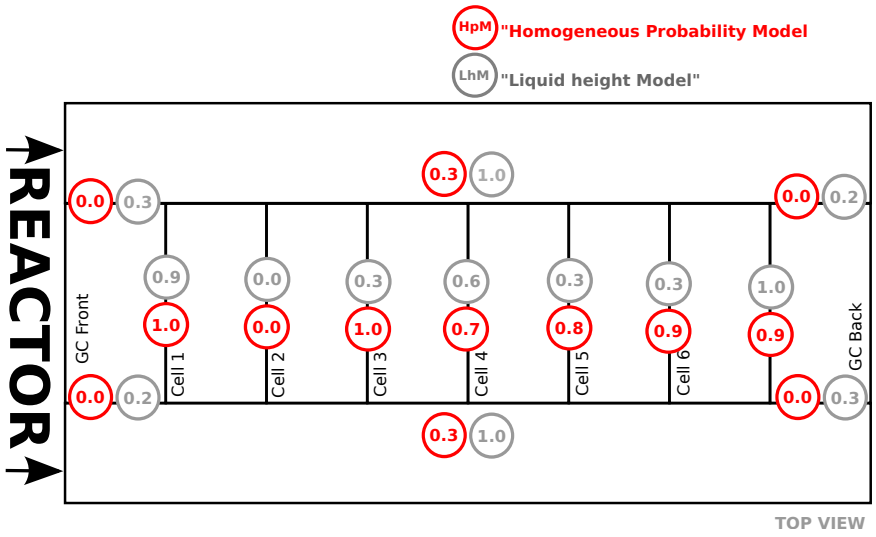

Figure 5.19: Detector projection in the (x, y) plane. Numbers in red represent the p value from the `HpM`. Numbers in gray represent the h value from the `LhM`. Each of them makes reference to the separation wall they are next to.

The remaining events after the $E_{i,dep}$ cut are then scanned to map out their collected charge distribution along the PMT array of the detector. For each of the four nearest neighboring cells of `Cell`i, located at the front, back and `GCD19` and `GCIN20` at the sides, the charge ratio with respect to `Cell`i is calculated according to Eq. 5.12. In Fig. 5.18, top, the light leak distributions from `Cell6` to `Cell5`, `GCBack`, `GCD19` and `GCIN20` are displayed. These distributions are fitted by using a *Mirror-GaussExp* function, described in App. B. The average *light leaks* are obtained as the weighted averaged of the fitted mean values μ_1 and μ_2. The weighting factors come from the normalization constants N of the *GaussExp* and *Gauss* functions, also described in App. B. It can be shown in Fig. 5.18, bottom, that also *light leaks* from long gamma catcher cells can be calculated using this method. This process is repeated for three different positions of ^{54}Mn, *top*, *middle* and *bottom*. To try to emulate as accurately as possible the homogeneous distribution of the calculated *light leaks* from cosmic rays, the simulated *light leaks* obtained from the fits are averaged over the three different positions.

In the case of Fig. 5.18, such *light leaks* have been obtained from setting $p_{67} = 0.9$ and $p_{65} = 0.9$. By adjusting the rest of p values the overall light cross-talk configuration can be tuned to match as accurately as possible what it is observed in data. Fig. 5.19 shows the final distribution of p values along the detector for `HpM`. It also shows the distribution of h values for `LhM`, described in the following section.

The implementation of the `HpM` lead to a good agreement between data and simulation in terms of the average *light leaks* between cells. It helped also to homogenize the simulated response of the individual cells with respect to calibration runs. However, despite the good agreement accomplished with this model, some discrepancies still arise when one compares the response at different heights of the cell. In fact, as explained above, the p value is computed homogeneous along the height of the wall, contrary to how the liquid fills it in the real detector. This means that the averaged *light leaks* calculated for simulations translates into a constant p value that underestimates the real cross-talk at the bottom and overestimates it at the top. In Fig. 5.20 the asymmetry

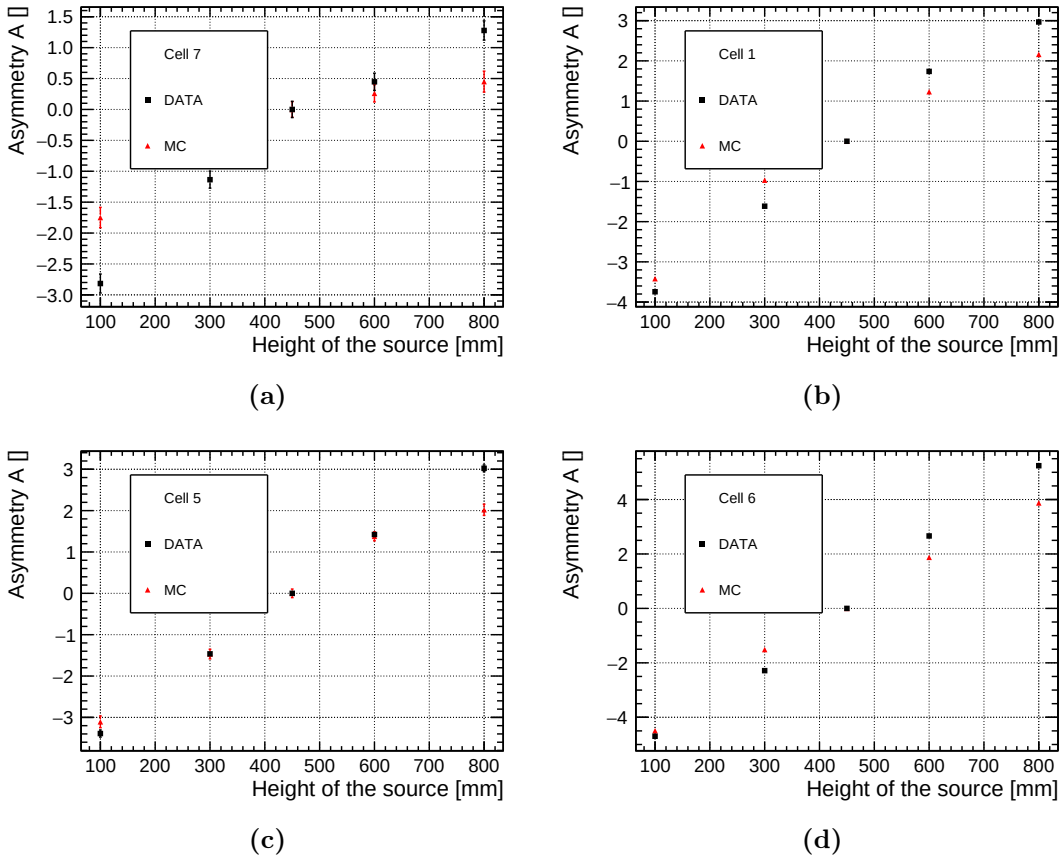

Figure 5.20: Asymmetry $\mathcal{A}^z_{mid}$ for different cells after tuning of *light leaks* using `HpM`. Numbers obtained from ^{54}Mn deployments at different heights for both data and simulation. Data used from calibration runs performed on 22.II.2017.

$\mathcal{A}^z_{mid}$ is shown for different heights X with respect to the *middle* position M. There it can be seen that for simulations $\mathcal{A}^z_{mid}$ is smaller in terms of absolute magnitude because *light leaks* are more homogeneous. In data happens the opposite, and hence $\mathcal{A}^z_{mid}$ are larger. This effect is specially notable for cells where *light leaks* are small and hence the liquid has not reached the top of the wall. For example in `Cell1`, with $\ell\ell_{1x} \sim 6\%$ discrepancies are larger than in `Cell6`, with $\ell\ell_{6x} \sim 12\%$. On the contrary, *intermediate cells* exhibit a much better agreement than *source cells*. The explanation for this comes from the topology of the events coming into play. Events at *top* in *intermediate cells* label events which origin is at the top of the *source cell*. However, gammas travel different paths regardless of their origin and, although in average *top* at *source cells* represents approximately *top* in *intermediate cells*, events are more homogeneous in the latter. This means that events labeled as *top* might be depositing the energy closer to the middle or even the bottom of the cell, and viceversa. Therefore, opposite contributions into the asymmetry $\mathcal{A}^z_{mid}$ average out and leave a good agreement between data and simulation.

In the next section the natural continuation of `HpM` will be discussed and its application to *Phase II* data.

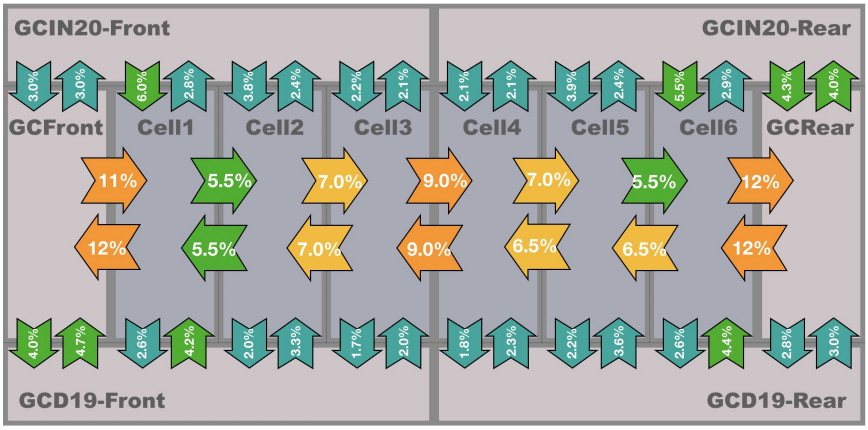

Figure 5.21: Detector projection in the (x, y) plane. The numbers display the average *light leaks* between cells calculated using cosmic muons [134] from standard neutrino runs (see App. A). Information from *Phase II* on the 24.IV.2018.

Liquid Height h Model in *Phase II*

It has been discussed in the previous section that the implementation of `HpM` did not completely match the response of *Phase I* data and simulation at all heights within the same cell. To palliate this, within this thesis the `LhM` has been implemented in the simulation code and has been mainly studied via *Phase II* data. This model has the particularity of allowing a more exact filling of the separation walls with `LS`. The meaning of the p value, now renamed to h value, has been shifted from a homogeneous probability to an amount of liquid introduced in the separation wall, filling it from bottom to top. The values for T and R remain the same as in Tab. 5.5. A visual representation of this model can be seen in Fig. 5.22. It must be noted that the way *light leaks* for *Phase II* have been calculated is the same as for *Phase I*, i.e by using cosmic muon events as described in App. A.

The tuning of the *light leaks* had to be performed anew for *Phase II*, displayed in Fig. 5.21. On one side, the mechanical defects on the separation walls between `TG` cells that provoked increased *light leaks* for *Phase I* were fixed. However, such fixes could not be performed for the walls between `TG` and `GC` volumes, and for them the *light leaks*

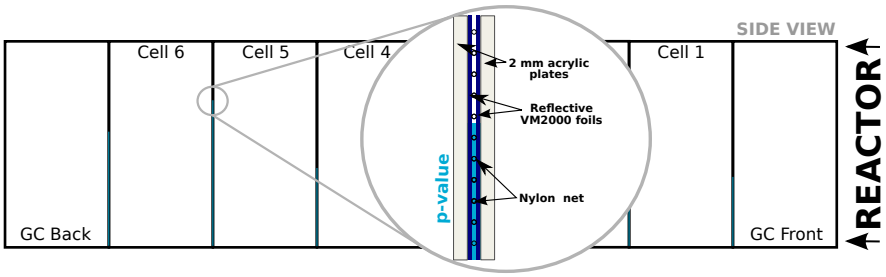

Figure 5.22: TG projection in the (x, y) plane. Zoomed it, there is a pictorial representation of the separation walls after the leak of `LS` and its corresponding h value from the `LhM`.

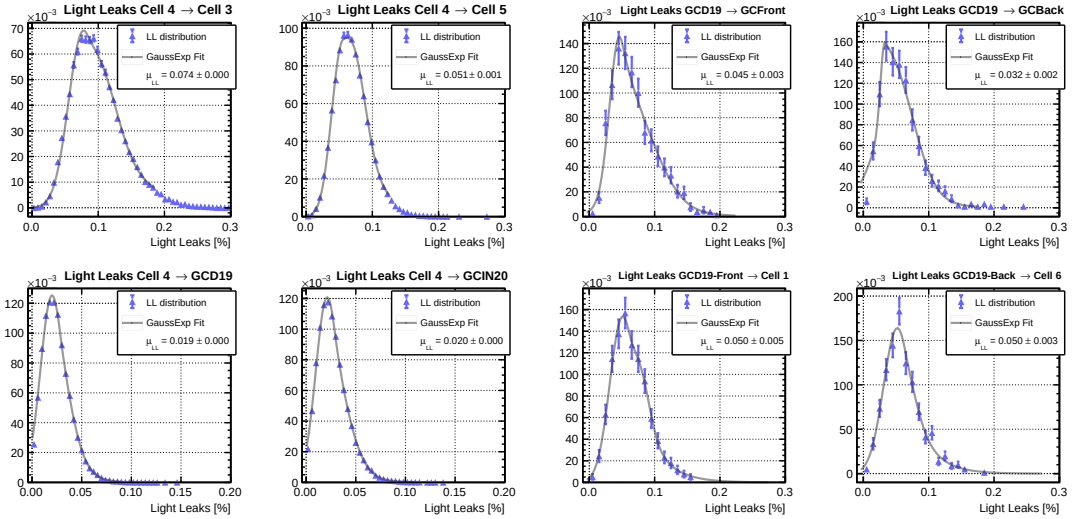

Figure 5.23: *light leaks* distribution from `Cell4` and `GCIN20` to their neighboring cells for simulation after tuning using `LhM`. Events extracted from ^{54}Mn deployments through internal calibration at *bottom*, *middle* and *top*.

remained similar. Furthermore, the acrylics on top of `Cell4` and `GCFront` were also repaired, fixing the aforementioned collection inefficiencies and leading to *light leaks* values comparable to the rest of the cells. In summary, at the beginning of *Phase II*, *light leaks* were approximately $\sim 5\%$ between `TG` cells, with the exception of $\ell\ell_{23} \sim 7.5\%$. The *light leaks* between `TG` and `GC` stayed at $\sim 15\%$ for `GCFront` and `GCBack`, and for `GCD19` and `GCIN20` it slightly increased to $\sim 6\%$ and $\sim 4\%$, respectively. All these numbers can be graphically observed in Sec. 6.3.1. They are also represented for the specific date of 24.IV.2018 in Fig. 5.21.

All these changes also induced a revamp of the $p \to h$ value for *Phase II*. The final configuration of h values of the `LhM` is displayed in Fig. 5.19. Under this model, the light leak calculation does not force an overcompensation of the h to account for smaller leaks at *bottom* and *middle*. With `HpM`, low p implied small leaks for all positions including *bottom*, and thus it had to be raised to match *light leaks* in data. With `LhM`, low h still implies relatively larger leaks for *bottom* and thus implies an overall decrease.

Fig. 5.24 displays the asymmetry $\mathcal{A}^z_{mid}$ for different cells and heights for *Phase II* data and simulations after implementing the `LhM`. Contrarily to what has been observed previously in Fig. 5.20, agreement is specially reached for *top* positions, where now the simulation does not overestimate the *light leaks*, and more generally through all positions except from *bottom*. This is due to an additional h_{bottom} value that has not been mentioned before, and that covers possible *light leaks* through the bottom plate reflective sandwich. This parameter covers the entire reflective surface beneath the `TG` and `GC` cells, and can be either set to 0 or to 1. Any number in between does not have a physical meaning due to the impossibility to have such sandwich anything but completely empty or completely full. The tuning of h_{bottom} has been performed using external calibration data [140] and responds to the best agreement possible using this method.

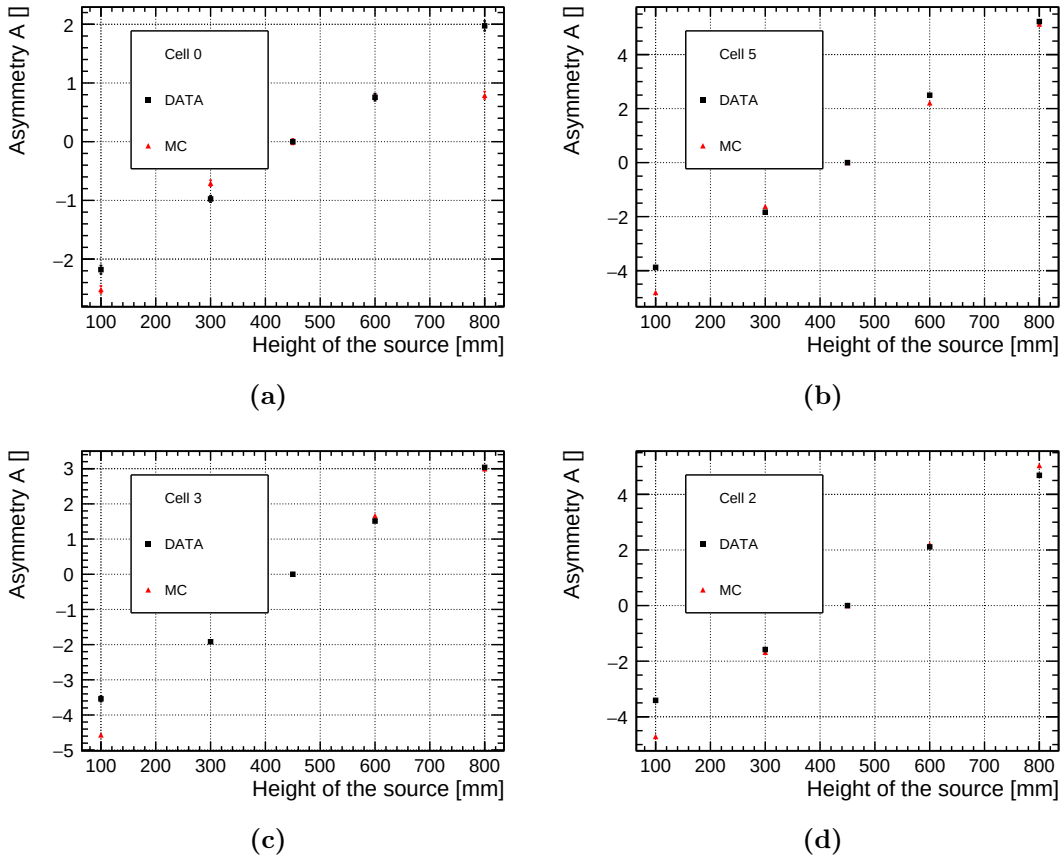

Figure 5.24: Asymmetry $\mathcal{A}^z_{mid}$ for different cells after tuning of *light leaks* using `HpM`. Numbers obtained from ^{54}Mn deployments at different heights for both data and simulation. Data extracted from calibration runs on 16.IV.2018.

Overall the implementation of `LhM` has been highly successful yielding a subpercent level of discrepancies between data and simulations for all positions with the exception of a $\sim 1\%$ level discrepancy for *bottom*. Currently this model is used to compare *light leaks* between data and simulations and allows to predict with great accuracy the response of each individual volume composing the detector to the percent level.

5.3.4 Absolute Light Yield of `TG` and `GC`

As discussed in Sec. 3.4, the LY of the liquid corresponds to the nominal amount of scintillation light produced per unit of energy deposited in it and varies for the two different liquids on the `TG` and `GC` respectively. The calibration of such parameter in the simulations has been done as the last step of the tuning for both *Phase I* and *Phase II*, after all the other optical factors have been addressed. Its implementation in the code comes directly as an integer number in the configuration files reflecting the amount of individual photon particles that are created per unit of energy deposited by an ionizing particle. This simple approach alleviates the simulation from an excessive amount of calculations by predetermining the total amount of light that will be generated per ionizing track. Therefore, changing the LY in the code only determines the normalization

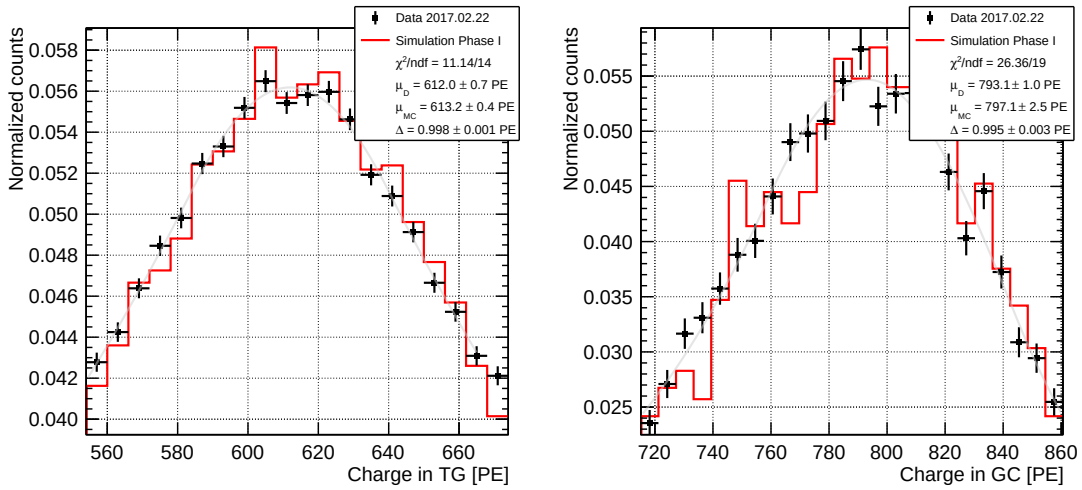

(a) **(b)**

Figure 5.25: Detector response to gamma emission from AmBe neutrons captured in hydrogen. Collected charge in (a) `TG` volume, (b) `GC` volume. AmBe has been placed at *middle* in `Cell6`, and *anti-Compton cut* described in Sec. 6.1.1 has been applied to the collected charge spectra.

of the simulated response and does not affect the propagation of light through the liquid.

The chosen *modus operandi* to tune the LY is by comparing the response in data and simulation to a distinctive and clean mono energetic gamma signal. From this comparison, a relative correction can be extracted to be applied into the simulation of the `LS` in **Stereo**. This process is done for both `LS` in `TG` and `GC`. The signal chosen to tune the LY comes from the gamma emission after the n-capture in hydrogen, with $E_\gamma \sim 2.22\,\text{MeV}$. The main advantage of this emission over other like the one from ^{54}Mn is that its energy is closer to the average positron energy of the IBD signal. Moreover, the effect of quenching in this range of energies is low. The neutron emitter used to generate n-captures is the AmBe source. For both data and simulation, the source has been deployed at *middle* position in the different cells.

The process of tuning starts with the distribution of collected charge in the full volume, either `TG` or `GC`. By doing this, the response of the `LS` is maximized and any bias from the collection efficiency of individual cells is minimized. To ensure events with energy deposition in the desired volume, a type of *anti-Compton cut* is applied. This cut is described in detail in Sec. 6.1.1, and its specific application on AmBe signal is discussed in Sec. 7.1.1. By comparing the absolute positioning of the 2.22 MeV for data and simulation, an estimation of LY can be performed. The discrepancy between both signals can be factored out and applied directly to the LY parametrization of the simulation. After two iterations, the discrepancy is below 0.5% as can be observed in Fig. 5.25. There are other parameters that can affect the global response of the detector to this peak, like the quantum efficiency of the PMTs or the quenching of light. For this reason, the tuning of the LY is performed after all the other corrections, effectively working as a final scaling.

Table 5.6: Light Yields used for *Phase I* and *Phase II* simulation in STEREO, together with experimental values obtained in lab measurements [131].

Component	Simulation [ph/MeV]	Lab data [ph/MeV]
Gd-Loaded LS	5400	6500
Gd-Unloaded LS	7000	8400
Ratio	1.30	1.30 ± 0.12

Although the main components of both liquids are basically identical, the loading of gadolinium in the TG affects greatly the overall emission of scintillation light. This is due to the overlap of the absorption bands of the Gd-complex and the main fluor PPO. While the latter tends to re-emit scintillation light, the former usually dissipates energy in other non-fluorescent ways. This effectively reduces the LY of TG by a 23% with respect to the GC, value that has been found in lab measurements at the MPIK [131]. The results of these studies are compared to simulation values of the LY for TG and GC in Tab.5.6. It can be seen there that the values for the simulation are slightly below the observed numbers in lab data, for both TG and GC. The cause for this could be the more efficient and practical light coupling achieved with the small sample used in the lab measurements. However, any global effect between simulation and lab data is weighted out in the relative LY between GC and TG. For this ratio, both results are in perfect agreement with each other, portraying a good understanding of the signal in both volumes.

5.4 Neutron Diffusion and Capture

Simulation of hadronic physics is a complicated topic that has been worked out extensively in the recent years in many experiments. QCD is the underlying theory defining the interactions between quarks and gluons, fundamental particles that constitute the main ingredient of hadronic interactions. However, applying it to neutrons and other hadrons is much more difficult than applying QED in electromagnetic interactions. Generally, contributions beyond leading order in perturbation theory to QCD interactions imply complex calculations that eventually break down in the infrared limit [37]. This means that low-energy phenomenology must rely on non-perturbative methods and mainly on numerical lattice simulations that require extreme computational power [38]. For this reason, observable magnitudes like cross-sections and branching ratios, are constantly being readjusted to account for the highest precision calculations available.

It is not the aim of this chapter to give an extensive description of QCD, instead this reference is left to the reader [39]. For STEREO, the only relevant hadronic processes are the ones involving low energy ($< 10\,\text{MeV}$) neutrons and the multiple atomic nuclei in the detector. However, still no theoretical model can work well for neutron interactions with all isotopes and therefore a data-driven approach is necessary. The framework provided by Geant4 allows for a flexible configuration of models registered at custom energy validity ranges. Neutron diffusion and transport data is loaded from the high precision QGSP_BIC_HP libraries [153], based on ENDF-VII data base [149]. From there, simulations can extract information about cross-sections, angular distribution, covariances and multiplicities of neutron interactions with nuclides. These interactions

include elastic scattering and neutron capture, specially relevant for **STEREO**.

It has been discussed previously in Sec. 3.1.1 that IBD processes are characterized by a correlated signal between *prompt* and *delayed* events. The correlation time Δt between both is characterized mainly by the thermalization and capture time of the neutron inside the liquid, and thus an accurate recreation of these processes is crucial to simulate the correlation signal. The way a neutron loses its energy in the `LS` is described in Sec. 3.4.2. Once its kinetic energy is low enough $\lesssim 1\,\text{eV}$, to match the vibrational motion of the target nuclei and molecules, thermal corrections to the cross-section of the different processes need to be included. High precision thermalization within `QGSP_BIC_HP` is not included by default. As part of the simulation tuning performed during this thesis, the process of thermal scattering has been tested for simulated neutrons. I has been included for energies $< 4\,\text{eV}$, overwriting in that range the standard elastic scattering data set. Vibrational states for molecules and atoms, besides the inherent correlation on temperature of the material, depend on the size, mass and bounding energies involved in these structures. For this reason, data for thermal scattering is given from dedicated experiments or solid state physics models for very specific materials and temperatures. The `LS` in **STEREO** has been designed and produced solely for this experiment and there is no data that match neutron transport at thermal energies for such specific organic composition. However, a good approximation can be done by choosing data from a material with similar molecular structure. For **STEREO**, a good substitute for a LAB-based scintillator to thermalize neutrons, that is also available in `Geant4`, is polyethylene (CH_2). Both LAB and CH_2 also share a similar hydrogen-to-carbon ratio ~ 2. Fig. 5.26 displays a comparison between AmBe calibration data and simulations of correlation time Δt. In Fig. 5.26(a), standard elastic scattering is used for low energy neutrons, while in Fig. 5.26(b) the thermal corrections described above have been included. It can be observed that the latter gives a much better agreement between data and simulation, specially for the first nanoseconds where the thermalization of neutrons dominates over the neutron capture time.

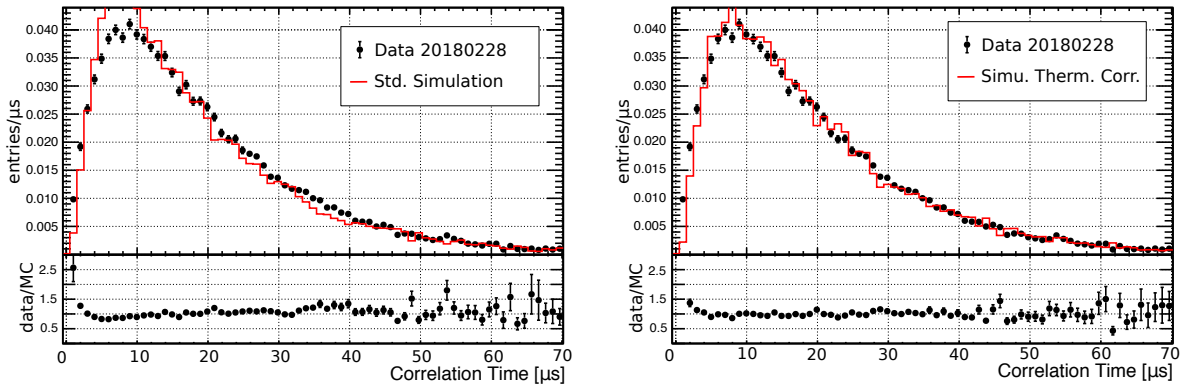

(a) **(b)**

Figure 5.26: Correlation time comparison between AmBe calibration data and simulation, both for *Phase II*. (a) Simulation uses standard libraries for low energy elastic scattering between neutron and nuclei. (b) Simulation uses specific thermal scattering libraries for neutrons through CH_2. Plots created by ALMAZAN [142].

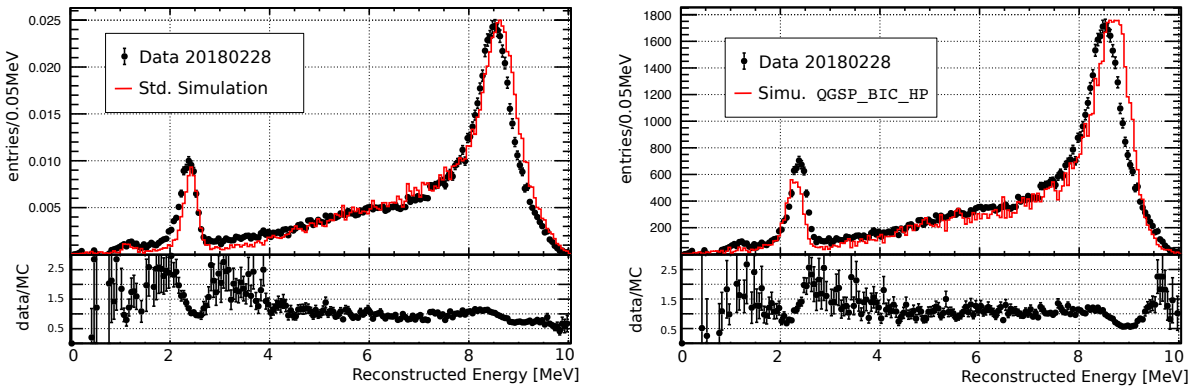

(a) **(b)**

Figure 5.27: Energy spectrum of *delayed* events from AmBe for data and simulation. (a) Simulation with gamma cascade from neutron capture in gadolinium customized for **STEREO**. (b) Simulation with gamma cascade from neutron capture in gadolinium obtained from `QGSP_BIC_HP` libraries. Plots provided by ALMAZAN [142].

It has been discussed in Sec. 3.4.2 that at low energies, both thermal scattering and radiative capture share the interaction cross-section of neutrons. Thus, also an accurate description of the neutron capture and a good depiction of the possible final states after the capture are necessary. A final state constitutes a stable daughter isotope and a set of photon emissions. The photon emission is characterized by the energy, momentum and multiplicity of said photons. The neutron capture process is generally covered for most isotopes within `QGSP_BIC_HP` libraries. This includes high precision final states for captures in hydrogen, carbon and iron, among many others. It also includes a complete set of data driven libraries for gadolinium isotopes. However, the data base of gamma cascades from gadolinium isotopes contains a set of multiple, and often incomplete, set of correlated emissions mixed with a complex photon continuum [152]. In segmented detectors like **STEREO** where selection cuts affect multiple volumes, a specially accurate knowledge on the topology of the cascade is mandatory to match simulations to data. For this reason, despite the good agreement obtained with simulations including `QGSP_BIC_HP` libraries, a dedicated gamma cascade has been computed for gadolinium isotopes. In Fig. 5.27 the energy spectrum of AmBe *delayed* events is depicted. Fig. 5.27(a) shows the result using the standard cascade from data driven libraries. Fig. 5.27(b) shows instead the dedicated gamma cascade for **STEREO**. The best agreement is observed for the latter case, where the full-energy peak from the captures in gadolinium is better modeled. The continuum between the gadolinium and hydrogen capture peaks, however, is better represented when using the `QGSP_BIC_HP` libraries. For *Phase I* and *Phase II* simulation code, only the customized model has been used.

5.5 Quantum Efficiency of the PMTs

Quantum efficiency (QE), in the context of photomultiplier tubes, corresponds to the fraction of scintillation photons that are converted into electrons by the photocathode

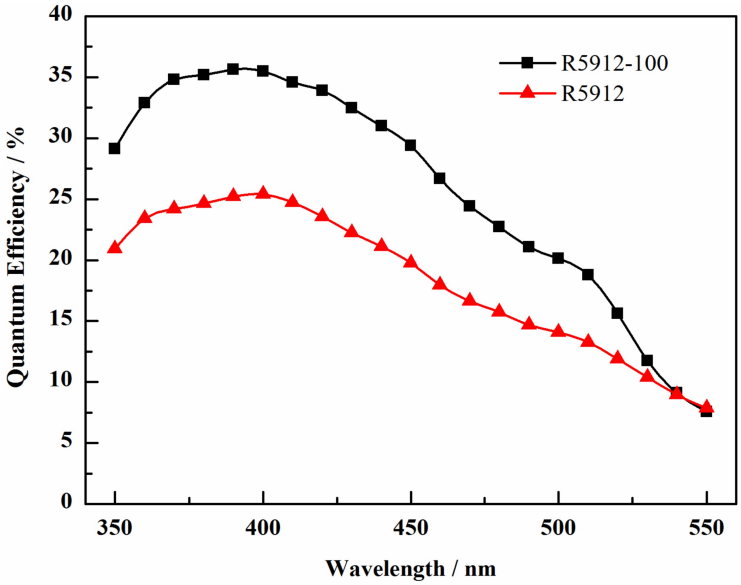

Figure 5.28: QE dependency on scintillation light wavelength for R5912-100 SBA and R5912 Hamamatsu PMT. [163]

of a given PMT. The QE directly impacts the total response of the detector, being proportional to the final signal obtained. As QE increases, so does the amount of scintillation light detected.

In Sec. 3.2.3 it has been discussed that the PMTs in **STEREO** are R5912-100 Hamamatsu models with SBA photocathode. The SBA provides an enhanced QE(λ = 430nm) $\sim$ 35%. In contrast, regular bialkali photocathodes usually reach a maximum of about $\sim$ 25% for same wavelengths. In Fig. 5.28, the behavior of QE(λ) is portrayed for both regular and SBA R5912 Hamamatsu PMTs. The definition of QE(λ) in the simulation of **STEREO** was initially based on the PMT libraries from the Double Chooz experiment. This implementation used the same geometrical and wavelength dependence of QE(r, λ) of the Hamamatsu PMT model R7081, but shifted by a constant factor to ensure SBA peak performance QE($r = 0, \lambda = 430$nm) $\sim$ 35% at the center of the PMT.

Explicit measurements from WANG et al. [163], however, gave a more complete and accurate approach to **STEREO** simulation. In their studies, measurements of the R5912-100 SBA cathode response to illumination with monocromatic laser of 3 mm diameter were made. The whole wavelength acceptance range of the center of the photocathode was tested, resulting in a full distribution QE(λ). In addition a 2-dimensional mapping of the surface (x, y) was also performed, providing also a distribution QE(x, y), Fig. 5.29. In this studies, a fair uniformity of values was exhibit, with maximum/minimum performances of 37.6/32% with an average of 34.6%.

After having permission to freely use data from [163], the mentioned distributions of QE have been introduced in the simulation of **STEREO**, substituting the old ones. This update carried with it two important changes. Firstly, the QE peak has increased by a 10% factor with respect to the previous value. Secondly, the spatial distribution of QE has been updated to fit accurately the size of the 8-inch PMT model of **STEREO**.

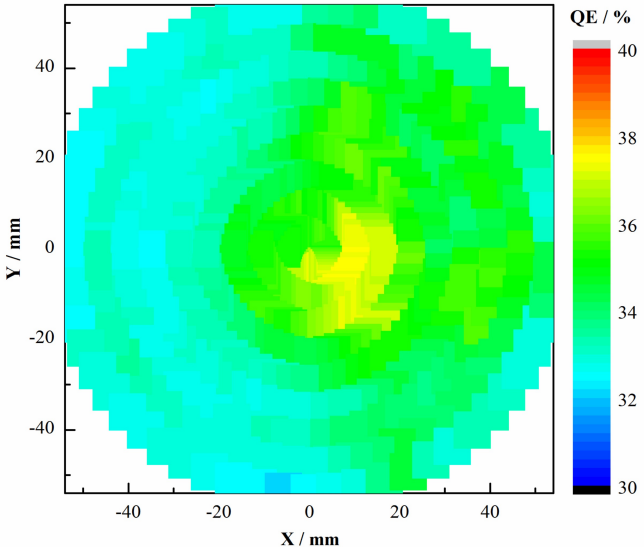

Figure 5.29: Geometrical dependence of the QE of a R5912-100 SBA Hamamatsu PMT. (x, y) axis represent the two longitudinal dimensions of the PMT conforming the main detection surface. [163]

In principle, an absolute change in QE would only change the absolute response of the detector, which in any case can be tuned by means of the LY described Sec. 5.3.4. However, a change in the geometry of the photon-PE conversions has an effect on the topology of events conforming the response of the detector. Such effect can be observed when comparing results of ^{54}Mn deployment at `Cell1`, `Cell4` and `Cell6` in Fig. 5.30, where the top-bottom asymmetry $\mathcal{A}_{bot}^{top}$ is plotted for simulations with and without corrected QE and data. The result is that tweaked QE drives the inhomogeneites closer to the values observed in the real experiment, and hence prove optimal for the data and simulation comparison.

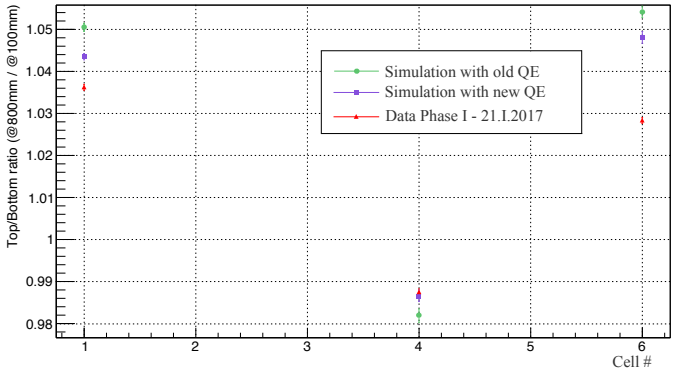

Figure 5.30: Asymmetry $\mathcal{A}_{bot}^{top}$ for ^{54}Mn deployment in `Cell1`, `Cell4` and `Cell6` for *Phase I* data and simulations with different QE for the PMTs.

5.6 Summary

Throughout this chapter the details of the `Geant4` simulation framework in **STEREO** have been discussed. The outline of the simulation process has been detailed and how the specific properties of the liquid are implemented to match simulated response with real data. The hydrogen fraction calculated from the implementation of the liquid in the simulation was found to be compatible with the measured value, while the proton number needs a correction factor of $c = 0.983 \pm 0.010$.

The effect of the quantum yield of the fluors in the simulated response of the detector was also tested for **STEREO**. In Sec. 5.1.2 it was shown how the effect of a reduction of ϕ_{PPO} is less impactful than an homologous reduction in ϕ_{bMSB}. It was also seen a stable response within the uncertainty range from the nominal value for laboratory measurements. These tests concluded that using the lab measured values [130] of the quantum yields for PPO and bis-MSB was a safe assumption for the simulation in **STEREO**.

In Sec. 5.2 the implementation of the calibration systems and sources in the simulation of **STEREO** was described. By using simulated internal calibration data a fine tuning of the simulated detector response was performed in Sec. 5.1. The attenuation length of the `LS` in simulation was tuned to yield the best agreement with data by comparing the response of the detector for internal calibration with a ^{54}Mn source. The results are fully compatible to the measured attenuation length in laboratory conditions of $\Lambda^{TG}_{\text{total}} = 6.9\,\text{m}$ showing also time stability between periods. This results were extrapolated also for the `LS` in the `GC` volume. A ^{54}Mn source was also used to fine tune the *light leaks* between cells for *Phase I* and *Phase II*, by means of two models that account for the intrusion of liquid within the separation walls. The *Liquid Height h Model* was observed to yield better agreement with data and thus to describe more precisely the loss of reflectance of the walls. The AmBe source was used to tune the light yield of the `LS` on `TG` and `GC`. The comparison with data and simulation allowed a re-scaling of the simulated response of the PMTs in both volumes by comparing it to the calibration data. The results for *Phase II* show an agreement with laboratory data for the relative values of the light yields of both liquids.

In Sec. 5.4, the implementation of the neutron transport and diffusion through the simulated `LS` was introduced. It was shown that thermal corrections to the low energy elastic scattering processes yielded a better agreement of the correlated time between *prompt* and *delay* events. It was also discussed the gamma cascade used as a final state after the neutron capture by gadolinium nuclei. A better agreement was obtained by using a customized cascade than using ENDF-VII libraries.

Finally, in Sec. 5.5 the implementation of an accurate quantum efficiency for the PMTs in the simulation was shown. It displayed an improved response of the detector in terms of vertical asymmetry while giving an overall increased signal.

"The real meaning of enlightenment is to gaze with undimmed eyes on all darkness"

Kazantzakis

Chapter 6

Analysis and Monitoring of Detector Response

In Sec. 3.4.3 it has been described how different particles deposit their energy in the LS. The scintillation light produced as result gets read-out by the PMTs at the top of the detector and transformed into charge units. The relationship between the initial energy deposited and the charge observed defines the energy scale of the detector. The energy scale plays a crucial role on the understanding of the detector response in **Stereo** and its formalism will be described throughout the present chapter. The calibration coefficients (cc) of the different cells constituting **Stereo** are the main ingredient of the energy reconstruction algorithm. The strategy developed along the present thesis for their calculation from calibration data is defined in Sec. 6.1. The formalism of the energy reconstruction and how it is uses both cc and *light leaks* to iteratively tune itself is explained in Sec. 6.2. Finally, throughout Sec. 6.3 the stability of the detector response and the energy reconstruction will be displayed for *Phase I* and *Phase II* in terms of the evolution of several observables like $\mathtt{cc}_i$ or $\mathcal{A}^{top}_{mid}$.

6.1 Calculation of Calibration Coefficients

In **Stereo**, the energy reconstruction algorithm is FED mainly with two components. One of them are the *light leaks* between cells, $\ell\ell_{ij}$, already described in Sec. 5.3.3 by Eq. 5.12. The second ingredient needed for the energy reconstruction algorithm is the translation between charge and energy for each cell. These values, defined as the $\mathtt{cc}_i$ for each Cell$i$, are obtained periodically via weekly calibration runs. To calculate the $\mathtt{cc}_i$, the natural approach would be to access a well-defined energy emission, like the one from the ^{54}Mn source, and observe the correspondent response of the PMTs of a single cell. However, the energy containment is geometrically limited by the position where the source is deployed and its distance to the neighboring cells. In order to obtain a reliable representation of $\mathtt{cc}_i$ that is equivalent for all cells, and also between data and simulation, a Full-Energy Deposition (FED) requirement have been imposed to the deposited energy and associated charge of ^{54}Mn events. By doing this, collected charge only from events with well-defined energy depositions are selected to calculate $\mathtt{cc}_i$,

$$\mathtt{cc}_i = \frac{Q_i^{\mathtt{FED}}}{E_i^{\mathrm{dep}}} \,. \tag{6.1}$$

The way FED events are selected is by applying the so-called *anti-Compton cut*, described in detail in Sec. 6.1.1. The application of this cut is specially important to calibrate *intermediate cells*, where the most of the statistics are from non-FED events with the source deployed at the *source cells*.

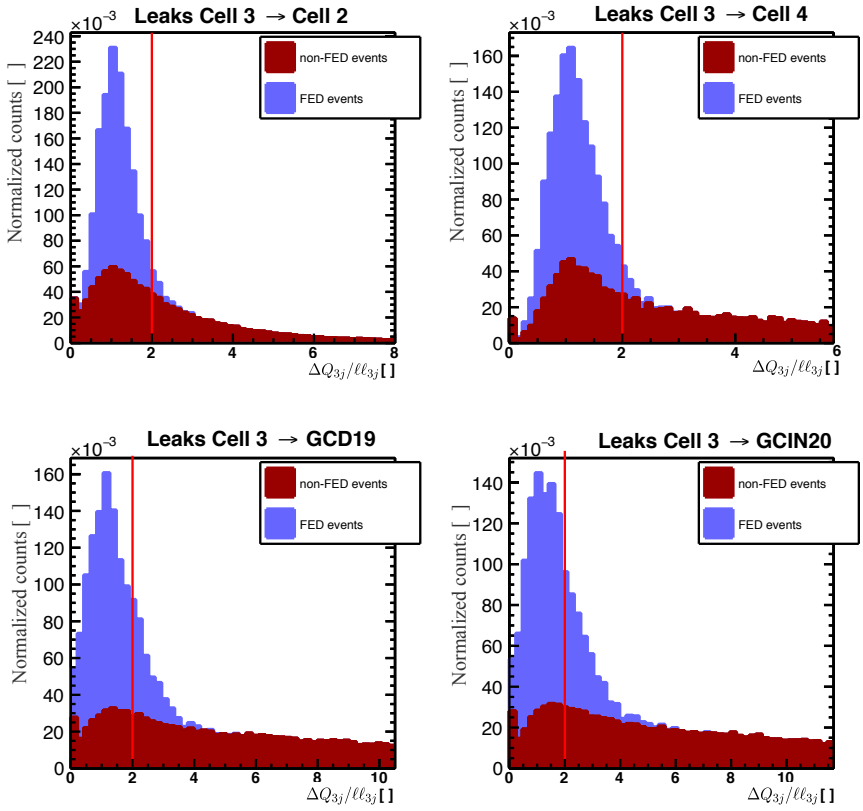

Figure 6.1: Representation of ΔQ_{ij} in terms of `Cell3` *light leaks*, in $k_{\ell\ell}$ units, towards its closest neighboring cells. `Cell3` is the only *intermediate cell* in *Phase II*. Two histograms drawn: blue for `FED` events; dark red for non-`FED` events. A line in red marks the optimal $k_{\ell\ell}$ for the cut in Eq. 6.3.

6.1.1 Anti-Compton Cut

To ensure a distribution highly populated with `FED` events, an *anti-Compton cut* is applied. This cut provides more definite peaks and in consequence allows a reliable determination of Q_i^{FED} from ^{54}Mn distributions. The cut also optimizes the rejection of non-`FED` events leading to deposited energies closer to the true E_i^{dep}. In order to characterize energy escapes from `Cell`i to the neighboring `Cell`j, the *anti-Compton cut* computes for each event the ratio ΔQ_{ij} of collected charges between them,

$$\Delta Q_{ij} = Q_i / Q_j \,, \tag{6.2}$$

in a similar fashion as for the calculation of $\ell\ell_{ij}$ in Eq. 5.12. However, Eq. 5.12 uses the fitted mean charge from true `FED` distributions to calculate average *light leaks*. In this case, Eq. 6.2 calculates the ratio of collected charges event by event, and then applies the cut on Eq. 6.2 as,

$$\text{if} \quad \forall j \neq i, \quad \Delta Q_{ij} \leq \ell\ell_{ij} \cdot k_{\ell\ell} \qquad \rightarrow \text{accept event}, \tag{6.3}$$

$$\text{else} \qquad \rightarrow \text{reject event}. \tag{6.4}$$

where the parameter $k_{\ell\ell}$ is a measure of the tightness of the cut. The right value

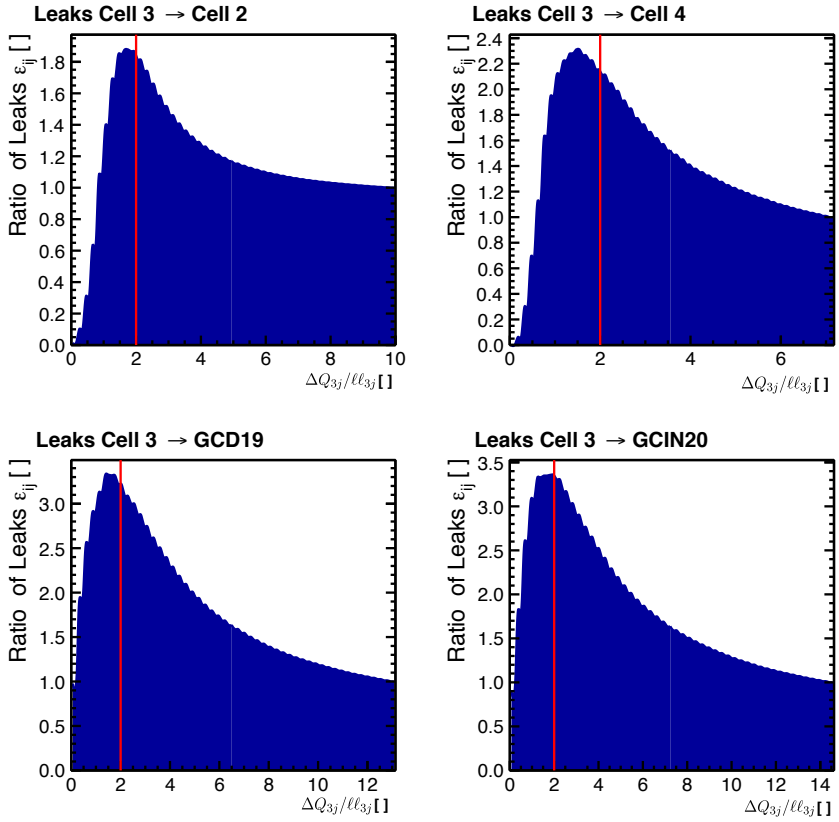

Figure 6.2: Representation of $\varepsilon_{ij}(k_{\ell\ell})$, Eq. 6.5, in terms of ΔQ_{ij} in $k_{\ell\ell}$ units, for `Cell3` *light leaks* towards its closest neighboring cells. As a red line, the optimal $k_{\ell\ell}$ is represented.

for $k_{\ell\ell}$ is not known a priori and has to be optimized. In Fig. 6.1, the simulated event distributions of $\Delta Q_{3j}/\ell\ell_{3j}$ towards the closest neighboring cells are displayed for `Cell3`, using ^{54}Mn deployments in `Cell4`. The blue distribution is for `FED` events and it displays the true *light leaks* between cells, also used in Sec. 5.3.3 to determine $\ell\ell_{ij}$. Indeed, the peak of this distribution is located at $\Delta Q_{ij} = \ell\ell_{ij}$. On the contrary, the red histograms portray how the rest of the events, the non-`FED` ones, are distributed. The latter show a more homogeneous and less sharpened behavior. This is because the non-`FED` histograms comprise gamma events that have been Compton-scattered outside of the cell carrying a continuum of energy. For this reason, at some point $\Delta Q_{ij} = \ell\ell_{ij} \cdot k_{\ell\ell}$ the distributions have to be cut, rejecting all remaining events with higher ΔQ_{ij}. A tentative cutting line at $k_{\ell\ell} = 2.0$ has been also drawn in Fig. 6.1, anticipating the result that will be discussed in the following paragraphs.

To calculate the appropriate $k_{\ell\ell}$, a new variable ε_{ij} that represents the ratio of leaks of `FED` and non-`FED` events between `Cell`i and `Cell`j has been created. This variable is built as a function of a continuous set of $k_{\ell\ell} \in [0, 15]$. For each value of $k_{\ell\ell}$, the function integrates the `FED`, $I_{\Delta Q}^{\text{FED}}$, and non-`FED` distributions, $I_{\Delta Q}^{\text{non-FED}}$, between $\Delta Q_{ij} \in [0, \ell\ell_{ij} \cdot k_{\ell\ell}]$. In other words, these integrals $I_{\Delta Q}$ represent how many events would be included if a cut on $\Delta Q_{ij} = \ell\ell_{ij} \cdot k_{\ell\ell}$ were to be performed. The function ε_{ij} is finally built as,

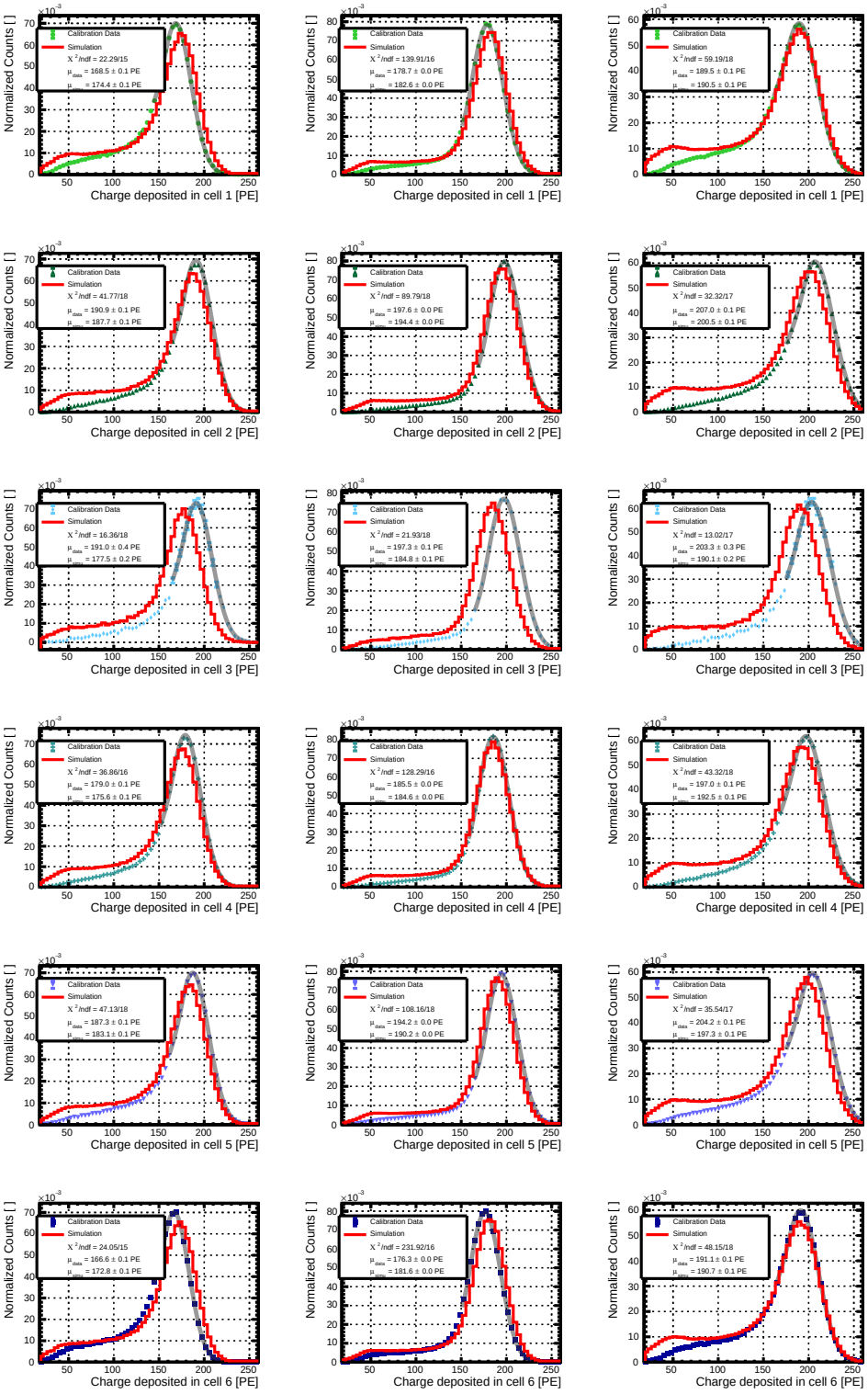

Figure 6.3: Collected charge distributions in different cells for calibration data and simulation of ^{54}Mn during *Phase II*. Distribution in `Cell3` uses ^{54}Mn source deployments in `Cell4`. Each column of plots represents a different height: left *bottom*, center *middle*, right *top*. All plots are represented after applying *anti-Compton cut* to their respective charge distribution.

$$\varepsilon_{ij}(k_{\ell\ell}) = \frac{I_{\Delta Q}^{\texttt{FED}}}{I_{\Delta Q}^{\text{non-}\texttt{FED}}} \,. \tag{6.5}$$

The representation of ε_{ij} of `Cell3` to its closest neighbors is depicted in Fig. 6.2, where a clear maximum can be spotted around $k_{\ell\ell} = 2.0$. Since $k_{\ell\ell}$ is defined as a multiple of $\ell\ell_{ij}$, it always adapts to the width and size of the overall *light leaks* from `Cell`i to `Cell`j. When inspecting every cell for `FED` and non-`FED` events, it can be found that in all cases they follow a similar profile, peaking at $k_{\ell\ell} \sim 2.0$. Thus, the optimal cut in ΔQ_{ij} between `Cell`i and `Cell`j is located at approximately twice the value of $\ell\ell_{ij}$, rejecting thus any event that fulfills,

$$\Delta Q_{ij} > 2 \cdot \ell\ell_{ij} \,. \tag{6.6}$$

The chosen value of $k_{\ell\ell}$ has been seen in Fig. 6.1 to be wide enough to cover most of the `FED` events. A more restrictive $k_{\ell\ell}$ could imply a biased selection of events with interaction vertices far from the border of the cell. This means that a certain fraction of Compton-scattered events has to be accepted as well.

The condition in Eq. 6.6 is applied both on data and simulations of ^{54}Mn, resulting in the peaked distributions seen in Fig. 6.3. These peaks are then fitted using a *GaussExp* function which is shown as a gray curve, from which the mean of the peak μ is read. Details on the *GaussExp* function and its parametrization can be found in App. B. Then, the charge $Q_i^{\texttt{FED}}$ and energy E_i^{dep} that define $\texttt{cc}_i$ in Eq. 6.1 are extracted as the averages over a specific range of events around the mean μ. This range is not symmetric, being essentially unbounded from the right side and limited to $\alpha\mu$ on the left side, with α being a certain *cutoff* parameter. The left side limit $\alpha\mu$ severs the contribution from remaining non-`FED` events into the $\texttt{cc}_i$, making it more stable to variations of the $\ell\ell_{ij}$ and *anti-Compton cut* that could cut events at the tail of the distribution. In Fig. 6.4 the impact of α on the $\texttt{cc}_i$ calculation is displayed. For values of $\alpha \gtrsim 0.75$, the low end of the peak is being cut, while the mean deposited energy remains approximately constant. This biases $\texttt{cc}_i$, leading to a rapid increase as α gets closer to the unity. For $\alpha < 0.75$, $\texttt{cc}_i$ starts a slow decrease that does not stabilize due to the continuous integration of events at the left-hand side of Fig. 6.3. The cutoff has been finally set to $\alpha = 0.75$, avoiding the rapidly evolving area in the vicinity of the main peak, but also not entering the high *light leaks* regime that is most sensitive to variations in the *anti-Compton cut*. In this region, the variability of $\texttt{cc}_i$ with respect to fluctuation in α is below the 0.5%.

Once the range of events is set, $Q_i^{\texttt{FED}}$ and E_i^{dep} can be obtained as the charge and energy averages of said ranges. Then, the $\texttt{cc}_i$ are calculated from Eq. 6.1. For calibration data, where no energy deposition distribution is available, E_i^{dep} from simulation is used. The process to calculate $\texttt{cc}_i$ developed along this thesis has been ran throughout both *Phase I* and *Phase II* for every ^{54}Mn calibration run, providing stable and coherent initial conditions for the energy reconstruction algorithm. The latter will be described in Sec. 6.2.

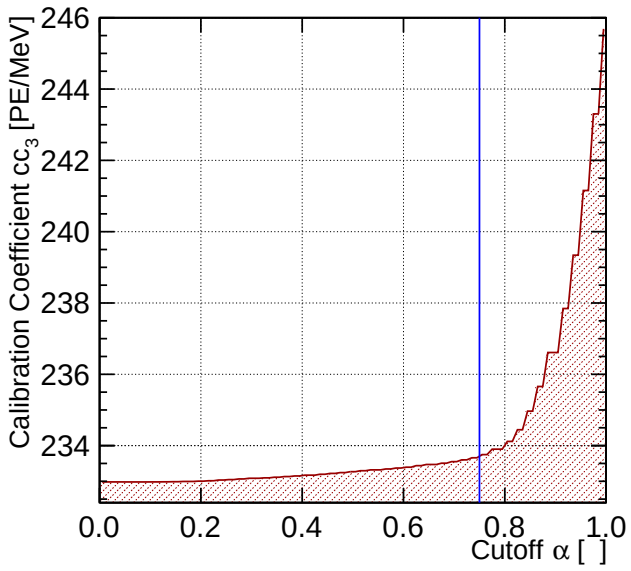

Figure 6.4: Stability of $\texttt{cc}_3$ in terms of the cutoff parameter α. The chosen cutoff $\alpha = 0.75$ is represented as a blue line.

6.2 Energy Reconstruction

The energy reconstruction has been developed by Blanchet and the team at CEA [146]. It has been anticipated in previous paragraphs that the energy reconstruction algorithm in **Stereo** requires a set of coefficients `cc` that translates from collected charge to deposited energy and that have been calculated in the previous section and now can be used to reconstruct the energy response of the detector. Together with the `cc`, also the *light leaks* between cells need to be introduced to the algorithm to account to correct for light collection effects. These corrections are especially relevant because time variations of the *light leaks* between cells, discussed in Sec. 6.3.1, are difficult to describe with high accuracy in a simulation with static ones.

Firstly, for any energy deposition in the detector the vertex cell needs to be found. This is done by computing the charge barycenter in the (x,y) plane. Weighting the positions of each of the PMTs by the charge they have collected gives the most probable position where the interaction has occurred. The vertex cell is the one that contains the barycenter. For an energy deposition E_i in the vertex `Cell`i, the charge collected in a neighboring `Cell`j is

$$Q_j = E_i \cdot \texttt{cc}_i \cdot \ell\ell_{ij} \,. \tag{6.7}$$

The description of any energy deposition distribution among the 10 detector cells can be generalized to,

$$Q_j = \sum_{i=0}^{9} E_i \mathcal{M}_{ij} \,, \tag{6.8}$$

where the matrix notation has been introduced with $M_{ij} \doteq \ell\ell_{ij} \cdot \texttt{cc}_i$. By definition

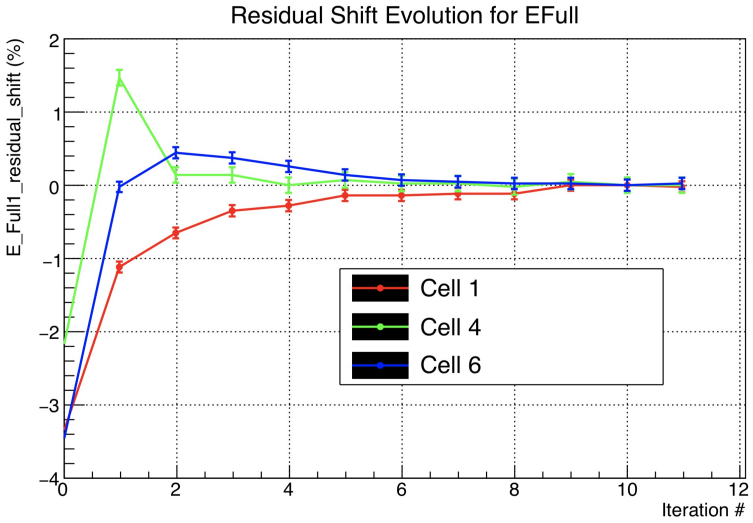

Figure 6.5: Residual δE^{full} on the energy reconstruction after certain iterations of fine tuning of $\texttt{cc}_i$ and $\ell\ell_{ij}$. On the second iteration residual is already $< 0.5\%$ [146].

$\ell\ell_{ii} = 1$. The i index runs on all the optical volumes of the detector: `GCFront`, from `Cell1` to `Cell6`, `GCBack`, `GCD19` and `GCIN20`. Then by inverting the matrix $\mathcal{M}$, the vector of deposited energies can be reconstructed from the vector of detected charges.

6.2.1 Fine Tuning of Energy Reconstruction

An important caveat of the procedure described in the previous section lies in the fact that simulation and data may not have identical energy depositions. This is visible, especially at *top* and *bottom*, when comparing the continuum contribution below the `FED` peaks. To address this issue and to correct for minor discrepancies on the $\ell\ell_{ij}$, an extended approach that propagates iteratively the *anti-Compton cut* from data to simulation has been developed. The main purpose is to define the same equivalent acceptance of `FED` events in both data and simulation, which means to include the same equivalent deposited energy.

After the first iteration represented in Eq. 6.8, the energy reconstruction in **Stereo** is fine tuned iteratively correcting $\texttt{cc}_i$ and $\ell\ell_{ij}$ in the process. For this purpose, the true energy distribution of `FED` events in `Cell`i from ^{54}Mn simulations is convoluted with the simulated detector response in reconstructed energy units. A gaussian fit of this convoluted distribution yields to the mean true energy deposited E_i^{true}. A gaussian fit is also applied to the gamma peak of the reconstructed energy spectra of ^{54}Mn, and from there the mean reconstructed energy E_i^{rec} is extracted. The discrepancy of these two values can be computed then as,

$$\delta E_i = \frac{E_i^{\text{rec}} - E_i^{\text{true}}}{E_i^{\text{true}}} \,. \tag{6.9}$$

This value represents how much the reconstruction of the energy differs from simulated true energy deposition. Such discrepancy can be translated as a correction to $\texttt{cc}_i$,

computed as

$$\delta \mathtt{cc}_i = \delta E_i \cdot \mathtt{cc}_i \,, \tag{6.10}$$

with the new $\mathtt{cc}_i$ being,

$$\mathtt{cc}_i + \delta \mathtt{cc}_i \rightarrow \mathtt{cc}_i \,. \tag{6.11}$$

Then, the energy reconstruction is checked again with Eq. 6.9 by using the tuned $\mathtt{cc}_i$. This process is repeated a few times until variations are of the order of $\sim 0.1\%$ or below. After the tuning of $\mathtt{cc}_i$, the response of the whole detector is tested with true information from simulation. In the same manner as for `FED` events in `Cell`i, now the `FED` event distribution in `TG` and `GC` is compared to the reconstructed energy spectrum. Any discrepancy observed,

$$\delta E^{\text{full}} = \frac{E^{\text{full}}_{rec} - E^{\text{full}}_{true}}{E^{\text{full}}_{true}} \,, \tag{6.12}$$

is attributed to a mismatch on the $\ell\ell_{ij}$ towards the four closest neighboring cells of `Cell`i. An identical correction is applied then to all four $\ell\ell_{ij}$ in the following way,

$$\delta \ell\ell_{ij} = \delta E^{\text{full}} \cdot \ell\ell_{ij} \,. \tag{6.13}$$

After these corrections are applied, the tuning of $\mathtt{cc}_i$ is re-initiated leading to an additional correction of $\ell\ell_{ij}$, if necessary. This whole process converges after a few iterations, as displayed by Fig. 6.5. At the end, the final set of $\mathtt{cc}_i$ and $\ell\ell_{ij}$ are fully coherent between data and simulation. The same reconstructed energy distributions are found and the remaining differences provide the scale of the systematic uncertainties of the method. As an example of the final energy reconstruction in **Stereo**, the spectrum of the ^{54}Mn source is depicted in Fig. 6.6.

Based on the 41 calibration runs taken during the *Phase I* of **Stereo**, the residual relative difference between δE^{full} is centered at 0 with a standard deviation of 0.2% for `TG` cells and 0.5% for `GC` cells. Analogous results are obtained for *Phase II*.

6.2.2 Uncertainties of Energy Scale

All sources of systematic uncertainties affecting the energy scale in **Stereo** are listed in Tab. 6.1. The first contribution comes from the computation of E^{true}, described in Sec. 6.2.1, and the uncertainties related to it. The second contribution is defined by the fluctuations of the ^{54}Mn anchor point over time, observed to be $\sim 0.3\%$ in Fig. 6.7(a). Fluctuations from the calculation of $\mathtt{cc}_i$ are included in this uncertainty.

The third contribution in Tab6.1 is extracted from the sub-percent level time evolution of the energy reconstruction, displayed in Fig. 6.11. This evolution is considered common for all the detector and thus is taken as a completely correlated uncertainty between cells. Finally, a last uncertainty is taken into account to cover the overall data to simulation disagreement, treated as uncorrelated cell-to-cell uncertainty. It is represented in Fig. 6.7(b), via the reconstruction of spallation neutron captures in hydrogen.

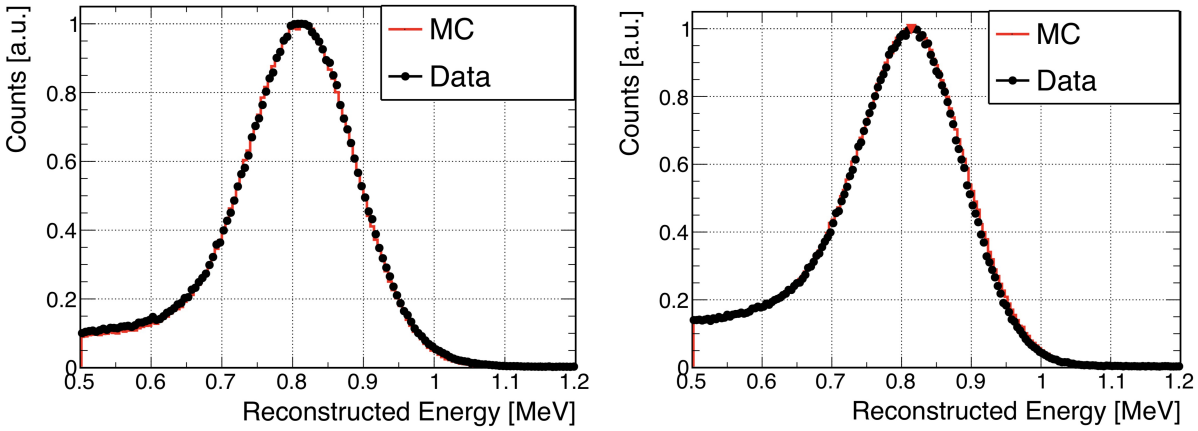

(a) (b)

Figure 6.6: Distribution of reconstructed energies after fine-tuning of the `cc` for a ^{54}Mn source (a) at *middle* of `Cell6`. (b) Averaged distribution for reconstructed energy at five positions, *top*, *mid-top*, *middle*, *mid-bottom* and *bottom* [146].

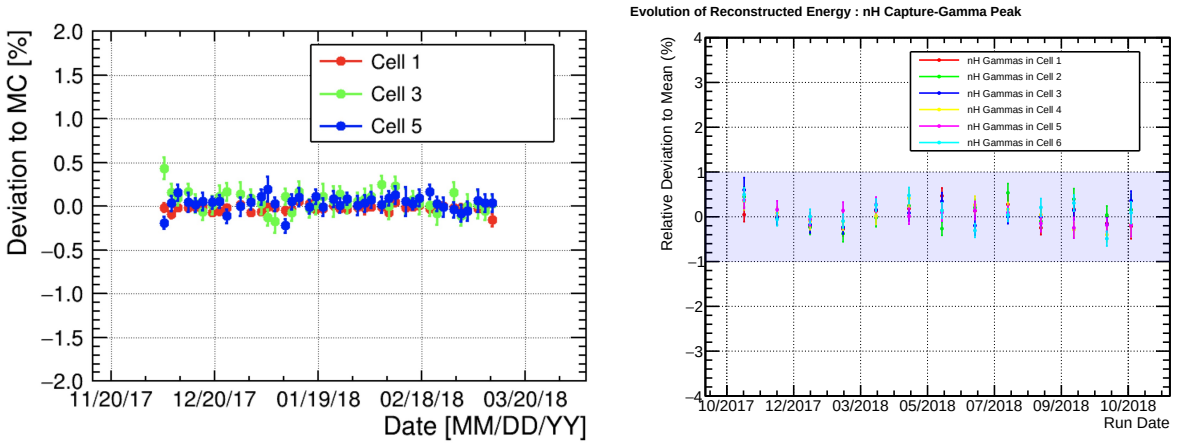

(a) (b)

Figure 6.7: Representation of systematic uncertainties on the energy scale of **Stereo** regarding data to simulation deviation for (a) ^{54}Mn peak anchoring after fine tuning; and (b) gamma emission peak from n-capture in hydrogen. [146].

6.3 Monitoring of the Response

6.3.1 Light Leaks

The plots displayed in Fig. 6.8 show the time evolution of $\ell\ell_{ij}$ for some of the cells in **Stereo**. The left side of each one of the plots represents the timeline of *Phase I*, followed by the reactor maintenance hiatus, and then *Phase II*. At the beginning of the *Phase I* timeline, the incident described in Sec. 5.3.3 where the glue of the separation walls lost its tightness can be appreciated. The filling of the interior of the walls with `LS` provoked a rapid increase of the *light leaks* between cells. As it has also been explained in Sec. 5.3.3, the mechanical defect in the acrylic buffer of `GCFront` and `Cell4` provoked

Table 6.1: List of uncertainties tied to the energy reconstruction in **STEREO**. They are divided into cell-to-cell fully correlated and fully uncorrelated.

source	cell-to-cell correlated	cell-to-cell uncorrelated
E^{true}	-	0.2%
^{54}Mn Anchor	-	0.3%
Stability	0.4%	-
Data/Simu	-	1.0%
Total	0.4 %	1.1%

a leak of the n-dodecane coupling the PMTs with these cells, reducing their light collection as a consequence. This can be clearly seen on the higher *light leaks* in Fig. 6.8(a) and Fig. 6.8(e) in comparison with other cells, which reach the $> 30\%$ value. Other affected cells with stable acrylic buffer experiment *light leaks* of the order of $\sim 13\%$. By using the correction in Eq. 5.13, one can find that the exceptionally high *light leaks* are explained by the leak in the acrylic buffer.

The separation walls between `TG` cells were fixed during the maintenance time between *Phase I* and *Phase II*, together with the acrylics on top of `Cell4` and `GCFront`. However, the walls between `TG` and `GC` could not be analogously repaired. Thus, for *Phase II* the increased *light leaks* between `Cell6` and `GCBack` remain identical at $\sim 13\%$, as seen in Fig. 6.8(g) and Fig. 6.8(h), while most of *light leaks* between `TG` cells go down to nominal values around 5%. In case of the separation wall between `Cell1` and `GCFront`, in Fig. 6.8(b) and Fig. 6.8(a), respectively, due to the aforementioned fixes on the acrylic, the *light leaks* went down from $\ell\ell_{10} \sim 35\%$ to $\ell\ell_{10} \sim 13\% \sim \ell\ell_{67}$. The *light leaks* between any `TG` cell and `GCIN20` and `GCD19` also remain at a higher than nominal value of $\sim 5\%$, seen in Fig. 6.8(i) and Fig. 6.8(j).

Throughout *Phase II*, a continuous increase of $\ell\ell_{34}$ and $\ell\ell_{43}$ is observed in Fig. 6.8(d) and Fig. 6.8(e). This is explained by a steady but continuous leak of `LS` inside the wall, as for *Phase I*. Such effect is also seen on the correlated increase of $\mathcal{A}_{mid}^{top}$ and $\mathcal{A}_{bot}^{mid}$, shown in Sec. 6.3.2.

6.3.2 Vertical Asymmetry

The vertical asymmetries $\mathcal{A}_{mid}^{top}$ and $\mathcal{A}_{bot}^{mid}$ have already been defined in Sec. 5.3.1. They represent the ratio between detector responses for events happening at two different heights within the same cell. These asymmetries are expected due to the differences in light collection depending on the distance between the production vertex and the PMTs. These asymmetries are monitored through time to observe the stability of the response. They show a correlation with the evolution of *light leaks* in Sec. 6.3.1 for both $\mathcal{A}_{mid}^{top}$, in Fig. 6.9(a), and $\mathcal{A}_{bot}^{mid}$, in Fig. 6.9(b). As discussed in Sec. 5.3.3, this could be explained by the gradual leakage of `LS` into the the separation wall, from bottom to top. For `Cell1` and `Cell6` there is no major evolution for neither of both asymmetries, with an exception on the first dates where some evolution of *light leaks* towards `GCIN20` is observed. For `Cell2` and `Cell5`, besides a small increase at early dates due to an increase of *light leaks* towards `GCIN20`, a stable behavior can be observed. On the contrary, `Cell3`

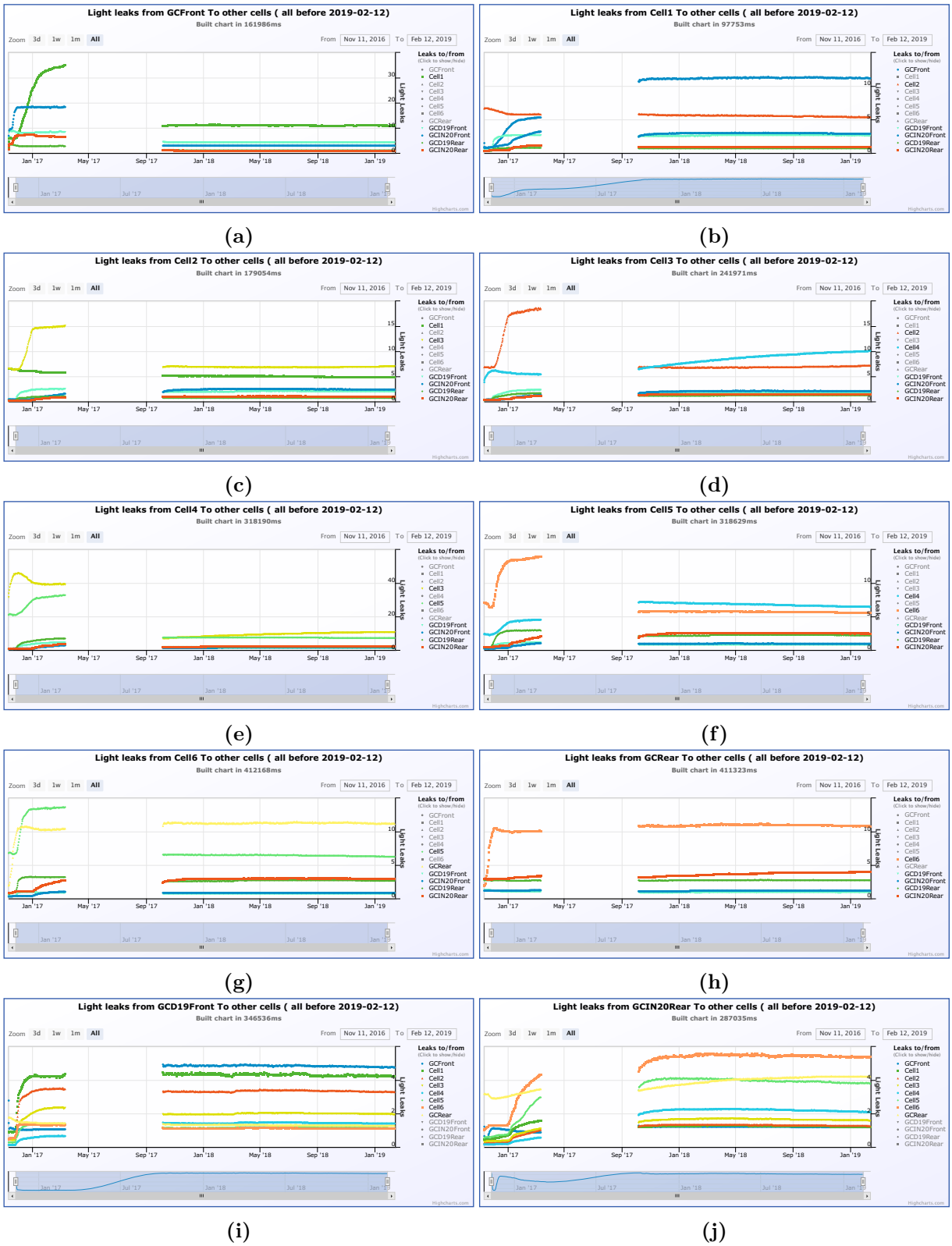

Figure 6.8: Evolution of *light leaks* between cells in **Stereo**. The two periods of data taking, *Phase I* and *Phase II*, are represented. Information extracted directly from **Stereo** monitoring tool [137]. The *light leaks* are constantly being calculated from cosmic ray events, as described in App. A.

and especially `Cell4` have an increase on $\mathcal{A}_{mid}^{top}$ and $\mathcal{A}_{bot}^{mid}$. For both of them the values have almost doubled during *Phase II*, in the same way as $\ell\ell_{34}$ and $\ell\ell_{43}$ have behaved.

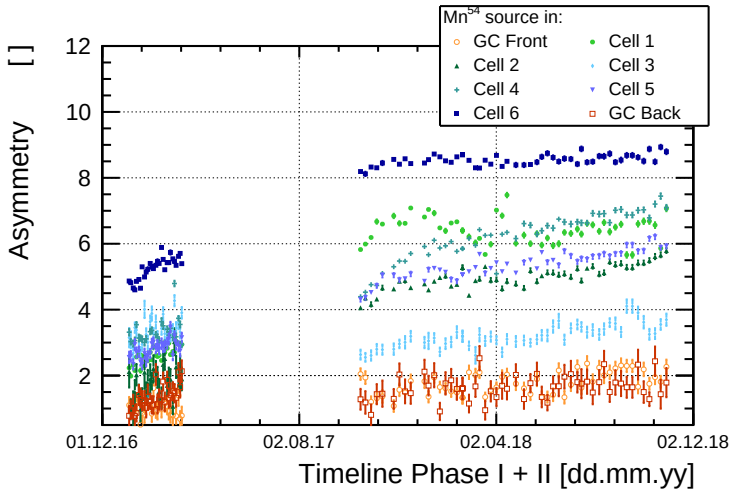

(a)

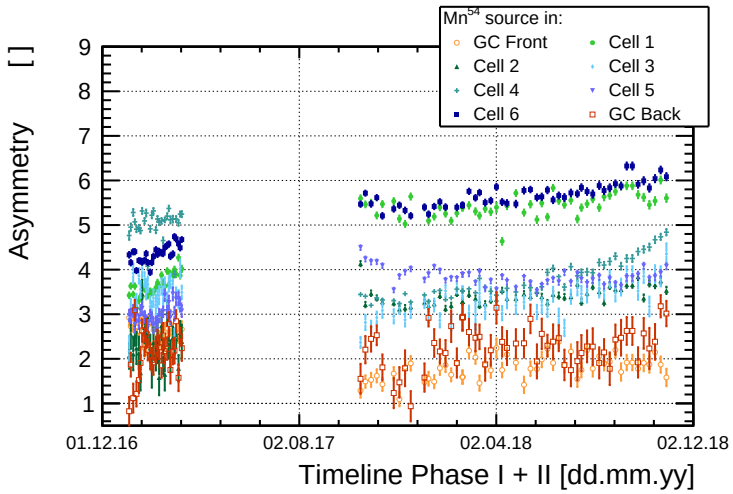

(b)

Figure 6.9: Monitoring of asymmetries (a) $\mathcal{A}_{mid}^{top}$ and (b) $\mathcal{A}_{bot}^{mid}$ for ^{54}Mn calibration data with collected charge in different cells. The *anti-Compton cut* described in Sec. 6.1.1 is applied to all distributions.

6.3.3 Calibration Coefficients

In Fig. 6.10 the evolution of the $\texttt{cc}_i$ over time can be observed. For each ^{54}Mn calibration run there is an associated $\texttt{cc}_i$ for each cell, showing a general trend of decreasing values over time. This decrease could be explained by a gradual reduction of the attenuation length of the `LS`, as will be discussed in Sec. 6.3.5. A reduction of $\sim 8\%$ can be observed for $\texttt{cc}_3$ and $\texttt{cc}_4$, where an increase of the *light leaks* is more notorious according Fig. 6.8(d) and Fig. 6.8(e). The rest of `TG` cells display a reduction of $\sim 4\%$. This shows that the calculation of $\texttt{cc}_i$ has a spurious dependence on the behavior of $\ell\ell_{ij}$, due to an imperfect cut on the non-`FED` events. A slight decrease of $\texttt{cc}_i$ for `GCBack`

and GCIN20 of $\sim 3\%$ and $\sim 6\%$ can also be observed, with a corresponding evolution of $\ell\ell_{79}$ and $\ell\ell_{97}$. The $\texttt{cc}_i$ for the rest of GC cells remain constant.

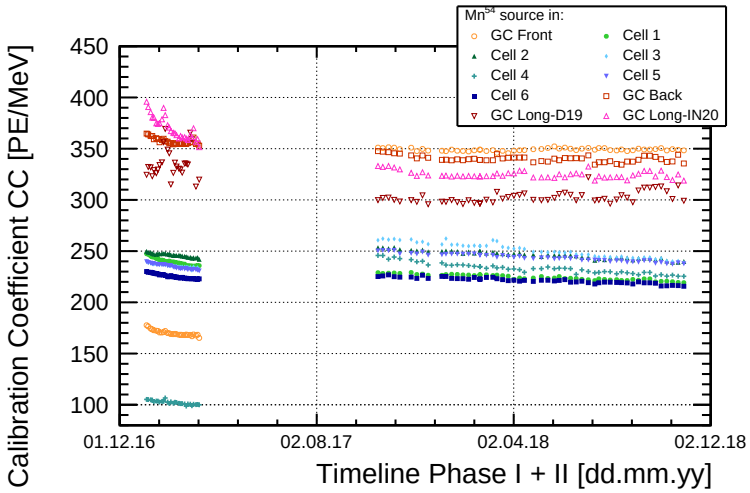

Figure 6.10: Evolution of $\texttt{cc}_i$ before tuning for all cells during *Phase I* and *Phase II*. A general slow decrease over time can be observed for TG cells.

6.3.4 Energy Reconstruction

The stability of the energy reconstruction is also controlled continuously. As described in Sec. 6.2.1, the algorithm adapts and corrects for time variations on $\ell\ell_{ij}$ and $\texttt{cc}_i$ by means of the fine tuning process. Therefore, a stable energy reconstruction is expected. An excellent stability is observed for ^{54}Mn peaks in Fig. 6.7(a). However, these peaks are used to anchor the energy reconstruction and an alternative set of independent events are used systematically to control it. In general, this is done via the gamma emissions from n-capture in hydrogen and gadolinium. Two sources of neutrons are frequent enough to give a reliable stability timeline. The first one is the monthly calibration with AmBe source, which is introduced internally to most of the cells to study the neutron efficiency of the IBD signal. The second option is to observe nuclear spallation neutron events induced by atmospheric muons nearby the detector. The total energy and the topology of energy deposits of these events both significantly differ from the ^{54}Mn calibrations and constitute a stringent test of the energy reconstruction. Both sources are displayed in Fig. 6.11(a) and Fig. 6.11(b) respectively. From these analyses an uncertainty of 0.4% has been introduced to the energy scale as shown in Tab. 6.1.

6.3.5 Total Detector Response

The overall stability of the response of the detector is controlled by the evolution of the total charge collected in all PMTs, both in TG and GC. This type of response can be observed in Fig. 6.12 for ^{54}Mn calibration data after being weighted by its nominal energy at 0.834 MeV. Each one of the plots in Fig. 6.12 represents deployment at a different position within the cell. Like for previous sections, both phases are represented at both sides of the empty hiatus, with slightly different behaviors. In *Phase I*, due to the acrylic buffer leakage at the top of Cell4 and GCFront the response is noticeably lower for deployments in Cell1 and Cell4, similarly to cc 0 and cc 4 in Fig. 6.10. This

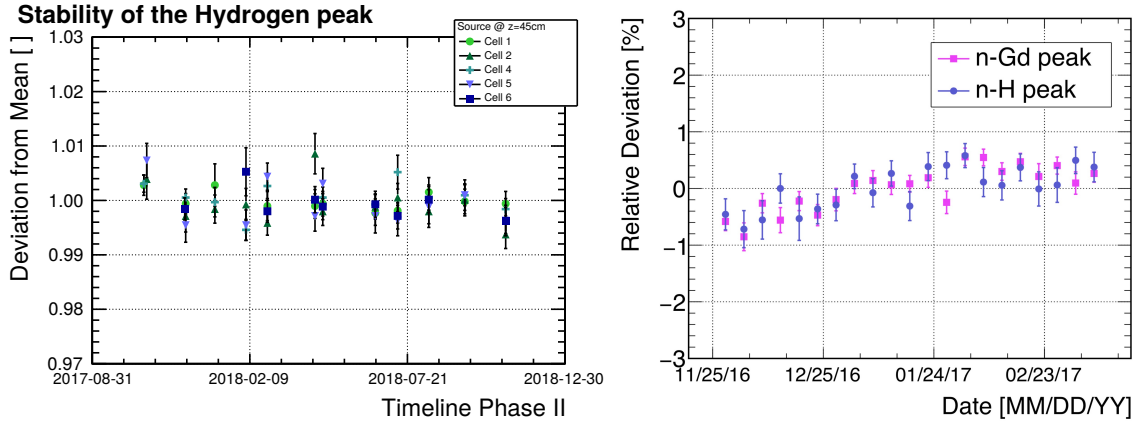

(a) (b)

Figure 6.11: Stability of the reconstructed gamma emission from n-capture in hydrogen for (a) AmBe calibration runs at *middle* [142] in *Phase II*, and (b) spallation neutrons from homogeneoulsy distributed cosmic events [146] in *Phase I*.

is corrected in *Phase II*. A common trend that can be seen for all distributions is a slow decrease of the response, following a similar trend as for their respective $\texttt{cc}_i$ in `TG` cells. As seen in Sec. 6.3.1, *light leaks* are stable for *Phase II*, with the exception of the separation wall between `Cell3` and `Cell4`. A plausible reason for this behavior would be a slow but continuous decrease of the attenuation length of the `LS` over time. In such case, the events at *top* would be affected less than *bottom* events due to their proximity, in average, to the PMTs.

From Fig. 6.12(b) a decrease of roughly 2.5% can be observed for *top*, while Fig. 6.12(a) Fig. 6.12(c) show a difference of about 5% for *bottom* and *middle* respectively. Such decrease is also supported by the observed increase of asymmetries $\mathcal{A}_{mid}^{top}$ and $\mathcal{A}_{bot}^{mid}$ in 6.3.2. Such degradation of the attenuation length could be expected by a small increase of impurities over time. Assuming an approximate overall degradation of a 4% for `TG` over the time lapse of two years, roughly a 2% of the response would reduce per year. Such effect can be considered non-critical for the operation of **STEREO**.

6.4 Summary

Throughout this chapter it has been shown how the collected charge in the detector can be effectively translated into energy by means of the calibration coefficients $\texttt{cc}_i$. These parameters contain the information about the light production in the `LS` and its associated energy deposition within each one of the cells. By means of ^{54}Mn internal calibration data, an algorithm to calculate the $\texttt{cc}_i$ on a weekly basis has been developed for this thesis, granting a continuous and stable energy reconstruction over time. An *anti-Compton cut* have been defined by the parameter $k_{\ell\ell}$ in such a way that the computation of the different $\texttt{cc}_i$ is independent on *energy leaks* and compatible for all cells, specially for *intermediate cells* where no source can be deployed. With the definition of the integration cutoff parameter α, the stability over the parametrization in the calculation of $\texttt{cc}_i$ have been ensured. It has also been described in this chapter the important role of the $\texttt{cc}_i$ on the the energy reconstruction algorithm, developed by the CEA group [146]. After a fine tuning process of $\texttt{cc}_i$ and $\ell\ell_{ij}$, the energy reconstruction

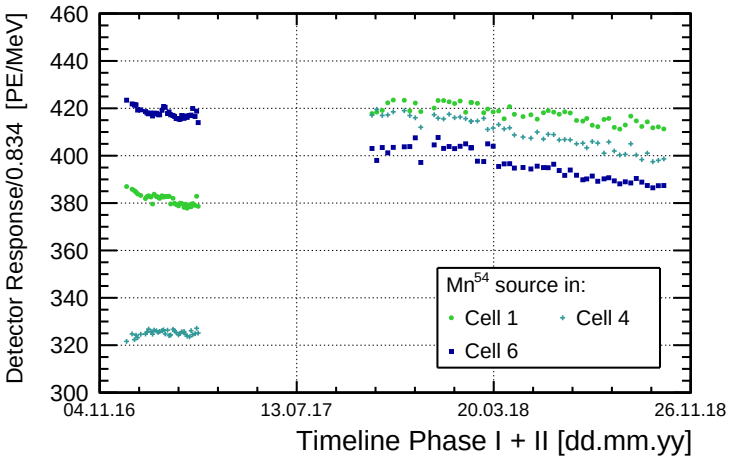

(a)

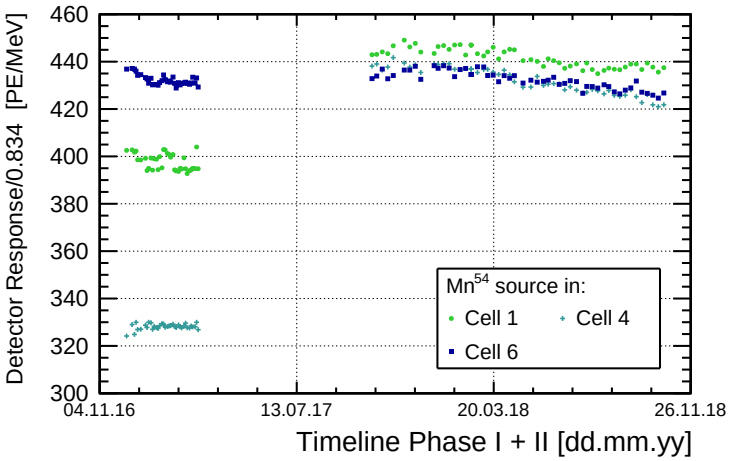

(b)

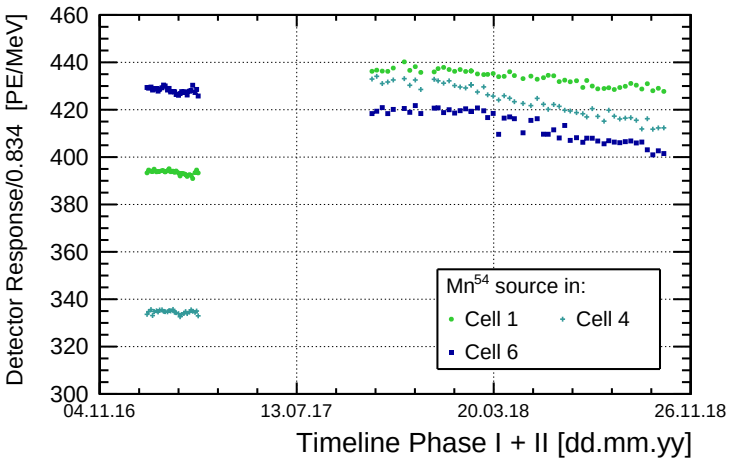

(c)

Figure 6.12: Evolution of the total response of the detector to ^{54}Mn deployments in `Cell1`, `Cell4` and `Cell6`. Three different positions of the source are shown: (a) *bottom*, (b) *top* and (c) *middle*.

is matched for both data and simulation showing the robustness of the method. The final uncertainty in the energy scale is a 1.1% uncorrelated cell-to-cell, and 0.4% correlated cell-to-cell.

Furthermore, the stability of the detector has been periodically monitored throughout this thesis by means of different variables. The transition between *Phase I* and *Phase II* carried a series of changes on the monitored response, after the fix of some mechanical defects. The *light leaks* between `TG` cells and the light collection of `Cell4` and `GCFront` were reverted to nominal values improving the overall response of the detector. For *Phase II* a slow but constant decrease on the overall signal is observed, together with an increase of the vertical asymmetries on the response of the cells. Such effect is justified by the expected reduction of the attenuation length of the `LS` and it has been shown to be perfectly understood and under control. The *light leaks* have been shown to be stable for *Phase II*, with the exception of the separation wall between `Cell3` and `Cell4`. From the experience of *Phase I*, the cause of such increase is also understood and corrected for in the simulation of **Stereo**, described in Sec. 5.3.3.

"This has been a day to die on,
now the day is almost done...
Here the pipes will lay beside me,
silent with the battle drum.
If friends in time be severed,
someday here we'll meet again
and I'll return to leave you never...
Be a piper to the end"

Knopfler

Chapter 7

Studies on the Quenching of Light

The kinetic energy of ionizing particles and their light output in liquid scintillator do not follow a linear relationship. In fact, the amount of light generated depends on the energy loss of the particle which increases as the particle slows down. This phenomenon is know as quenching of light and have been previously discussed in Sec. 3.4.3. For liquid scintillators, this behavior can be characterized by the Birks' parameter k_B that can be experimentally measured. The understanding of energy non-linearities is crucial to analyze the antineutrino spectra in **Stereo** and to test compatibility with different oscillatory hypothesis. For this reason, part of this thesis has focused on developing a method to calculate an effective k_B for electrons from calibration data and to implement it on the **Stereo** simulation. The details of the method and its implementation has been detailed along this chapter. Sec. 7.1 describes the results obtained for the LS in TG volume for *Phase I* calibration data, the measured quenching curve and the χ^2 analysis performed to find k_B. The methodology used for this purpose is discussed in Sec. 7.1.1, including how calibration sources are used and compared to simulated data. Extensions of the model for the LS in GC volume and *Phase II* calibration data have also performed and they are described in Sec. 7.2. Other approaches to calculate this parameter have also been performed in **Stereo**. Sec. 7.1.2 shows a summary of their results and how they are combined with the method developed in this thesis to produce a final value for k_B.

7.1 Quenching on Target Volume

In Sec. 3.4.3 it has been already discussed how energy from ionizing particles crossing the LS is transformed into scintillation light. This light is read by the PMTs as a charged signal, amplified, and then digitalized by the DAQ system during the pre-processing of data. More energy deposition means larger observed signals, but this relation is not completely linear due to the quenching of light in the LS. As discussed in Sec. 3.4.3, the loss of light by quenching increases for particles with larger ionization power dE/dx. This magnitude increases rapidly as the kinetic energy of the particle drops, so ionizing particles with low energies tend to suffer more from quenching effects.

Energy non-linearities in the neutrino energy spectra come directly from the positron *prompt* signal, which have a very similar ionization power as electrons at low energies. However, in **Stereo** no electron have been used. The way to estimate non-linearities in the *prompt* spectra is, instead, by analyzing the different responses of the detector to a wide range of well-defined energies from gamma emissions of calibration sources, described in Sec. 3.6. Gammas are neutral particles and do produce scintillation in the medium themselves, but quenching from electrons produced by Compton-scatterings

Table 7.1: List of all gamma peaks used for the SecM. Each emission is associated to a integer number i from 0 to 8 according to their respective energy, in ascending order.

Source	i	E_{nom} [MeV]
^{124}Sb	0	0.603
^{137}Cs	1	0.663
^{54}Mn	2	0.834
^{65}Zn	3	1.115
^{24}Na	4	1.137
^{124}Sb	5	1.690
H (n,γ)	6	2.224
^{24}Na	7	2.754
AmBe	8	4.438

and photoelectric effect can be observed in gamma events. Since the overall kinetic energy of the electrons is proportional to the nominal energy of the gamma emissions, the response of the detector to the deployment of each of the calibration sources is affected differently by quenching. The list of energies used is depicted in Tab. 7.1.

7.1.1 Stitched Energy-Charge Method

To estimate kB, a broad set of simulations for all sources using different kB_{simu} have been produced and compared with real data. This analysis has been with information from calibration runs performed during *Phase I*. In this section the calibration data used specifically dates from 22.II.2017, point in time when *light leaks* had reached a very stable configuration. An intrinsic property of the LS like kB is not expected to vary from cell to cell, nor from *top* to *bottom*. For this reason, deployments in only one cell and position, namely Cell6 at *middle*, suffice. In addition, to avoid any cell-to-cell effect on the charge deposition, it is required that the charge is fully collected in Cell6, with the necessary exception of the $i = 8$ peak from AmBe that will be described later.

The Stitched energy-charge Method (SecM), developed in this thesis, corresponds to one of the three methods used to describe and quantify the quenching effects in **Stereo**. The other two approaches will be reviewed in Sec. 7.1.2. The SecM is performed for every individual source in several steps that carry over information from one to another. The step 1 uses true information from simulated spectra to accurately extract the deposited energy $\overline{E}^i_{\text{dep}}$ for every gamma emission i and its corresponding observed charge $\overline{Q}^i_{\text{MC,dep}}$. The next step, step 2, uses all $\overline{Q}^i_{\text{simu,dep}}$ of the source as initial conditions to fit the complete spectrum. From the fit results, the mean value μ^i_{simu} for each charge peak from the distribution is extracted and used in step 3. There, the values obtained for μ^i_{simu} for a given source are used as initial conditions to fit the homologous spectra of calibration data. From this fit, the set of μ^i_{data} are extracted in a similar fashion as μ^i_{simu}. In step 4, several quenching curves are drawn from the results from step 2 and step 3 for simulation and data respectively. These curves are fitted in step 5 to a certain function, and from the results of such fit the optimal kB_{simu} to match kB in data is extracted. The full algorithm is represented in the flowchart of Fig. 7.1, and each of the steps will be detailed in the following sections.

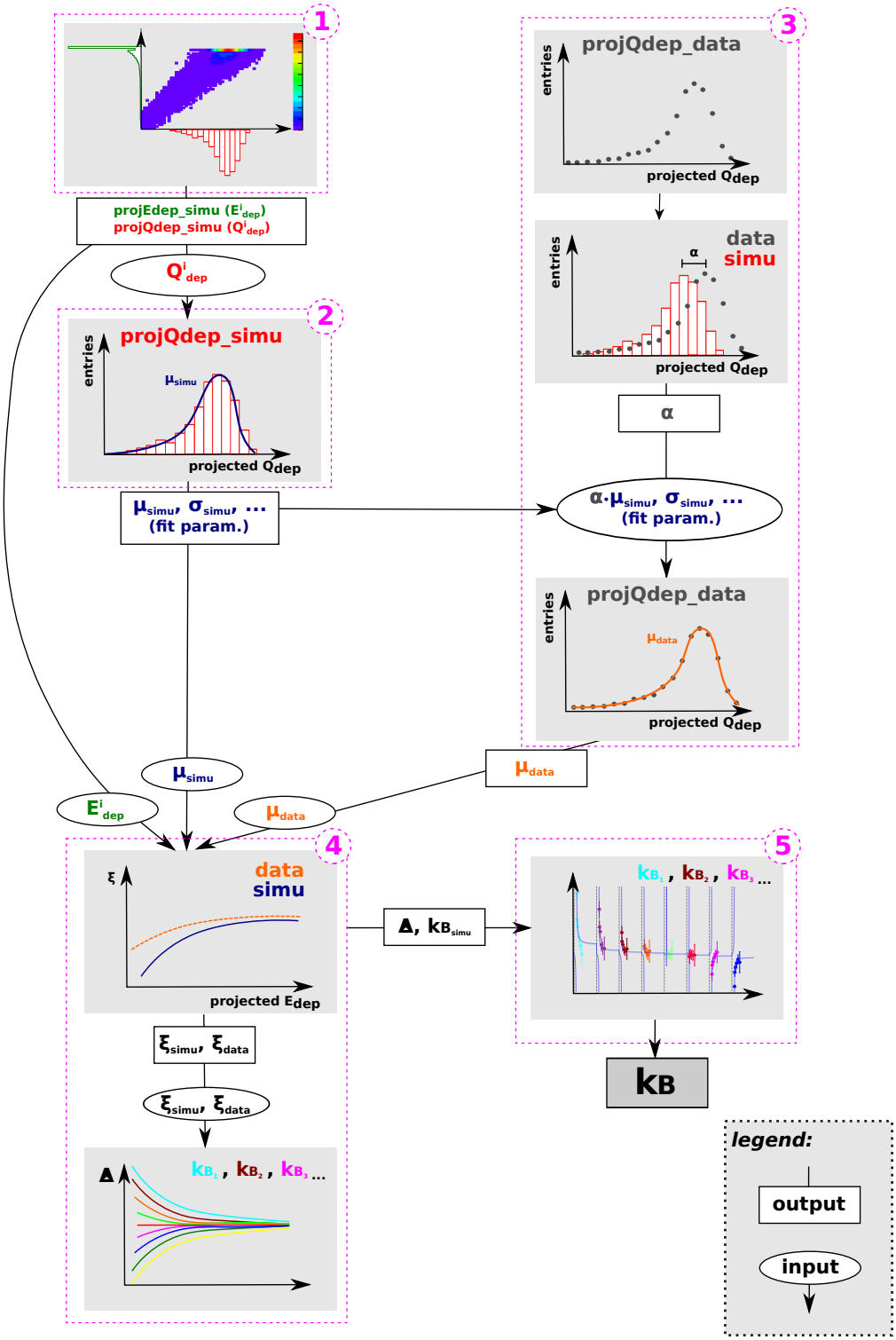

Figure 7.1: Chart summarizing the 5 steps followed in the SecM to estimate the kB_{simu} that better matches calibration data in **Stereo**. Each step receives some input and gives some output. Data is depicted as grey dots and simulation as red histograms.

Step 1: Extract Deposited Energy and Charge Correlation from Simulation

For the first step in the `SecM`, only simulations are used. The main objective of this step is to find the deposited charge observed in the detector when a gamma fully deposits its energy in a single cell. In Chap. 5, it has been discussed that simulations are created with two main trees of information, both containing the same amount of events. From `DATA` and `MC` trees the charge and energy deposited in `Cell6` are extracted respectively. After the selection cuts discussed in the next paragraph, both data sets are stitched together following a one-to-one correlation forming a two-dimensional histogram called `projEdep`, as depicted in Fig. 7.1(1). The two projections in the charge and energy axis are also kept as one-dimensional histograms, `projQdep-simu` and `Edep`, with bin sizes of 4 PE and 16 keV respectively.

Before the analysis is performed, an *anti-Compton cut* is applied to `projEdep` distribution. In Sec. 6.1.1 it has been described how the application of *anti-Compton cut* rejects events with high amount of *energy leaks* and enhances the selection of `FED` events in a single cell. This cut triggers every time there is a charge deposition in a neighboring cell above the threshold determined by the correspondent *light leaks* and $k_{\ell\ell}$, defined previously in Eq. 6.3. By doing this, the charge spectra are cleaned from events with escaping gammas and in general help to define and narrow the main peaks. These type of cuts are applied in the same fashion to data and simulations and intend to affect them in the same way. In contrast to the analysis performed in Sec. 6.1.1, the quenching analysis uses not only ^{54}Mn but the whole set of calibration sources. The ones that have multiple gamma emissions, like ^{124}Sb or ^{24}Na, require a tweaked *anti-Compton cut* treatment. In these cases, events with an energy leak of one gamma should not be rejected as far as any other emission stays and deposits its energy in `Cell6`. For this reason, the rejection of the event is set to happen when the *anti-Compton cut* is triggered more than $n_\gamma - 1$ times, where n_γ is the number of simultaneous gamma emissions.

Fig. 7.2(a) and Fig. 7.2(c) show the resulting two-dimensional distributions of deposited energy and associated charge in `Cell6` for ^{137}Cs and ^{24}Na, after the application of the *anti-Compton cut*. `projEdep` is obtained for each source and `kB` tested, and from it a pair of variables $(\overline{E}^i_{\text{dep}}, \overline{Q}^i_{\text{simu}})$ is extracted for each gamma emission i. It has been discussed in Sec. 6.1.1 that the `Edep` distribution is characterized by a sole bin of `FED` events followed by an edge plus a continuum created from energy losses after one or more Compton-scatterings. These shapes can be appreciated in Figs. 7.2(b) and 7.2(d), being the latter the result of a multi-gamma emission. $\overline{E}^i_{\text{dep}}$ is thus extracted directly as the center of the highest bin, b_{yE}, within a 2% range around E^i_{nom} in `Edep`, where E^i_{nom} is the nominal energy of the gamma emission i. This way of extracting $\overline{E}^i_{\text{dep}}$ ensures that there is no contribution from the energy loss region. It must be noted that due to gamma interactions with non-scintillating *dead* materials, like for instance the metal of the tube, the relation between deposited and nominal energy $\overline{E}^i_{\text{dep}} \lesssim E^i_{\text{nom}}$ holds true.

To extract the collected charge $\overline{Q}^i_{\text{simu}}$ corresponding to $\overline{E}^i_{\text{dep}}$, the bin b_{yE} previously extracted from `Edep` is used. Each energy bin in the `projEdep` spectrum has its own charge distribution projected along charge-axis. The resultant distribution for the bin b_{yE} is a completely symmetrical gaussian function, result of the convolution of the true energy deposited with the resolution of the detector in `Cell6`. $\overline{Q}^i_{\text{simu}}$ is then obtained as the average charge of this distribution. This value will be used in the next step as

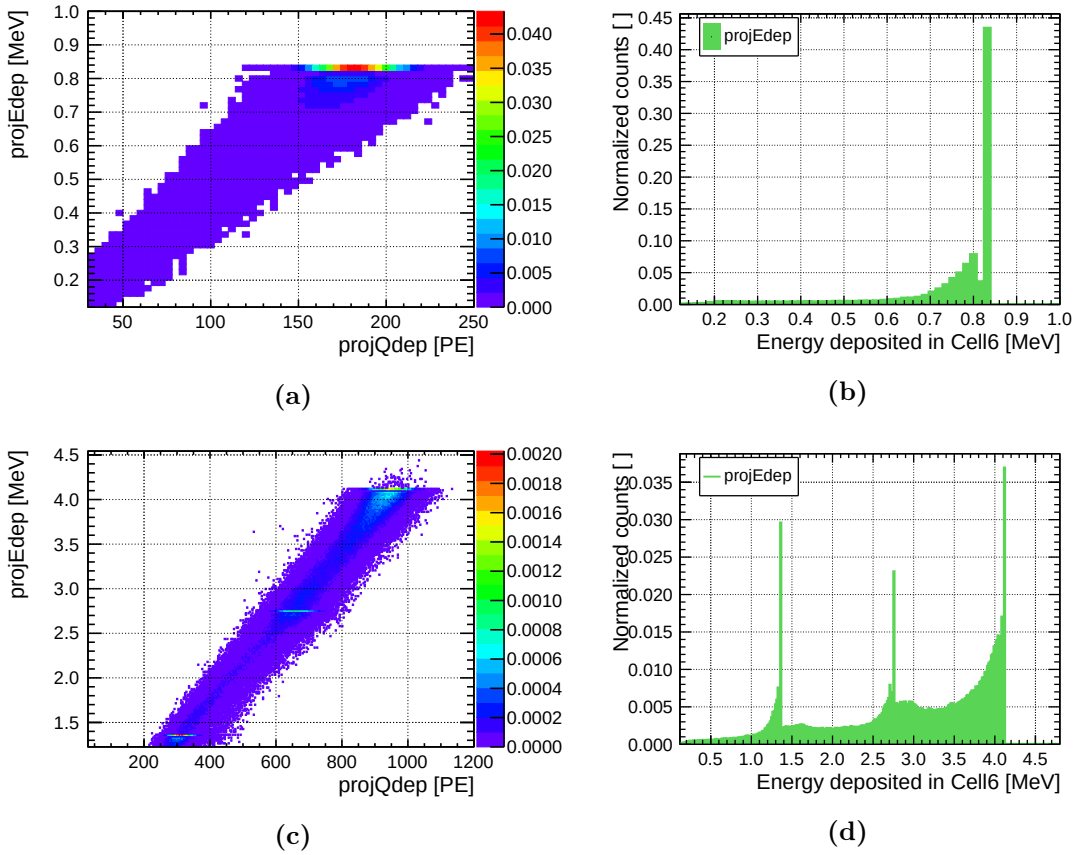

Figure 7.2: Representation of the energy deposition for single and multi-gamma sources. (a) Two dimensional `projEdep` distribution, where the main energy deposition at $\sim$ 0.834 MeV can be observed. (b) `Edep` distribution for ^{54}Mn. The correlation between `projQdep-simu` and `Edep` for ^{54}Mn can be appreciated specially for the main energy deposition, point corresponded with most of the charge deposition. (c) Two dimensional `projEdep` distribution for ^{24}Na, where the two main emissions are seen individually at $\sim$ 1.3 MeV and $\sim$ 2.7 MeV and together at $\sim$ 4 MeV. (d) `Edep` distribution for ^{24}Na.

starting point for the fit of each one of the i emission contributions to the spectrum of a source. $\overline{E}^{i}_{\text{dep}}$ will be stored until the final step when the quenching curve is drawn.

Special attention have to be taken when analyzing the deposited energy correspondent to the AmBe source. As discussed in Sec. 3.4.2, fast neutrons lose their kinetic energy mainly via neutron-nucleus scattering. The recoil energy of these nuclei provokes the ionization of the `LS` and hence scintillation light is produced as a result. The energy carried by proton recoils is usually of the order of the kinetic energy of the neutron. It has been shown in Fig. 5.7 that this energy is typically distributed between 2 MeV and 6 MeV for fast neutrons from AmBe. Since these signals happen during the thermalization of the neutron, they overlap with the energy deposition of the gamma emission. Such effect creates an effective and asymmetric broadening of the 4.44 MeV gamma peak and complicates the extraction of deposited charge and energy solely from the gamma emission. In fact, as can be seen in Fig. 7.3(a), the contribution of the proton recoil to the main peak increases the mean energy deposited in the region up $\sim$ 7 MeV. This increased energy is not linearly translated in the deposited charge due

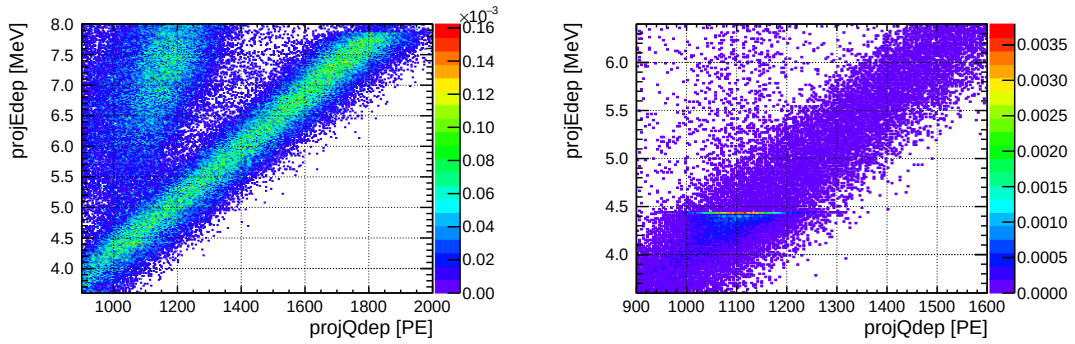

(a) **(b)**

Figure 7.3: `projEdep` distributions for the $i = 8$ peak at 4.44 MeV. (a) AmBe source deployed in `Cell6` and charge collection at `Cell5`. (b) AmBe source deployed in `Cell6` and charge collection at `Cell6`. The former has been fitted using *GaussExp*. The latter has been fitted with *Double-GaussExp* to account for the contribution from the proton recoil.

to a harder quenching of light for proton and nuclei recoil events. Therefore, the extraction of a properly correlated $(\overline{E}^i_{\text{dep}}, \overline{Q}^i_{\text{simu}})$ is not possible by using the `projEdep` distribution displayed in Fig. 7.3(a).

To solve the problem it can be argued that a PSD cut, as described in Sec. 3.4.4, could be applied. The main idea for such cut would be to distinguish between events containing only proton recoil or only gammas. In this specific case, however, both type of events share a common origin and thus are detected in the same signal. Studies performed by Sergeyeva V at LAPP [139] by using different cuts on the PSD showed a negligible effect on discrimination of proton recoils from gammas, at the expense of a large loss on statistics.

The solution that has been chosen is to extract $(\overline{E}^i_{\text{dep}}, \overline{Q}^i_{\text{simu}})$ deposited in `Cell5` while AmBe source is deployed in `Cell6`. Neutrons have a much more reduced mobility than gammas and rarely escape the origin cell. This can be found by doing a quick calculation of the mean free-path [159]

$$\ell = \sum_i (\sigma_i n_i)^{-1}\,, \tag{7.1}$$

where σ_i is the sum of the cross sections for all possible processes between neutron and target particle i, and n_i the amount of such particles per unit volume. For this calculation, only neutron scattering on H and C nuclei will be assumed, given that they are the most dominant in the `LS`. Using data from ENDF-VII [149], total cross-section for ~ 5 MeV neutrons with H and C is $\sim \sigma_H \cong \sigma_C = 2$ b. Making use of results from Sec. 5.1.1, the number of H in the `TG` volume is $N_H \sim 1.08 \cdot 10^{29}$. The hydrogen-to-carbon ratio was measured to be $r^{tot}_{H/C} = 1.55 \pm 0.03$ [136], yielding a number of carbon atoms of $N_C \sim 270 \cdot 10^{29}$. Using

$$n_i = N_i / V_{TG}, \quad \text{with } V_{TG} = 1813\,\text{l}, \tag{7.2}$$

and plugging the results into 7.1, one gets an approximate $\ell \sim 4$ cm. Knowing from

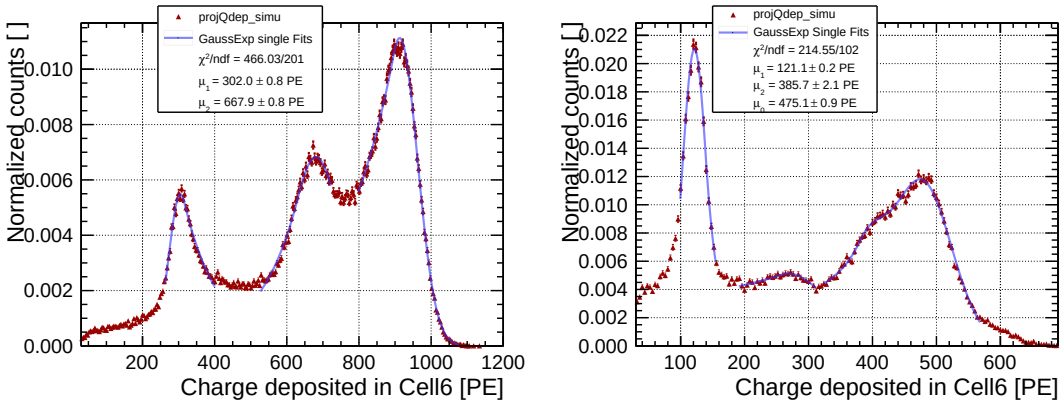

Figure 7.4: Starting point of the multi-function fit for (a) ^{24}Na and (b) ^{124}Sb. In blue there are represented several individual fits from which the initial parameters of the complete fit of the spectra are extracted. These fits are not correlated to each other and thus converge quickly with a typical number of iterations of $\lesssim 50$. In Tab. 7.2 the individual functions used for each peak are listed.

Sec. 5.2 that the calibration tube in `Cell6` is at 12 cm from `Cell5`, it can be assumed that the energy of proton recoils is generally deposited in the cell of origin. However, this does not necessarily mean that neutrons cannot travel from cell to cell. As discussed in 3.4.2, once thermalized, neutrons have a relative long journey before being captured and during their path they can slowly move from one volume to another in their random walk. Here it has been assumed that the total cross-section represents the scattering cross-section, since neutron capture is heavily outweighed at this range of energies.

From these quantitative arguments, it can be concluded that most of the scintillation light observed from the kinetic energy of the neutron in the neighboring cells comes from *light leaks* of events in `Cell6`. By requesting energy and charge deposition in `Cell5`, the desired low contamination from proton recoils is guarantees. This effect is clearly seen in Fig. 7.3(b), where a definite peak at 4.44 MeV is displayed with only a timid contribution from higher energies. It can also be observed that, in comparison with Fig. 7.3(a), the high energy continuum from the gamma cascade following a n-capture in gadolinium is greatly reduced. This method has been used to safely extract $(\overline{E}^8_{\text{dep}}, \overline{Q}^8_{\text{simu}})$, and also to fit μ^8_{simu} and μ^8_{data} in step 2 and step 3 respectively.

Step 2: Fit Simulated Charge Spectra

The symmetric charge distribution of the b_{yE} energy bin from where $\overline{Q}^i_{\text{simu}}$ is calculate in step 1 is not available in real data. For this reason, once $\overline{Q}^i_{\text{simu}}$ is extracted from the true information in the simulation, it needs to be translated into a parameter that can be observed and extracted for both data and simulation. This parameter, namely μ^i_{data} and μ^i_{simu}, come from the equivalent fit of data and simulation, `projQdep-data` and `projQdep-simu` respectively. In this step the values $\overline{Q}^i_{\text{simu}}$ are used as the starting point to fit `projQdep-simu`. First of all, each of the peaks in the spectrum associated to a gamma emission is fitted individually and from them $\mu^{(0)i}_{\text{simu}}$ is extracted. The superscript

Table 7.2: List of functions used to fit the different `Qdep` distributions in the `SecM`. These functions are described in more detail in App. B.

source/i	Individual Fit Function	General fit function	Num. Parameters
^{124}Sb/0	*GaussExp*	*Quad-GaussExp*	20
^{124}Sb/5	*Double-GaussExp*	*Quad-GaussExp*	20
^{137}Cs/1	*GaussExp*	*GaussExp*	4
^{54}Mn/2	*GaussExp*	*GaussExp*	4
^{65}Zn/3	*GaussExp*	*GaussExp*	4
^{24}Na/4	*GaussExp*	*Triple-GaussExp*	12
^{24}Na/7	*Double-GaussExp*	*Triple-GaussExp*	12
H n-capture/6	*GaussExp*	*GaussExp*	4
AmBe/8	*Double-GaussExp*	*Double-GaussExp*	8

$^{(0)}$ represents that $\mu^{(0)i}_{\text{simu}}$ corresponds to the first iteration of the fit. For mono-gamma sources this is the first and last step and $\mu^{(0)i}_{\text{simu}} = \mu^{i}_{\text{simu}}$. But for multi-gamma sources it will serve as starting point for the fit of the complete spectrum. An example of individual fits for both multi-gamma sources, ^{24}Na and ^{124}Sb, is depicted in Fig. 7.4(a) and Fig. 7.4(b). All functions used to fit the spectra of calibration sources are summarized in Tab. 7.2 and described in App. B. Without adequate initial conditions that sever the available parameter space, the amount of parameters used make the fit prone to divergences. The parameter k determining the start of the exponential contribution has been proven to be specially dangerous for the convergence. For this reason, results from the individual fits of the correspondent gamma emissions have been used as starting conditions for the fit. It also speeds up the process and reduce the number of iterations used by the fitter.

For mono-gamma sources, a *GaussExp* function in the range $[0.80\cdot\overline{Q}^{i}_{\text{simu}}, 1.20\cdot\overline{Q}^{i}_{\text{simu}}]$ is sufficient to fit `projQdep-simu` with $\bar{\chi}^2 \sim 1$. The plateau to the left of the main peak represents *light leaks* towards neighboring cells and has not been included in the fit. An example of a mono-gamma fit is shown in Fig. 7.5(a). Multi-gamma sources, however, represent complex distributions that require for more elaborated fit functions. ^{24}Na source counts with three well-defined contributions, depicted in Fig. 7.4(a). `FED` events of one of the two gamma, either $i = 4$ or $i = 7$, can be observed around $\overline{Q}^{4}_{\text{simu}} \sim 300$ PE and $\overline{Q}^{7}_{\text{simu}} \sim 700$ PE respectively. The third contribution, around $\overline{Q}^{4+7}_{\text{simu}} \sim 900$ PE corresponds to the case where both gammas have been observed simultaneously in `Cell6`. Often, for multi-gamma sources $\overline{Q}^{i} + \overline{Q}^{j} \neq \overline{Q}^{i+j}$ due to insufficient energy containment for double-gamma events. For this reason, the parametrization of the double-gamma peak cannot be derived from the other two peaks and needs to be addressed individually on the complete fit. The function *Triple-GaussExp* has been chosen to fit ^{24}Na spectra. This function contains 12 parameters, 4 for each of the *GaussExp* function representing the gamma peaks. The total function has been fitted over the range $[0.20\cdot\overline{Q}^{4}_{\text{simu}}, 1.20\cdot\overline{Q}^{4+7}_{\text{simu}}]$, covering all features of the distribution. While the parameters μ^{4}_{simu} and μ^{7}_{simu} are only allowed to fluctuate within a 2% margin, the rest have loose limits to accommodate the fit. An example of the fitted ^{24}Na distribution is shown in Fig. 7.5(b).

The function defined to fit the `Qdep` spectra from ^{124}Sb, *Quad-GaussExp*, contains

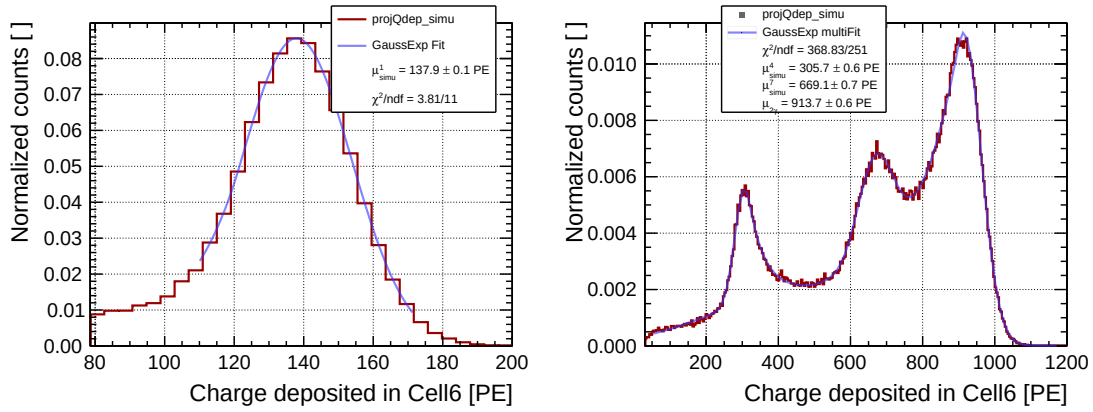

(a) **(b)**

Figure 7.5: `projQdep-simu` distributions for (a) ^{137}Cs and (b) ^{24}Na fitted to their respective fit functions. Fit functions are drawn in translucent blue. Both simulations are computed with a $\texttt{kB}_{\text{simu}} = 0.095\,\text{mm/MeV}$.

20 different parameters. Details on the different emissions of ^{124}Sb can be seen in Sec. 5.2. In the same manner as for ^{24}Na source, all peaks are taken into account and included in the complete fit as *GaussExp* contributions. The lowest energy peak $i = 0$ is located at $\overline{Q}^0_{\text{simu}} \sim 120$ PE. Together with it, a small contribution can be included to its left-hand side in `projQdep-simu`, at $\overline{Q}^{0'}_{\text{simu}} \sim 100$ PE. It corresponds the $3 \rightarrow 1$ chain of gammas with $\sum_\gamma = 722.3\,\text{MeV}$. Even if this emission has more energy, the correspondent response is lower that for $i = 0$ due to larger quenching effects. To fit all these parts a *Double-GaussExp* is used. The second peak of the distribution, in energetic order, corresponds to the observation of the chained emission of the aforementioned gammas, located at $\overline{Q}^{0+0'}_{\text{simu}} \sim 250$ PE. As for any other double-peak, it is not used for the quenching analysis, but its effect has to be taken into account when performing the complete fit. The last contribution to the spectrum comes also as a *Double-GaussExp*, and corresponds to the $i = 5$ peak at $\overline{Q}^5_{\text{simu}} \sim 400$ PE and the sum of both $i = 0$ and $i = 5$ gammas at $\overline{Q}^{0+5}_{\text{simu}} \sim 450$ PE. An example of the fit performed for the ^{124}Sb source is given in the Step 3, using calibration data as reference.

In Sec. 5.2 it has been discussed that there are two main signals coming from an AmBe source: the emission of a neutron and an accompanying 4.44 MeV gamma $\sim 60\%$ of the times. As discussed in previous paragraphs, the gamma emission is often overlapped by the detection of proton recoils caused by neutron collisions with nuclei. It is clear that the topologies of the events comprising this spectrum are different. Fitting the whole spectrum with the same function could be problematic due to the non-trivial combination of each of these contributions, which cannot be immediately disentangled without performing a time-correlated pair search on `projQdep-simu`. Thus, in contrast to the previously discussed sources, both $i = 6$ and $i = 8$ peaks have been fitted individually. The $i = 6$ peak has been fitted to a *Double-GaussExp*, where the auxiliary gaussian adapts to cover the quasi-continuum contribution from the gadolinium n-capture tail. The $i = 8$ peak, due to a lingering contribution from proton recoil, has been fitted instead to a *Double-GaussExp*. Examples of the fit of AmBe-related peaks are shown in Figs. 7.6(a) and 7.6(b).

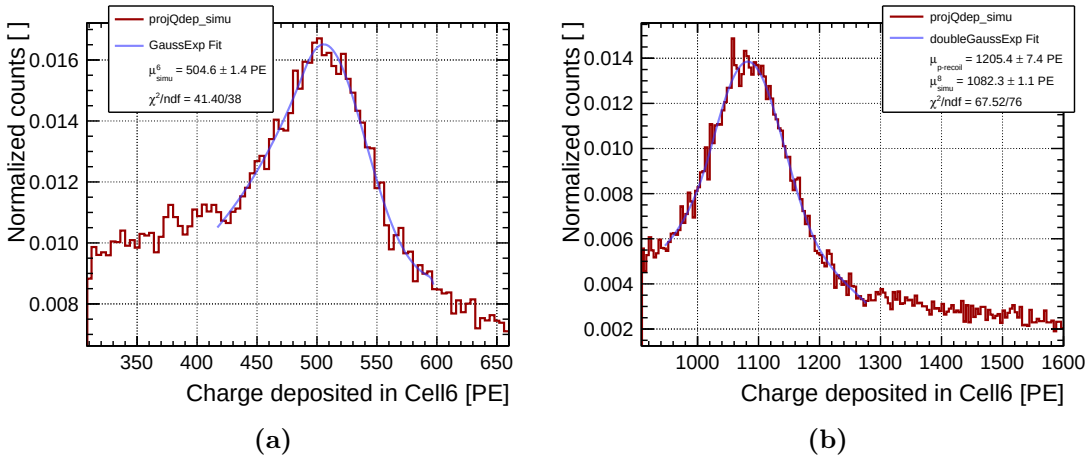

Figure 7.6: `projQdep-simu` distributions for (a) $i = 6$ peak at 2.22 MeV gamma from n-capture in hydrogen and (b) $i = 8$ peak at 4.44 MeV from AmBe gamma emission. The former has been fitted using *GaussExp*. The latter has been fitted with *Double-GaussExp* to account for the contribution from the proton recoil.

Once the fits have converged, the mean charge deposited is extracted as the parameter μ^i_{simu} for each of the gamma peaks. Both the mean charge μ^i_{simu} and with the deposited energy $\overline{E}^i_{\text{dep}}$ obtained in step 1, will be used in Step 4 to draw quenching curves for each $\texttt{kB}_{\text{simu}}$.

Step 3: Fit Charge Spectra from Calibration Data

In this step, the same course of action used for simulations is taken to analyze real calibration data. Deposited charge distribution is extracted from pre-processed calibration data and stored in a histogram `projQdep-data`. The same *anti-Compton cut* than in Step 1 is applied to this distribution, ensuring a high ratio of `FED` events in `Cell6`. As in previous chapters, values for *light leaks* in data are extracted from cosmic rays, method described in App. A.

Along Chap. 5 it is shown how the simulation framework developed in this thesis has been fine tuned to reproduce the response of the detector. More explicitly, in Sec. 5.2 an agreement at the subpercent level is portrayed for the different calibration sources. By virtue of this agreement, charge distributions for both data and simulations can be described by the same model or fit function, allowing the use of parameters obtained as output from the fit of `projQdep-simu` as initial conditions for the fit of `projQdep-data`. This approach holds well for most of the parameters of the fit. However, the absolute normalization of the charge spectra of simulation depends on the $\texttt{kB}_{\text{simu}}$ chosen. Since multiple simulations will be compared to data, a corrected parameter $\mu^{(0)i}_{\text{data}} = \alpha^i \cdot \mu^i_{\text{simu}}$ is introduced as initial condition for the fit. The correction α^i is calculated ad hoc by comparing the position of the bin with maximum height in the nearby of the corresponding peak i between `projQdep-simu` and `projQdep-data`. The ratio between the position of the respective bins gives a first order correction α^i. For the multi-gamma spectra, the starting point $\mu^{(0)i}_{\text{data}} = \alpha^i \cdot \mu^i_{\text{simu}}$ is then refined by performing a first individual fit of each of the contributions, in the same manner as in Step 2. The results of the fits

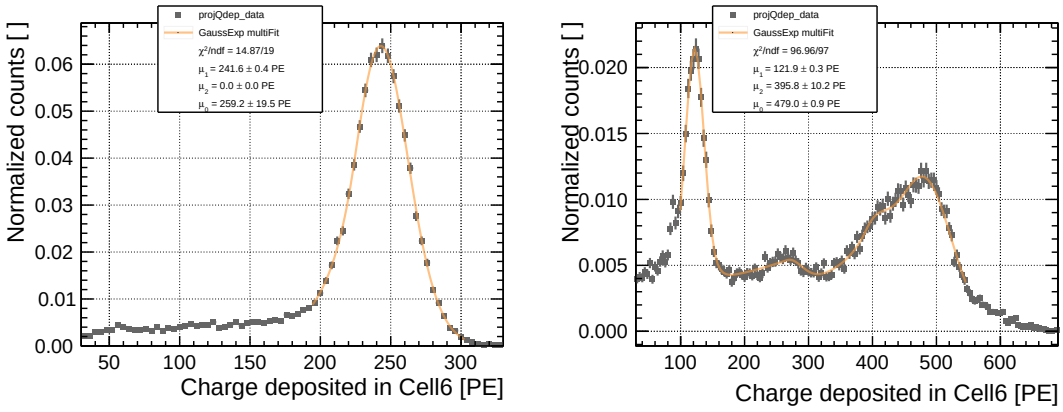

(a) (b)

Figure 7.7: `projQdep-data` distributions for (a) ^{65}Zn and (b) ^{124}Sb 124 fitted to their respective fit functions. In grey, charge distributions. In translucent orange, fit functions listed in Tab. 7.2.

for ^{65}Zn and ^{124}Sb are showed in Fig. 7.7.

Once the fit is performed, the mean charge deposited μ^i_{data} is extracted from the output parameters. In the same fashion as for simulation data, the conversion factor f^i_{simu} and the quenching factor ξ^i_{simu} are calculated for Step 4.

Intermission: Analysis of Systematic Uncertainties

From step 1 to step 3, $\overline{E}^i_{\text{dep}}$ and $\overline{Q}^i_{\text{simu}}$ have been calculated and inserted into several multi-parameter fits to extract the mean charges μ^i for each peak. The calculation of the final uncertainty on μ^i will be relevant in step 5 in order to give a quantitative statement on `kB` in **STEREO**. So far, uncertainties that have been shown are extracted from the fit of μ^i for data and simulation. These are treated as purely statistical, since they appear from the error and probabilistic distribution of the bins around each one the peaks. They have been seen to vary between the $r^i_{\delta\mu_{\text{stat}}} = 0.1\%$, mostly for mono-gamma sources, and $r^i_{\delta\mu_{\text{stat}}} = 0.2\%$, where

$$r^i_{\delta\mu_{\text{stat}}} = 100 \cdot \frac{\delta\mu^i_{\text{stat}}}{\mu^i}\,, \tag{7.3}$$

represents the relative statistical uncertainty corresponding to μ^i. However, some of the choices taken during the analysis have an effect on the final result regardless of the amount of statistics used. Among these systematic uncertainties, special attention have been put into the initial choice of $\overline{E}^i$ and $\overline{Q}^i$ from the `projEdep` distribution. The former is obtained as the center value of the highest bin on the `Edep` distribution in the region around E_{nom}, and thus it comes with an intrinsic uncertainty of half bin $\delta\overline{E} = 8\,\text{keV}$. The latter, $\overline{Q}^i$, carries an uncertainty $\delta\overline{Q}$ that comes strictly from the standard deviation of `Qdep` around $\overline{Q}^i$ as

$$\delta\overline{Q} = \sqrt{\frac{1}{N(N-1)}\sum_{j=1}^{N}(\overline{Q} - Q_j)^2}\,, \tag{7.4}$$

where j runs through the N bins in the histogram. `Edep` and `Qdep` distributions are completely correlated from the nature of the observation of the energy deposition in the detector, and therefore all energies in each bin of `Edep` are distributed in `Qdep` for said bin and averaged out to calculate `Qdep`. Under this perspective the uncertainty $\delta\overline{E}$ will be embedded into $\delta\overline{Q}$ for the study of systematic uncertainties.

The fit of `projQdep-simu` and `projQdep-data` uses $\overline{Q}^i \pm \delta\overline{Q}^i$ as starting point, first for the individual fits, and later for the combined fit. $\delta\overline{Q}^i$ is not parsed into the fits and thus the final uncertainty of μ^i is then only statistical, as mentioned above. This is done by parsing to the fit as initial condition the two limit cases $\overline{Q}^i + \delta\overline{Q}^i$ and $\overline{Q}^i - \delta\overline{Q}^i$ instead of $\overline{Q}^i$. These two fits will yield μ^i_+ and μ^i_- for each peak respectively, and from the difference between them the percentage of uncertainty

$$r^i_{\delta Q\pm} = 100 \cdot \frac{|\mu^i_\pm - \mu^i|}{\mu^i}\,, \tag{7.5}$$

can be defined. The rest of parameters extracted from the fit are irrelevant to the calculation of the quenching curve as far as the fit converges with a reasonable *goodness of fit*. Thus, the effect of $\delta\overline{Q}^i$ in the final μ^i is used as a representation of the uncertainty on the whole fit. Results from these calculations, shown in percentage of the parameter μ^i, can be seen in the third and fourth columns of Tab. 7.4 and Tab. 7.3 for data ans simulation, respectively. There it can be seen that the ^{124}Sb spectra are the most sensitive to a change on the initial conditions, followed by the high energy peak of ^{24}Na. For these multi-gamma sources, the peak corresponding to their high energy emissions overlaps with the double-gamma peak, makes the fit specially sensitive to the choice of $\overline{Q}^i$ and $\overline{Q}^{i+j}$. This also applies to the low energy gamma $i = 0$ from ^{124}Sb, which had a to be fitted including an additional contribution to the left of the peak.

Together with the choice of initial conditions, the systematic effects tied to the range of the fit have also been investigated. A complete fit of the spectrum requires that all important features of the distribution are taken into account. The limits chosen, described in step 2, often cover most of the histogram including areas prior and beyond the peaks. For mono-gamma sources it has been observed that enlarging or reducing the fit range by a 5% had negligible effects in the resulting parameters nor in the convergence. For multi-gamma sources, the range of both the individual and the complete fits have

Table 7.3: Compendium of statistical and systematic uncertainties affecting the estimation of μ^i for each emission i in simulation.

Source/i	$r_{\delta\mu_{\text{stat}}}$	$r_{\delta Q+}$	$r_{\delta Q-}$	range +5%	range −5%	cell-to-cell	$r_{\delta\mu_{\text{sys}}}$
^{124}Sb/0	0.10%	0.75%	0.50%	0.25%	0.25%	-	1.00%
^{137}Cs/1	0.10%	$< 0.10\%$	$< 0.10\%$	$< 0.10\%$	$< 0.10\%$	-	neglect
^{54}Mn/2	0.10%	$< 0.10\%$	$< 0.10\%$	$< 0.10\%$	$< 0.10\%$	-	neglect
^{65}Zn/3	0.10%	$< 0.10\%$	$< 0.10\%$	$\sim 0.10\%$	$\sim 0.10\%$	-	0.15%
^{24}Na/4	0.10%	$< 0.10\%$	$< 0.10\%$	$\sim 0.10\%$	$\sim 0.10\%$	-	0.15%
^{124}Sb/5	0.20%	1.25%	0.75%	0.25%	0.25%	-	1.50%
H (n,γ)/6	0.20%	$< 0.10\%$	$< 0.10\%$	$\sim 0.25\%$	$< 0.10\%$	-	0.25%
^{24}Na/7	0.10%	0.10%	0.25%	0.10%	0.25%	-	0.5%
AmBe/8	0.20%	$< 0.10\%$	$< 0.10\%$	$< 0.10\%$	0.25%	0.50%	0.60%

Table 7.4: Compendium of statistical and systematic uncertainties affecting the estimation of μ^i for each emission i in data.

Source/i	$r_{\delta\mu_{\text{stat}}}$	$r_{\delta Q+}$	$r_{\delta Q-}$	range +5%	range −5%	cell-to-cell	$r_{\delta\mu_{\text{sys}}}$
^{124}Sb/0	0.10%	0.75%	0.50%	0.10%	0.35%	-	1.0%
^{137}Cs/1	0.10%	$< 0.10\%$	$< 0.10\%$	$< 0.10\%$	$< 0.10\%$	-	neglect
^{54}Mn/2	0.10%	$< 0.10\%$	$< 0.10\%$	$< 0.10\%$	$< 0.10\%$	-	neglect
^{65}Zn/3	0.10%	$< 0.10\%$	$< 0.10\%$	$< 0.10\%$	$< 0.10\%$	-	neglect
^{24}Na/4	0.10%	$< 0.10\%$	$< 0.10\%$	$\sim 0.10\%$	$\sim 0.10\%$	-	0.15%
^{124}Sb/5	0.10%	1.00%	0.50%	0.25%	0.25%	-	1.20%
H (n,γ)/6	0.20%	$< 0.10\%$	$< 0.10\%$	0.25%	$< 0.10\%$	-	0.25%
^{24}Na/7	0.10%	0.10%	0.25%	0.10%	0.25%	-	0.5%
AmBe/8	0.20%	$< 0.10\%$	$< 0.10\%$	$< 0.10\%$	0.25%	0.50%	0.60%

been tested. For the ^{24}Na source it has been observed that a shift on the limits of the complete fit has negligible effects on the results. However, changes on the limits of the individual fits has been proven to yield slightly different values for $\mu^{(0)i}$ which ends up leading to small systematic effects on μ^i not larger than 0.25%. This is specially relevant for the high energy gamma $i = 7$, where increasing the range leads to an overlapping with the double gamma peak. In contrast to ^{24}Na, the results from ^{124}Sb source are affected by shifting the limits of both individual and complete fits. It can be seen in Fig. 7.7(b) that the complex spectrum from ^{124}Sb has no soft borders, and both at high and low energies there are additional contributions not taken into account in the fit. The overall effect of modifying the borders for both type of fits is reflected in the fifth and sixth columns of Tab.7.3 and Tab.7.4 for simulation and data respectively.

A final consideration on the systematic analysis needs to be done regarding the extraction of the 4.44 MeV point from the AmBe source. It has been described in step 2 that this point is obtained from charge deposited in `Cell5` due to proton recoil contamination. The conversion from charge in `Cell5` to charge in `Cell6` comes along with an uncertainty from the calculation of $\texttt{cc}_5$ and $\texttt{cc}_6$, calculated in Sec. 6.1. By using Eq. C.3, $\delta\texttt{cc}_5$ and $\delta\ \texttt{cc}_6$ can be propagated to obtain $\delta\frac{\texttt{cc}_6}{\texttt{cc}_5} = 0.005$. The relative contribution in percentage amounts to

$$r_{\delta\texttt{cc}} = 100 \cdot \frac{\delta\frac{\texttt{cc}_6}{\texttt{cc}_5}}{\frac{\texttt{cc}_6}{\texttt{cc}_5}} = 0.50\% \,. \tag{7.6}$$

This uncertainty drives the systematics for the 4.44 MeV point. The final systematic uncertainty $\delta\mu_{\text{sys}}$ has been calculated as the sum in quadrature of all the individual contributions. The relative magnitude is defined again as,

$$r_{\delta\mu_{\text{sys}}} = 100 \cdot \frac{\delta\mu^i_{\text{sys}}}{\mu^i} \,. \tag{7.7}$$

Step 4: Calculate Quenching Curve

After step 3, a wide range of mean charges μ^i and their correspondent deposited energies E^i_{dep} are available for data and for simulations with different $\texttt{kB}_{\text{simu}}$. For each one of these sets a quenching curve can be drawn in terms of the quenching factor,

$$\xi(E^i_{\text{dep}}, \texttt{kB}) = \frac{\mu^i / E^i_{\text{dep}}}{\mu^6 / E^6_{\text{dep}}} \,. \tag{7.8}$$

The denominator in Eq. 7.8 represents the anchoring point to which all quenching curves are normalized. By doing this, linearity can be studied by direct comparison between curves of data and simulations, removing any dependence on the absolute normalization of the charge spectra. During the first analysis of quenching effects in **Stereo**, also a result from this thesis, the anchor point selected was $i = 2$ from the ^{54}Mn source [123]. However, high energy gammas are less affected by quenching non-linearities, making them more reliable candidates to anchor the curves. For the results presented in this manuscript, the analysis from [123] is revisited with the $i = 6$ peak from n-capture in hydrogen at 2.22 MeV as anchor point. One consequence from this choice can be seen in Fig. 7.8(b), where $\xi(E^i_{\text{dep}}, \texttt{kB})$ is displayed for the different $\texttt{kB}_{\text{simu}}$ and also for data. There, each curve crosses the point $\xi(E^6_{\text{dep}}, \texttt{kB}) = 1$ due to the anchoring at $i = 6$. Other high energy emissions have been contemplated to normalize the quenching curves. The two available options are either $i = 7$ from ^{24}Na and $i = 8$ from AmBe. However, as shown in the intermission, both peaks have larger associated systematic uncertainties, making $i = 6$ the preferred option. The uncertainty of μ_i is translated to $\xi(E^i_{\text{dep}}, \texttt{kB})$ by means of Eq. C.3, for both statistical and systematic components.

The relative comparison between experimental and simulated quenching curves can be performed by defining the ratio between data and simulation as

$$\Delta(E^i_{\text{dep}}, \texttt{kB}_{\text{simu}}) = \frac{\xi(E^i_{\text{dep},\texttt{kB}})}{\xi(E^i_{\text{dep},\texttt{kB}_{\text{simu}}})} \,. \tag{7.9}$$

The distribution of $\Delta(E^i_{\text{dep}})$ can be observed in Fig. 7.8(a) for each $\texttt{kB}_{\text{simu}}$. The uncertainty for each $\delta\Delta(E^i_{\text{dep}}, \texttt{kB}_{\text{simu}})$ point is calculated from Eq. C.3 as a propagation of the uncertainty of $\xi(E^i_{\text{dep}}, \texttt{kB}_{\text{simu}})$ and $\xi(E^6_{\text{dep}}, \texttt{kB}_{\text{simu}})$, and the relative uncertainty is given by,

$$r_{\delta\Delta}(E^i_{\text{dep}}, \texttt{kB}_{\text{simu}} = 100 \cdot \frac{\delta\Delta(E^i_{\text{dep}}, \texttt{kB}_{\text{simu}})}{\Delta(E^i_{\text{dep}}, \texttt{kB}_{\text{simu}})} \,. \tag{7.10}$$

Each of the curves in Fig. 7.8 displays a different behavior depending on how close $\texttt{kB}_{\text{simu}}$ is to $\texttt{kB}$. By definition, $\Delta(E^i_{\text{dep}}, \texttt{kB}_{\text{simu}})$ is also normalized to the 2.22 MeV point in the same way as $\xi(E^i_{\text{dep}}, \texttt{kB}_{\text{simu}})$. This anchoring defines the way the curve for each $\texttt{kB}_{\text{simu}}$ behaves. For high $\texttt{kB}_{\text{simu}}$ values, simulated response for low-energy gammas is below what can observed for data and thus $\Delta(E^i_{\text{dep}}, \texttt{kB}_{\text{simu}}) > 1$. This clearly determines the regime where $\texttt{kB}_{\text{simu}} > \texttt{kB}$. For higher energies than the anchor point the quenching effect is small and thus no clear behavior can be seen outside the uncertainty bars. As $\texttt{kB}_{\text{simu}}$ approaches the experimental value, the distributions in Fig. 7.8(a) start

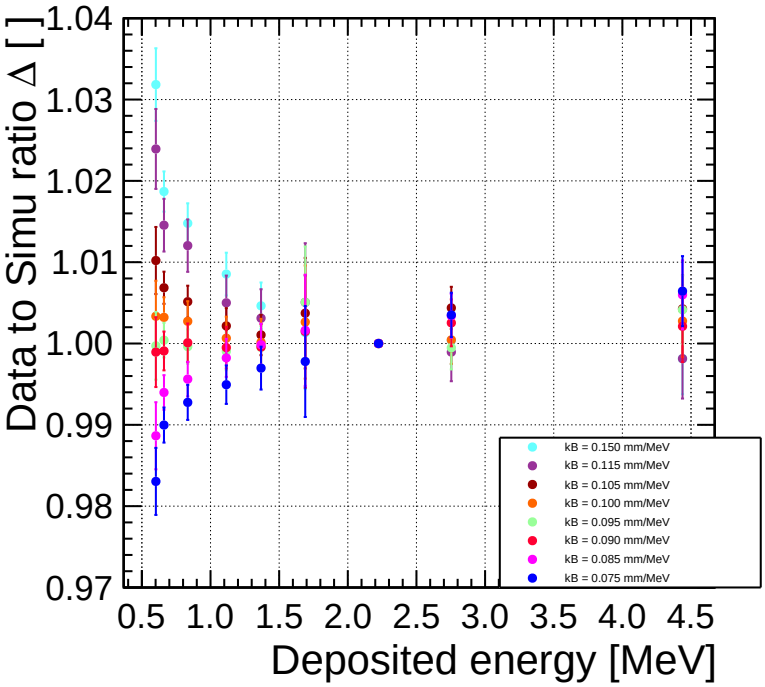

(a)

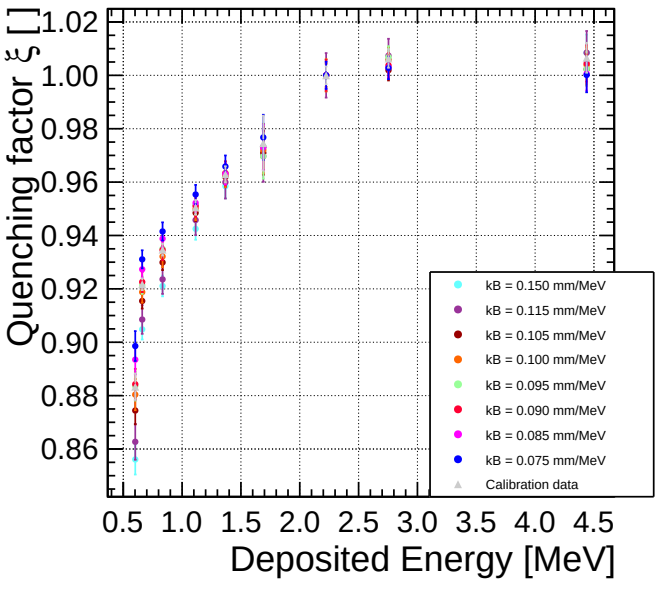

(b)

(c)

Figure 7.8: Quenching curves in terms of (b) the quenching factor $\xi(E^i_{\text{dep}})$ and (a) the data to simulation ratio $\Delta(E^i_{\text{dep}})$, for a variety of different $\texttt{kB}_{\text{simu}}$. Low enegies display clearly the effect of the quenching. When comparing simulation to data in (b), a descending parabola is observed for $\texttt{kB}_{\text{simu}} > \texttt{kB}$ and an ascending parabola for $\texttt{kB}_{\text{simu}} < \texttt{kB}$. The combination of both creates the shape of a kitchen funnel, depicted in (c) by the picture *Cutting the Stone*, 1494, from Hieronymus Bosch [169].

flattening around $\Delta(E^i_{\text{dep}}, \texttt{kB}_{\text{simu}}) \sim 1.0$, for the whole energy range. The best agreement can be observed between $0.100 \geq \texttt{kB}_{\text{simu}} \geq 0.090\,\text{mm/MeV}$. On the contrary, continuing towards the bottom of Fig. 7.8(a), simulated low-energy gammas create a signal that is quenched less than for data, leading to the regime where $\texttt{kB}_{\text{simu}} < \texttt{kB}$ and thus $\Delta(E^i_{\text{dep}}, \texttt{kB}_{\text{simu}}) < 1$. The representation of both behaviors create at low energies opposing distributions that together resemble the shape of a kitchen funnel [168]. In step 5, all these quenching curves will be compared and used to fit the optimal $\texttt{kB}_{\text{simu}}$ that represents data with highest accuracy.

Step 5: Test the Optimal $\texttt{kB}_{\text{simu}}$

In the final step of the SecM, the comparison between data and simulations portrayed by the $\Delta(E^i_{\text{dep}}, \texttt{kB}_{\text{simu}})$ curve in Fig. 7.8(a) will be translated into a quantitative statement on the optimal $\texttt{kB}_{\text{simu}}$. In the scenario where simulated quenching perfectly reproduces data ratio $\Delta(E^i_{\text{dep}}, \texttt{kB}_{\text{simu}} = \texttt{kB}) = 1$ for all energies E^i_{dep}. Comparing then $\Delta(E^i_{\text{dep}}, \texttt{kB}_{\text{simu}})$ directly to a flat distribution would point out the $\texttt{kB}_{\text{simu}}$ from the simulated range that is most compatible with kB. However, this method does not provide an sufficiently accurate description of kB in the simulation and can be improved. A more refined approach to find the optimal $\texttt{kB}_{\text{simu}}$ has been developed in this thesis. It consists on fitting the observed $\Delta(E^i_{\text{dep}}, \texttt{kB}_{\text{simu}})$ distribution to an analytical expression that explicitly depends on kB from where it can be extracted. This function is not known a priori, but knowing that $\Delta(E^i_{\text{dep}}, \texttt{kB}_{\text{simu}} = \texttt{kB}) = 1$, it can be expanded around $\texttt{kB}_{\text{simu}} = \texttt{kB}$ in terms of a Taylor series [166],

$$\begin{aligned}\Delta^{\text{ana}}(E^i_{\text{dep}}, \texttt{kB}_{\text{simu}}) =& \Delta(E^i_{\text{dep}}, \texttt{kB}) + \\ &+ \frac{\partial \Delta(E^i_{\text{dep}}, \texttt{kB}_{\text{simu}})}{\partial \texttt{kB}_{\text{simu}}}\bigg|_{\texttt{kB}_{\text{simu}} = \texttt{kB}} \cdot (\texttt{kB}_{\text{simu}} - \texttt{kB}) + \mathcal{O}(\texttt{kB}_{\text{simu}} - \texttt{kB})^2\end{aligned} \tag{7.11}$$

which has been truncated to first order. This approximation can be considered valid as long as $\texttt{kB}_{\text{simu}} - \texttt{kB} \gtrsim 10 \cdot (\texttt{kB}_{\text{simu}} - \texttt{kB})^2$, condition fulfilled by the range of $\texttt{kB}_{\text{simu}}$ used in step 4. The first order derivative portrayed in Eq. 7.11 can be built in different ways, depending on the number of parameters used. The curves in 7.8(a) can intuitively be related to a fraction function of the type $f(x) \sim \frac{1+x}{1-x}$. One of the simplest and most flexible functions that can be used is defined by four independent parameters p_0, p_1, p_2 and p_3,

$$\frac{\partial \Delta(E^i_{\text{dep}}, \texttt{kB}_{\text{simu}})}{\partial \texttt{kB}_{\text{simu}}} = \left(\frac{p_0 + p_1 E^i_{\text{dep}}}{p_2 + p_3 E^i_{\text{dep}}} \right) . \tag{7.12}$$

By plugging Eq. 7.12 into Eq. 7.11, and using $\Delta(E^i_{\text{dep}}, \texttt{kB}) = 1$, the final fit function becomes,

$$\Delta^{\text{ana}}(E^i_{\text{dep}}, \texttt{kB}_{\text{simu}}) = 1 + \left(\frac{p_0 + p_1 E^i_{\text{dep}}}{p_2 + p_3 E^i_{\text{dep}}} \right) \cdot (\texttt{kB}_{\text{simu}} - p_4) , \tag{7.13}$$

where p_0, p_1, p_2 and p_3 are complementary parameters and p_4 corresponds to the optimal kB that matches data. Eq. 7.13 needs to describe all quenching curves in 7.8(a) simultaneously with their respective $\texttt{kB}_{\text{simu}}$. The contribution $(\texttt{kB}_{\text{simu}} - p_4)$ ensures that

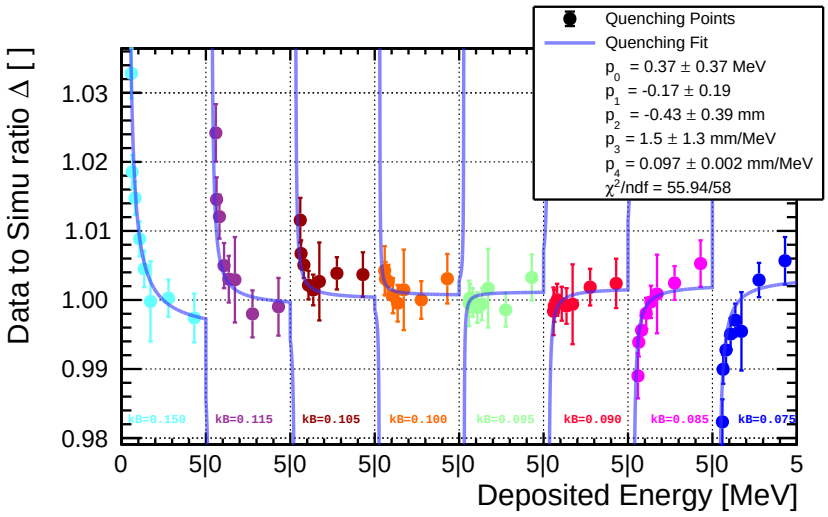

Figure 7.9: Distribution of $\Delta(E^i_{\text{dep}}, \texttt{kB}_{\text{simu}})$ extracted from Fig. 7.8 and fitted to Eq. 7.13. All gamma peaks are included in the fit.

the behavior of the curves for $\texttt{kB}_{\text{simu}} > \texttt{kB}$ is flattened as $\texttt{kB}_{\text{simu}}$ approaches kB, provoking a reflection of the parabolic trend when $\texttt{kB}_{\text{simu}} < \texttt{kB}$.

One of the strengths of using such function is that it depends on $\texttt{kB}_{\text{simu}}$ and thus it can take advantage of all simulations performed. The results of the fit can be seen in Fig. 7.9, where the quenching curves from Fig. 7.8 have been distributed along the x-axis together with their uncertainties. The fit shows overall good agreement with the distribution of points, yielding a $\bar{\chi}^2 \sim 1$. However, p_0, p_1, p_2 and p_3 parameters display rather high uncertainties after the fit, of the same order of magnitude as their respective values. This issue arises from the relatively large fluctuations of the high energy emissions above the anchor point at 2.22 MeV. These fluctuations affect directly the shape of the derivative from Eq. 7.12, increasing thus the uncertainty on the curve. The p_4 parameter, on the contrary, is more stable than the rest of the parameters. The relative uncertainty of $\sim 2\%$ for p_4 is lower than the simulated step taken between $\texttt{kB}_{\text{simu}}$. This is related to the fact that p_4 does not rely as much on the individual points but on the overall flatness of the distribution for each $\texttt{kB}_{\text{simu}}$. The region of larger flatness is visibly $0.100 \geq \texttt{kB}_{\text{simu}} \geq 0.090\,\text{mm/MeV}$, and thus p_4 is mostly limited to that area. Despite the accurate value obtained for kB, the remaining uncertainties of the fit portray an insufficient robustness on the fit that could lead to a potential bias on the final number. Specially taking into account that the values driving these uncertainties are precisely the ones at high energies that should affect less the determination of the quenching. For this reason, the same analysis has been performed for a smaller range of energies, without the two high energy gamma points, $i = 7$ and $i = 8$. The result of this fit is shown in Fig. 7.10. It can be seen that, while $\bar{\chi}^2$ remains similar than for Fig. 7.9, when taking the reduced range all parameters are more accurately fitted. In order to accommodate the new fit, p_4 has shifted from $p_4 = 0.097$ to $p_4 = 0.093$. Although this new result is still within the uncertainty range from the previous fit, it shows that high energy points were biasing the optimal kB to a value representing a larger quenching.

The choice for anchoring point used to fix the $\xi(E^i_{\text{dep}}, \texttt{kB}_{\text{simu}})$ distribution, namely the $i = 6$ peak at 2.22 MeV, has been already described in step 4. This choice, however,

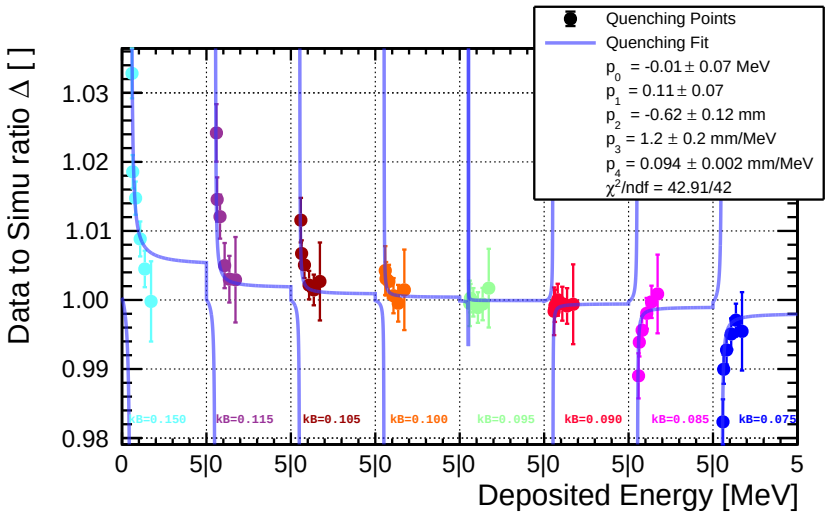

Figure 7.10: Distribution of $\Delta(E^i_{\text{dep}}, \texttt{kB}_{\text{simu}})$ extracted from Fig. 7.8 and fitted to Eq. 7.13. Peaks $i = 7$ from ^{24}Na and $i = 8$ from AmBe are excluded from the fit.

could be the source of additional systematic uncertainties that have been investigated in the following lines. The process in step 4 has been repeated for all points used in Fig. 7.10 as anchoring points for $\xi(E^i_{\text{dep}}, \texttt{kB}_{\text{simu}})$. The corresponding quenching curves have been fitted to Eq. 7.13 in the same manner as described above, and the resulting kB has been listed in Tab. 7.5 together with their associated uncertainties. These uncertainties have been calculated as the averaged systematic and statistical relative uncertainties of all $\Delta(E^i_{\text{dep}}, \texttt{kB}_{\text{simu}})$ points,

$$r_{\delta \texttt{kB}_{\text{sys}}} = \sum_i \frac{1}{n_\gamma} r^i_{\delta\Delta_{\text{sys}}}, \tag{7.14}$$

$$r_{\delta \texttt{kB}_{\text{stat}}} = \sum_i \frac{1}{n_\gamma} r^i_{\delta\Delta_{\text{stat}}}, \tag{7.15}$$

with $r^i_{\delta\Delta_{\text{sys}}}$ and $r^i_{\delta\Delta_{\text{stat}}}$ obtained from Eq. 7.10.

All values of kB from Tab. 7.5 are in agreement with each other well within the uncertainties. Since the standard deviation of these values $\sigma_{\texttt{kB}} = 0.0005\,\text{mm/MeV}$ adds a negligible contribution to the final uncertainty, the $i = 6$ has been set as anchor point while the rest are used as cross-checks. Finally, the effective quenching factor obtained

Table 7.5: Optimal kB values obtained for different anchoring points by fitting $\Delta(E^i_{\text{dep}}, \texttt{kB}_{\text{simu}})$ to Eq. 7.13. Statistic uncertainty comes from Eq. 7.14

Anchor [MeV]	kB [mm/MeV]	$\delta\texttt{kB}_{\text{stat}}$ [mm/MeV]	$\delta\texttt{kB}_{\text{sys}}$ [mm/MeV]
n-capt H (2.223)	0.0938	0.0023	0.0024
^{124}Sb (0.603)	0.0945	0.0028	0.0035
^{137}Cs (0.662)	0.0941	0.0018	0.0021
^{54}Mn (0.832)	0.0936	0.0017	0.0020
^{65}Zn (1.115)	0.0930	0.0025	0.0024

Table 7.6: Summary of results on the quenching analysis by the three different approaches taken for **STEREO** during *Phase I*.

Approach	$\mathtt{kB}$ [mm/MeV]	$\delta\mathtt{kB}^{\text{stat}}$ [mm/MeV]	$\delta\mathtt{kB}^{\text{sys}}$ [mm/MeV]	$\delta\mathtt{kB}$ [mm/MeV]
SecM	0.094	0.002	0.002	0.003
LAPP Method	0.089	0.014	0.011	0.018
CEA Method	0.114	0.010	0.011	0.015

by the SecM for the LS in the TG volume is,

$$\mathtt{kB} = 0.0938 \pm 0.0023(\text{stat}) \pm 0.0024(\text{sys}) \text{ mm/MeV}. \tag{7.16}$$

7.1.2 Final Quenching

Until now, only the results from the SecM have been discussed. During the process of tuning the quenching in the simulation of **STEREO** other approaches were taken with the aim of shredding light to possible biases of the analysis method used, and cross-check results. One of the alternative approaches, performed by Sergeyeva V at LAPP [141], is based on energy and charge depositions in Cell5 with calibration data from Cell6 and Cell4. As for the SecM, the main motivation for such approach is to avoid contamination from proton recoils for the AmBe source as much as possible. The main difference with the SecM strives from the fact that all sources are analyzed in Cell5 in order to minimize cell-to-cell effects. For AmBe, calibration data from Cell4 is used, where the distance towards the detection volume is larger than from Cell6. The rest of sources are placed in Cell6.

Another type of analysis has been performed by Blanchet A at CEA [138] by means of the reconstructed energy Erec spectra from the different sources deployed in Cell6. In this approach, Erec is compared to the expected energy reconstruction of a perfectly linear simulated response. The latter is obtained by convoluting the Edep distribution with a gaussian obtained from requesting true FED events in the simulation. By comparing data and simulation to the expected linear behavior of the energy reconstruction, quantifiable non-linearities can be calculated. This method also requires energy deposition in Cell6 by forcing $< 0.2\,\text{MeV}$ depositions in neighboring cells.

Results from the two aforementioned methods and the SecM are listed all together in Tab.7.6. Next to their respective $\mathtt{kB}$ values, statistical and systematic uncertainties associated to each of the measurements are also listed and added in quadrature. All three values for $\mathtt{kB}$ have been then combined by means of a weighted average,

$$\overline{\mathtt{kB}} = \frac{\sum_j \mathtt{kB}_j/\sigma_j}{\sum_k 1/\delta\mathtt{kB}_k}\,, \tag{7.17}$$

$$\overline{\delta\mathtt{kB}} = \sqrt{\frac{\sum_j \frac{(\overline{\mathtt{kB}}-\mathtt{kB}_j)^2}{\delta\mathtt{kB}}}{\sum_k 1/\delta\mathtt{kB}_k}}\,, \tag{7.18}$$

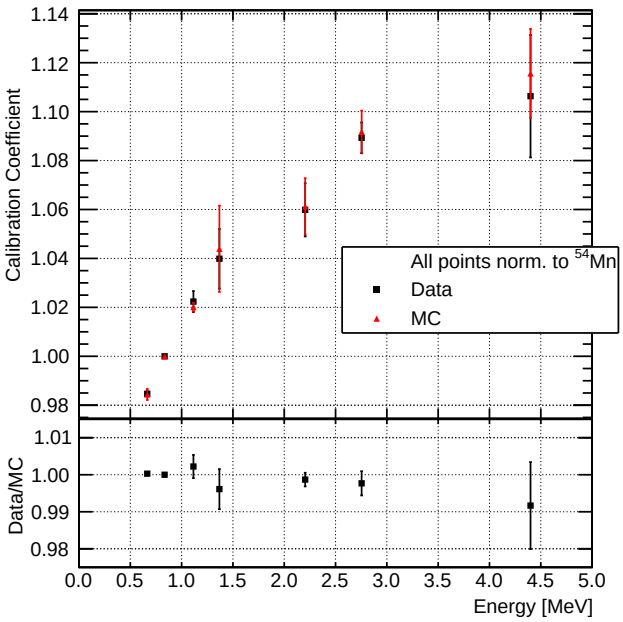

Figure 7.11: Quenching curves in terms of $\xi(E^i_{\text{dep}}, \texttt{kB}_{\text{simu}} = 0.096)$, for a combined analysis with LAPP and `SecM` points. In red, simulation `kB` = 0.096 mm/MeV. In black, calibration data from 22.II.2017 during *Phase I*. At the bottom, data to simulation ratio $\Delta(E^i_{\text{dep}}, \texttt{kB}_{\text{simu}} = 0.096)$ [123].

to yield the final value representing quenching in the **STEREO**:

$$\overline{\texttt{kB}} = 0.096 \pm 0.007\,\text{mm/MeV}\,. \tag{7.19}$$

Results from LAPP and `SecM` have been summarized in Fig. 7.11 [123]. There, simulation and data $\xi(E^i_{\text{dep}}, \texttt{kB}_{\text{simu}} = 0.096)$ points for ^{137}Cs, ^{54}Mn, ^{65}Zn, ^{24}Na and AmBe are represented. They are all anchored to the ^{54}Mn point. The values for these points correspond to the average from both analyses. The source ^{124}Sb has been excluded because it was not a common used source between both methods. The simulated quenching curve corresponds to `kB` = 0.096 mm/MeV, and it is in direct comparison with calibration data for *Phase I*. At the bottom of Fig. 7.11, the ratio $\Delta(E^i_{\text{dep}}, \texttt{kB}_{\text{simu}})$ between data and simulation is portrayed.

7.2 Extensions of the `SecM`

7.2.1 Extension to Gamma Catcher Volume

In this section, the non-linear quenching effects on the `LS` of the `GC` volume have been investigated. It has been already discussed in Sec. 3.4.3 that these non-linearities come mainly from the ionization process, mostly dependent on the main solvents of the liquid. Since `LS` in both volumes are composed by a similar concentration of solvents, there are no strong arguments to expect very different quenching for `TG` and `GC`.

The studies on $\texttt{kB}^{\text{GC}}$ have been carried on using the `SecM` for a range of $\texttt{kB}_{\text{simu}}$ around $\overline{\texttt{kB}} = 0.096$ mm/MeV. The calibration data and simulations used in this study are the same as for step 1, with the only difference that now the volume where charge

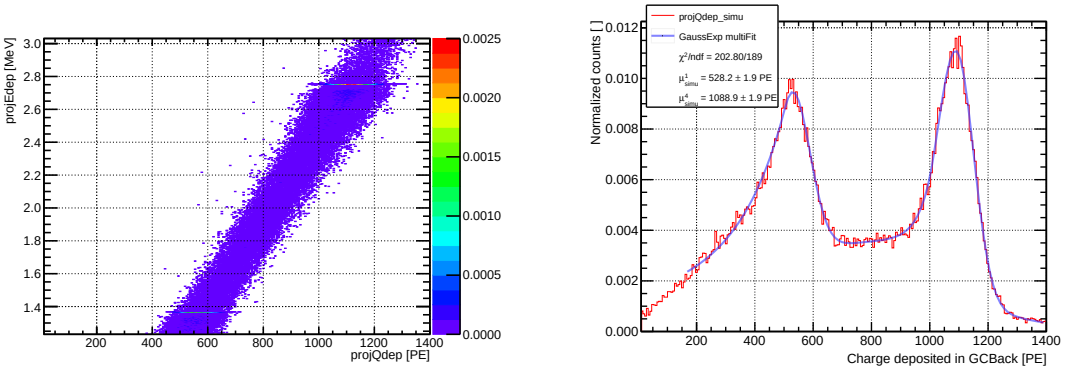

(a) **(b)**

Figure 7.12: `projQdep-data` distributions for (a) ^{65}Zn and (b) ^{124}Sb 124 fitted to their respective fit functions. In grey, charge distributions. In translucent orange, fit functions listed in Tab. 7.2.

and energy depositions are requested is `Cell7`, while sources continue being deployed at *middle* inside `Cell6`. By doing this, there is an observable reduction of statistics available for the fit that increases the contribution of the statistical uncertainty to the final value.

As a representation of step 1, the two-dimensional distribution `projEdep` for the ^{24}Na source is displayed in Fig. 7.12(a), and the charge-axis projection `projQdep-simu` in Fig. 7.12(b). From these plots, it can be observed that the double-gamma peak from ^{24}Na has mostly vanished from the spectrum, leading to more defined single peaks. This is a side effect of requesting charge and energy deposition in `Cell7`, where the detection of two gammas simultaneously is much less frequent than single gammas.

Following step 2 and step 3, mean deposited charges μ^i for each gamma emission i are extracted from the fits of `projQdep-simu` and `projQdep-data`. From these, the quenching curves are also drawn in terms of $\xi(E^i_{\text{dep}}, \texttt{kB}^{\text{GC}})$ and $\Delta(E^i_{\text{dep}}, \texttt{kB}^{\text{GC}})$, as depicted in Fig. 7.13(a) and Fig. 7.13(b). Systematic uncertainties have been kept the same than for previous studies on `TG`, seen in the intermission, with the exception of cell-to-cell correction uncertainty for $i = 8$. Statistical uncertainties, on the contrary, have increased noticeably to $r_{\delta\Delta} \sim 3.5\%$, as anticipated in previous paragraphs due to the reduced amount of events in the spectra.

The data set in Fig. 7.13(b) has been parsed through step 5 in order to find the optimal $\texttt{kB}^{\text{GC}}$ that describes energy non-linearities of calibration data in `Cell7`. Again, Eq. 7.13 has been fitted simultaneously to all $\Delta(E^i_{\text{dep}}, \texttt{kB}^{\text{GC}})$ distributions. Two different fits have been produced with all gamma emissions and removing the two peaks with highest energy, $i = 7$ and $i = 8$. Both are shown in Fig. 7.14(a) and Fig. 7.14(b) respectively. Both fits yield the same result within uncertainty level, finally setting

$$\texttt{kB}^{\text{GC}} = 0.093 \pm 0.003(\text{stat}) \pm 0.002(\text{sys})\ \text{mm/MeV}. \tag{7.20}$$

As stated above, the systematic uncertainty used corresponds to the same obtained for final value of `kB` in `TG` for the `SecM`. The main purpose of this analysis is to prove the compatibility between $\texttt{kB}^{\text{GC}}$ and `kB`. Since both values are completely equivalent even

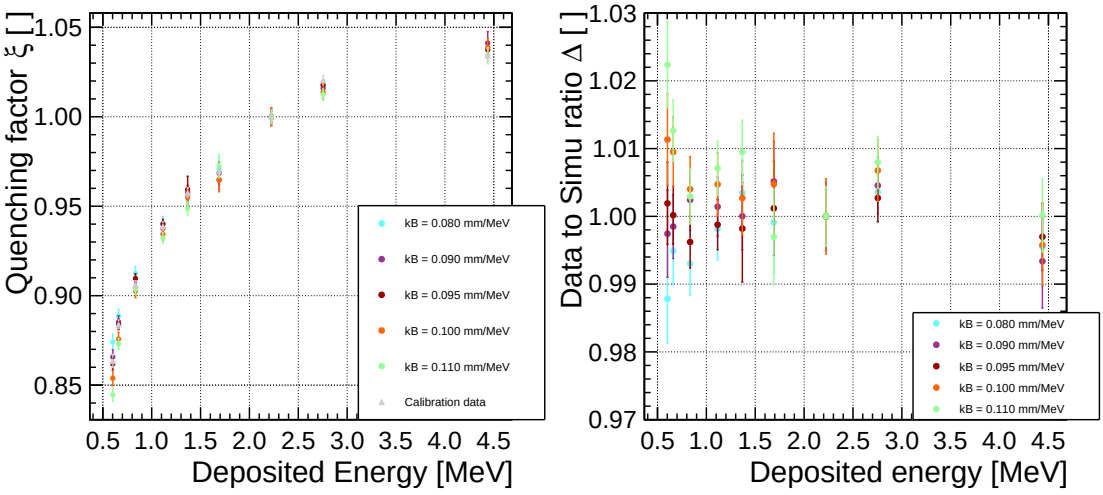

(a) (b)

Figure 7.13: Quenching curves for LS inside the GC in terms of (a) the quenching factor $\xi(E^i_{\text{dep}}, \texttt{kB}^{\text{GC}})$ and (b) the quenching ratio $\Delta(E^i_{\text{dep}}, \texttt{kB}^{\text{GC}})$.

within statistical uncertainties, in-depth analysis of the systematic effects has not been performed.

7.2.2 Extension to *Phase II*

The energy scale of the detector has been seen in Sec. 6.3.4 to remain stable throughout the two phases of data taking. It is then expected that energy non-linearities on the detector response have not increased for *Phase II* and thus, a full quenching analysis has been considered not necessary. Instead, a compatibility study has been performed between calibration data from *Phase I* and *Phase II*. Such analysis has been done only for liquid in the TG volume, and results have been understood for GC as well.

During *Phase II* there have been several calibration rounds with the whole range of

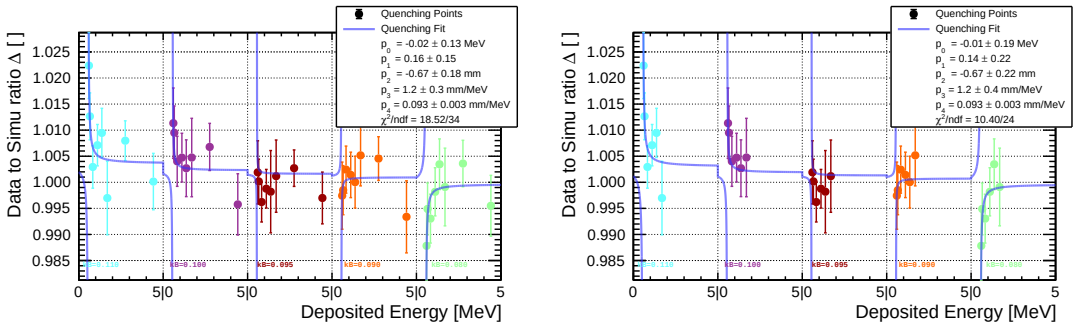

(a) (b)

Figure 7.14: Distribution of $\Delta(E^i_{\text{dep}}, \texttt{kB}^{\text{GC}})$ extracted from Fig. 7.13(b) and fitted to Eq. 7.13. (a) All gamma peaks are included in the fit. (b) Peaks $i = 7$ from ^{24}Na and $i = 8$ from AmBe are excluded from the fit.

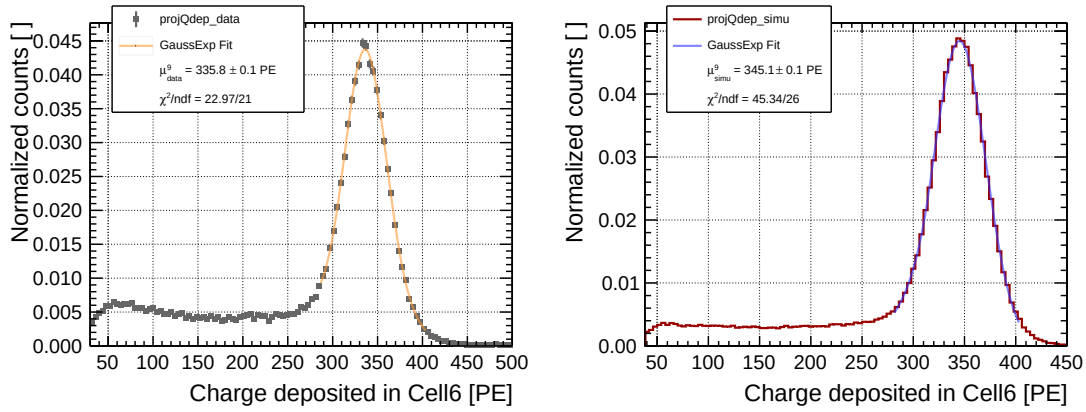

(a) (b)

Figure 7.15: Results from fitting (a) `projQdep-simu` and (b) `projQdep-data` for the ^{45}K source used during the calibration runs for *Phase II*. The function used is *GaussExp* for (a) and *Double-GaussExp* for (b).

calibration sources described in Sec. 3.6. With them, the stability of `kB` can be cross-checked to ensure a correct response of the detector. In this section, calibration data from the 26.IV.2018 is analyzed and compared to results obtained in the previous sections for data from 22.II.2017. As depicted in Tab. 3.1 in Sec. 3.6, ^{124}Sb and ^{65}Zn sources have not been used because they could not be produced. To compensate, the ^{45}K source covers the space around $\sim 1.5\,$MeV. The deposited charge spectrum from ^{45}K has been fitted in the same way as for ^{65}Zn, using a *GaussExp* in simulation and using a *Double-GaussExp* in data. Fig. 7.15 displays the results of both fits.

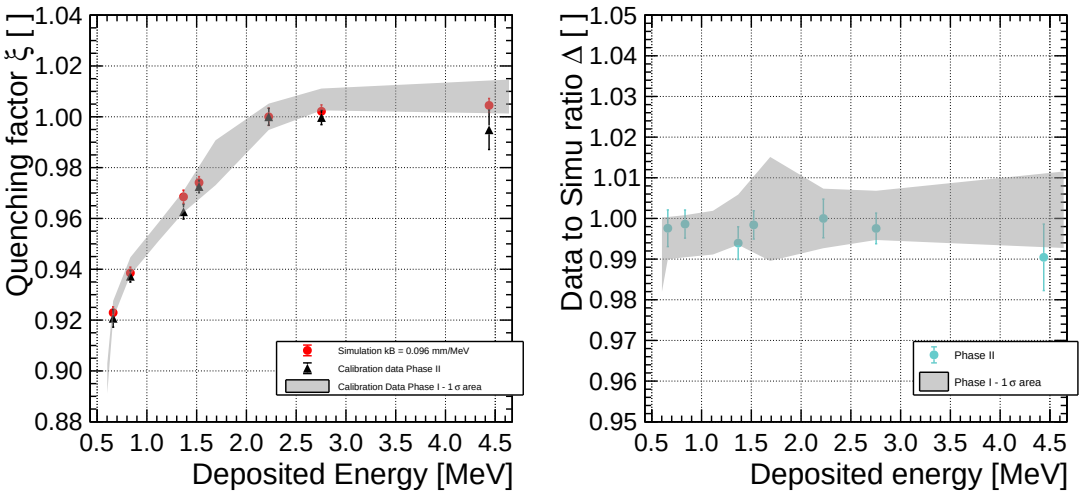

(a) (b)

Figure 7.16: Quenching curves in terms of (a) the quenching factor $\xi(E^i_{\text{dep}})$ and (b) the data to simulation ratio $\Delta(E^i_{\text{dep}})$ for *Phase II* calibration data, in black, and simulation with $\texttt{kB}_{\text{simu}} = 0.096\,$mm/MeV, in red. The quenching curve corresponding to *Phase I* is represented as a grey shadow covering the 1σ area.

The analysis have been peformed using the SecM described throughout steps 1 to 5. The resultant ξ quenching curve for *Phase II* is displayed in Fig. 7.16(a). There, it is compared with the corresponding simulated curve using $\texttt{kB}_{\text{simu}} = 0.096\,\text{mm/MeV}$, value obtained in the previous sections. For each one of the points of the curve, it can be seen that data and simulation are compatible within the uncertainty bars, being the agreement specially notable for the mono-gamma sources like ^{137}Cs and ^{45}K. The expected curve within 1σ assuming identical behavior as for *Phase I* is represented as a grey shadow beneath the curve. This expected curve has been drawn from results shown in Fig. 7.8 for calibration data. All points for *Phase II* lie within the uncertainty limits. Fig. 7.16(b) shows the same data points but in terms of the data-to-simulation ratio Δ, defined in Eq. 7.9. There, discrepancies between data and simulation are shown to be below the 1% level showing a good agreement between kB and $\texttt{kB}_{\text{simu}}$ with a $\bar{\chi}^2 = 1.3$. The same agreement between *Phase I* and *Phase II* as for 7.16(a) can be observed, where all *Phase II* points lie within the uncertainty shadow of *Phase I*. From this analysis it can be concluded that the LS has controlled and stable energy-related non-linearities on the detector response.

7.3 Summary

The understanding of the energy non-linearities associated to the response of the detector is crucial to perform an accurate spectral analysis of antineutrinos. During this chapter the procedure of characterization of these non-linearities have been described by means of the Stitched energy-charge Method (SecM). This 5-step algorithm has been developed as part of this thesis and makes use of a wide set of calibration sources to perform an iterative comparison between data and simulations.
In step 1 and step 1 of the SecM, the relation between deposited energy and collected charge in a single cell is investigated and used to draw quenching curves for simulations with different test non-linearities $\texttt{kB}_{\text{simu}}$. The exact same procedure is then applied to data in step 3 and the respective quenching curve is also drawn. In step 4 curves for data and simulations are compared by building a ratio for each $\texttt{kB}_{\text{simu}}$ used, and finally in step 5 the effective kB that would describe data in the simulations is extracted from a fit. This value has been found to be $\texttt{kB} = 0.0938 \pm 0.0023(\text{stat}) \pm 0.0024(\text{sys})$ mm/MeV for the LS in TG. The associated statistical and systematic uncertainties to this method are thoroughly addressed in the intermission.
The combination of this result with two alternative approaches developed by other teams of the **Stereo** collaboration has yielded to the official Birks' parameter of $\overline{\texttt{kB}} = 0.096 \pm 0.007\,\text{mm/MeV}$. After this result, the SecM has been used to perform a similar quenching analysis for the LS in the GC volume, which has resulted in a compatible Birks' parameter $\texttt{kB}^{\text{GC}} = 0.093 \pm 0.003(\text{stat}) \pm 0.002(\text{sys})$ mm/MeV.. These tests have also been extended to the *Phase II* period of data taking with a slightly different set of sources yielding also full compatibility with the already measured non-linearities. All in all, the SecM has proven to be a very adaptable and robust way of quantifying energy non-linearities in **Stereo**.

Conclusions

Neutrino oscillations have puzzled physicists for many decades since the first deficit of solar neutrinos was observed. Titanic international efforts have managed to give a successful explanation to the most ambiguous observations in neutrino physics. However, the recently discovered anomaly in the reactor neutrino sector has shaken the grounds of the understanding of neutrinos once more. To test the light sterile neutrino at short baselines hypothesis that could solve this anomaly, the **STEREO** experiment has set sail towards terra incognita and since 2016 its detector is undoubtedly measuring neutrino interactions, at a rate of $\sim 400\nu$/day.

An oscillation of reactor neutrinos with a squared mass difference of $\Delta m^2 \sim 1\,\text{eV}$ implies an oscillation length at the meter scale. For this reason, a detector like **STEREO**'s would be able to distinguish an oscillation signal by comparing neutrino energy spectra at different baselines, determined by the segmentation of the detector. Using one of the cells as reference, the **STEREO** analysis performs spectral ratios between cells and compares them to different simulated oscillatory and non-oscillatory hypotheses. For this reason, an excellent agreement between data and simulations is crucial to perform quantitative statements on the existence of sterile neutrino oscillations. Throughout this thesis major upgrades of the simulation framework of **STEREO** have been developed, obtaining as a result a very good agreement with observed data. ^{54}Mn calibration data has been used as the main tool for comparison between data and simulation.

The simulation in **STEREO** is built within the `Geant4` framework, including the detector geometry and shielding, particle transport and neutron physics. The simulation of the scintillation light production and its propagation is controlled by the dedicated set of libraries DCGLG4SIM used for the Double Chooz experiment and also based in `Geant4`. The effect of quantum yield of the fluors in the liquid scintillator have been tested in the simulation. Changes in the secondary fluor, bis-MSB, have been shown to have greater impact in the overall response than the primary fluor, PPO. Regardless, this response have been observed to have a stable plateau around the nominal values measured at the MPIK lab.

Other optical parameters used to simulate the liquid scintillator have been also tested in the simulation and tuned to a subpercent level agreement with calibration data. A particular effort has been put in testing the effect of the attenuation length of the liquid scintillator. Laboratory measurements showed values of $\sim 7\,\text{m}$ and $\sim 11\,\text{m}$ for target and gamma catcher liquid scintillators respectively. The effect of this parameter is best observed by comparing the response of the detector to events at different distances from the photomultipliers. Results from simulations portray a full compatibility with experimental values and hence these have been parametrized in the simulation framework.

During the first period of data taking of **STEREO**, a decrease of light collection of

GCFront and Cell4 could be observed. This effect has been confirmed by simulations to come from the emptying of the acrylic buffer. The removal of the oil bath that couples the cell with the photomultipliers is translated into a decrease of $\sim 60\%$ on the total simulated light collection, matching the experimental observations. In addition, an unexpected and rapid evolution of the light-cross talk between cells right after the commissioning phase of **Stereo** required a re-modeling of the optical separation between cells. Two different models have been implemented independently for the two phases of data taking of **Stereo**, and both replicate the effect of liquid scintillator in contact with the reflective plate. The first one, called the Homogeneous Probability p model, addresses the issue by applying a constant factor along the separation wall that increases the transmission of light in detriment of its reflection. The second mode, the Liquid Height h model is the natural upgrade of the former optical model, where a certain amount of liquid scintillator is introduced into the separation wall filling it from bottom to top. The main advantage of this latter method is that it affects differently bottom and top parts of the detector. The implementation of this model has brought the data to simulation agreement of the the vertical asymmetries in the response of the detector to the percent level, leading to a more homogeneous simulated response of the detector.

The simulation of neutron mobility is a very delicate topic in neutrino detection experiments. In **Stereo**, neutrons take approximately $\sim 15\,\mu s$ to be captured. The assessment of this magnitude in the simulation is necessary to fine tune the expected neutrino signals in the **Stereo** detector. Thermal scattering corrections have been included from the precision QGSP_BIC_HP libraries, notably improving the simulated behavior of neutrons during the thermalization time. This is translated into an increased simulation capture time that is in better agreement with data.

The non-linear quenching of the energy greatly determines the overall energy spectrum observed. Such effect can be described by means of the Birks' parameter k_B, and its implementation in the simulation is decisive to properly produce oscillated and non-oscillated neutrino spectra that can be compared with observations. There has been no experimental measurement of k_B in **Stereo**. For that reason, the Stitched energy-charge Method has been developed in this thesis to calculate an effective k_B for simulations directly from calibration runs. By the virtue of this method, data is continuously compared to simulations with different values of k_B, finally yielding a best fit for the quenching of $k_B = 0.0938 \pm 0.0023(\text{stat}) \pm 0.0024(\text{sys})$ mm/MeV). With this result, discrepancies $< 0.5\%$ are observed for all energies used during the tuning, with special agreement for mono-gamma sources. The combination of this analysis with parallel approaches from other teams in the experiment resulted in an official $\overline{k_B} = 0.096 \pm 0.007\,\text{mm/MeV}$. The Stitched Energy-Charge algorithm has been also used to draw conclusions on the k_B corresponding to the liquid scintillator inside the gamma catcher volume, showing agreement between both values. This result has been shown to be stable within uncertainties along the whole period of data taking.

The algorithm that reconstructs the energy spectra out of collected charge distributions is performed by the CEA team, and it is fed by several input parameters that define the topology of light collection in the detector. Part of these parameters are the so-called calibration coefficients, that represent the charge-to-energy conversion factor per cell. A special procedure has been designed during this thesis for their accurate

calculation, ensuring independence of the light cross-talk between cells by the application of fine tuned selection cuts. Such analysis has been performed for both data and simulation with the aim of producing equivalent energy reconstruction for both. By means of calibration data and spallation neutron analyses, the energy reconstruction is shown to be stable over time with a final uncertainty of 1.1% uncorrelated cell-to-cell, and 0.4% correlated cell-to-cell.

All the improvements performed in the simulation of **Stereo** along this thesis are reflected in the energy scale of the simulated neutrino energy spectrum. The comparison of cell-wise spectral distortions between measured and simulated neutrino signals has allowed **Stereo** to exclude a good part of the allowed parameter space for the sterile oscillation hypothesis. This was firstly shown in the Rencontres du Moriond 2018 [125] and followed by the International Neutrino conference 2018 in Heidelberg [126], culminating in the first publication soon afterwards [124]. With these results it has been also excluded with 3σ confidence level the initial best fit yielded by the reactor antineutrino plus gallium anomaly analyses. According to dedicated sensitivity studies, **Stereo** will have the statistics to inspect the remaining parameter space allowed by the neutrino oscillation hypothesis. Equipped with the future-proof simulation framework tested and developed throughout this thesis as its astrolabe, **Stereo** has set sail for a total of 300 days of reactor-on data taking. Soon, terra incognita will be within reach for **Stereo**, and with it the chance to finally unravel the existence of sterile neutrinos.

Appendix A

Light Leaks Estimation from Cosmic Rays

During regular data taking, vertical cosmic ray events are tagged by the muon veto with an efficiency of 99.9% [124], as described in Sec. 3.3.3. The main purpose for tagging muon events is to reject them, apply a time window cut over coincidence candidates and avoid correlated background. Cosmic events happen at the $\sim$ kHz rate that fluctuates according to atmospheric conditions [134]. Light cross-talk between cells in **STEREO**, also referred as *light leaks* during this thesis, are monitored using cosmic ray events.

As most of the monitoring software, the technique that extracts *light leaks* from cosmic rays was developed by the LPSC group [134]. It revolves around non-saturation energy depositions from these particles in the cell where *light leaks* are being calculated. In the specific case of muons, the minimum ionization $dE/dx \sim 2\,\mathrm{MeV/cm}$ for carbon [54] which can be approximated to the `LS` of **STEREO**, assuming a density $\sim 1\,\mathrm{gcm}^3$ to simplify the extrapolation. For vertical or quasi-vertical muons, a path of $\sim 90\,\mathrm{cm}$ from top to bottom of the cell is traveled, leaving behind a maximum energy deposition of about 180 MeV. Translated into charge, it roughly adds up to $45000 - 50000$ PE in a

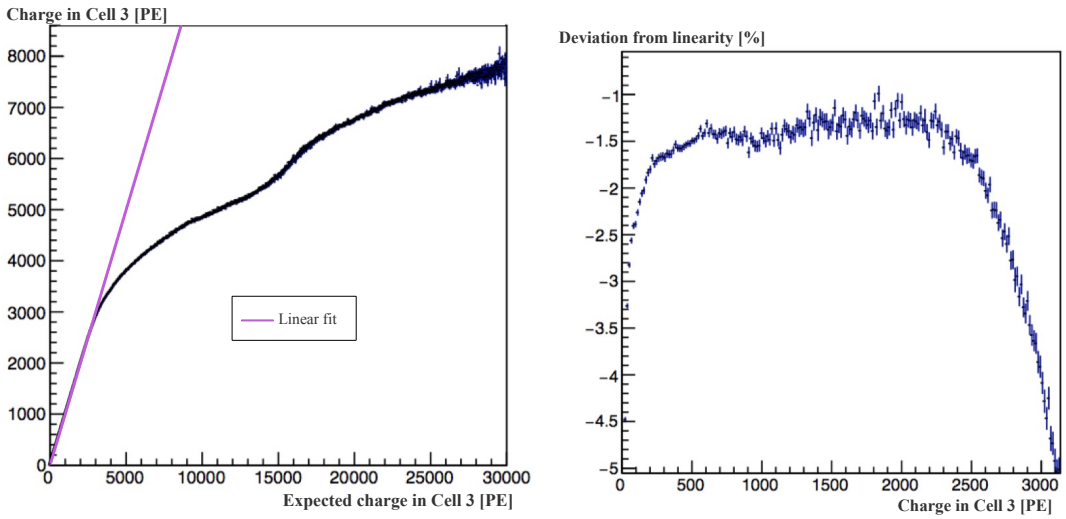

(a) **(b)**

Figure A.1: Linearity of the response of the PMTs in `Cell3` using physics runs, scaled to the response of one single PMT. (a) Expected response from known *light leaks* versus real response. The non-linear regime starts above the $\sim$ 2500 PE threshold. (b) Deviation from linearity of the real response showed in (a) [135].

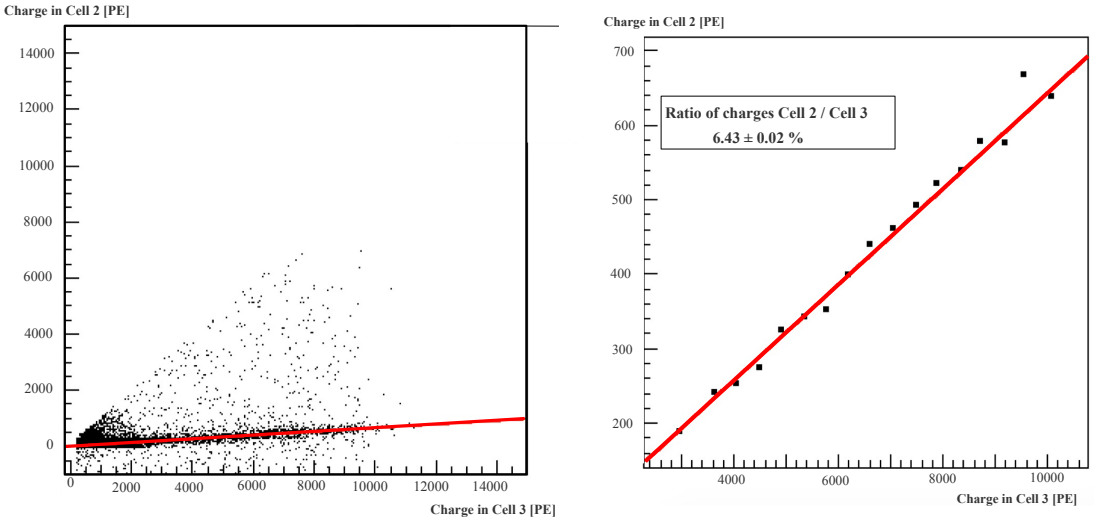

(a) **(b)**

Figure A.2: Correlation between charge desposited in `Cell3` and `Cell2` for vertical muons tagged in `Cell3`. (a) Complete scatter plot for deposited charges in both cells. (b) Fit range from which the *light leaks* value is extracted.

single cell, well beyond the linear range of the PMTs described in Fig. 3.17, extracted from periodic LED calibrations. Even though physical signals have wider responses and thus the linear response of the PMT can be extended up to $\sim$ 2500 PE [135], signals are far from linearity. In Fig. A.1(a) it can be seen real versus expected deposited charge in `Cell3`. The latter is calculated as the correspondent charge deposition to generate the observed charges a neighboring cell, e.g `Cell2`, according to the observed *light leaks*. Indeed, this kind of plot can only be produced once the *light leaks* have been calculated as described in the next paragraph.

Saturated signals cannot be used to extract reliable charge information from the cell crossed by the muon and thus neither from the *light leaks*. For this reason, from all cosmic data, only the events with signals within the linear range of the PMTs are used to calculate the *light leaks*. The method used requires then that the charge deposited in the main cell lies between 3000 and 11500 PE, roughly giving 2500 PE per PMT. For cells with bad light collection, as `Cell4` and `GCFront` during *Phase I*, the range is adjusted to 900 and 3400 PE. Charge deposited in neighboring cells is then extracted and compared with the charge deposited in the main cell, as displayed in Fig. A.2(a). The events displayed are in Fig. A.2(b) are fitted to a linear function and from the slope the value for *light leaks* can be extracted between the main cell and each one of its neighboring cells. Generally, the average *light leaks* during a period of 48 h is used to avoid run-to-run discrepancies.

Appendix B

Fit Functions

In this appendix, the different functions used to fit charge distributions have been described. Generally, a clean mono-energetic deposition from a particle in a certain detector would be observed as a pure Gaussian distribution

$$g(x; N, \mu, \sigma) = \frac{N}{\sqrt{2\pi\sigma^2}} \exp\left\{-\frac{(x-\mu)^2}{2\sigma^2}\right\}, \tag{B.1}$$

where the standard deviation σ of the bell corresponds to the energy resolution of the detector. μ is the most probable value of the distribution which is also the mean value, and N is a generalized normalization factor. However, experimental factors like insufficient background substraction, imperfect energy containment or detection inefficiencies usually widen and distort the response of the detector. One way to characterize detector signals is to fit only the peak deposition with a simple Gaussian function in Eq. B.1. This approach depends heavily on the range chosen for the fit, the chosen binning of the distribution and the cleanness of the signal. A most common fit function used is the Crystal Ball [158],

$$\mathcal{C}(x; \alpha, n, \mu, \sigma) = N \cdot \begin{cases} \exp\left\{-\frac{(x-\mu)^2}{2\sigma^2}\right\}, & \text{if } \frac{x-\mu}{\sigma} > -\alpha \\ \left(\frac{n}{|\alpha|}\right)^n \exp\left\{\frac{-|\alpha|^2}{2}\right\} \left(\frac{n-|\alpha|^2}{|\alpha|} - \frac{x-\mu}{\sigma}\right)^{-n}. & \text{otherwise} \end{cases} \tag{B.2}$$

With 5 parameters, it consists of a Gaussian core portion (σ, μ) that becomes an exponential tail (n) below a certain threshold indicated by the parameter α. A Crystal Ball fit was often used to parametrize the detector response to ^{54}Mn source deployments at the beginning of this thesis. However, the complex parametrization in Eq. B.2 tended to deliver unstable results for *intermediate cells* like `Cell3` or `GCIN20`, and it was completely unsuitable for multi-gamma sources with multiple peaks to be fitted. For that reason, the staple fit function used along the analysis of this thesis was shifted to a *GaussExp* function, described in the next sections.

The *GaussExp* function

The *GaussExp* function has been extracted from [157]. This functions has a similar concept as the Crystal Ball, with a main Gaussian contribution followed by an exponential

tail,

$$\mathcal{G}(x; N, k, \mu, \sigma) = N \cdot \begin{cases} \exp\left\{-\dfrac{(x-\mu)^2}{2\sigma^2}\right\}, & \text{if } \dfrac{x-\mu}{\sigma} \geqslant -k \\ \exp\left\{\dfrac{k^2}{2} + k\dfrac{x-\mu}{\sigma}\right\}, & \text{otherwise}. \end{cases} \tag{B.3}$$

This function is defined by 4 parameters. Again, μ and σ represent the Gaussian mean and standard deviation, and k represents the decay constant of the exponential tail. However, the number of parameters have been reduced by one with respect to Eq. B.2, where n and α have been combined into k which is also the number of standard deviations from μ to the start of the exponential tail. Both Eq. B.2 and Eq. B.3 have an identical Gaussian part and a very similar exponential tail that has been simiplified in the case of the *GaussExp*. As can be seen in the next sections, the *GaussExp* function can be easily modified for multi-gamma sources, leading to stable and coherent results in Chap. 6 and Chap. 7.

Mirror-GaussExp

The exponential tail of a *GaussExp* function can be recomputed to the right side of the Gaussian. The resulting function takes the form,

$$\mathcal{Q}(x; N, k, \mu, \sigma) = N \cdot \begin{cases} \exp\left\{-\dfrac{(x-\mu)^2}{2\sigma^2}\right\}, & \text{if } \dfrac{x-\mu}{\sigma} \leq k \\ \exp\left\{\dfrac{k^2}{2} + k\dfrac{x-\mu}{\sigma}\right\}, & \text{otherwise}, \end{cases} \tag{B.4}$$

where the only change with respect to Eq. B.3 is the point where the Gaussian becomes the exponential tail.

Double-GaussExp

The natural evolution of a *GaussExp* is the *Double-GaussExp* function, which accounts for a double peak in a distribution. The function is defined as the sum of two *GaussExp*,

$$\mathcal{G}_2(x; \mathbf{p}_1, \mathbf{p}_2) = \mathcal{G}(x; \mathbf{p}_1) + \mathcal{G}(x; \mathbf{p}_2). \tag{B.5}$$

This function has a total of 8 parameters $\mathbf{p}_1 = \{N_1, k_1, \mu_1, \sigma_1\}$ and $\mathbf{p}_2 = \{N_2, k_2, \mu_2, \sigma_2\}$.

Triple-GaussExp for ^{24}Na

The ^{24}Na source emits two gammas simultaneously. The response for such signal for a single cell in **Stereo** is a combination of two single-gamma peaks plus a peak corresponding to the detection of both gammas. The function is defined by a sum of two *GaussExp*, and a *Mirror-GaussExp*,

$$\mathcal{G}_3(x; \mathbf{p}_1, \mathbf{p}_2, \mathbf{p}_3, N_g, \mu_g, \sigma_g) = \mathcal{G}(x; \mathbf{p}_1) + \mathcal{Q}(x; \mathbf{p}_2) + \mathcal{G}(x; \mathbf{p}_3). \tag{B.6}$$

This function has a total of 12 parameters $\mathbf{p}_1 = \{N_1, k_1, \mu_1, \sigma_1\}$, $\mathbf{p}_2 = \{N_2, k_2, \mu_2, \sigma_2\}$ and $\mathbf{p}_3 = \{N_3, k_3, \mu_3, \sigma_3\}$.

Quad-GaussExp for ^{124}Sb

^{124}Sb is a multi-gamma source with a myriad of different simultaneous emissions. In this function a total of five peaks are accounted, two as *Double-GaussExp* functions and the remaining one as a single *GaussExp*. The sum of all contributions becomes,

$$\mathcal{G}_4(x;\mathbf{p}_1,\mathbf{p}_2,\mathbf{p}_3,\mathbf{p}_4) = \mathcal{G}_2(x;\mathbf{p}_1,\mathbf{p}_2) + \mathcal{G}(x;\mathbf{p}_3) + \mathcal{G}_2(x;\mathbf{p}_4,\mathbf{p}_5). \tag{B.7}$$

This function has a total of 20 parameters $\mathbf{p}_1 = \{N_1, k_1, \mu_1, \sigma_1\}$, $\mathbf{p}_2 = \{N_2, k_2, \mu_2, \sigma_2\}$, $\mathbf{p}_3 = \{N_3, k_3, \mu_3, \sigma_3\}$, $\mathbf{p}_4 = \{N_4, k_4, \mu_4, \sigma_4\}$, $\mathbf{p}_5 = \{N_5, k_5, \mu_5, \sigma_5\}$.

Appendix C

Error calculations

For a given function f of N independent variables $\alpha_1, ..., \alpha_N$, its associated uncertainty δ_f can be calculated as

$$\delta^2_{f(\alpha_1,...,\alpha_n))} = \sum_i^N \delta^2_{\alpha_i} \cdot \left(\frac{\partial f}{\partial \alpha_i}\right)^2 , \tag{C.1}$$

where δ_{α_i} corresponds to the standard deviation of the variable α_i [167]. The symbol $\partial f/\partial \alpha_i$ denotes the partial derivative of function f with respect to variable α_i. Eq.C.1 assumes that all variables are completely uncorrelated and independent from each other. This formula have been used to approximate the uncertainty of different magnitudes used along this thesis. The following lines compile all of them.

- The uncertainty of a product,

$$\delta^2_{A\cdot B} = (B\delta_A)^2 + (A\delta_B)^2 . \tag{C.2}$$

- The uncertainty of a ratio,

$$\delta^2_{\frac{A}{B}} = \left(\frac{A}{B}\right)^2 \left[\left(\frac{\delta_A}{A}\right)^2 + \left(\frac{\delta_B}{B}\right)^2\right] . \tag{C.3}$$

- The uncertainty of an asymmetry,

$$\delta^2_{\frac{A-B}{A+B}} = \left(\frac{2}{(A+B)^2}\right)^2 [(B\delta_A)^2 + (A\delta_B)^2] . \tag{C.4}$$

List of Figures

List of Tables

Acknowledgements

This thesis has been a challenge, endured mainly because of the good people I have had around along these years. The lines below are my personal acknowledgement to these people.

First and foremost, I would like to show my gratitude to my advisor, Prof. Lindner, for the opportunity to work at the Max-Planck-Institut in such a thrilling field as sterile neutrino oscillations, and for his guidance and counseling on my career as scientist. I would like to thank also JProf. Gastaldo for her charming predisposition to become one of my thesis referees. In this regard, my thanks also go to Prof. Grebel and Dr. Marrodan for their availability and eagerness to examine me this Spring.

A special mention should be made to JDr. Almazan for introducing me to Dr. Buck, who bought me a beer and convinced me that doing Monte Carlo simulations about the quenching of light in liquid scintillators was a good idea. Without them I would now be hopelessly unemployed.

Dr. Buck[2] should be thanked again for his important role of tutor, giving important and pertinent advice about topics, directions and priorities throughout my thesis. I would like to ask for a big and sound round of applause to the Reactor Neutrino group at the MPIK, for they have bravely helped on the corrections of my thesis even in the darkest hours pre-Moriond. These people are no other than Dr. Buck[3], Dr. Schoppmann, JDr. Almazan[2] and Dr. Bonhomme. You are the real champs. Without saying goes how much I enjoyed the lengthy and productive discussions about physics, neutrinos and german folklore. I also must recall the unforgettable contributions to our group from an emeritus academic, Dr. Haser. Wherever you are, keep the dream alive.

I would like to thank all my colleagues from the small but powerful **Stereo** collaboration. They say that great things come in small packages, and without Almazan[3] et al. I would not have experienced how much adrenaline and stress a small package can give. Honorific mentions to Dr. Sergeyeva and Dr. Minotti, who are unfortunately not longer with us (in **Stereo**). Special thanks to our spokesperson Dr. Lhuillier for his great scientific support and consideration in many parts of my thesis. Salut!

Props to all my colleagues from the MPIK with whom I have shared many laughs and anecdotes too stupid to be told, at least sober. On one side, cheers to the theoretical group, from where I would like to draw a special mention to the now Londoner Dr. Campos. And on the other side, my thanks to the XENON group that kept inviting me to join them for dinner regardless of how many times I was too busy to go. From this group, I would like to highlight Dr. Eurin and Dr. Mayani for their deficient aptitudes at managing the Frank and Mayan empires, respectively. Also, I feel compelled to mention my fellow Spaniard, MSc. Herrero, for taking everything with a grain of salt, specially the bad jokes.

It would be unfair not to remark the singular assistance brought by Dr. Buck[4] towards the completion of this thesis, in the shape of a Bavarian crate filled of full-bodied, mildly sweet and light-colored hope. This time around it is my turn to honor such token

of sportsmanship.

Also a special thanks has go to Dr. Rodejohann, for his titanic effort to join the younglings, learn their customs and make their experience at the IMPRS unforgettable. I can only hope that he will sneak me in for the next retreat. And I could never forget to give credit to the cornerstone of the division, Berneiser and Schwarz. If us physicists are the muscle, they are definitely the soul. Please, never stop smiling.

Now it is time for hugs and emotional mentions to my personal relatives that would make Snow White cringe. Lets start with my dear panecillos. Thanks to both of you, JDr. Almazan[4] and Montero who bought me some chill and relaxation when the pressure cooker risked explosion. I know the only thing you wanted is a free meal, but I love you anyway.

My boys from the old world did literally nothing to help this thesis get to fruition. Regardless, I would like to mention them here in honor to all the good laughs, beers and retarded jokes we have had over the years, and hopefully the many more to come. In particular, Navarro for his special talent to throw the dice while maniacally laughing to make me rage-quit, JDr. Contreras for all the never ending gaming nights and the time to man up, JDr. Aguado for being the most bizarre harvester of onions to ever slay a dragon, and tete Navarro for teaching me the honor code of the drunkard.

Obviament no puc deixar de mencionar la indispensable contribució dels meus pares a lo que s'ha convertit en el major repte de la meua vida. Sense vosatros res d'açò havera sigut possible. Desde Trondheim a Munich, i desde Munich a Heidelberg... hem corregut molt de mon. Pero caminava tranquil. Sabia que on estiguera, sempre anaveu en mi. A pesar dels alts i baixos que hem passat com ha familia, he de agrair-vos que sempre ens hagem mantengut units, i que sempre ens hen volgut incondicionalment. Inclús quan era xicotet i donava pel sac per a menjarme el bollit, o arrivaba tart a tots els puestos. Gràcies per estar sempre amb mí, estiga a deu o a deu mil kilometres de casa, en directe o darrere del ordenador. Esta tesis es per a vosaltres, heu hem conseguit. Vos vull.

Y por supuesto no podría olvidarme de Guirau et al, quienes con el paso del tiempo os habéis convirtiendo en parte de mi familia. Gracias por los buenos momentos, el apoyo incondicional y los arroces de pescado bajos en sal durante estos años de tanto estudio. And this is solely for Crespo, to whom I decided to write in English with a noble intention to get her to study and put some effort. Gotcha!

Last but definitely not least I would love to thank my melloni for her support. Hand in hand, we worked together from the lazy afternoons until the night of fate. Your passion broke the unbreakable chains and the rage awakened. For your sweet spirits, pretty things and Stitch, you are my dearly beloved. And remember, Ohana means family, and family means that nobody gets left behind... or forgotten. Mkaukau?

Bibliography

[1] Rutherford E, *Uranium radiation and the electrical conduction produced by it.* Philosophical Magazine. **47**, 284, 1899

[2] Hahn O et al., *Magnetische Spektren der Beta-Strahlen des Radiums.* Phys. Zeit. **12**, 1911, 1099-1101, 1911

[3] Chadwick J, *Intensitätsverteilung im magnetischen Spektrum von $\beta-$Strahlen von Radium B+C.* Verhandlungen der Deutschen Physikalischen Gesellschaft **16**, 1911, 383-391, 1914

[4] Noether E, *Invariante Variationsprobleme.* Math-phys. Klasse. 235-257, 1918

[5] Dirac P, *The Quantum Theory of the Emission and Absorption of Radiation.* Proceedings of the Royal Society of London A. **114**, 767, 243-65, 1927

[6] Dirac P, *The quantum theory of the electron.* Proceedings of the Royal Society of London, A **117**, 778, 610-624, 1928

[7] Pauli W, Reprint of the letter in *The idea of the neutrino.* Physics Today. **31** (9): 23-28, 1978 [1930]

[8] Fermi E, *Tentativo di una teoria dei raggi β.* Il Nuovo Cimento, **9**, 1, 1934.

[9] Alvarez L, *Nuclear K Electron Capture.* Phys. Rev. **52**, 134-135, 1937.

[10] Klein O, *On the theory of charged field.* Fourth talk at New Theories in Physics conference, Paris, 1939

[11] Pauli W, *On the earlier and more recent history of the neutrino.* Neutrino Physics, 1957

[12] Anderson C, *The Positive Electron.* Phys. Rev. **43** (6), 491, 1933

[13] Chadwick J, *Possible existence of the neutron.* Nature **129**, 798, 1932

[14] Reines F and Cowan CL, *Detection of free antineutrino.* Phys. Rev. **92**, 830, 1953

[15] Reines F and Cowan CL et al., *Detection of free antineutrino: a confirmation.* Science. **124**, 3212, 103-4, 1956

[16] Lederman L et al., *Observation of high-energy neutrino reactions and the existence of.* Phys. Rev. Lett. **9**, 36, 1962

[17] Perl ML et al., *Evidence for Anomalous Lepton Production in e^+e^- annihilation.* Phys. Rev. Lett. **35**, 221489, 1975

[18] Kodama K et al. [DONUT Collaboration], *Observation of Tau Neutrino Interactions*. Phys. Lett. B **504**, 218-224, 2001

[19] Hernandez J et al. [Particle Data Group], *Review of particle properties*. Phys. Lett. B **239** VI.22-VI.23, 1990

[20] Schael S et al. [SLD Electroweak group, DELPHI, ALEPH, SLD, SLD Heavy flavor group, OPAL, LEP Electroweak working group, L3], *Precision electroweak measurements of the Z resonance*. Phys. Rept **427**, 257, 2006

[21] Lee T and Yang C, *Question of Parity Conservation in Weak Interactions*. Phys. Rev. **104**, 254, 1956

[22] Wu CS et al., *Experimental Test of Parity Conservation in Beta Decay*. Phys. Rev. **105**, 1413-1415, 1957

[23] Goldhaber M et al., *Helicity of Neutrinos*. Phys. Rev. **109**, 1015, 1958

[24] Feynman R and Gell-Mann M, *Theory of the Fermi Interaction*. Phys. Rev. **109**, 193, 1958

[25] Glashow S, *The renormalizability of vector meson interactions*. Nucl. Phys. **10**, 107, 1959

[26] Salam A and Ward J, *Weak and electromagnetic interactions*. Nuovo Cimento. **11**, 4, 568-577, 1959

[27] Weinberg S, *A Model of Leptons*. Phys. Rev. Lett. **19**, 1264-66, 1967

[28] Yukawa H, *On the interaction of Elementary Particles I*. Proc. Phys.-Math. Soc. Jpn. **17**, 48, 48-57, 1935

[29] Higgs P, *Broken symmetries, massless particles and gauge fields*. Phys. Lett. **12**, 2, 132-133, 1964

[30] Englert F and Brout R, *Broken symmetry and the mass of gauge vector mesons*. Phys. Rev. Lett. **13**, 9, 321-323, 1964

[31] Guralnil G et al., *Global conservation laws and massless particles*. Phys. Rev. Lett. **13**, 20, 585-587, 1964

[32] Pich A, *The Standard Model of Electroweak Interactions*. arXiv:1201.0537, 2012

[33] Arnison G et al. [UA1 Collaboration], *Experimental observation of large transverse energy electrons with associated missing energy at* $\sqrt{s} = 540\ GeV$. Phys. Lett. B **122**, 1, 103-116 1983

[34] Banner M et al. [UA2 Collaboration], *Observation of single isolated electrons of high transverse momentum in events with missing transverse energy at the CERN pp collider*. Phys. Lett. B **122**, 5-6, 476-485, 1983

[35] Arnison G et al. [UA1 Collaboration], *Experimental Observation of Lepton Pairs of Invariant Mass Around* $95 GeV/c^2$ *at the CERN SPS Collider*. Phys. Lett. B **126**, 1, 398-410, 1983

[36] Bagnaia P et al. [UA2 Collaboration], *Evidence for $Z_0 \to e^+e^-$ at the CERN anti-p p Collider*. Phys. Lett. B **129**, 130-140, 398-410, 1983

[37] Soper D, *Basics of QCD perturbation theory*. arXiv:hep-ph/9702203v1, 1997

[38] Bazavov A, *Nonperturbative QCD simulations with 2+1 flavors of improved staggered quarks*. Reviews of Modern Physics. **82**, 2, 1349-1417, 2010

[39] Robert C, *Three Lectures on Hadron Physics*. arXiv:1509.02925v1, 2015

[40] Cerenkov P, *Visible radiation produced by electrons moving in a medium with velocities exceeding that of light*. Phys. Rev. **52**, 378-379, 1937.

[41] Davies H et al., *Theory of Bremsstrahlung and Pair Production*. Phys. Rev. **93**, 788-795, 1954.

[42] Birks J, *The theory and practice of scintillation counting*. Pergamon Press, New York, 1964

[43] Pontecorvo B, *Mesonium and Antimesonium*. Soviet physics, Journal of Experimental and Theoretical Physics **6**, 429-431, 1958 [translation]

[44] Pontecorvo B, *Inverse Beta Decay and Non-conservation of Lepton Charge*. Soviet physics, Journal of Experimental and Theoretical Physics **7**, 172-173, 1958 [translation]

[45] Maki Z, Nakagawa M and Sakata S, *Progress on the theoretical physics*. Physics **28**, 870, 1962

[46] Wolfenstein L, *Neutrino oscillations in matter*. Phys. Rev. D **17**, 9, 2369-2374, 1978

[47] Mikheyev S, Smirnov A and Yu A, *Resonance enhancement of oscillations in matter and solar neutrino spectroscopy*. Soviet Journal of Nuclear Physics. **42**, 6, 913-917, 1985

[48] Aseev VN et al., *Upper limit on the electron antineutrino mass from the Troitsk experiment*. Phys. Rev. D **84**, 112003, 2011

[49] Kraus C et al., *Final results from phase II of the Mainz neutrino mass searching tritium β decay*. Eur. Phys. J. C **40**, 4, 447-468, 2005

[50] Angrik J et al. [KATRIN Collaboration], *KATRIN design report*. FZKA-7090, 2004

[51] Lesgourgues J, *Neutrinos in Cosmology*. Review in PDG 2017 edition

[52] Majorana E, *Theory of the Symmetry of Electrons and Positrons*. Nuovo Cim. **14**, 71-184, 1937

[53] Schechter J et al., *Neutrino Masses in SU(2)$\times$U(1) Theories*. Phys. Rev. D **22**, 2227, 1980

[54] Tanabashi M et al., *Particle Data Group*. Phys. Rev. D **98**, 030001, 2018

[55] David R et al., *Search for Neutrinos from the Sun.* Phys. Rev. Lett. **20**, 1205, 1968

[56] Hirata KS et al. [KamiokaNDE-II Collaboration], *Observation of a Neutrino Burst from the Supernova SN1987A.* Phys. Rev. Lett. **58**, 14, 1490-1493, 1987

[57] Hirata KS et al. [KamiokaNDE-II Collaboration], *Observation of a small atmospheric ν_μ/ν_e ratio in Kamiokande.* Phys. Lett. B **280**, 146-152, 1992

[58] Fakuda Y et al. [Super-Kamiokande Collaboration], *Evidence for oscillation of atmospheric neutrinos.* Phys. Rev. Lett., Letters. **81**, 8, 1562-1567, 1998

[59] Ahmad Q et al. [SNO Collaboration], *Measurement of the Rate of $\nu_e + d \rightarrow p + p + e^-$ Interactions Produced by ^8B Solar Neutrinos at the Sudbury Neutrino Observatory.* Phys. Rev. Lett. **87**, 071301, 2001

[60] Alimonti G et al., *Science and Technology of BOREXINO: A Real Time Detector for Low Energy Solar Neutrinos SOLAR NEUTRINOS.* Astropart. Phys. **16**, 3, 205, 2002.

[61] Gavri V et al. [SAGE Collaboration], *Solar Neutrino Results from SAGE.* Particles and Nuclei, Letters. **108**, 5, 2001

[62] Kirsten T [GALLEX Collaboration], *GALLEX solar neutrino results.* Progress in Particle and Nuclear Physics **40**, 85-99, 1998

[63] Eguchi K et al. [KamLAND Collaboration], *First results from KamLAND: Evidence for reactor anti-neutrino disappearance.* Phys. Rev. Lett. **90**, 021802, 2003

[64] Giunti C et al., *Statistical Significance of the Gallium Anomaly.* Phys. Rev. C **83**, 065504, 2011

[65] Boehm F et al. [CAL TECH-GRENOBLE-TUM Collaboration], *Experimental Study Of Neutrino Oscillations At A Fission Reactor.* Phys. Lett. B **97**, 310-314, 1980

[66] Cavaignac J et al. [Bugey Collaboration], *Indication for Neutrino Oscillation From a High Statistics Experiment at the Bugey Reactor.* Phys. Lett. B **148**, 387-394, 1984

[67] Zacek G et al. , *Neutrino-oscillation experiments at the Gösgen nuclear power reactor.* Phys. Rev. D **34**, 2621, 1986

[68] Declais Y et al. [Bugey Collaboration], *Search for neutrino oscillations at 15-meters, 40-meters, and 95-meters from a nuclear power reactor at Bugey.* Phys. Lett. B **434**, 3, 503-532, 1995

[69] Apollonio M et al. [Chooz Collaboration], *Limits on Neutrino Oscillations from the CHOOZ Experiment.* Phys. Lett. B **466**, 415, 1999

[70] Boehm F et al. [Palo Verde Collaboration], *Search for Neutrino Oscillations at the Palo Verde Nuclear Reactors.* Phys. Rev. Lett. **84**, 3764, 2000

[71] Wen L et al., *Reactor Neutrino Experiments: Present and Future.* arXiv:1803.10162v1, 2018

[72] Fogli G et al., *Hints of $\theta_{13} > 0$ from Global Neutrino Data Analysis*. Phys. Rev. Lett. **101**, 141801, 2008

[73] Abe Y et al. [Double Chooz Collaboration], *Indication of Reactor $\bar{\nu}_e$ Disappearance in the Double Chooz Experiment*. Phys. Rev. Lett. **108**, 131801, 2012

[74] An F et al. [Daya Bay Collaboration], *Observation of Electron-Antineutrino Disappearance at Daya Bay*. Phys. Rev. Lett. **108**, 171803, 2012

[75] Ahn J et al. [RENO Collaboration], *Observation of Reactor Electron Antineutrinos Disappearance in the RENO Experiment*. Phys. Rev. Lett. **108**, 191802, 2012

[76] An F et al. [JUNO Collaboration], *Neutrino physics with JUNO*. J. Phys. G **43**, 030401, 2016

[77] Aberle C et al., *Large Scale Production of the Liquid Scintillator for the Double Chooz Experiment*. Nucl. Phys. B **229**, 448, 2012.

[78] Von Feilitzsch F et al., *Experimental beta-spectra from ^{239}Pu and ^{235}U thermal neutron fission products and their correlated antineutrino spectra*. Phys. Lett. B **162**, 162-166, 1982

[79] Schreckenbach K et al., *Determination of the antineutrino spectrum from ^{235}U thermal neutron fission products up to 9.5 MeV*. Phys. Lett. B **160**, 325-328, 1985

[80] Hahn A et al., *Antineutrino spectra from ^{241}Pu and ^{239}Pu thermal neutron fission products*. Phys. Lett. B **218**, 365-368, 1989

[81] Haag N et al., *Experimental Determination of the Antineutrino Spectrum of the Fission Products of ^{238}U*. Phys. Rev. Lett. **112**, 122501, 2014

[82] Vogel P et al., *Reactor antineutrino spectra and their application to antineutrino-induced reactions*. Phys. Rev. C **24**, 1543, 1981

[83] Klapdor H et al., *Calculation of the antineutrino spectrum from thermal fission of ^{235}U*. Phys. Lett. B **112**, 22, 1982

[84] Vogel P et al., *Angular distribution of neutron inverse beta decay, $\bar{\nu}_e + p \rightarrow e^+ + n$*. Phys. Rev D **60**, 053003, 1999.

[85] Kopeikin V et al., *Components of antineutrino emission in nuclear reactor*. Phys. Atom. Nucl. **67**, 1963, 2004

[86] Fallot M et al., *New Antineutrino Energy Spectra Predictions from the Summation of Beta Decay Branches of the Fission Products*. Phys. Rev. Lett. **109**, 202504, 2012

[87] Hayes A et al., *Systematic Uncertainties in the Analysis of the Reactor Neutrino Anomaly*. Phys. Rev. Lett. **109**, 202504, 2014

[88] Hayes A et al., *Reactor Neutrino Spectra*. Ann. Rev. Nucl. Part. Sci. **66**, 219, 2016

[89] Huber P, *Determination of antineutrino spectra from nuclear reactors*. Phys. Rev. C **84**, 024617, 2011

[90] Mueller Th A et al., *Improved predictions of reactor antineutrino spectra.* Phys. Rev. C **83**, 054615, 2011

[91] Mention G et al., *Reactor antineutrino anomaly.* Phys. Rev. D **83**, 073006, 2011

[92] An F et al. [Daya Bay Collaboration], *Measurement of the Reactor Antineutrino Flux and Spectrum at Daya Bay.* Phys. Rev. Lett. **116**, 061801, 2016

[93] Abe Y et al. [Double Chooz Collaboration], *Improved measurements of the neutrino mixing angle θ_{13} with the Double Chooz detector.* J. High Energy Phys. **10**, 086, 2014

[94] Seo SH et al. [RENO Collaboration], *New results from RENO and the* 5 MeV *excess.* Proceedings AIP conderence **1666**, 080002, 2015

[95] Kopp J et al., *Improved predictions of reactor antineutrino spectra.* J. High Energy Phys **05**, 050, 2013

[96] Giunti C et al., *Pragmatic view of short-baseline neutrino oscillations.* Long, Phys. Rev. D **88**, 073008, 2013

[97] Hayes A et al., *Systematic Uncertainties in the Analysis of the Reactor Neutrino Anomaly.* Phys. Rev. Lett. **112**, 202501, 2014

[98] Hayes A et al., *Possible origins and implications of the shoulder in reactor neutrino spectra.* Phys. Rev. D **92**, 033015, 2015

[99] Buck C et al., *Investigating the spectral anomaly with different reactor antineutrino experiments.* Phys. Lett. B **765**, 159-162, 2017

[100] An F et al. [Daya Bay Collaboration], *Measurement of the Reactor Antineutrino Flux and Spectrum at Daya Bay.* Phys. Rev. Lett. **118**, 251801, 2017

[101] Abe K et al. [T2K Collaboration], *Search for CP Violation in Neutrino and Antineutrino Oscillations by the T2K Experiment with* 2.2×10^{21} *Protons on Target.* Phys. Rev. Lett. **121**, 171802, 2018

[102] Abe K et al. [T2K Collaboration], *Search for light sterile neutrinos with the T2K far detector Super-Kamiokande at a baseline of 295km.* arXiv:1902.06529v1, 2019

[103] Aguilar A et al. [LSND Collaboration], *Evidence for neutrino oscillations from the observation of $\bar{\nu}_e$ appearance in a $\bar{\nu}_\mu$ beam.* Phys. Rev. D **64**, 112007, 2001

[104] Aguilar-Arevalo A et al. [MiniBooNE collaboration], *Improved search for $\bar{\nu}_\mu \to \bar{\nu}_e$ oscillations in the MiniBooNE experiment.* Phys. Rev. Lett. **110**, 161801, 2013

[105] Aguilar-Arevalo A et al. (MiniBooNE collaboration), *Significant excess of electron-like events in the MiniBooNE short-baseline neutrino experiment.* Phys. Rev. Lett. **121**, 221801, 2018

[106] Bahcall J et al. [GALLEX Collaboration], *Limits on the electron-neutrino oscillations from the GALLEX ^{51}Cr source.* Phys. Lett. B **348**, 121, 1995

[107] Bahcall J et al. [GALLEX Collaboration], *Gallium solar neutrino experiments: Absorption cross-sections, neutrino spectra, and predicted event rates*. Phys. Rev. C**56**, 3391-3409, 1997

[108] Abdurashitov J et al. [SAGE Collaboration], *Measurement of the response of a Ga solar neutrino experiment to neutrinos from a ^{37}Ar source*. Phys. Rev. C **73**, 045805, 2006

[109] Ashenfelter J et al. [PROSPECT Collaboration], *The PROSPECT Reactor Antineutrino Experiment*. arXiv:1808.00097v1, 2018

[110] Ashenfelter J et al. [PROSPECT Collaboration], *First search for short-baseline neutrino oscillations at HFIR with PROSPECT*. arXiv:1806.02784v4, 2018

[111] Abreu Y et al. [SoLid Collaboration], *SoLid: An innovative anti-neutrino detector for searching oscillations at the SCK-CEN BR2 reactor*. Nucl. Instr. and Methods A **845**, 467-470, 2017

[112] Manzanillas L [on behalf of SoLid Collaboration], *Performance of the SoLid Reactor Neutrino Detector*. Proceedings ICHEP2018 conference, arXiv:1811.05694v1, 2018

[113] Alekseev I et al. [DANSS Collaboration], *Search for sterile neutrinos at the DANSS experiment*. Physics Lett B **787**, 56-63, 2018

[114] Danilov M [on behalf of DANSS Collaboration], *Recent results of the DANSS experiment*. Proceedings La Thuile 2018 conference, arXiv:1811.07354v1 , 2018

[115] Ko Y et al. [NEOS Collaboration], *Sterile neutrino search at NEOS Experiment*. Phys. Rev. Lett. **118**, 121802, 2017

[116] Kim J [on behalf of NEOS Collaboration], *Status of NEOS Experiment*. Talk at LLWI 2019, 2019

[117] Serebrov A et. al [Neutrino-4 Collaboration], *Experiment Neutrino-4 and restrictions for sterile neutrino*. arXiv:1708.00421, 2017

[118] Serebrov A et. al [Neutrino-4 Collaboration], *The first observation of effect of oscillation in Neutrino-4 experiment on search for sterile neutrino*. arXiv:1809.10561, 2018

[119] Gariazzo S et al., *Updated Global 3+1 Analysis of Short-BaseLine Neutrino Oscillations*. arXiv:1703.00860

[120] Giunti C et al., *eV-scale Sterile Neutrinos*. arXiv:1901.08330v1

[121] Adamson P et. al [Daya Bay and MINOS Collaborations], *Limits on Active to Sterile Neutrino Oscillations from Disappearance Searches in the MINOS, Daya Bay, and Bugey-3 Experiments*. Phys. Rev. Lett. **117**, 151801, 2016

[122] Lhuillier D et al., *Proposal of a search for sterile neutrinos at ILL: the* **Stereo** *experiment*. Proposal **Stereo** Experiment, 2012

[123] Allemandou N et al., *The* **Stereo** *Experiment*. arXiv:1804.09052v2, 2018

[124] Almazan H et al., *Sterile Neutrino Constraints from the* **Stereo** *Experiment with 66 days of Reactor-on Data*. Phys. Rev. Lett. **121**, 16, 161801, 2018

[125] Lhuillier D [on behalf of **Stereo** Collabotion] *Search for Sterile ν at Short Baseline The* **Stereo** *Experiment*. Talk at 53rd Rencontres du Moriond, 2018

[126] Lamblin J [on behalf of **Stereo** Collabotion] *Latest Results of the* **Stereo** *Experiment*. Talk at XXVIII International Conference on Neutrino Physics and Astrophysics, doi:10.5281/zenodo.1286998 , 2018

[127] Bernard L [on behalf of **Stereo** Collabotion] *Latest Results of the* **Stereo** *Experiment* [title not set yet]. Talk at 54rd Rencontres du Moriond, 2019

[128] Lhuillier D et al., *ILL Data*. doi: 10.5291/ILL-DATA.ST-6, doi: 10.5291/ILL-DATA.ST-7

[129] Lhuillier D et al., *ILL Data*. doi: 10.5291/ILL-DATA.ST-8, doi: 10.5291/ILL-DATA.ST-9.

[130] Buck C et al., *Light Propagation and Fluorescence Quantum Yields in Liquid Scintillators*. JINST, **10** P09007, 2015

[131] Buck C et al., *Production and Properties of the Liquid Scintillators used in the Stereo Reactor Neutrino Experiment*. JINST, **14,** P01027, 2019

[132] Thoreau A, *Acrylic Plates ,internal note*. Stereo docDB, stereo-doc-80-v1, 2015

[133] Materna T, *Caractérisation optique du VM2000*. Stereo docDB, stereo-doc-9-v2, 2014

[134] Real JS, *Light Leaks determination using neutrino run*. Stereo docDB, stereo-doc-165-v6, 2016

[135] Real JS, *Simulation of Muons in the* **Stereo** *Experiment*. Stereo docDB, stereo-doc-96, 2015

[136] TU München, **Stereo** *liquid scintillator elemental analysis (CHN)*. Stereo docDB: stereo-doc-517-v1, 2016

[137] Helaine V et al., **Stereo** *NOMAD, and monitoring tools Quick Tutorial*. Stereo docDB: stereo-doc-135-v6

[138] Blanchet A, *Quenching Effect on Energy Reconstruction*. Stereo docDB, stereo-doc-398-v1

[139] Sergeyeva V, *AmBe PSD study for quenching*. Stereo docDB, stereo-doc-560-v1

[140] Sergeyeva V, *MC pValues in VM2000 sandwiches: only GC interface*. Stereo docDB, stereo-doc-560-v1

[141] Sergeyeva V, *`GC cc` & quenching plots for blessing and comment*. Stereo docDB, stereo-doc-654-v1

[142] Almazan H, *Neutron studies in* **Stereo**. Stereo docDB, stereo-doc-9-v2, 2015-2018

[143] Minotti A, *Light Leaks calculation methods: ^{54}Mn and neutrino runs*. Stereo docDB, stereo-doc-205-v1, 2017

[144] Lhuillier D, *Energy escale and kB*. Stereo docDB, stereo-doc-484

[145] Helaine V et al., *Electronics for the* **Stereo** *experiment*. arXiv:1610.00003v1, 2016

[146] Blanchet A, *Energy Reconstruction in the* **Stereo** *experiment*. Poster Neutrino 2018, Heidelberg

[147] Kandzia F, *Search for a sterile neutrino with the* **Stereo** *experiment: shielding optimisation and energy calibration*. High Energy Physics - Experiment. Universite Grenoble Alpes, 2017

[148] Mutti P et al. *Nomad more than a simple sequencer*. Proceedings ICALEPCS conference, 2011

[149] National Nuclear Data Center, *Online data base of the Evaluated Nuclear Structure Data File*. http://www.nndc.bnl.gov/ensdf/, 2018.

[150] National Nuclear Data Center, *ENDF/B-VIII.0 Nuclear Data for Science and Technology: Cross Sections, Covariances, Fission Product Yields and Decay Data*. Nuclear Data Sheets **148**, 1-420, 2018

[151] Nuclear Energy Agency *Java-based Nuclear Data Information System 4.0*. https://www.oecd-nea.org/janis/

[152] Nucleide org, *Gd-158 isotope*. http://www.nucleide.org/Laraweb/

[153] Wright D, *A Short Guide to Choosing a Physics List*. Geant4 Tutorial at Jefferson Lab, SLAC, 2012

[154] Pelowitz D, *MCNPX users Manual Version 2.7.0*. LA-CP-11-00438, 2011

[155] Agostinelli S et al. [GEANT4 Collaboration], *GEANT4: A Simulation toolkit*. Nucl. Instrum. Meth. A506 250-303, 2003

[156] Hagmann C et al., *Cosmic-ray Shower Library (CRY)*. UCRL-TM-229453 , 2012

[157] Das S, *A simple alternative to the Crystal Ball function*. arXiv:1603.08591, 2016

[158] Das S *A simple alternative to the Crystal Ball function*. arXiv:1603.08591, 2016

[159] Knoll G, *Radiation Detection and Measurement*. 3rd ed. John Wiley and Sons, New York, 2000.

[160] Hamamatsu Photonics KK, *Large Photocathode are photomultiplier tubes*. https://www.hamamatsu.com/resources/pdf/etd/LARGE_AREA_PMT_TPMH1286E.pdf, 2016

[161] Bauer C et al., *Qualification Tests of 474 Photomultiplier Tubes for the Inner Detector of the Double Chooz Experiment*. arXiv:1104.0758v2, 2011

[162] Haser J et al., *Afterpulse Measurements of R7081 Photomultipliers for the Double Chooz Experiment*. arXiv:1301.2508v1, 2013

[163] Wang W et al., *Performance of the 8-in. R5912 photomultiplier tube with super bialkali photocathode.* JINST, **10**, 08, 001-001 2015

[164] Janecek M, *Optical Reflectance Measurements for Commonly Used Reflectors.*

[165] Scherzinger J et al., *Tagging fast neutrons from an 241Am/9Be source.* arXiv:1405.2686, 2014

[166] Abramowitz M et al. *Handbook of Mathematical Functions with Formulas, Graphs, and Mathematical Tables.* New York: Dover Publications, 1970

[167] Ku H, *Notes on the use of propagation of error formulas.* Journal of Research of the National Bureau of Standards C **70**, 4, 262, 1966

[168] Snodgrass M, *Encyclopedia of Kitchen History.* Taylor & Francis Group, p162-163: Impact of funnel in modern Neutrino Physics, 2005

[169] Bosch H, *Cutting the Stone.* Museo Nacional del Prado, Madrid, painted in 1494